Scaling Flexible Marine Propellers for Model Testing

MSc Thesis

J. Weersma

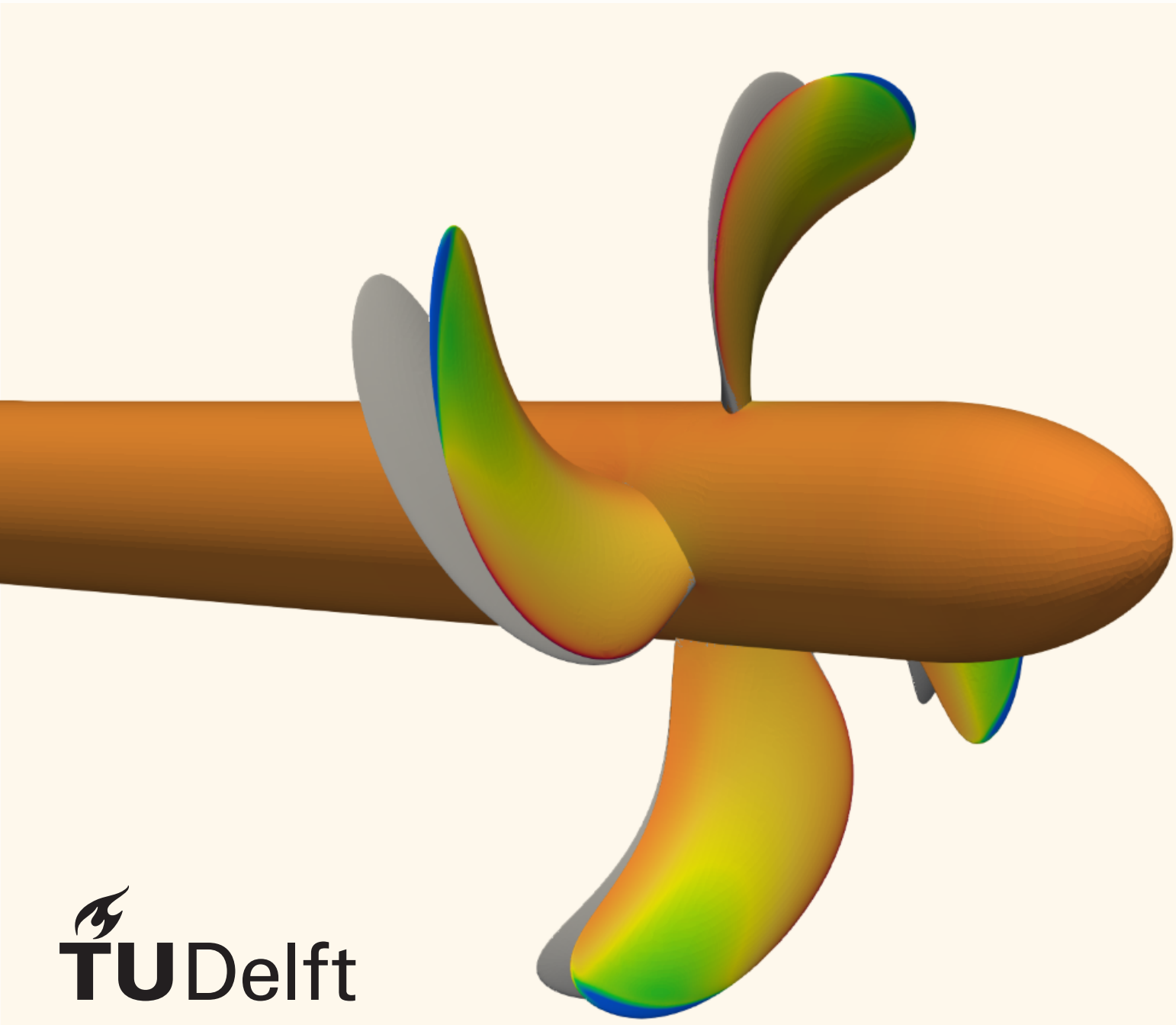

TU Delft

Thesis for the degree of MSc in Marine Technology in the specialisation of Ship Hydromechanics

Scaling Flexible Marine Propellers for Model Testing

by

J. Weersma

September 17, 2025
Faculty of Mechanical Engineering, Delft University of Technology

Thesis Supervisors

Responsible supervisor:	Prof. dr. ir. T.J.C. van Terwisga
Daily supervisor:	Ir. L.P. Lagendijk
Supervisor:	Dr. ir. H.C.J. van Wijngaarden
Supervisor:	Ir. H.C. Neatby

Thesis Exam Committee

Prof. dr. ir. J.T.C. van Terwisga
Ir. L.P. Lagendijk
Dr. ir. H.C.J. van Wijngaarden
Ir. H.C. Neatby
Dr. J. Jovanova
Dr.ir. A.H. van Zuijlen

Document Information

Thesis number:	MT.24/25/055.M.
Student number:	5144396
Author contact e-mail:	

TU Delft

Preface

Dear reader,

This report is written to complete my Master's thesis research. With this complete, I am only a few final steps away from obtaining my Master's degree in Marine Technology at Delft University of Technology. Over the past months, I have had the valuable opportunity to deepen my understanding of flexible marine propellers, numerical simulations and fluid-structure interaction, developing essential skills needed for scientific research.

This project would not have been possible without the support and guidance of many individuals. I would first like to thank Tom van Terwisga. Tom, thank you for your supervision throughout this project, as well as for the guidance you provided for my project abroad and your enthusiastic and inspiring lectures. You could always make the time and effort to help, which I am genuinely impressed and thankful for.

In addition, I want to thank Laurens-Jan Lagendijk for his guidance throughout this project. Laurens-Jan, thanks for your assistance, the weekly meetings (most weeks even more) and invaluable input throughout the project. I wish you all the best for the rest of your PhD thesis. Also, I want to express my appreciation to Erik van Wijngaarden and Holly Neatby for sharing their expertise on composite, flexible marine propellers and their valuable insights during the update meetings.

Furthermore, I would like to thank my family and friends for their support. Moppies, Oesters, Ank, Af, Thijs, Gerben, Maaike, Hidde, and Jolien, thank you for the endless coffee breaks, bike rides, and for occasionally preparing my dinner. Ian and Gonny, thank you so much for everything you did for me over the last 24 years. Lars, thanks for always being there. I cannot say how much I appreciate your help, reading my work, providing feedback, discussing problems and taking care of me when I forget to drink or eat.

I wish you all a pleasant reading. Reading this report will deepen your knowledge of flexible marine propellers and scaling laws for (flexible) propeller model tests. May it help you steer smoothly through the sometimes turbulent waters of hydrodynamics.

J. Weersma
Delft, September 2025

Abstract

Composite materials can be used to fabricate flexible marine propellers, which can improve efficiency and reduce underwater radiated noise. Since the hydrodynamic performance of flexible propellers is determined by their deformation under fluid loading, similarity laws for flexible propeller scaling should account for the deformation in model experiments. This study introduces a non-dimensional parameter to characterise the deformation of flexible propellers and evaluates it through time-domain fluid–structure interaction simulations. A coupled solver combines unsteady Reynolds-Averaged Navier–Stokes equations with a finite-element structural solver. The study focuses on the Wageningen C4-40 propeller geometry under uniform inflow and is limited to isotropic materials.

A set of non-dimensional relations is derived through dimensional analysis, with a form of the Cauchy number expressing deformation amplitude. Validation using a Reynolds–Cauchy similarity approach on two geometrically similar propellers of different diameters confirms consistent deformation and less than 5% difference in thrust and torque coefficients between model and full-scale propeller. The disparities in performance results are attributed to numerical artefacts in the fluid solver, as the results indicate that the $k-\omega$ SST turbulence model is sensitive to near-wall resolution.

Achieving full-scale Reynolds numbers in propeller test facilities is not feasible, yet simulations demonstrate that flexible propellers are sensitive to viscous forces. The study observes disparities in deformation extent across Reynolds numbers. The deformation of flexible propellers improves flow attachment over the blades. The overall Reynolds-number trends remain similar to the rigid results: thrust coefficients increase and torque coefficients decrease as Reynolds numbers increase. The open-water efficiency depends on both coefficients, and larger Reynolds numbers result in higher efficiencies.

The Froude–Cauchy scaling approach proves suitable for model experiments; however, material availability limits practical implementation. This study indicates that the steady-state deformation is primarily governed by stiffness, with negligible impact from the structural-to-fluid density ratio. In contrast, in unsteady conditions, the structural-to-fluid density ratio affects the modal frequencies, which describe the dynamic behaviour of propeller blades. Particularly, propellers with high skew, rake, or with anisotropic material properties are affected by structural-to-fluid density. Furthermore, this analysis observes that the first blade mode of a zero-skew angle propeller is pure bending, and a 30% variation in structural density does not alter the natural frequency of this blade. However, coupled bend-twist modes are sensitive to the structural density, which therefore affects blade deformation in unsteady conditions.

In conclusion, the extent of propeller deformation can be controlled by a non-dimensional parameter expressing the ratio of elastic to hydrodynamic forces. For steady open-water conditions, deformation is additionally a function of Reynolds number. In unsteady conditions, the structural-to-fluid density ratio becomes relevant, as it alters coupled bend-twist modal frequencies. Thus, the deformation extent in this regime is, in addition to the Reynolds number, a function of fluid damping and the ratio of natural frequency to revolution rate. This study offers a basis for accurate scaling of flexible propellers in both experimental and computational studies.

Contents

List of Figures

Nomenclature

Abbreviations

Abbreviation	Definition
3-D	Three-dimensional
AFM	Absolute Formulation Method
AoA	Angle of Attack
BEM	Boundary Element Method
CAD	Computer Aided Design
CFD	Computational Fluid Dynamics
DNS	Direct Numerical Simulation
FEM	Finite Element Method
FFT	Fast Fourier transform
FSI	Fluid Structure Interaction
FVM	Finite Volume Method
IMO	International Maritime Organization
ITTC	International Towing Tank Conference
MARIN	Maritime Research Institute Netherlands
MVG	Moving Grid Formulation
LE	Leading Edge
RANS	Reynolds Averaged Navier-Stokes
TE	Trailing Edge
URANS	Unsteady Reynolds Averaged Navier-Stokes
URN	Underwater Radiated Noise

Symbols

Latin Symbols

Symbol	Definition	Unit
A	Cross-sectional area	$[m^2]$
A_D	Developed blade area	$[m^2]$
A_E	Expanded blade area	$[m^2]$
A_O	Disc area	$[m^2]$
A_P	Projected blade area	$[m^2]$
A_P/A_O	Projected blade area ratio	$[-]$
A_E/A_O	Expanded blade area ratio	$[-]$
a	Acceleration	$[m/s^2]$
b	Width	$[m]$
C	Courant number $(= U\Delta t/\Delta x)$	$[-]$
Ca	Cauchy number $(= E/\rho U^2)$	$[-]$
C_F	Force coefficient $(= F/(0.5\rho U^2 A))$	$[-]$
C_F	Skin friction coefficient $(= \tau_w/(0.5\rho U^2))$	$[-]$
C_L	Lift coefficient $(= L/(0.5\rho U^2 A))$	$[-]$
C_M	Moment coefficient $(= M/(0.5\rho U^2 AL))$	$[-]$
C_p	Pressure coefficient $(= (p - p_\infty)/(0.5\rho U^2))$	$[-]$
$C_{p,min}$	Minimum pressure coefficient	$[-]$
c	Chord length	$[m]$
c_s	Speed of Sound	$[m/s]$
c/D	Chord-to-diameter ratio	$[-]$
D	Drag force	$[N]$
D	Diameter	$[m]$
E	Young's modulus	$[Pa]$

Symbol	Definition	Unit
EI	Bending rigidity	$[Nm^2]$
Eu	Euler number $(= \Delta p/0.5\rho U^2)$	$[-]$
F	Force	$[N]$
Fr	Froude number $(= U/\sqrt{gD})$	$[-]$
f_h	Hydrodynamic force	$[N]$
f	Camber	$[m]$
f	Frequency	$[1/s]$
f/c	Camber-to-chord ratio	$[-]$
G	Shear modulus	$[Pa]$
GJ	Torsional rigidity	$[Nm^2]$
g	Gravitational acceleration	$[m/s^2]$
I	Moment of inertia	$[m^4]$
I_a	Added mass moment of inertia	$[m^4]$
i_G	Generator line rake	$[m]$
i_p	Propeller tip rake	$[m]$
i_s	Skew-induced rake	$[m]$
i_T	Total rake	$[m]$
J	Advance ratio $(= V_a/nD)$	$[-]$
K	Bend-twist coupling rigidity	$[Nm^2]$
K_B	Bending stiffness	$[N/m]$
K_T	Thrust coefficient $(= T/\rho n^2 D^4)$	$[-]$
K_Q	Torque coefficient $(= Q/\rho n^2 D^5)$	$[-]$
k	Stiffness	$[N/m]$
L	Lift force	$[N]$
L_2	L_2 norm	$[-]$
M	Moment	$[Nm]$
Ma	Mach number $(= U/c_s)$	$[-]$
m	Mass	$[kg]$
m_a	Added Mass	$[kg]$
m_a/m_s	Added-mass-to-structural mass ratio	$[-]$
N_p	Total number of grid nodes	$[-]$
n	Revolution rate	$[1/s]$
n	Normal coordinate	$[m]$
P	Pitch	$[m]$
P/D	Pitch ratio	$[-]$
P_D	Delivered power $(= TV)$	$[W]$
P_E	Effective power $(= 2\pi Qn)$	$[W]$
p	Local static pressure	$[N/m^2]$
p_∞	Free stream static pressure	$[N/m^2]$
p_v	Vapour pressure	$[N/m^2]$
Q	Torque	$[Nm]$
R	Radius flow curvature	$[m]$
R	Propeller radius	$[m]$
R	Resulting force	$[N]$
Re	Reynolds number $(= UL/\nu)$	$[-]$
r	Section radius	$[m]$
S	Surface	$[m^2]$
St	Strouhal number $(= fL/U)$	$[-]$
T	Thrust force	$[N]$
t	Time	$[s]$
t	Thickness	$[m]$
t/c	Thickness-to-chord ratio	$[-]$
U	Velocity	$[m/s]$
u	Velocity component	$[m/s]$
$\bar{u}$	Time mean velocity	$[m/s]$
u_τ	Friction velocity	$[m/s]$
u^+	Non-dimensional velocity	$[-]$
V	Volume	$[m^3]$

Symbol	Definition	Unit
V_a	Advance velocity	$[m/s]$
V_r	Resultant velocity	$[m/s]$
V_s	Ship speed	$[m/s]$
v	Velocity component	$[m/s]$
We	Weber number $(= \sigma/(\rho U^2 D))$	[-]
w	Wake fraction $(= (V_s - V_a)/V_s)$	[-]
x	Spatial coordinate	$[m]$
y	Spatial coordinate	$[m]$
y^+	Non-dimensional wall distance	$[-]$
z	Spatial coordinate	$[m]$

Greek Symbols

Symbol	Definition	Unit
α	Angle of Attack	$[^\circ]$
β	Hydrodynamic pitch angle/Resultant flow angle	$[^\circ]$
Δ/D	Propeller bending amplitude	$[-]$
ζ	Damping coefficient	$[-]$
η_o	Open water efficiency $(= (K_T J)/(K_Q 2\pi))$	$[-]$
θ	Pitch angle	$[^\circ]$
θ	Propeller twisting amplitude	$[^\circ]$
θ_{fp}	Face pitch angle	$[^\circ]$
θ_{ip}	Propeller rake angle	$[^\circ]$
θ_{nt}	Noise-tail pitch angle	$[^\circ]$
θ_o	No-lift or Effective pitch angle	$[^\circ]$
θ_s	Skew angle	$[^\circ]$
θ_{sp}	Propeller skew angle	$[^\circ]$
λ	Scale ratio	$[-]$
μ	Dynamic viscosity	$[Pa \cdot s]$
ν	Kinematic viscosity	$[m^2/s]$
ν	Poisson's ratio	$[-]$
ρ	Density	$[kg/m^3]$
ρ_s/ρ_f	Structural-to-fluid density ratio	$[-]$
σ	Cavitation number	$[-]$
σ	Surface tension	$[Pa]$
τ	Shear stress	$[Pa]$
ϕ	Local flow quantity	[...]
ω	Frequency	$[1/s]$
ω_n	Natural frequency	$[1/s]$
ω_0	Fundamental natural frequency	$[1/s]$
ω_0^{wet}	Fundamental wet natural frequency	$[1/s]$
ω_B	Bending frequency	$[1/s]$
$\omega_{wet}/\omega_{dry}$	Wet-to-dry frequency ratio	$[-]$

1 Introduction

Since the introduction of marine propellers, design innovations have continuously aimed to enhance ship speed and propulsive efficiency. In 1894, Parsons identified thrust breakdown caused by vapour cavitation as a significant issue [11]. Cavitation not only affects thrust but also causes vibrations, erosion, and underwater radiated noise [5, 6, 55]. Underwater radiated noise has risen significantly due to the growth in ship size and global shipping traffic [35]. The noise has critical implications, particularly for military vessels that rely on low acoustic signatures and ships using systems like sonar that require quiet operational environments [5]. Additionally, increasing research shows that chronic exposure to ship noise affects the behaviour of marine animals [28, 63], leading to stricter noise regulations, such as those introduced by the European Union [20] and the International Maritime Organization [40]. Meanwhile, the maritime sector also has to reduce its greenhouse gas emissions to minimise its ecological footprint [39]. Adjusting propeller geometry to mitigate cavitation often results in reduced efficiency. Designers frequently accept cavitation as a necessary compromise, with efficiency losses estimated at 5 to 10% [61]. However, with the new noise regulations, there is a need for new propeller designs that are both efficient and cavitation-free.

Composite materials offer possibilities in the optimisation of marine propellers. While ship propellers are traditionally made of metals, more recent research shows the advantages and potential of composite laminates. Composites have better seawater corrosion resistance than metals [79]. Generally, the fatigue resistance of composites is better than that of metals [70, 79, 101]. In addition, composites have lower magnetic signatures than metals, particularly interesting for naval use [70, 79]. Optimising material properties enables composites to achieve a high strength-to-stiffness ratio while maintaining a low weight [34, 70, 79]. Moreover, using composite laminates can result in a flexible marine propeller [4, 65, 67]. A flexible propeller can deform to variations in fluid loading. Therefore, flexible propellers can lead to better vibration control, higher cavitation inception speeds, and greater efficiencies in off-design conditions [15, 71, 80, 90]. Furthermore, larger propeller diameters can be applied [60].

The ability of flexible propellers to passively adapt to variations in fluid loading introduces additional freedom in propeller design, but also adds complexity to scaling propellers for model tests. Open-water characteristics are frequently determined through model experiments. Essential for scaling flexible marine propellers is that the flexible model propeller retain the shape of its full-scale counterpart when deforming [97]. Achieving equal deformation between the model and full-size propellers requires consistently scaled fluid-structure interaction [53, 100]. Combined Froude-Cauchy similarity or Mach similarity results in consistently scaled fluid-structure interaction [21]. The Young's modulus must be scaled by the scale factor when applying combined Froude-Cauchy similarity. Finding an appropriate material for the model scale propeller is challenging, as highlighted by Young [101]. Applying Mach scaling to test fast vessels is also a challenge in testing facilities, as tests must be performed at full-scale speed [21]. If this is possible, measuring equipment may not be used at such high thrust and torque values, and model tests still cannot be performed [97].

The objective of this study is to examine scaling approaches to perform model-scaled open-water tests of flexible propellers. In particular, flexible marine propellers require a non-dimensional parameter to characterise the extent of their deformation. Accordingly, the research question to investigate during the thesis is:

Which non-dimensional parameter controls the deformation extent of flexible marine propellers?

This report presents the findings of this thesis. The following sub-questions are defined to answer the main research question:

- Which non-dimensional parameters follow from the relevant variables for flexible marine propellers?
- What are the Reynolds number effects on the performance of rigid marine propellers in the applied simulations?

- What are the scale effects when satisfying the Cauchy number using a combined Reynolds-Cauchy similarity approach for flexible marine propellers?
- What are the Reynolds number effects on the performance of flexible marine propellers?
- What is the influence of structural density on the steady and dynamic response of a flexible marine propeller?

Within the scope of this thesis, time-domain Fluid-Structure Interaction simulations of flexible marine propellers are performed. The workflow developed by Lagendijk [62] is used to perform these simulations. In this workflow, a flow solver using unsteady Reynolds-Averaged Navier-Stokes equations is coupled with a Finite Element Method structural solver. This partitioned approach enables the assessment of the interaction between the deformable propeller and fluid. The fluid solver uses a finite-volume method. The k–ω SST turbulence model of Menter [82] is implemented, without any transition models.

Open-water characteristics determined from model experiments are typically tested in a towing tank or a cavitation tunnel. These tests result in a steady loading by definition. The simulations are performed using a uniform inflow field. The fluid flow is described in an absolute formulation, known as an AFM steady approach. Using this formulation, the flow equations are solved in the moving reference frame but written in terms of absolute reference frame quantities [75].

The structural characteristics of a composite material depend on its components, geometry, and the distribution of the fibres and matrix [19]. The composite structure produces an anisotropic material response, enabling the use of bend-twist coupling in the design of flexible marine propellers [62]. Optimising the structural characteristics of a composite material is not within the scope of this study. To limit computational complexity, this study uses isotropic material properties in the numerical simulations to investigate the deformation behaviour.

The time domain simulations are performed using the unsteady Reynolds-Averaged Navier-Stokes equations with a linear two-way coupling to the structural solver [62]. The numerical simulations use a strongly coupled approach. Within each time step, the solutions for both the flow and structural domains are exchanged multiple times until a converged solution is reached and the forces are in equilibrium [45]. A linear constitutive relation governs the structural response. The bending stiffness remains constant during deformation, provided that the deformations are sufficiently small.

This study consists of ten chapters. Chapter 2 provides background on marine and composite propellers. Chapter 3 introduces the derivation and relevance of non-dimensional parameters for model-scale testing, answering the first sub-question. Chapter 4 explains the working principles of the Fluid-Structure Interaction solver used in this study. These three chapters partly build on the definition study completed earlier in this thesis project [96]. Chapter 5 answers the second sub-question by analysing Reynolds effects on rigid marine propellers. Chapter 6 addresses the third sub-question, comparing results from full-size and model-scale propellers using a combined Reynolds-Cauchy similarity approach. Chapter 7 focuses on the Reynolds effects on flexible propellers, answering the fourth sub-question. Chapter 8 discusses results for different material densities, covering both steady-state performance and dynamic behaviour, thereby answering the final sub-question. Chapter 9 provides a discussion that validates the rigid simulation results. Additionally, this section evaluates the assumptions made, discusses their impact, and offers suggestions for future research. Finally, Chapter 10 presents the conclusions to answer the main research question and provides recommendations for model testing of flexible marine propellers.

2
Marine Propellers

This chapter provides relevant background information on marine propellers and composite propellers. The goal of this chapter is to provide the necessary context for understanding the study presented in this report. This chapter partially builds on the definition study completed earlier in this thesis project [96]. The following questions will be answered:

- What are the working principles of a marine propeller?
- What are the classical design variables of a marine propeller blade?
- How are propellers compared in terms of performance?
- What are the design challenges involved in optimising marine propeller performance?
- What benefits do the properties of composite materials offer for propellers?

The first section outlines the operating principles of a marine propeller, while the second section focuses on the classical design variables of a propeller blade. The section that follows explains the concept of open-water efficiency, which is used to compare propeller performance. The fourth section focuses on the design challenges of propellers. The final section presents the benefits of composite propeller blades.

2.1. Working Principle

A right-handed Cartesian reference frame is used throughout this thesis. The x-axis is positive in the forward direction and aligned with the shaft axis, the y-axis is positive towards the port side, and the z-axis is positive vertically upwards. Figure 2.1 presents several propeller parameters. The leading edge, abbreviated as LE, is the edge that first encounters the fluid. The propeller shown in Figure 2.1 is right-handed, rotating in a clockwise direction. The trailing edge, in short TE, lies opposite the leading edge. In forward operating conditions, the propeller face is the pressure side of the blade, while the propeller back is the suction side. The propeller reference line, also called the directrix, lies perpendicular to the shaft axis, aligns with the z-axis and crosses the propeller root at the mid-chord position.

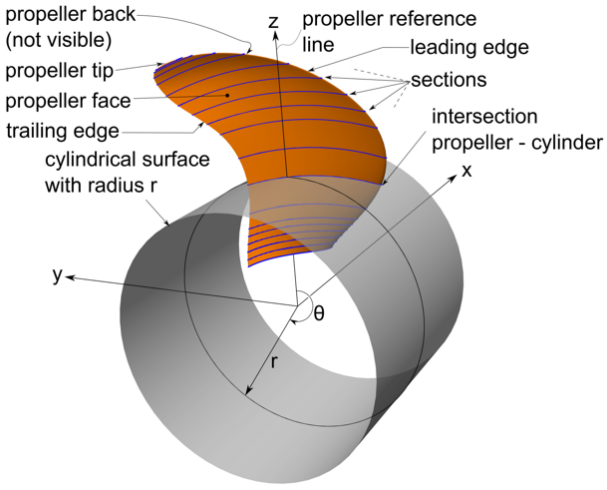

Figure 2.1: Propeller variables. A right-handed Cartesian reference frame is used. From MARIN [74]

2.1.1. Profiles

A propeller generates a lift force, denoted as L, with its blades using foil-shaped profiles. These profiles, referred to in Figure 2.1 as ”sections”, are obtained by examining a cross-section of a blade at a constant radius from the hub. Figure 2.2 illustrates a typical foil section. The straight line connecting the leading edge to the trailing edge is termed the chord line, and its length is called the chord length, c. The camber line is the curve passing midway between the upper and lower surfaces of the section. In this thesis, the term ”camber” is defined according to the definition provided by Carlton [12]. The camber of the section, marked with f, is the distance of the camber line above the chord line measured perpendicular to the chord line. Camber leads to an asymmetry between the pressure and suction sides.

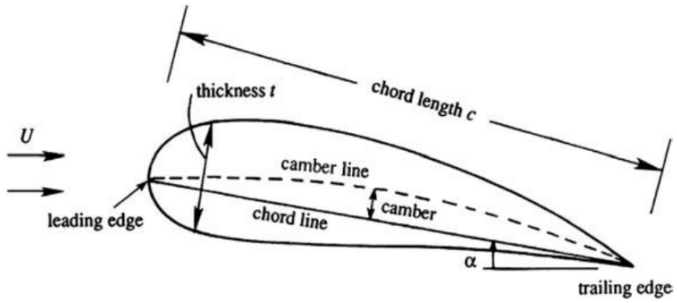

Figure 2.2: Foil-shaped profile. From Kundu et al. [59]

2.1.2. Lift

A profile generates lift through the flow of fluid over its surface. This section provides a more in-depth understanding of the principles governing lift generation, enabling a deeper understanding of the various propeller geometries. For simplicity, the analysis assumes an ideal flow, which neglects the effects of viscosity. Streamlines visualise the flow over a profile, and a fluid particle on one of these streamlines is considered. This particle has a height dn normal to the foil surface, a width dx and a depth dy. Gravity effects are negligible. The particle is moving along the streamline. Therefore, the weak form of the Bernoulli equation is valid:

$$p + 1/2\rho U^2 = \text{Constant along a streamline} \tag{2.1}$$

In Equation 2.1, p represents the static pressure term, while the velocity U together with the fluid density ρ contribute to the dynamic pressure term, $1/2\rho U^2$. According to Bernoulli’s principle, if the speed of a particle moving along a streamline remains constant, the pressure along the streamline must also remain unchanged. A curved streamline causes the velocity vector to change direction. Any change in direction requires an acceleration, a, which is caused by a force following Newton’s second law: $F = m{\cdot}a$. The mass of the fluid particle is equal to $m = \rho_f{\cdot}dx{\cdot}dy{\cdot}\ dn$, in which ρ_f the fluid density is. The centripetal force, responsible for the change in velocity direction, acts perpendicular to the flow:

$$F = \frac{mU^2}{R} \tag{2.2}$$

In Equation 2.2, R represents the radius of the curvature of the streamline. The centripetal force acting on the fluid particle must arise from a pressure differential across the height dn, as gravity and viscosity are neglected. The force generated by this pressure differential is given by:

$$F = dp \cdot A \tag{2.3}$$

The term dp in Equation 2.3 represents the pressure difference, and A is the area, which for the fluid particle is equal to $dx{\cdot}dy$. Combining Equations 2.2 and 2.3 results in:

$$\frac{\rho \cdot dx \cdot dy \cdot dn \cdot U^2}{R} = dp \cdot dx \cdot dy \tag{2.4}$$

So that:

$$\frac{dp}{dn} = \frac{\rho \cdot U^2}{R} \tag{2.5}$$

When $dp/dn < 0$, the fluid accelerates, and the curvature is in the opposite direction to dn. Figure 2.3 illustrates this for the upper surface. The curvature opposing dn causes the flow to accelerate, and the pressure near the foil is smaller than p_{atm}. Near the lower surface, the pressure is higher than p_{atm}, and there

is a decrease in velocity. In an ideal, irrotational flow, the fluid would wrap around the trailing edge, causing a large pressure gradient and a locally infinitely large velocity gradient. In real flows, viscosity enforces the Kutta condition, ensuring the flow leaves the trailing edge smoothly. This requirement determines the amount of circulation around the foil, which is proportional to the lift force. Thus, lift arises because curved streamlines create a pressure differential, and any shape that induces asymmetric curvature can generate lift.

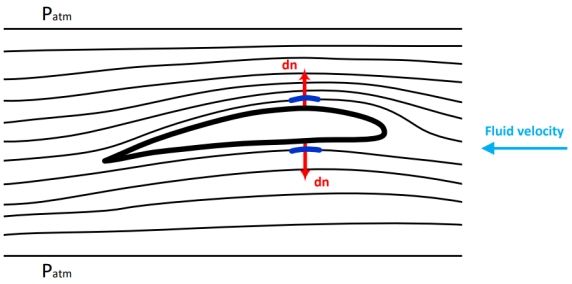

Figure 2.3: Streamlines around a foil-shaped profile. Modified from Samya [89]

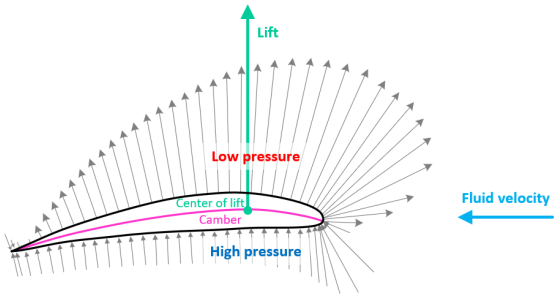

Figure 2.4: Pressure vectors due to the flow over a profile. From Aviation Stack Exchange [66]

A cambered foil section curves the flow and generates lift even when the angle of attack is zero. In Figure 2.5 of Gudmundsson [31], the lift coefficient is plotted against the angle of attack for three profiles with different camber. The lift coefficient is a non-dimensional value of the lift force and given as $C_L = L/(0.5\rho U^2 A)$. The slopes of the lift curves are consistent across the three profiles. Cambered sections produce additional lift, comparable to the effect of an increased incidence angle. For positively cambered sections, the lift curve shifts upward and to the left, while for negatively cambered sections, it shifts downward and to the right.

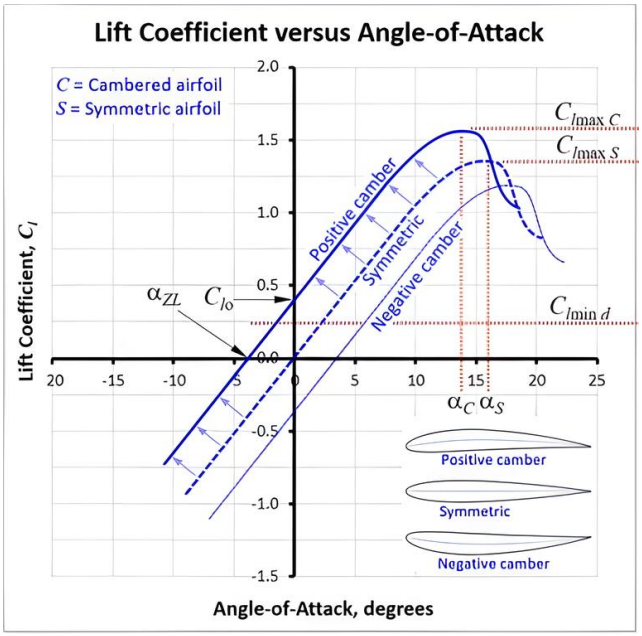

Figure 2.5: Lift Coefficient versus angle of attack for three foil sections with different camber. Cambered sections produce additional lift, while stall effects occur at lower angles of attack. From Gudmundsson [31]

2.1.3. Boundary Layer Flow

The viscous effects of flows are typically confined to a thin layer near the surface of the foil, known as the boundary layer. Much of the following explanation of boundary layer flow and separation is provided by Kundu et al. [59]. Ideal flow analysis can predict fluid velocity away from solid surfaces and surface-normal pressure forces (when the boundary layer on the surface is thin and attached). However, viscous effects, such as skin friction and energy dissipation, are neglected.

A viscous fluid flowing over a solid surface must satisfy the no-slip boundary condition. This boundary condition states that a fluid layer in contact with a solid boundary must have the same velocity as the boundary itself. The relative velocity components (u and v) are equal to zero. Viscous fluids cannot resist shear. The

velocity rapidly increases, reaching the external flow speed a small distance away from the wall. The result is that the velocity gradients and viscous shear stresses are large near the body in the boundary layer.

Depending on the length, velocity, and viscosity of the fluid, as well as the properties of the body, the boundary layer can be either laminar or turbulent. A laminar flow is a flow regime characterised by a smooth, orderly fluid flow without any mixing between layers of fluid. There are gradual changes along the length of the boundary layer in a laminar flow. A turbulent regime is highly unsteady. A turbulent flow is characterised by mixing, with elements of the fluid moving somewhat randomly throughout the boundary layer. A turbulent boundary layer is much thicker, has more momentum, and the wall shear stress, denoted as τ_w, is much greater. Consequently, the friction force is larger compared to a laminar boundary layer.

As presented by Kundu et al. [59], the pressure gradient can be favourable or adverse in a boundary layer. A favourable pressure gradient is present in an accelerating stream, where $\partial p/\partial x < 0$. An adverse pressure gradient is present when $\partial p/\partial x > 0$. An adverse pressure gradient causes the boundary-layer flow to decelerate, thicken, and develop a point of inflection, illustrated in Figure 2.6. If the adverse pressure gradient is strong enough or extends over a long distance, the flow next to the surface can reverse direction. This reverse flow causes boundary layer separation, commonly referred to as stalling on the surface of a foil. Stall onset depends on several factors, including the foil's shape and surface roughness. Stall effects are important to consider in propeller designs. Profiles with a large angle of attack can result in a pressure difference between the pressure and the suction side of the profile at the trailing edge. This pressure differential at the trailing edge between the sides causes instabilities, referred to as trailing-edge separation. A profile with a positive camber generates a stronger adverse pressure gradient near the trailing edge, causing stall at lower angles of attack [31]. Boundary layer separation reduces the lift force generated by propeller blades and increases pressure drag. Figure 2.5 shows that for a symmetric airfoil, stall effects cause a decrease in lift coefficient for angles of attack larger than 16 degrees.

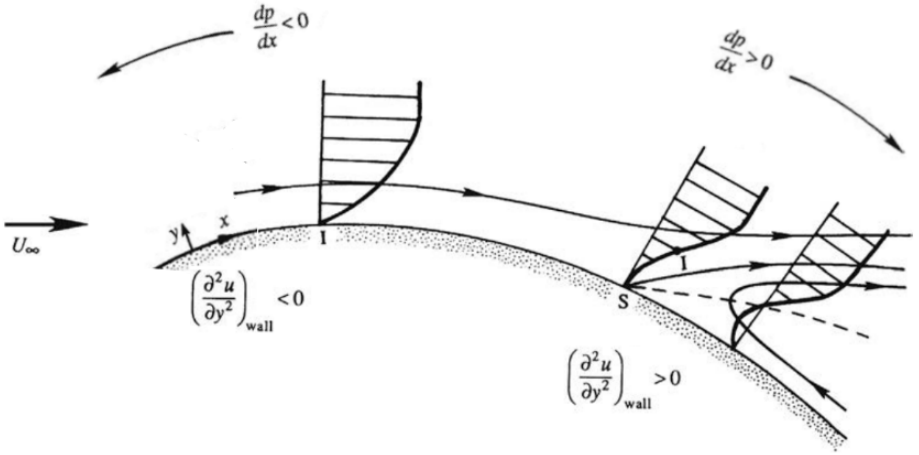

Figure 2.6: Velocity profiles across a boundary layer with favorable ($\partial p/\partial x < 0$) and adverse ($\partial p/\partial x > 0$) pressure gradients. The streamline emerges from the surface at the separation point, located at S, and the inflection point is indicated as I. Modified from Kundu et al. [59]

2.1.4. Resulting Forces

A propeller blade operating in water experiences a resulting force, which can be decomposed into multiple force components. The previous section explained how a profile generates a lift force through the flow of fluid over its surface. Viscous effects in the boundary layer will also result in a drag force, denoted as D. The lift force and the drag force act respectively perpendicularly and oppose the blade's motion. The resulting hydrodynamic force, R, can be resolved in an axial and tangential direction as well. The force in the axial direction is termed the thrust force, T. The torque is the force in the tangential direction and is indicated with Q.

Figure 2.7 of Klein Woud and Stapersma [98] illustrates a simplified propeller blade cross-section along with the resulting forces. The resultant velocity, denoted with V_r, that impacts the propeller is a combination of the advance velocity, V_a, and the propeller's circumferential speed, which is $2\pi r n_p$. This resultant velocity interacts with the propeller blade at a specific angle α, known as the angle of attack, AoA. The angle of attack is the difference between the pitch angle, denoted by θ, and the resultant flow angle, which is also known as the hydrodynamic pitch angle and expressed as β.

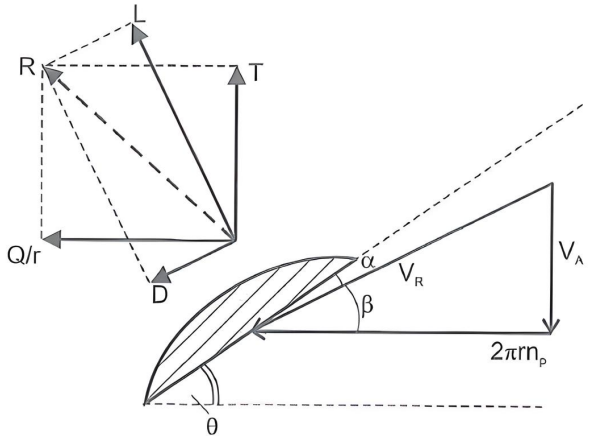

Figure 2.7: Cross section of a propeller blade with forces resulting from the inflow- and rotational velocity. From Klein Woud and Stapersma [98]

2.2. Propeller Geometry

The foil-shaped profiles make up the propeller blade. The basic outlines commonly used to describe the shape of the propeller blade, as defined by Carlton [12], are illustrated in Figure 2.8. The projected outline, A_P, is determined by looking at a propeller blade normally, along the shaft centre line, into the y-z plane. The developed outline, denoted by A_D, represents a helical view where the pitch of each section is zero. The expanded outline, A_E, is not an outline in a true geometric sense. The expanded outline plots the chord lengths at their correct radials about the propeller reference line while the pitch angle of each section is zero.

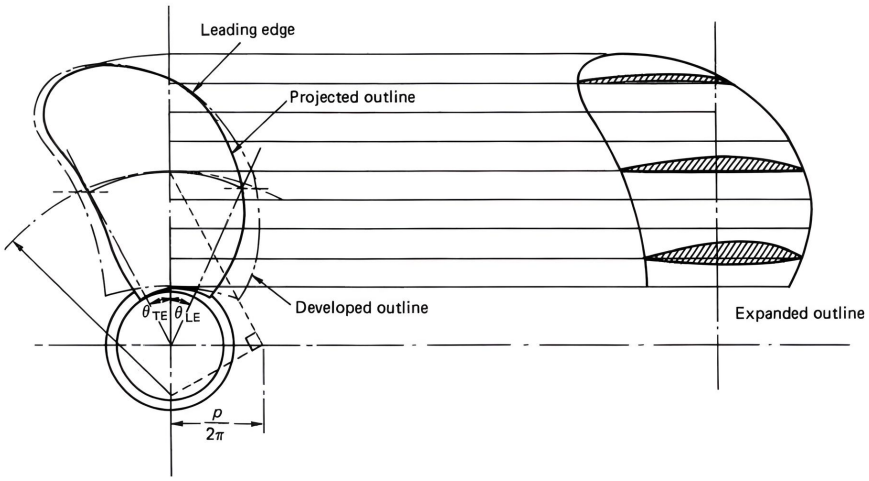

Figure 2.8: Propeller outline definitions. From Carlton [12]

2.2.1. Pitch

The pitch of a propeller represents the horizontal distance it would theoretically cover over one revolution, considering no camber and no thrust. This distance is defined as P, as it moves over the surface of a cylinder with radius, r. The pitch angle, denoted by θ is given by Equation 2.6:

$$\theta = tan^{-1}(\frac{P}{2\pi r}) \tag{2.6}$$

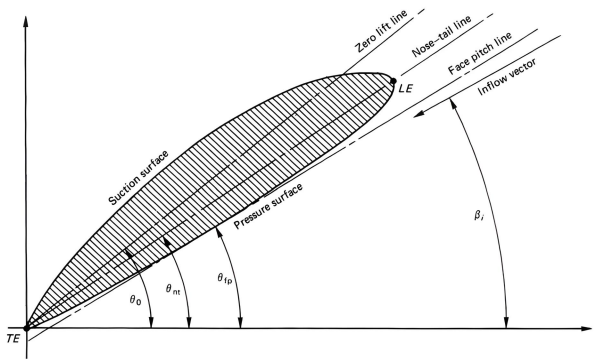

Figure 2.9: Pitch lines. From Carlton [12]

In the literature, different definitions of the pitch line can be found. These are the nose-tail pitch, face pitch, effective or "no-lift" pitch and hydrodynamic pitch. Figure 2.9 illustrates these pitch lines. The nose-tail pitch line is the most commonly used pitch reference. In this study, "pitch" refers to the nose-tail pitch unless stated otherwise. Often, the pitch ratio is used instead of the pitch distance. The pitch ratio is the ratio between the pitch distance and propeller diameter, equal to P/D. This ratio is used because it has no dimension and thus remains constant at different propeller scales.

The effective pitch or zero lift line is the line at which the inflow would produce zero lift from the foil section, and it is thus dependent on the camber of the section. The hydrodynamic pitch is the angle of the incident flow, representing a hydrodynamic inflow. It is not a geometric characteristic of the propeller [98]. The angle β in Figure 2.7 represents the hydrodynamic pitch.

Figure 2.7 shows that the angle of attack from the resultant velocity is the difference between the pitch and inflow angles. The pitch angle and camber determine the angle of attack, which in turn affects the load on the propeller blades and the generated lift. However, as Figure 2.5 illustrates, a too-large angle of attack will lead to stall.

2.2.2. Skew

Skew is an asymmetry a blade has in the y-z-plane, i.e. in the projected propeller outline. The skew angle, $\theta_s(x)$, of a blade section is the angle between the directrix and a line through the midchord point of a section as a function of the radius, with x defined as r/R. An angle forward in the direction of the rotation is considered negative. Carlton [12] defines the propeller skew angle, θ_{sp}, as the largest angle between the shaft centre line and the mid-chord point of the entire blade. He also categorises propeller skew into two types: balanced and biased skew designs. In the balanced skew design, the line through the mid-chord points intersects the directrix at least twice within the inner regions of the blade. In biased skew designs, this is not more than once. Figure 2.10 shows both $\theta_s(x)$ and θ_{sp}.

Skew can reduce unsteady pressure forces and increase cavitation inception speeds [18]. Skew can also limit sheet cavitation, as the sheet cavitation immediately changes to tip cavitation [5]. In addition, a high-skew propeller distributes the pressure fluctuations on the hull caused by the blade passing, which helps to reduce vibrations [29].

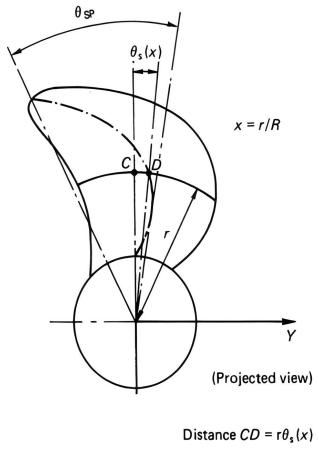

Figure 2.10: Definition of skew. From Carlton [12]

2.2.3. Rake

Rake is the backwards slope of a profile in the x-z-plane; it represents the axial shift of the blades from the origin. Propeller rake is divided into two components: generator line rake, i_G and skew-induced rake, i_s. The total rake of the section to the propeller reference line, which is i_T, is the sum of these two. The generator line rake represents the distance, parallel to the x-axis, from the directrix to the point where the section's helix at a given radius intersects the x-z-plane [12].

Skew and rake are linked because the helical effect of blade sections introduces a cross-coupling effect. Figure 2.11 shows two cylindrical sections, one at the root of the propeller and the other at some radius (r) between the tip and root of the blade. The skew-induced rake is the helical distance around the cylinder from the mid-chord point of the section to the projection of the propeller reference line when viewed normally to the y-z-plane. The propeller rake, i_p, and propeller rake angle, θ_{ip}, are measured at the propeller tip, shown in Figure 2.12 [12].

Rake directed away from the ship hull (along the negative x-axis) is called positive rake or backward rake. Backwards rake is used to increase the tip clearance, which is the distance between the propeller tip in its top position and the hull. The rake distribution is primarily linear when increased tip clearance is the only purpose [55].

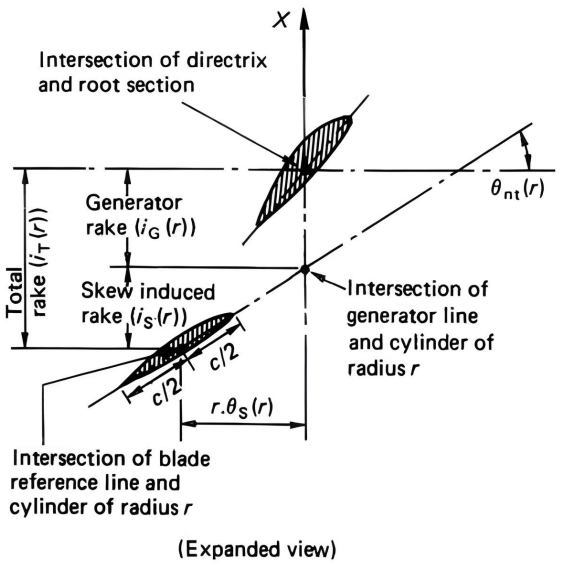

Figure 2.11: Definition of total rake. From Carlton [12]

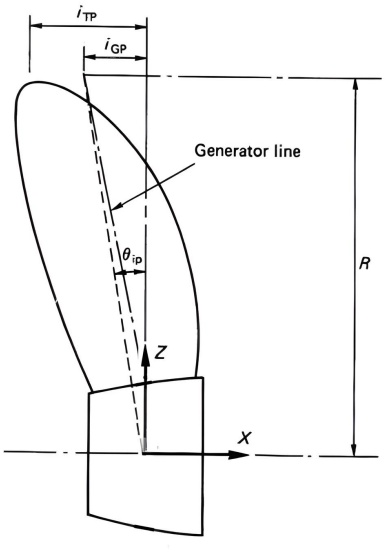

Figure 2.12: Tip rake definition. From Carlton [12]

To assess and compare the performance of different propellers, it is essential to define hydrodynamic performance measurement methods. The Rankine–Froude momentum theory [27] derives the ideal efficiency of a propeller. The ideal efficiency represents the maximum possible efficiency under theoretical conditions by modelling the propeller as an actuator disk operating in an inviscid, irrotational, and incompressible flow. However, the ideal efficiency does not include rotational, viscous, or non-uniformity losses.

In comparison, open-water efficiency includes all hydrodynamic losses from axial, rotational, and viscous effects. The open water efficiency is obtained with a uniform inflow and does not account for interaction losses between the ship and the propeller. Open water characteristics are frequently determined from model experiments, typically tested in a towing tank or cavitation tunnel [13]. These tests result in a steady loading by definition. Non-dimensional characteristics are used to express and compare the general performance of different propellers. The definition of the thrust coefficient, K_T, the torque coefficient, K_Q and the advance ratio, J, are given in Equation 2.7, 2.8 and 2.9 respectively. The physical importance of J is that it is proportional to the tangent of the angle between the advance velocity and the circumferential speed of the propeller.

$$K_T = \frac{T}{\rho n^2 D^4} \tag{2.7}$$

$$K_Q = \frac{Q}{\rho n^2 D^5} \tag{2.8}$$

$$J = \frac{V_a}{nD} \tag{2.9}$$

The open-water propeller efficiency, η_o, is measured as the ratio between delivered power by the torque, P_D and the effective power of the thrust, P_E:

$$\eta_o = \frac{P_E}{P_D} = \frac{TV_a}{2\pi Qn} = \frac{K_T J}{K_Q 2\pi} \tag{2.10}$$

Figure 2.13 shows an open-water propeller diagram of the Wageningen B-Series propellers with four blades and an expanded blade area ratio of 0.7. The diagram presents the thrust coefficient, torque coefficient, and open-water efficiency for different pitch ratios. This figure represents a typical open-water diagram for a set of fixed-pitch propellers operating in a non-cavitating environment at a positive advance ratio.

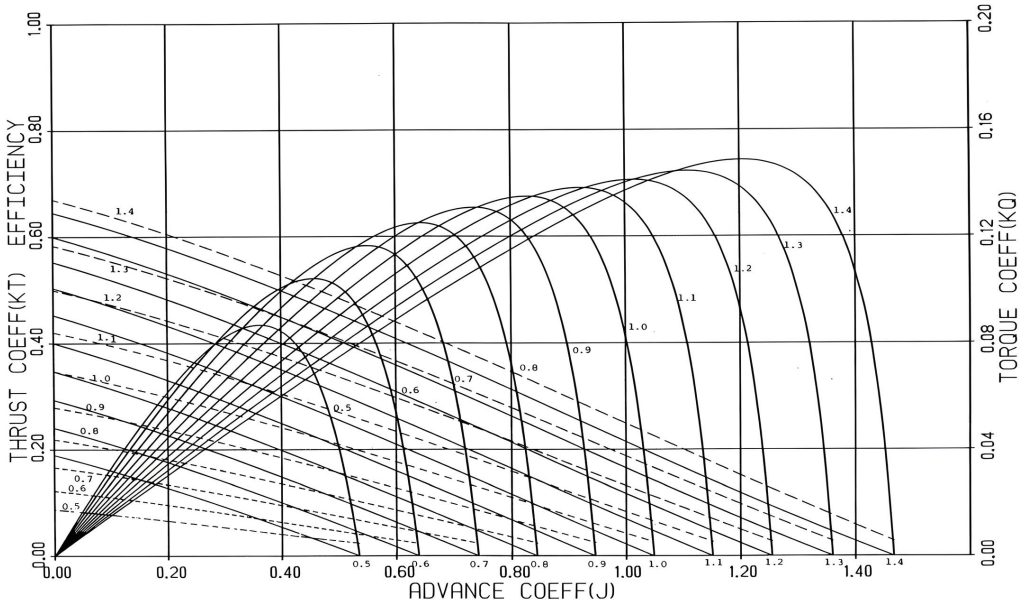

Figure 2.13: The open water diagram of the Wageningen B-Series propeller with four blades and an expanded blade area ratio of 0.7. From Bernitsas et al. [2]

The diagram shows that the thrust and torque coefficients decrease as the advance ratio increases. The maximum value for the thrust and torque coefficients occurs for a J-value equal to zero, which is called the bollard pull condition.

2.3. Propeller Design Challenges

The key challenge for a propeller designer is to achieve the highest possible efficiency for the required thrust force. However, the performance of a propeller operating behind the hull differs from its open-water characteristics due to the unsteady inflow generated by the wakefield. Moreover, higher efficiency often leads to cavitation, which in turn causes noise and vibrations.

A ship's movement through the water induces uneven flow velocity, contributing to the wakefield at the propeller plane. The wake in the propeller plane is called the nominal wake and represents only a small part of the total wakefield [12]. Generally, the axial velocities of the wake are expressed as a fraction of the ship's speed. The wake fraction, denoted as w, is the difference between the ship's speed, V_s, and advance velocity in front of the propeller and is defined as [98]:

$$w = \frac{V_s - V_a}{V_s} \tag{2.11}$$

The advance velocity can be expressed in terms of ship speed with the definition in Equation 2.11 as:

$$V_a = (1 - w) \cdot V_s \tag{2.12}$$

The axial and tangential inflow velocity changes throughout one propeller revolution, causing fluctuations in the angle of attack. Specifically, at the top or 12 o'clock position, the axial inflow velocity is lower than in other positions. Lower inflow velocities lead to a greater angle of attack and increased loading on the blade in this position [29]. As a result, the effective thrust force lies above the shaft axis. Furthermore, thrust eccentricity exists because of the tangential velocity components in the wakefield and the propeller's rotation. The variation of velocity components throughout one propeller revolution leads to an imbalance in loading. The fluctuation in loading is reacted at the bearings, forming a substantial contribution to the bearing forces [12]. Fluctuations in loads can lead to undesirable effects such as cavitation dynamics, pressure pulses, and underwater radiated noise [29].

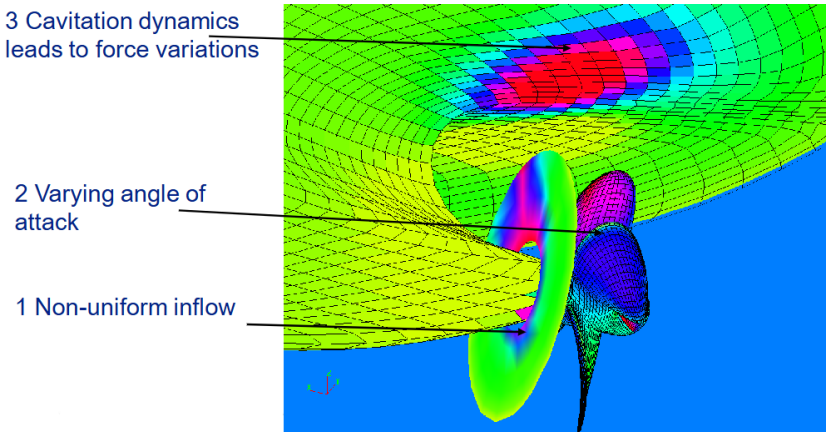

Figure 2.14: Influence of the ship's wakefield. The non-uniform inflow field leads to varying angles of attacks, which then result in cavitation dynamics and fluctuations in reaction forces. From Lagendijk [61]

2.3.1. Cavitation

When the pressure of a liquid drops below its vapour pressure, a phase change occurs. The change of phase from liquid to vapour due to a reduction of pressure is termed cavitation. Cavitation has several negative effects, including noise generation [5] and erosive damage to the propeller blade [55]. Excessive cavitation can lead to a decline in hydrodynamic performance [12]. Local high flow velocities, as well as accelerations and oscillations of the flow, can cause low pressures. A prerequisite for cavitation is the occurrence of weak spots in the flow, which break the bond between the water molecules. The presence of nuclei, i.e. microbubbles in the water, results in those weak spots. The presence of nuclei in the water depends on the circumstances. In seawater, for example, there are nuclei of all sizes, and the inception pressure will be equal to the vapour pressure [55, 91].

The initiation of cavitation is referred to as cavitation inception. Cavitation inception and the development of a cavity depend upon the geometry of the propeller blade and the flow condition [84]. The cavitation number, known as σ, is a dimensionless number used to characterise the flow condition. The definition of the cavitation number is:

$$\sigma = \frac{p_\infty - p_v(T)}{\frac{1}{2}\rho U^2} \tag{2.13}$$

In Equation 2.13, p_∞ stands for the free stream static pressure; p_v for the liquid vapour pressure; U for the free stream velocity; and ρ the liquid density.

The local pressure, symbolised as p, is expressed in non-dimensional terms as the pressure coefficient, which is denoted as C_p [55]:

$$-C_p = -\frac{p - p_\infty}{\frac{1}{2}\rho U^2} \tag{2.14}$$

Cavitation inception will occur if the local pressure is equal to or smaller than the vapour pressure, i.e. $p \leq p_v$. Therefore, cavitation inception will occur if:

$$-C_{p_{\text{min}}} \geq \sigma_v$$

Here, $C_{p,min}$ represents the minimum value of the pressure coefficient on the profile. Cavitation can develop in several forms, depending on the blade geometry, water quality and operating conditions [55]. Sheet cavitation arises when the pressure minimum is fixed at a surface location, resulting in a phase discontinuity that forms a sheet [57]. Vortex cavitation occurs when the pressure minimum is centred in a vortex, creating a rotating tube. This type of cavitation is not erosive when it is not excessive, but it is a source of noise [58]. Bubble cavitation develops when the pressure minimum is present in the fluid or on a surface without forming a sheet or vortex cavity. Bubble cavitation often results from a sudden pressure drop across the blade, lowering the local C_p below the vapour pressure and producing bubbles. The phase discontinuity of bubble cavitation is approximately spherical. The dynamic behaviour of bubble cavitation can lead to severe erosion, similar to sheet cavitation [56]. Figure 2.15 presented by Bosschers [5] illustrates these cavitation types and additional patterns found on ship propellers.

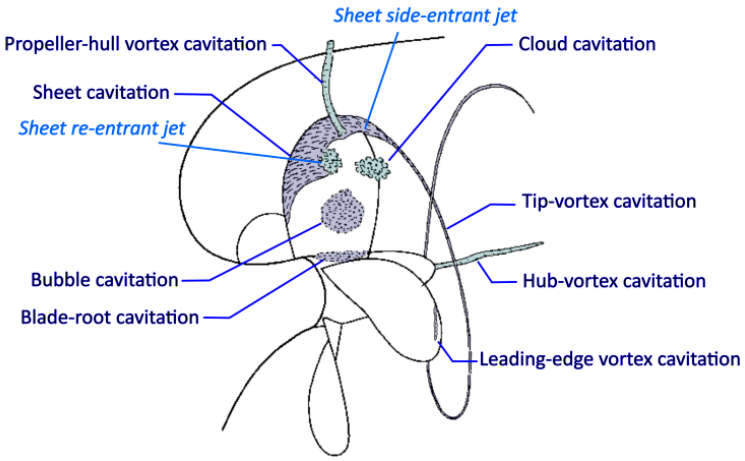

Figure 2.15: Illustration of possible cavitation patterns on ship propellers. From ITTC procedure 7.5-02-03-03.2 [86] modified by Bosschers [5]

The curvature of a fluid particle's path near the foil causes the fluid to accelerate. This acceleration results in a low-pressure peak on the suction side of the blade profile near the leading edge. Such a low-pressure peak makes the propeller blade vulnerable to cavitation inception [25]. Specifically, at the top or 12-o'clock position, where the axial inflow velocity is lower than in other positions, the increased angle of attack further enhances the acceleration, increasing the probability of cavitation [29]. Moderate levels of cavitation do not affect the propeller's performance. Serious cavitation activity is necessary to obtain thrust and torque breakdown. Cavitation-related issues, including hull vibrations, noise, and material erosion, can arise regardless of the cavitation level necessary to impact thrust and torque. Even minimal cavitation can lead to these problems [13]. To achieve high efficiency, propellers inevitably experience some cavitation. Designers frequently accept cavitation as a necessary compromise, with efficiency losses estimated at 5 to 10% [61].

2.3.2. Underwater Radiated Noise

Ship noise is relevant both onboard and underwater. Underwater radiated noise, abbreviated as URN, has increased significantly over the past 50 years due to anthropogenic sources. This rise is partly due to the growth in ship sizes and shipping traffic during this period [35]. Underwater radiated noise is crucial for, e.g., the acoustic signature of military ships and the effective operation of low-noise onboard systems, such as sonar. However, underwater shipping noise can also harm marine life [5, 63].

Propeller cavitation significantly contributes to underwater radiated noise [5]. Cavitation, hull vibration, and engine noise form the acoustic footprint of a ship. Most ship-generated noise is continuous and low-frequency. An increasing number of studies, including those by Götz et al. [28] and Lancaster et al. [63], show that chronic exposure to ship noise affects the behaviour of marine animals. In particular, sound masking negatively impacts their behaviour and overall ocean health. Sound masking occurs when ship noise interferes with the sounds generated by marine animals, fish, and molluscs.

Cavitation and the resulting noise are strict constraints for military, oceanographic, and research vessels, where any cavitation is unacceptable due to their specific operations. For most other ships, however, efficiency is prioritised. Completely avoiding cavitation, especially at the blade tip near the 12 o'clock position, requires significant unloading of the blade tip. Tip unloading compromises propeller efficiency and increases fuel costs. As a result, cavitating tip vortices, and occasionally sheet cavitation near the tip, are commonly accepted on these ships as a practical trade-off [5].

There are increased regulations regarding noise levels, as research has shown that underwater shipping noise can harm marine life. The European Union has adopted recommendations for maximum acceptable levels of continuous underwater noise, such as that generated by shipping [20]. Additionally, the Sub-Committee on Ship Design and Construction of the International Maritime Organization, known as IMO, has developed an Action Plan to prevent and reduce underwater radiated noise from ships. The goal is to minimise the negative effects of underwater noise on the marine environment. The action plan includes the development of targets and policies for underwater noise reduction [40].

2.4. Composite Marine Propellers

Composite materials offer possibilities in the optimisation of marine propellers. A composite material system consists of two or more phases on a macroscopic scale, designed to have better mechanical properties than the individual materials. The structural characteristics of a composite material depend on its components, geometry, and the distribution of the phases. The distribution of the components determines the homogeneity and uniformity of the composite. Many material properties, such as stiffness and strength, are direction-dependent. A material is isotropic when the properties are the same in all directions or are independent of the orientation of reference axes. A material is anisotropic when the properties at a specific point change depending on the direction [19].

While ship propellers are traditionally made of metal, recent research has shown the advantages of composite laminates for propellers. The most common reinforcement materials used for marine applications are glass and carbon fibres. Glass fibres are commonly used for their cost-effectiveness and workability. Carbon fibres are used for highly optimised structures. Typical matrix materials used for marine composites include polyesters, vinyl esters, and epoxies [101].

2.4.1. Benefits of Composite Marine Propellers

Using composites in marine propeller design can improve efficiency, durability, and performance. Some benefits of composite propellers come from the inherent properties of the composite material. Composites have better seawater corrosion resistance than metals [79]. Nonetheless, galvanic corrosion problems can occur and need to be considered. Particularly for naval use, the low magnetic signature of composites can be beneficial [70, 79].

Additional advantages arise from optimising material properties through adjustments in ply orientations, fibre volume fraction, and stacking sequence. This optimisation enables composite materials to achieve a high strength-to-stiffness ratio while maintaining a low weight [34, 70, 79]. Furthermore, the use of composites can result in flexible marine propellers [4, 65, 67]. A flexible propeller can deform to variations in fluid loading. The material properties of composites can cause an effect called bend-twist coupling. When the propeller is loaded with positive ship speed and positive propeller speed, the thrust generates a bending force in the forward direction on the blades, causing rake deformation. The bend-twist coupling causes the blade to twist, resulting in a reduction in the pitch angle. Since the blade root is rigidly connected to the hub, no pitch reduction occurs near the root, and the most significant pitch reduction occurs at the tip. This reduction in pitch at the tip leads to tip unloading, resulting in a decrease in thrust [62]. The bend-twist coupling can be used to passively adjust the pitch distribution of the blades and help maintain a near-optimal angle of attack for a blade section [101].

This deformation can lead to better vibration control and higher cavitation inception speeds, therefore reducing noise and cavitation [71]. Tip unloading reduces pressure pulses, allowing for a larger propeller diameter and a smaller tip clearance [60]. The tip unloading also results in increased cavitation inception speeds. Solomon and Ravinder [90] found improved cavitation properties in their study. In addition to cavitation behaviour, flexible propeller designs could improve performance. Mulcahy et al. [80] show in their study that flexible composite propellers can improve performance in off-design conditions and improve propulsive efficiency. As stated by Marsh [76], improved propulsive performance will lead to fuel savings. Consequently, composite propellers could provide a solution to the growing international regulations on emissions and underwater radiated noise, as also suggested by Maljaars and Kaminski [71].

3
Scaling Laws for Model Tests

Composite materials offer possibilities in the optimisation of marine propellers, as composites can improve the propeller's efficiency, durability, and performance. Furthermore, the use of composites can result in flexible marine propellers [4, 65, 67]. The ability of composite propellers to passively adapt to variations in fluid loading introduces additional design freedom. However, the flexibility of these propellers also adds complexity to the scaling of the propellers for model tests, as model-scaled propellers must replicate the full-scale deformation. Model tests are essential for evaluating performance and comparing different propellers. Open water tests assess and compare the performance of propellers in uniform flow. These tests are conducted with model-scale propellers in cavitation tunnels and towing tanks, as this approach is both technically feasible and more cost-effective. Nonetheless, significant differences between model and full-scale performance can arise due to model, scale and measurement effects. Dimensional analysis can help develop scaling laws and understand scale effects. This section will answer the following research sub-question:

'Which non-dimensional parameters follow from the relevant variables for flexible marine propellers?'

These non-dimensional parameters lead to the scaling laws that must be satisfied during model tests. The first section explores dimension analysis using Buckingham's Π-theorem. The following section discusses the considerations for model-scale testing. The third section focuses on the practical aspects of scaling rigid marine propellers for open-water tests. This section also highlights important factors to consider. The final section addresses the challenges of scaling flexible structures and explains how scaling flexible propellers differs from scaling rigid propellers.

3.1. Dimensional Analysis

In dimensional analysis, physical quantities and their units are used to understand the relationships between different physical quantities. Natural laws are independent of any unit system created by humans. Therefore, all physical relationships can be expressed in dimensionless form. This approach is convenient for comparison since scientists and engineers use various units (for instance, meters or inches) worldwide. Moreover, it can also help simplify problems and develop scaling laws. Dimensional analysis is important for comparing different propellers and testing model-size propellers to derive results applicable to full-size propellers.

E. Buckingham presented a general method for deriving non-dimensional parameters through dimensional analysis [10]. This method is known as the Π-theorem. In this theorem, an equation describes the relationship between n different physical quantities. The symbols $q_1, q_2, \ldots, q_n$ represent these n variables involved in the equation. There must be a functional relationship that can be expressed in the following form:

$$f(q_1, q_2, ..., q_n) = 0 \tag{3.1}$$

Buckingham states that the number of independent non-dimensional groups equals the number of physical quantities involved minus the number of dimensions involved. Each non-dimensional group is called a Π-group. So for n different variables with r independent dimensions, $n-r$ independent Π-groups can form the complete set that spans the parametric solution space:

$$\phi(\Pi_1, \Pi_2, ..., \Pi_{n-r}) = 0 \text{ or } \Pi_1 = \phi(\Pi_2, \Pi_3, ..., \Pi_{n-1}). \tag{3.2}$$

The process of dimensional analysis involves multiple steps. The first step is to select the relevant variables and parameters to include in the analysis. These variables and parameters come from the problem's geometry, boundary conditions, initial conditions, and material properties. Assumptions regarding the flow, such as whether it is isothermal or incompressible, can simplify the analysis by reducing the number of variables. For example, parameters like thermal conductivity, heat capacities, and thermal expansion coefficients may not be considered. All physical quantities can be expressed in terms of fundamental dimensions. Table 3.1 provides

the parameters related to (flexible) propellers. The three fundamental dimensions, mass (M), length (L), and time (T), express these parameters.

Physical Quantity or Property		**Dimensions**
Fundamental Quantities		
Time		$[T]$
Mass		$[M]$
Length		$[L]$
Angle		$[1]$
Physical parameters		
Diameter	D	$[L]$
Thickness	t	$[L]$
Chord	c	$[L]$
Pitch	P	$[L]$
Camber	f	$[L]$
Rake	$Rake$	$[L]$
Skew	$Skew$	$[1]$
Revolution rate	n	$[T^{-1}]$
Density	ρ	$[ML^{-3}]$
Velocity	u	$[LT^{-1}]$
Dynamic Viscosity	μ	$[ML^{-1}T^{-1}]$
Surface Tension	σ	$[MT^{-2}]$
Gravitational Acceleration	g	$[LT^{-2}]$
Force	F	$[MLT^{-2}]$
Pressure	p	$[ML^{-1}T^{-2}]$
Moment	M	$[ML^{2}T^{-2}]$
Young's Modulus	E	$[ML^{-1}T^{-2}]$
Poisson's Ratio	ν	$[1]$
Frequency	f	$[T^{-1}]$

Table 3.1: Physical quantities and dimensions related to flexible propellers

With these variables, a dimensional matrix is formed. The dimensional matrix is created by listing the powers of the dimensions for each parameter.

	D	t	c	P	f	$Rake$	$Skew$	n	ρ	u	μ	σ	g	F	p	M	E	ν	f
M	0	0	0	0	0	0	0	0	1	0	1	1	0	1	1	1	1	0	0
L	1	1	1	1	1	1	0	0	-3	1	-1	0	1	1	-1	2	-1	0	0
T	0	0	0	0	0	0	0	-1	0	-1	-1	-2	-2	-2	-2	-2	-2	0	-1

Table 3.2: Dimensional matrix listing the powers of the dimensions for each parameter

The rank of this matrix, the size of the largest square submatrix with a nonzero determinant, equals three. It follows that the number of dimensionless groups equals $19 - 3 = 16$. The dimensionless groups can be constructed by exponent algebra or by inspection. The non-dimensional relationships found for flexible marine propellers are given in Table 3.3, which answers the first sub-question. Some familiar non-dimensional numbers can be recognised in these Π-groups or by combining these groups.

Π-group	Relation	Known as	Also written as
1	t/c	Thickness-to-chord ratio	
2	c/D	Chord-to-diameter ratio	
3	P/D	Pitch ratio	
4	f/c	Camber-to-chord ratio	
5	$Rake/D$	Rake-to-diameter ratio	
6	$Skew^{\circ}$	Skew angle	
7	$u\ /\ nD$	Advance ratio	$J = V_a/nD$
8	$\mu\ /\ \rho uD$	Reynolds number	$Re = \rho UL/\mu$
9	$\sigma/\ \rho u^2 D$	Weber number	$We = \rho U^2 L/\sigma$
10	$u^2\ /\ gD$	Froude number	$Fr = U/\sqrt{gD}$
11	$F\ /\ \rho\ u^2 D^2$	Force (Thrust) coefficient	$K_T = T/\rho n^2 D^4$
12	$p/\rho\ u^2$	Euler number	$Eu = \Delta p/0.5 * \rho U^2$
13	$M/\rho\ u^2 D^3$	Moment (Torque) coefficient	$K_Q = Q/\rho n^2 D^5$
14	$E/\rho\ u^2$	Cauchy number	
15	ν	Poisson's ratio	
16	fD/u	Strouhal number	

Table 3.3: Matrix of Π-groups with their dimensionless definitions and physical significance.

3.2. Similarity Laws

Most experiments in ship hydrodynamics, such as open-water propeller tests, are carried out with model scales. Model, scale and measurement effects may influence the test results. Consequently, considerable differences can arise between the model scale and the full-size prototype. Model and scale effects can be avoided by satisfying all similarity laws. These laws are defined using non-dimensional parameters, such as those listed in Table 3.3. The parameter λ describes the scaling ratio or scale factor:

$$\lambda = \frac{L_F}{L_M} \tag{3.3}$$

The subscript F describes the full size, and the subscript M is the model size. Generally, scale effects for a specific phenomenon increase with the scale ratio as not all similarity laws can be satisfied [37]. The selected scale balances technical requirements for similitude and what is economically feasible. In the case of propeller tests, the dimensions of the towing tank or cavitation tunnel constrain the model scale sizes. A physical scale model exactly replicates its full-size prototype and has no scale effects if it satisfies the following criteria:

- Geometric similarity
- Kinematic similarity
- Dynamic similarity

Geometric similarity requires that both the full-size prototype and the scaled model have the same shape, i.e. all length dimensions in the model are scaled down by a factor λ. Consequently, model lengths, areas and volumes scale with λ, λ^2 and λ^3, respectively, in relation to the full size prototype. While geometric similarity is essential, it does not need to include the most minor details. For instance, it is nearly impossible to scale surface roughness exactly. This discrepancy is generally acceptable if the roughness is sufficiently small or effects can be considered empirically [64].

Kinematic similarity refers to the consistent ratio of time and velocities between model size and full size. Kinematic similarity refers to the similarity in motion between the model scale and the full-scale system. This concept requires that the ratios of time, velocity, and acceleration remain constant between the model scale and the full scale at all times [64].

Dynamic similarity refers to the condition where all forces in the flow are scaled by the same factor, meaning that the force vectors retain the same direction for both the model and the real-world prototype. Ergo, dynamic similarity requires constant ratios of all forces, and the ratios among different forces must be identical in both the model and the full-size version. The non-dimensional parameters, such as the Froude, Reynolds, Weber, Cauchy, Strouhal, and Euler numbers, represent ratios between forces and must be equal between the scaled model and the full-size model. These non-dimensional parameters can also be used to interpret physical phenomena in the flow [59, 64].

3.3. Scaling of Rigid Marine Propellers for Open Water Tests

For traditional, rigid marine propellers, scaling laws for open-water tests are well established [78]. The main parameter that needs to be determined in a propulsion test is the thrust (and, similarly, the torque) for a given full-scale ship speed. Appropriate scaling methods result in equal thrust and torque coefficients between the scaled model and the full-size propeller. The non-dimensional parameters, defined in Table 3.3, must be equal for both the model and the full-scale propeller for correct scaling. A function of the non-dimensional parameters expresses the thrust coefficient:

$$K_t = f(t/c, C/D, P/D, f/C, rake/D, skew^\circ, J, Re, We, Fr, \sigma, Ca) \tag{3.4}$$

The resulting thrust coefficient will be identical for the model and full-scale propeller if the quantities on the right-hand side of Equation 3.4 are appropriately scaled [97]. These quantities express the geometric, kinematic and dynamic similarity laws.

Geometric similarity can always be obtained regarding the thickness-to-chord ratio, chord-to-diameter ratio, camber-to-chord ratio, skew angle and pitch ratio. Propeller blades have a non-uniform cross-section to maximise efficiency and control, avoid cavitation, and ensure structural integrity. As a result, blade thickness, camber, chord length, skew, rake, and pitch angle vary along the radial direction. It is thus crucial to satisfy geometric similarity in all three dimensions so that the model-scale propeller accurately replicates the full-size propeller hydrodynamics [100].

Kinematic similarity is obtained by performing model-scale tests with the same advance ratio as the full-size propeller. The advance ratio establishes a fixed relationship between advance velocity and revolution rate. Kinematic similarity is always ensured, as either or both advance velocity and revolution rate can be adjusted. When performing model tests considering a non-uniform wake, an extra kinematic scaling requirement is to scale the propeller inflow properly. The ratio of local velocity should be similarly distributed as in the full-scale wake [97].

Dynamic similarity between model- and full-scale propellers is impossible to achieve when using the same fluid. The non-dimensional numbers representing the different force ratios help simplify the scaling. The numbers highlight the importance of keeping specific non-dimensional numbers consistent during model tests to ensure meaningful results.

The Cauchy number represents the ratio between elastic forces and inertial forces. The Cauchy number must be considered for elastic structures, but is not significant for rigid marine propellers. The Mach number replaces the Cauchy number for compressible flows, which are isentropic processes. The Mach number is defined as $M = U/c_s$, where c_s is the speed of sound [59]. Mach number similarity can typically be disregarded for marine propulsors as the flow compressibility effects of water are negligible. [59] [99].

The Strouhal number defines the ratio of unsteady acceleration to advective acceleration. This number determines the importance of unsteady fluid acceleration in flows with oscillations [59]. It is relevant for periodic flows, such as oscillations in vortex streets behind bluff bodies or flows driven by imposed frequencies [46]. Similarity of this number is not needed for propeller model tests.

The Weber number expresses the ratio between inertial and surface tension forces [59]. This parameter becomes significant when the flow involves a free surface, such as when a propeller operates sufficiently close to the surface, disturbing the free surface or drawing air [13]. Additionally, it is used for precise scaling of cavitation (inception). Weber similarity is not required for open water propeller model tests as the propeller is assumed to be sufficiently submerged [13].

Alongside the Weber number, the cavitation number is critical for scaling cavitation [54]. The cavitation number has a similar structure to the Euler number [64]. The Euler number is important in determining the absolute pressure level in the fluid. An increase in the atmospheric pressure at the water's surface will increase the pressure everywhere in the water, influencing the hydrostatic pressure [64]. The International Towing Tank Committee, abbreviated as ITTC, provides guidelines for model-scale propeller open-water tests. The open water tests in towing tanks should be conducted under atmospheric conditions and with a minimum shaft immersion of 1.5 times the propeller diameter [42].

The Reynolds number describes the ratio of inertial to viscous forces and is essential in viscous regimes. Phenomena such as boundary layer behaviour depend highly on this parameter [59]. Achieving Reynolds number similarity is difficult in cavitation tunnels or towing tanks because the model-scale speed must be faster than the full-scale speed. The viscous effects are relatively small compared to inertial forces for most design conditions. Specifically, when the Reynolds number exceeds $5 * 10^6$, the flow over the blades is fully turbulent, and the response becomes practically independent of the Reynolds number. Most full-scale propellers operate at a large enough Reynolds number to have primarily turbulent flow over the blade surface. In contrast, model-scale propellers often experience laminar flow over significant portions of the blades, particularly near the leading edge. This discrepancy arises because model-scale Reynolds numbers are typically around $1 * 10^6$ or lower in most test facilities due to size and speed limitations. Therefore, careful assessment of whether laminar or transitional flow may develop on certain parts of the blade surface is necessary [101]. These scale effects arising from differences in boundary layer phenomena depending on the Reynolds number can influence the performance characteristics [13]. A turbulent boundary layer significantly reduces the performance characteristics of the propeller as a result of reduced thrust and increased torque. Laminar boundary layers, on the other hand, are prone to flow separation under adverse pressure gradients, which also reduces the thrust and increases pressure drag [50].

The ITTC guidelines specify that propeller open water tests should be conducted at a minimum of two Reynolds Numbers. One should match the Reynolds number used for evaluating the propulsion test and must not be lower than $2 * 10^5$. The other should be as high as possible [42]. The ITTC also provides a procedure describing an analytical method to predict full-size propeller performance from model test results [41].

The Froude number expresses the ratio of inertial forces to gravitational forces. Froude similarity allows for smaller advance velocities more easily achieved in cavitation tunnels and towing tank studies [78]. However, Froude scaling is typically less relevant for most hydrofoils and marine propellers, as gravitational forces are usually minor compared to inertial and viscous forces [21]. In open-water tests, where the propeller is sufficiently submerged and operates in a non-cavitating environment, Froude similarity is not required. By neglecting Froude similarity, open-water model tests can be conducted at higher speeds, enabling experiments at higher Reynolds numbers [92]. Increased Reynolds numbers during model tests minimise any flow separation at the trailing edge or laminar flow on the suction side of the blade [13].

The Froude number is essential in flows influenced by gravity, such as when surface waves are generated, and for model tests investigating cavitation behaviour. Given a specific ambient pressure, an equal Froude number between the model and full-scale propeller ensures that the cavitation number remains constant throughout the flow field. When neglecting Froude similarity, the local cavitation number over the height, symbolised by z, will change. Taking into account the change in pressure over the height results in:

$$\sigma_v(z) = \frac{p - \rho g z - p_v}{\frac{1}{2}\rho U^2} = \frac{p - p_v}{\frac{1}{2}\rho U^2} - \frac{\rho g z}{\frac{1}{2}\rho U^2} = \sigma_v - \frac{\rho g z}{\frac{1}{2}\rho U^2} = \sigma_v - \frac{2}{Fr(z)^2}$$

The local cavitation number scales with $1/Fr^2$. A difference in the Froude number results in a difference in the local cavitation number based on the model's height. The local cavitation number is closer to the surface for model tests where the Froude number is unequal.

Table 3.4 overviews the non-dimensional numbers and their influence when testing rigid model scale marine propellers for open water tests.

Number	Ratio	When significant?	Example flow	Rigid propeller open water test
Cauchy number	Elastic force/Inertial force	Fluid-structure interactions	Elastic structure	Rigid, so not significant
Mach number	Compressibility force/Inertial force	Compressible flows	Shock waves	Not significant
Weber number	Inertial force/Surface tension force	Flow involves a free surface	Precise scaling cavitation/propeller close to surface	Not significant
Strouhal number	Unsteady/Steady acceleration	Periodic flows	Vortex street	Not significant
Euler number	Pressure force/Inertial force	Highly pressured flows	Cavitation	Towing tank: ITTC guidelines; Cavitation tunnel: adjustable
Reynolds number	Inertial force/Viscous force	Viscous flows	Boundary layers	Impossible: ITTC guidelines
Froude number	Inertial force/Gravitational force	Gravitational influenced flows	Free surface waves	Similarity is possible, if Reynolds is high enough

Table 3.4: An overview of the non-dimensional numbers and their influence when testing rigid model scale marine propellers for open water tests

3.4. Scaling of Flexible Propellers

The ability of composite propellers to passively adapt to variations in fluid loading introduces additional freedom in propeller design but also adds complexity to scaling flexible propellers for model tests. Essential for scaling flexible marine propellers is that the flexible model propeller retains the full-scale deflected shape during operation [97]. Both steady deflections in open water conditions and unsteady vibrations of the propeller blades during in-behind ship operation must be appropriately scaled.

A model propeller deforms equally to the full-size propeller for consistently scaled fluid-structure interaction. The 3-D deformation patterns and load-deformation behaviour must be preserved during model tests. To maintain the same inertial coupling between bending and torsion, the elastic axis must be identical between the model and the prototype. Ergo, the normalised variation of the effective bending rigidity, EI, torsional rigidity, GJ, and bend-twist coupling rigidity, K, along the radial direction must be the same [53, 100].

The performance of flexible propellers is dependent on the propeller shape and deformation. The modal frequencies describe the dynamic behaviour of structures, such as propeller blades. The first bending frequency, ω_B, depends on the bending stiffness, structural mass and hydrodynamic added mass:

$$\omega_B \propto \sqrt{\frac{K_B}{m + m_A}} \tag{3.5}$$

Here K_B is the bending stiffness, m is the structural mass, and m_a is the hydrodynamic added mass.

$$K_B \propto \frac{EI}{D^3}, \quad m \propto \rho_s D^3, \quad m_A \propto \rho_f D^3 \tag{3.6}$$

Geometric similarity is always ensured, accordingly $I \propto D^4$. From this follows:

$$\omega_B \propto \sqrt{\frac{ED^4}{D^6(\rho_f + \rho_s)}} \Rightarrow \omega_B \propto \frac{1}{D}\sqrt{\frac{E}{\rho_f + \rho_s}} \tag{3.7}$$

For complex geometries and blades made of anisotropic material, the first bending frequency of a blade may not be pure bending. Generally, the modal frequencies can be expressed as multiples of the bending and torsional frequencies [100]. The torsional deflection forces are similar to the elastic bending forces. The shear modulus, G, takes the place of Young's modulus. The shear modulus for an isotropic material is equal to:

$$G = \frac{E}{2(1 + \nu)} \tag{3.8}$$

When flexible marine propellers operate in a wake, the blades deform dynamically. Therefore, the modal frequencies should be scaled properly. The bending frequencies should scale with the propeller's revolution rate to obtain similar blade deformation during a revolution:

$$\frac{\omega_m}{n_m} = \frac{\omega_f}{n_f} \Rightarrow \sqrt{\frac{E_m}{(\rho_f + \rho_s) D_m^2 n_m^2}} = \sqrt{\frac{E_f}{(\rho_f + \rho_s) D_f^2 n_f^2}} \tag{3.9}$$

This form represents the ratio between bending forces, which are proportional to ED^2 and hydrodynamic inertial forces, proportional to $\rho_f n^2 D^2$ and propeller inertial force, proportional to $\rho_s n^2 D^2$. The elastic force, hydrodynamic inertial force and propeller inertial force are represented by F_E, F_H and F_I, respectively.

In addition to the scaling of the model frequency during a revolution, the relative blade deformation should also be considered. The amplitude of the bending, denoted by Δ/D, can be expressed as [100]:

$$\frac{\Delta}{D} \propto \frac{F_H D^2}{EI} f_{FSI}(\zeta, \frac{\omega}{n}) \propto \frac{\rho_f n^2 D^2}{E} f(\zeta, \frac{\omega}{n}) \tag{3.10}$$

In this equation, $f_{FSI}(\zeta, \frac{\omega}{n})$ is a function of the damping coefficient, described by ζ, and the frequency ratio, derived in Equation 3.9. This function is related to the fluid damping and the inertial forces caused by the fluid-structure interaction. The amplitude of the twisting, described by θ, should also be taken into account. A similar expression to Equation 3.10 can be formulated for the twisting; however, the shear modulus replaces the Young's modulus [100]. Equation 3.10 is a representation of the Cauchy number, similar to that given in Table 3.3, and is important to consider for flexible propeller model tests. In addition to elastic bending, hydrodynamic inertial and propeller inertial forces, other forces involved in the deformation of flexible marine propellers are the gravitational and viscous forces.

The ratio of inertial to gravitational forces leads to the Froude number. The gravitational forces acting on the propeller are small compared to the inertial forces when the propeller is sufficiently submerged [21]. The gravitational force has a negligible effect on the deformation of flexible propellers in open-water tests with non-cavitating flow. For these tests, strict adherence to Froude similarity is not required [92, 100].

It is known that similarity in Reynolds number, representing the inertial to viscous forces ratio, is impossible to obtain in towing tanks or cavitation tunnels [100, 101]. This discrepancy can lead to different boundary layer regimes [59], which in turn influence the performance characteristics of the propeller and introduce viscous scale effects [12, 49]. When the Reynolds number is sufficiently high, viscous effects have a negligible impact on the propeller's hydroelastic response [21]. However, as tests at typical towing tank or cavitation tunnel speeds are performed at lower Reynolds numbers, this could affect the deformation behaviour. Model testing at low Reynolds numbers may not only influence the propeller's thrust and torque as experienced for rigid model testing but also alter its deformation behaviour. This effect, in turn, could further impact the overall performance characteristics of the flexible propeller.

4
Simulation Methodology

Simulations of flexible marine propellers are performed to evaluate the deformation behaviour and to test different scaling methods. This thesis applies the workflow developed by Lagendijk [62] to perform time-domain Fluid-Structure Interaction, abbreviated with FSI, simulations of flexible marine propellers. The geometric description of an undeformed propeller serves as input for this workflow. The result of the workflow is a new geometry description of the deformed geometry, which allows visualisation of the blade deformation. This Chapter will answer the following questions:

- How does the structural solver work?
- How does the fluid solver work?
- How are the structural and fluid solvers combined in a Fluid-Structure Interaction Solver?

The first section will explain how the structural solver works, which uses a Finite Element Method. The second section will dive into the flow solver, which is based on unsteady Reynolds-Averaged Navier-Stokes equations. The last section will describe how these two solvers are combined and used for the FSI simulations of flexible marine propellers.

4.1. Structural Solver

A marine propeller blade has a non-uniform cross-section to maximise efficiency, maximise control and avoid cavitation. A propeller blade is a continuous mechanical system, and the equation of motion cannot be solved analytically. This workflow uses a Finite Element Method (FEM) structural solver. A FEM structural solver approximates continuous functions as discrete models. A Procal Propeller Geometry file describes the geometry of an undeformed propeller shape using the classical propeller design parameters at various sections and serves as input for the solver. The CAD program Rhinoceros [1] transforms this propeller description into a solid propeller geometry, which is discretised and simulated.

4.1.1. Equation of Motion

The mass, damping, and stiffness properties of a structure describe its dynamic behaviour. For larger structures, such as marine propeller blades, the system typically has multiple degrees of freedom, and matrices represent the mass, damping, and stiffness, denoted as [M], [C], and [K], respectively. The acceleration, velocity, and displacement are vectors with their length corresponding to the number of degrees of freedom for a system, and are denoted by $\{\ddot{x}\}$, $\{\dot{x}\}$ and $\{x\}$, respectively. The equation of motion is equal to [87]:

$$[M]\{\ddot{x}\} + [C]\{\dot{x}\} + [K]\{x\} = \{F\} \tag{4.1}$$

A discrete system consists of a finite number of well-defined components, while a continuous system implies an infinite number of elements. As the number of degrees of freedom increases, solving the motion equations becomes more complex, necessitating the use of numerical methods. Partial differential equations describe the equations of motion for continuous systems.

4.1.2. Finite Element Method

Finite systems can approximate continuous problems and can subsequently be solved numerically. This study uses a FEM solver. The problem's domain, in this case, the propeller blade, is discretised into a finite number of points and subdomains, termed nodes and finite elements, respectively. The elements connect at the nodes. Figure 4.1 illustrates a system discretised into finite elements and nodes. Within each finite element, an approximation of the equation of motion is defined. The values of this function depend on the values specified at the nodes of each element. The result is an algebraic equation set that can be solved. The steps of the finite element analysis involve discretisation, formation of element equations, assembly of the element equations, modification, and interpretation [93, 102].

Discretisation

A mesh is a collection of discretised elements representing the problem domain, and its construction process is called meshing. A finer mesh has more elements. Using a finer mesh or introducing more nodes on an element will result in more accurate solutions. However, both increase the computational cost of the FEM analysis [17]. A mesh can be refined in selected areas to reduce computational cost while increasing accuracy. The refinement will increase fidelity in those areas.

In this workflow, only one blade is discretised. This blade is copied to make a mesh for the propeller. The hub is considered rigid and is not part of the mesh. The blade grids consist of hexahedral elements where the propeller is discretised over the face and back surface and in the thickness direction [62]. Hexahedral elements are 3-dimensional elements that yield more accurate solutions than other 3-D elements [3]. The mesh is refined over the face and back surface of the blade. The desired number of cells over the blade surface is prescribed as input for the simulation. There is also a mesh refinement in the radial direction at the blade root region. This refinement improves the convergence behaviour of the FSI simulations. The distribution of cells over the blade surface and in the chordwise direction depends on the blade's geometry to ensure that the cells are approximately square in shape. The thickness discretisation is explicitly prescribed. Quadratic elements are used, which are elements with an extra node on each edge. Quadratic elements create elements with curved boundaries [102] to obtain quadratic rather than linear relations, which prevents shear locking [62].

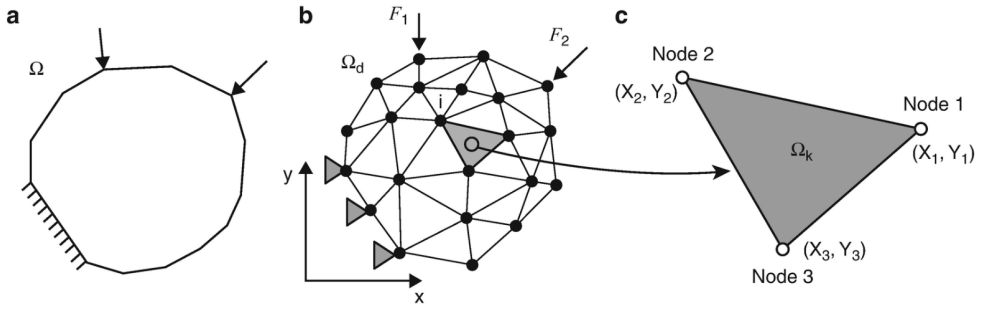

Figure 4.1: A systems domain is discretised into triangular elements. The nodes connecting the elements hold local approximations of the function. From Tekkaya and Soyarslan [93]

Structural Simulation

The code Aster [26] structural solver simulates the structural grid. The blade-hub connection is a clamped boundary condition, with the hub assumed to be rigid. The simulation provides the mass matrix, stiffness matrix, and dry modes of a single blade. The solver constructs mapping files that relate the surface nodes to specific locations in the mass and stiffness matrices. There is also an intnodes file generated, which contains the nodes at the interface between fluid and structure [62].

4.2. Flow Solver

The motion of a fluid is described with the Navier-Stokes equations. These are non-linear partial differential equations, and generally, an analytical solution cannot be found. Computational Fluid Dynamics, abbreviated as CFD, is used to find numerical solutions to fluid motion problems. This workflow uses ReFRESCO, which is a viscous-flow CFD code that solves multiphase (unsteady) flows using the incompressible Navier-Stokes equations, complemented with turbulence models. The equations are discretised using a finite-volume approach [75].

4.2.1. Navier Stokes Equations

The Navier-Stokes equations are partial differential equations which describe the motion of viscous fluids. The equations originate from conservation laws.

Conservation laws

Certain quantities are conserved in nature, as they are neither created nor destroyed. In a fluid, these quantities are mass, momentum and energy. The equation of conservation for energy comes into play for highly compressible flows, high Mach numbers and temperature changes or chemical reactions [9]. Therefore, this section will only dive deeper into the mass and momentum equations.

The conservation of mass states that the rate of change in mass is equal to a net flux. This equation is also called the continuity equation. For an arbitrary control volume, V, enclosed by a surface, S, with unit outward normal vector $\hat{n}$, the continuity equation is written at the integral scale as:

$$\frac{\partial}{\partial t}\int_V \rho\, dV + \int_S \rho \underline{u} \cdot \hat{n}\, dS = 0 \tag{4.2}$$

The momentum equation follows from Newton's Second Law, $F = ma = \frac{\partial}{\partial t}(mu)$. For a fluid, this principle states that the rate of change of momentum equals the sum of the momentum flux, body forces, and surface forces. Body forces, here represented by **B**, commonly arise from gravitational or electromagnetic force fields. Body forces are proportional to mass and distributed through the fluid. Surface forces, here denoted by **T**, act on fluid elements through surface contact and are proportional to the contact area [59]. The momentum equation is expressed as:

$$\frac{\partial}{\partial t}(\rho \underline{u}) + \boldsymbol{\nabla} \cdot (\rho \underline{\underline{u}}\, \underline{u}) = \boldsymbol{\nabla} \cdot \mathbf{T} + \rho \mathbf{B} \tag{4.3}$$

Assumptions

Two key assumptions simplify these equations. The first assumes that the fluid (water) behaves as a Newtonian fluid. The relationship between stress and deformation follows a linear constitutive equation for Newtonian fluids. The second assumption states that the fluid is incompressible, meaning that the density of a fluid particle remains constant over time. The shear stress, τ_{ij}, for a Newtonian, incompressible fluid is given as:

$$\tau_{ij} = \mu \left(\frac{\partial u_i}{\partial x_j} + \frac{\partial u_j}{\partial x_i} \right) \tag{4.4}$$

In this equation, μ is the dynamic viscosity, u_i and u_j are velocity components and x_i and x_j spatial coordinates. The surface forces are distinguished in a viscous part as given in Equation 4.4 and a pressure term $p\mathbf{I}$. With these assumptions, the momentum equation of Equation 4.3 can be written in integral form as:

$$\frac{\partial}{\partial t}\int_V (\rho \underline{u})\, dV + \int_S \rho \underline{\underline{u}}\, \underline{u} \cdot \hat{n}\, dS = \int_S \mathbf{T} \cdot \hat{n}\, dS + \int_V \rho \mathbf{B}\, dV, \text{ With } \mathbf{T} = -p\mathbf{I} + \mu(\nabla \underline{u} + \nabla \underline{u}^T) \tag{4.5}$$

The continuity equation described in Equation 4.2 and the momentum equation of Equation 4.5 form the Navier-Stokes Equations for incompressible flows.

4.2.2. Finite Volume Method

The Navier-Stokes Equations are non-linear partial differential equations, and an analytical solution can only be found for a few relatively simple cases. CFD is used to find numerical solutions to the Navier-Stokes equations [59]. A mesh is generated of the continuous fluid domain to obtain numerical approximations. Discrete equations that relate the discrete values describe the fluid flow and replace the partial differential equations. Various discretisation methods, similar to the Finite Element Method, can be used. ReFRESCO discretises the equations using a finite-volume approach [75].

A Finite Volume Method, FVM, discretises the total fluid domain into control volumes. The mesh size strikes a balance between the accuracy of the calculation and the computational costs. The Finite Volume Method uses the integral form of the Navier-Stokes Equation, as presented in Equation 4.2 and 4.5, to calculate fluxes across the surfaces of the control volumes. These fluxes have to maintain mass conservation. The fluid variables are defined in the centre of the cells and considered as the averages of the cell's volume [75]. Figure 4.2 shows a control volume.

The fluid grid in the simulations is a cylindrical domain surrounding the propeller with a diameter 10 times the propeller diameter. This unstructured grid mainly consists of hexahedral elements and some tetrahedra and pyramids at the connection layer between refinement levels [62].

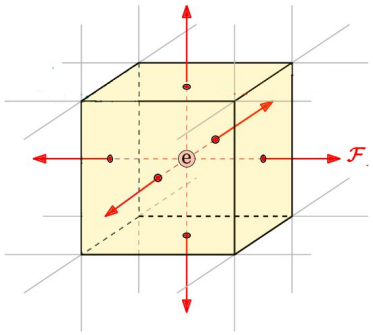

Figure 4.2: Cell-centred FVM: Fluid variables are defined at the cell centre, and fluxes are computed across its surfaces. From Haider et al. [33]

Time Step

The time step in the simulations is an important factor to consider. The Courant number represents the coupling between the time step, mesh size and flow velocity:

$$C = \frac{U\Delta t}{\Delta x} \tag{4.6}$$

In Equation 4.6, the fluid velocity equals U, the time step is Δt, and the cell length is Δx. If the Courant number exceeds one, a fluid particle moves through multiple grid cells in a single time step. This reduces solution accuracy and can lead to numerical instabilities [38].

4.2.3. Turbulence

Turbulence is a highly unsteady, three-dimensional phenomenon that occurs at very low length and time scales. This study will not resolve all fluid motion scales using Direct Numerical Simulation, known as DNS. DNS requires a very fine mesh, making the simulations computationally intensive and costly. The flow solver models turbulence effects by averaging the flow equations and applying additional closure models, rather than directly resolving turbulence.

The averaging process of the flow equations is called Reynolds averaging. The Reynolds-Averaged Navier-Stokes, or short RANS equations are obtained by averaging the Navier-Stokes equations. The average of the non-linear term in the Navier-Stokes equations gives two terms: the product of the average and the co-variance. The covariance of two quantities is non-zero if the quantities are correlated, which is often the case in turbulent flows. Therefore, the averaging process will result in extra terms. The RANS equations are not closed due to these extra terms, and additional turbulence models are needed.

The RANS equations can be solved in a time-dependent manner, allowing for time-dependent changes in the flow field. These unsteady Reynolds-Averaged Navier-Stokes equations, shortened by URANS, still utilise the Reynolds averaging of the Navier-Stokes equations but do not average the flow in time as strictly as RANS. Figure 4.3 visualises the difference between URANS, RANS and DNS for a quality ϕ over time.

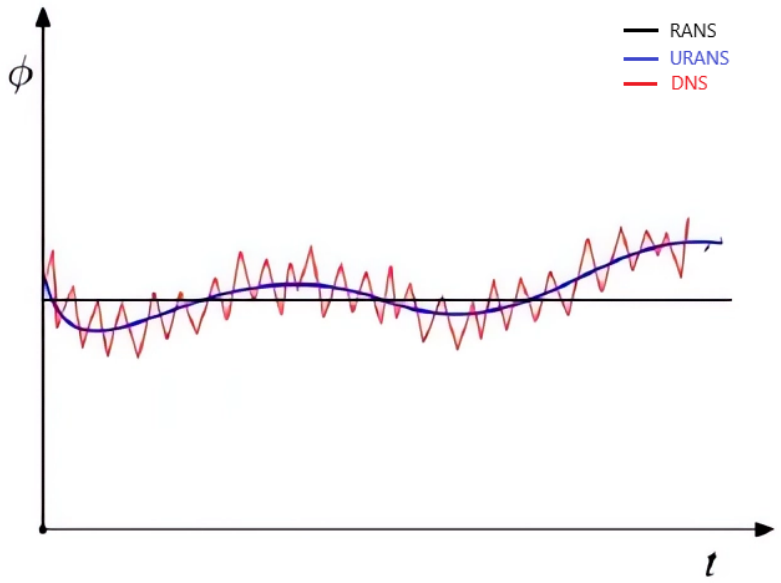

Figure 4.3: Visualisation of the difference between URANS, RANS and DNS simulations for a quality ϕ over time

Turbulence Models

The effect of turbulence can be interpreted as an increase in viscosity when using the URANS equations. This turbulent viscosity, or eddy viscosity, is computed using turbulence models and is characterised by the velocity and length scales of the turbulence eddies. The turbulence model implemented in ReFRESCO is the $k-\omega$ SST model of Menter [82]. This model is a so-called 2-equation model, which provides equations for the turbulence kinetic energy and the turbulence length scale. The model can be used to predict properties of a given turbulent flow with no prior knowledge of the turbulent structure [75].

Y-Plus Value

A viscous fluid flow over a solid surface must satisfy the no-slip boundary condition [59]. In a turbulent flow, the turbulent fluctuations must therefore go to zero at the wall to satisfy this condition. The near-wall flow has very strong velocity gradients. The time mean velocity, $\bar{u}$, near a solid boundary, depends upon fluid density, kinematic viscosity, shear stress at the wall and on the distance from the wall, denoted by ρ, ν, τ_w and y, respectively [72]. A friction velocity, u_τ, is introduced and defined by [8]:

$$u_\tau = \sqrt{\frac{\tau_w}{\rho}} \tag{4.7}$$

This velocity is used in dimensional analyses to obtain two non-dimensional quantities, namely a non-dimensional length, y^+, and non-dimensional velocity, u^+ [8]:

$$y^+ = \frac{y}{\nu}\sqrt{\frac{\tau_w}{\rho}} = \frac{u_\tau y}{\nu} \tag{4.8}$$

$$u^+ = \bar{u}\left(\frac{\tau_w}{\rho}\right)^{-\frac{1}{2}} = \frac{\bar{u}}{u_\tau} \tag{4.9}$$

From dimensional analysis, it follows that the non-dimensional velocity is a function of only the non-dimensional length: $u^+= f(y^+)$, known as the law of the wall. In a turbulent flow, the turbulent fluctuations must go to zero at the wall to satisfy the no-slip condition. This results in a very small layer next to the wall, where $u^+ = y^+$. This layer is known as the viscous or laminar sublayer [8]. One can interpret y^+ as a local Reynolds number, which means that its magnitude determines the relative importance of viscous forces. The viscous sublayer is the region very close to the wall, for y^+-values below five. Here, the fluid velocity is very low, and the viscous force is completely dominant. In this layer, the wall gradients are substantial, and an accurate representation of the near-wall region is necessary for a successful prediction of wall-bound turbulent flows [81].

Turbulence models are modified to resolve the entire viscosity-affected region, including the viscous sublayer. The first cell centre must lie in the viscous sublayer when using a turbulence model, such as the $k-\omega$ SST turbulence model, to solve the near-wall region [81]. Determination of the shear-stress at the wall requires the use of near-wall cells typically present with a non-dimensional height of y^+ equal to 1 or less [43].

4.3. Fluid Structure Interaction Simulation

The numerical simulation enables fluid-structure interaction simulations of the propeller, allowing visualisation of blade deformation and performance characteristics [62].

This study employs a partitioned approach, utilising separate software for the fluid and structural components [62]. This approach has the advantage that the software is optimised for fluid and structural problems, and the existing solution methods do not need to be changed. A coupling mechanism is necessary to manage interactions between solvers. The partitioned approach allows for the use of distinct grids for the fluid and structural domains. Typically, the fluid domain requires a finer mesh than the propeller blade for accurate solutions [45]. One drawback of the partitioned approach is that the equations are not solved simultaneously in time, which potentially results in additional errors.

A strongly coupled approach can minimise the possible errors due to the fluid-structure interaction coupling. In the strongly coupled approach, the solutions for both the flow and structural domains are exchanged multiple times per time step until a converged solution is reached [45]. The solver uses a grid deformation method where the loads and displacement are transferred using radial basis functions. Radial basis functions are mathematical functions whose value depends on the distance between the nodes. Radial basis function interpolation is used to propagate the effect of blade deformation to the whole fluid domain and the effect of the fluid load on blade deformation [30]. Compact support radial basis functions are applied with a support radius of D/6. This radius defines the region around the surface nodes within which the grid points deform. Outside this radius, the grid remains undeformed [62].

The FSI simulation starts with a simulation of a rigid propeller to obtain a converged initial flowfield. After this, the FSI simulation for the flexible propeller is performed. The workflow results in a new geometry description of the deformed geometry. The results enable comparison between input and output geometry, allowing for the determination of propeller deformation based on changes in classical design parameters. Furthermore,

the results facilitate the evaluation of the sectional deformations of the blades at different radial positions [62]. Figure 4.4 shows a flow chart for the procedure for a single time-step of the simulation [75].

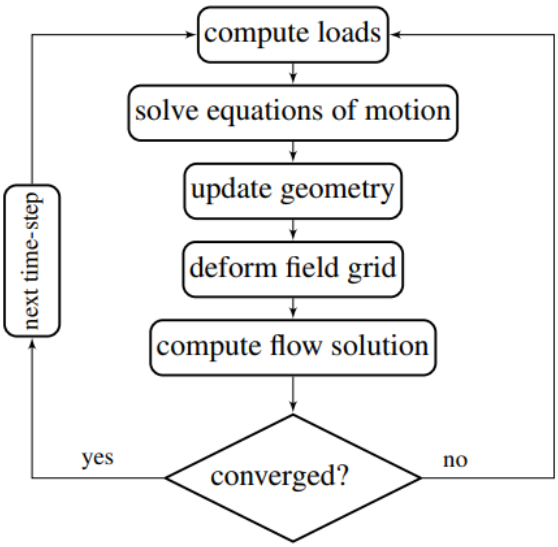

Figure 4.4: Flow chart for a time-step of the fluid-structure interaction simulation using a strongly coupled approach. From Jongsma et al. [45]

4.4. Propeller Geometry and Material Properties

All simulations in this report use the Wageningen C4-40 propeller, which has four blades, a 40% blade area ratio, and a pitch ratio of P/D = 0.8. This geometry has been designed and tested at the Maritime Research Institute Netherlands, known as MARIN. The performed propeller tests included experiments with flexible materials for this geometry. Figure 4.5 presents the outline of the C4-40 propeller geometry. MARIN constructed their flexible model propeller from POM-C, a thermoplastic polymer with isotropic properties and a Young's modulus of 3 GPa. The Young's modulus applied in the flexible simulations of this study is derived from the Cauchy number defined in Equation 3.9 of the MARIN experiments, to ensure comparable values across all cases.

Figure 4.5: Outline of the Wageningen C4-40 propeller

Geometric propeller properties follow from the CAD program Rhinoceros [1], which transforms a tabular propeller description into a solid propeller geometry. Table 4.1 lists the geometric propeller properties.

C4-40 Propeller Properties			
Projected blade area ratio	A_P/A_O	0.362	$[-]$
Expanded blade area ratio	A_E/A_O	0.396	$[-]$
Skew angle	θ_s	28.27	$[^\circ]$
Pitch ratio at r/R=0.7	$(P/D)_{0.7}$	0.800	$[-]$
Mean pitch ratio	$(P/D)_{mean}$	0.768	$[-]$
Chord-to-diameter ratio at r/R=0.7	$c_{0.7}/D$	0.2545	$[-]$
Thickness-to-chord at r/R=0.7	$t_{0.7}/c$	0.044	$[-]$

Table 4.1: Geometric propeller properties of the C4-40 propeller

5
Reynolds Effects on Rigid Propellers

The model scale effects due to differences in Reynolds numbers are known as the Reynolds effects and pose challenges in predicting propeller performance at model scales. Reynolds effects can impact the propeller performance characteristics, and significant differences can arise between the results of various procedures [12]. This chapter will answer the following sub-question:

'What are the Reynolds number effects on the performance of rigid marine propellers in the applied simulations?'

This chapter presents the open-water characteristics of a rigid propeller for different Reynolds numbers, helpful in analysing the scale effects of flexible propellers in the following chapters. The first section presents the input of the numerical simulations. The second section presents the test results, including the open-water diagram, the relative difference between the various Reynolds numbers tested, and visualisations of the skin friction coefficient and streamlines over the blade. The final section summarises the main conclusions.

5.1. Simulation Input

Numerical simulations are conducted to determine the rigid propeller performance for a range of positive advance ratios in open-water conditions. These simulations are performed with the Wageningen C4-40 propeller, with a pitch ratio of 0.8. Figure 4.5 shows the outline of this propeller. Table 4.1 lists the main propeller properties. All simulations are performed with a propeller diameter of 2 meters.

This chapter presents the results of simulations conducted for various Reynolds numbers. The Reynolds number is defined following the ITTC definition:

$$Re_{0.7} = \frac{c_{0.7}\sqrt{V_A^2 + (0.7\pi nD)^2}}{\nu} \tag{5.1}$$

Here, $c_{0.7}$ is the propeller chord length at position $r/R = 0.7$, V_a the advance velocity of the fluid, n the propeller revolution rate, D the propeller diameter and ν the kinematic viscosity of the fluid. The revolution rate and advance velocity are adjusted to ensure a constant Reynolds number over the range of advance ratios. The lowest value is slightly below the minimum Reynolds number of $2 * 10^5$ recommended by the ITTC guidelines for open-water propeller tests [42]. Since full-scale propellers operate at Reynolds numbers of the order 10^7 [49], a maximum value of $5.0 * 10^7$ is selected for the simulations. Table 5.1 lists the input settings for all Reynolds numbers for the range of advance ratios.

Re [-]	$1.0 * 10^5$		$1.0 * 10^6$		$1.0 * 10^7$		$5.0 * 10^7$	
J [-]	n [RPM]	V_a [m/s]	n [RPM]	V_a [m/s]	n [RPM]	V_a [m/s]	n [RPM]	V_a [m/s]
0	3.187	0.000	31.87	0.000	318.7	0.000	1593	0.000
0.1	3.183	0.011	31.83	0.106	318.3	1.061	1592	5.306
0.2	3.174	0.021	31.74	0.212	317.4	2.116	1587	10.57
0.3	3.157	0.032	31.57	0.316	315.7	3.157	1579	15.78
0.4	3.135	0.042	31.35	0.418	313.5	4.180	1568	20.90
0.5	3.107	0.052	31.07	0.518	310.7	5.179	1554	25.89
0.6	3.074	0.061	30.74	0.615	307.4	6.149	1537	30.74
0.7	3.037	0.071	30.37	0.709	303.7	7.085	1518	35.42
0.8	2.995	0.080	29.95	0.799	299.5	7.986	1497	39.92
0.9	2.949	0.088	29.49	0.885	294.9	8.848	1475	44.23

Table 5.1: Operational input settings for various Reynolds numbers for a range of positive advance ratios.

5.2. Results

This section presents the results of rigid propeller simulations to examine the effects of Reynolds numbers. First, the open-water diagram is presented and discussed. Then, plots of the percentage difference for the tested range of Reynolds numbers are given. Finally, the skin friction coefficient over the blade surface and the streamlines over the blade surface are provided and analysed.

5.2.1. Open Water Diagram

Figure 5.1 shows the open water results for positive advance ratios, for the range of Reynolds numbers tested. The open-water diagram displays the non-dimensional thrust coefficient, torque coefficient, and open-water propeller efficiency, as defined in Equations 2.7, 2.8, and 2.10, respectively.

Figure 5.1 shows that the Reynolds number has a visible effect on both thrust and torque coefficient. A higher Reynolds number shows a higher K_T value for a certain J value. The variation in K_Q shows a trent opposite to K_T. Higher Reynolds numbers result in a lower K_Q value for a certain advance ratio. Looking at the efficiency, the higher the Reynolds number, the higher η_o.

The Reynolds number determines the boundary layer flow over the blade's surface. The flow solver calculates the flow using a turbulence model and does not use transition models. So for all Reynolds numbers, a fully turbulent flow is solved. Higher Reynolds numbers result in a thinner turbulent boundary layer, which can more easily follow the blade's curvature [59]. This reduces boundary layer separation, allowing the propeller blades to generate more lift while experiencing less drag. The open-water efficiency depends on both the thrust and the torque coefficient. The efficiency increases for higher K_T values as well as for smaller K_Q values.

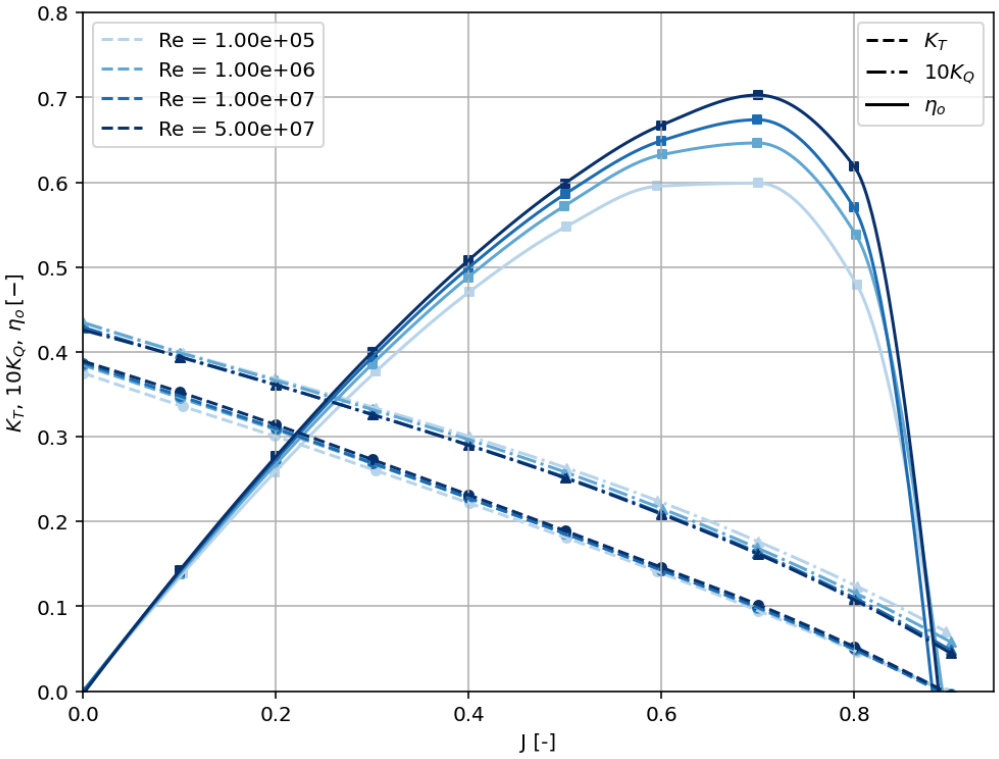

Figure 5.1: Open water diagram of the rigid Wageningen C4-40 propeller with a pitch ratio of 0.8 for different Reynolds numbers. The thrust coefficient and open-water efficiency increase for increasing Reynolds numbers, while the torque coefficient decreases as the Reynolds number increases.

5.2.2. Percentage Difference Between Reynolds Numbers

In the simulations, the predicted performance of the rigid propeller is sensitive to variations in Reynolds number. If variations do not influence the deformation of flexible propellers in terms of Reynolds number, the same magnitude of differences between Reynolds numbers is expected for flexible propeller simulations. This section quantifies the order of magnitude of the Reynolds effects for the rigid propeller simulations.

Figure 5.2 shows the percentage difference between the thrust coefficient, torque coefficient and open water efficiency for the different Reynolds numbers. All percentage differences are relative to the case with a Reynolds number of $5*10^7$, which corresponds to a typical order of magnitude for full-scale Reynolds numbers [49]. Figure 5.2 presents the results for an advance ratio of 0.8, where the most considerable difference between results is found. Similarly, Rijpkema et al. [88] found the largest variations in thrust, and consequently in propeller efficiency, at higher advance ratios. Their study attributed this to the larger extent of the leading-edge vortex at the lower advance ratios. This leading-edge vortex induces reattachment and a turbulent boundary layer, resulting in better agreement between Reynolds number cases. At higher advance ratios, the influence of Reynolds number becomes more pronounced as boundary-layer behaviour differs more strongly. Appendix A presents the results of other advance ratios.

For the operational condition of Figure 5.2, the relative difference of the torque coefficient between $Re = 1 * 10^5$ and $Re = 5 * 10^7$ equals 14.8%. This difference is equal to 1.1% for the advance ratio of 0.1. The thrust coefficient has a difference of -11.3% when comparing $Re = 1 * 10^5$ and $Re = 5 * 10^7$ for J equals 0.8. For all advance ratios below 0.6, this difference is around -5% between $Re = 1 * 10^5$ and $Re = 5 * 10^7$.

The difference in open water efficiency between $Re = 1 * 10^5$ and $Re = 5 * 10^7$ is -22.5% for J equals 0.8. The open-water efficiency is a combination of trust and torque coefficient and will decrease for both lower K_T values and for higher K_Q values. Ergo, for all positive advance ratios η_o increase for higher Reynolds numbers. The smallest relative difference for the open-water efficiency is for J equals 0.1, when disregarding the bollard pull case, for which efficiency is always zero by the definition in Equation 2.10. For J equals 0.1, the difference in efficiency is equal to -2.4% between $Re = 1 * 10^5$ and $Re = 5 * 10^7$.

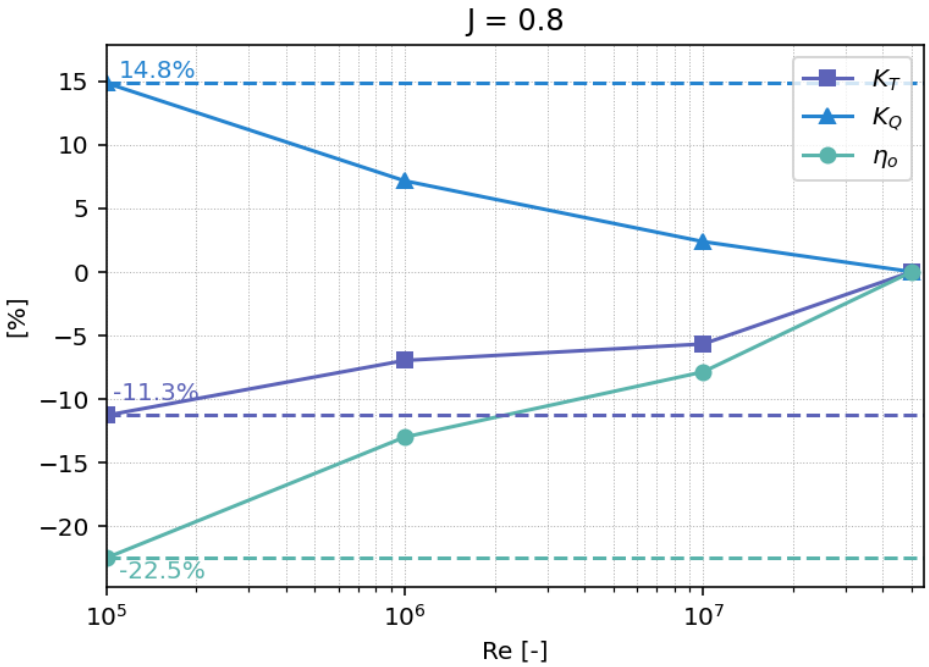

Figure 5.2: Percentage differences in K_T, K_Q, and η_o across Reynolds numbers, with respect to the case of $Re = 5 * 10^7$. Results are for the rigid C4-40 propeller at an advance ratio of 0.8. The variation of the Reynolds number shows an increase in the thrust coefficient and a decrease in the torque coefficient as the Reynolds number increases.

5.2.3. Skin Friction Coefficient and Streamlines

This section analyses the skin friction coefficient and streamlines over the blade surfaces for different Reynolds numbers, helping to explain the differences in open-water performance visible in Figure 5.1. Skin friction, also known as wall shear stress, is the flow tangential stress on a solid surface. A viscous fluid flowing over a solid surface must satisfy the no-slip boundary condition. The no-slip condition results in a velocity gradient at the surface, causing a shear force. The shear stress acting on a surface by a flowing viscous fluid is known as wall shear stress [59]. The skin friction is defined as the non-dimensionalised skin friction coefficient, C_F:

$$C_F = \frac{\tau_w}{\frac{1}{2}\rho_f U_\infty^2} \tag{5.2}$$

Where τ_w is the local wall shear stress, ρ_f expresses the fluid density and U_∞ denotes the free-stream velocity.

The free-stream velocity is usually taken at the inlet of the fluid domain [14], in this case equal to V_a. The skin friction coefficient is a valuable parameter in boundary layer flows. This coefficient specifies the fraction of the local dynamic pressure that is felt as shear stress on the surface. An increase in the Reynolds number for a fully turbulent flow will result in a lower C_F value [59]. As the Reynolds number increases, the viscous forces become relatively smaller compared to the inertial forces. Consequently, the shear stress exerted by the flow on the surface decreases for the same local dynamic pressure, resulting in a lower skin friction coefficient.

Figures 5.3 and 5.4 illustrate the skin friction coefficient and streamlines over the propeller blades' suction and pressure side for the tested Reynolds numbers for a J-value of 0.1. A slight decrease in the skin friction coefficient is visible with an increase in the Reynolds number on both the pressure and suction sides. The streamlines become more circumferentially directed with increasing Reynolds numbers for both sides. For all Reynolds numbers, the streamlines show flow separation near the trailing edge on the blade's suction side. This separation region near the trailing edge decreases in size as the radius decreases from higher to lower values on the suction side. For all cases, the streamlines also show some extent of leading-edge flow separation on the suction side of the blades. However, only the streamlines in Figure 5.3c and 5.3d reveal a clear leading-edge vortex. Figure 5.4a presents an increase in skin friction coefficient near the trailing edge on the pressure side of the blade at a Reynolds number of $1 * 10^5$. In addition, the streamlines are less circumferentially directed compared to the three cases with higher Reynolds numbers. The streamlines and skin friction coefficient indicate flow separation near the trailing edge, which does not occur at the three higher Reynolds numbers.

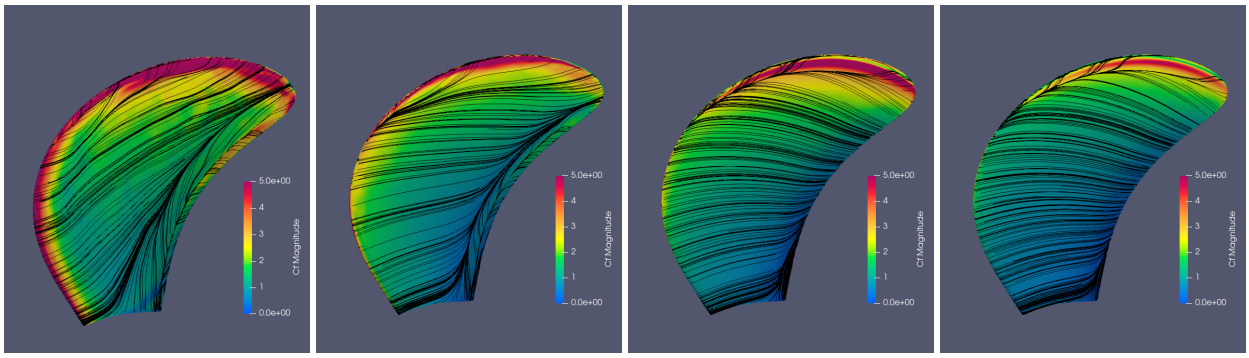

(a) $Re = 1 * 10^5$ **(b)** $Re = 1 * 10^6$ **(c)** $Re = 1 * 10^7$ **(d)** $Re = 5 * 10^7$

Figure 5.3: Streamlines and skin friction coefficient on the suction side of the rigid C4-40 propeller blade tested at a J of 0.1. For increasing Reynolds number, the skin friction coefficient decreases slightly. The streamlines are more circumferentially directed for higher Reynolds numbers.

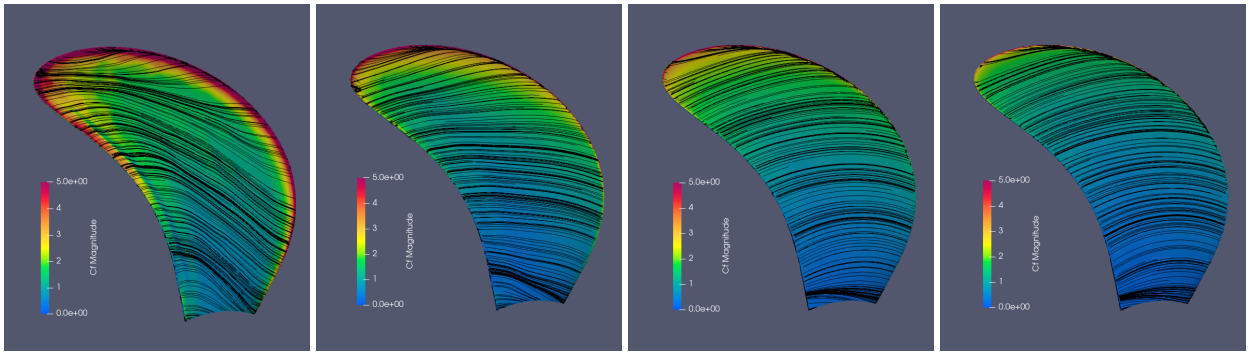

(a) $Re = 1 * 10^5$ **(b)** $Re = 1 * 10^6$ **(c)** $Re = 1 * 10^7$ **(d)** $Re = 5 * 10^7$

Figure 5.4: Streamlines and skin friction coefficient on the pressure side of the rigid C4-40 propeller blade tested at a J of 0.1. For increasing Reynolds number, the skin friction coefficient decreases. The streamlines are more circumferentially directed for higher Reynolds numbers.

Figures 5.5 and 5.6 illustrate the skin friction coefficient and streamlines over the propeller blades' suction and pressure side for a J-value of 0.7. This advance ratio is around the most optimal working point of the propeller, as visible in Figure 5.1. A decrease in C_F is visible with an increase in the Reynolds number on both the pressure and suction sides. The streamlines become more circumferentially directed for both sides as the

Reynolds number increases. For $Re = 1 * 10^5$ and $1 * 10^6$, the separation near the trailing edge on the suction side is over almost the entire length of the trailing edge. In contrast, for $Re = 1 * 10^7$ there is some trailing edge separation at the lower radii, and Figure 5.5d presents hardly any trailing edge separation. Figures 5.6b, 5.6c, and 5.6d show a small leading-edge vortex on the pressure side of the blades. The size of the vortex and the radial position at which it forms vary depending on the Reynolds number. The leading-edge vortex is less pronounced looking at the streamlines of Figure 5.6a. For this Reynolds number, the increase in skin friction near the trailing edge and streamlines reveals flow separation at the pressure side. For all these cases, there is less boundary layer separation for the optimal working point compared to Figure 5.3 for the more heavily loaded cases.

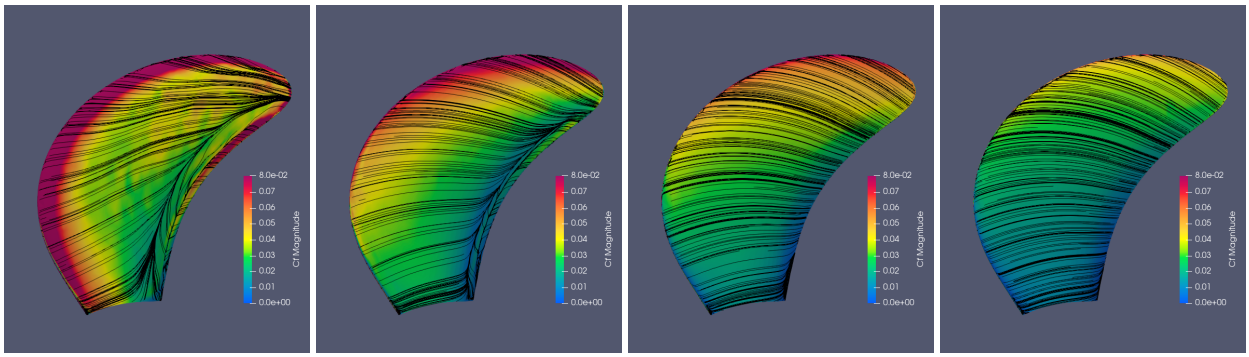

(a) $Re = 1 * 10^5$ **(b)** $Re = 1 * 10^6$ **(c)** $Re = 1 * 10^7$ **(d)** $Re = 5 * 10^7$

Figure 5.5: Streamlines and skin friction coefficient on the suction side of the rigid C4-40 propeller blade tested at a J of 0.7. As the Reynolds number increases, the skin friction coefficient decreases, and the streamlines become more circumferentially directed.

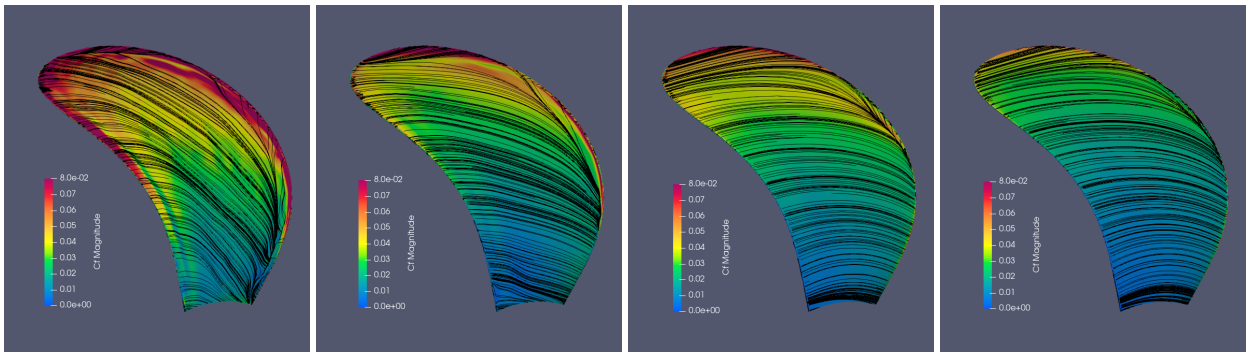

(a) $Re = 1 * 10^5$ **(b)** $Re = 1 * 10^6$ **(c)** $Re = 1 * 10^7$ **(d)** $Re = 5 * 10^7$

Figure 5.6: Streamlines and skin friction coefficient on the pressure side of the rigid C4-40 propeller blade tested at a J of 0.7. As the Reynolds number increases, the skin friction coefficient decreases, and the streamlines become more circumferentially directed.

The momentum of the boundary layer flow close to the hub cannot follow the propeller's blade shape. For higher Reynolds numbers, the boundary layer becomes thinner and has more energy [59]. Consequently, the flow follows the blade's shape more easily, which explains the decrease in flow separation as the Reynolds number increases. This explains that the boundary-layer shows a more circumferentially directed flow at higher Reynolds numbers. For J equals 0.1, all cases experience some trailing edge separation on the suction side. In contrast, for a J of 0.7, the highest Reynolds number shows no flow separation on the suction side. In heavily loaded conditions, such as those occurring near bollard pull, the flow must follow a greater curvature as a result of an increased AoA. Thus, there is less boundary layer separation around the optimal working point compared to more heavily loaded cases.

The results are consistent with Reipema et al. [88]. At lower advance ratios, all blades exhibit some extent of a leading-edge vortex on the suction side of the blades. This leading-edge vortex induces flow reattachment, producing a turbulent boundary layer. Consequently, there is an improved agreement of flow between Reynolds number cases, as evidenced by the minor differences in the skin-friction coefficient for the low advance ratios. At higher advance ratios, the influence of Reynolds number becomes more pronounced. The skin friction coefficient decreases more with the increase of Reynolds number, as boundary-layer behaviour differs more strongly. Appendix A shows the blade figures of other advance ratios.

5.3. Conclusion

In this chapter, FSI simulations were carried out for rigid propellers in open-water conditions to answer the second sub-question of this thesis: *'What are the Reynolds number effects on the performance of rigid marine propellers in the applied simulations?'* The performance prediction and boundary-layer flow are analysed in detail for a range of Reynolds numbers, from minimal model scale Reynolds number ($Re = 1 * 10^5$) up to full-scale ($Re = 5 * 10^7$) Reynolds numbers. The flow solver is implemented with the $k - \omega$ SST turbulence model without the use of a transition model.

The Reynolds number determines the boundary layer flow over the propeller blades. A turbulent boundary layer becomes thinner and has more energy for higher Reynolds numbers [59]. Therefore, the boundary-layer flow becomes more circumferentially directed for increasing Reynolds numbers. The skin friction coefficient decreases, and blades experience less flow separation as the Reynolds number increases. Independent of the Reynolds number, there is less boundary layer separation around the optimal working point compared to more heavily loaded cases. For advance ratios around the propeller's most efficient operating condition, simulations with larger Reynolds numbers show noticeably less flow separation, while at lower Reynolds numbers, there is still some flow separation for these near-optimal operating conditions. In contrast, for heavily loaded cases with a large angle of attack, this relative difference is less, as all blades experience trailing-edge flow separation independent of the Reynolds number. For these lower advance ratios, the blades exhibit some extent of a leading-edge vortex on the suction side. As a result of the turbulent flow reattachment, there is better agreement between Reynolds number cases in the skin friction coefficient. At higher advance ratios, boundary-layer behaviour differs more strongly, and the influence of Reynolds number becomes more pronounced.

Those effects are visible in the open water diagram of the rigid C4-40 propeller. The variation of the Reynolds number shows an increase in the thrust coefficient and a decrease in the torque coefficient as the Reynolds number increases. Within the performed simulations of this study, the effect comparing the results between $Re = 1 * 10^5$ and $Re = 5 * 10^7$ on K_T is between -5 and -11.3%, depending on the operating condition. This difference between $Re = 1 * 10^5$ and $Re = 5 * 10^7$ on K_Q is between 1.1 and 14.8%. The open-water efficiency is a combination of both and increases for higher Reynolds numbers. The relative difference between $Re = 1 * 10^5$ and $Re = 5 * 10^7$ on η_o is between -2.4 and -22.5% depending on the advance ratio.

6

Scaling Flexible Propellers using the Cauchy Number

Scaling flexible propellers for model tests adds complexity to the scaling methods. The deformation of a flexible propeller must remain consistent during a revolution and be scaled accurately. Equation 3.10 derives a representation of the Cauchy number. This number should be equal between the model and the full-scale propeller to obtain equal blade deformation. This chapter will answer the following sub-question:

'What are the scale effects when satisfying the Cauchy number using a combined Reynolds-Cauchy similarity approach for flexible marine propellers?'

The first section will elaborate on various scaling methods, while the second section provides an overview of the input settings used in the performed simulations. The third section presents the results, including the open-water diagram, the relative difference in results between the cases, plots of the flexible propeller deformation, and visualisations of the skin-friction coefficient and flow streamlines over the blades. A discussion of the results follows, and the chapter concludes with the main insights.

6.1. Scaling Flexible Propellers using Froude-Cauchy, Reynolds-Cauchy and Mach Similarity

The deformation of flexible propellers must scale appropriately, as the performance of flexible propellers is dependent on the deformed geometry. The following representation of the Cauchy number is derived in Chapter 3 to replicate the correct relative blade deformation:

$$Ca = \frac{E}{\rho_f D^2 n^2} f(\zeta, \frac{\omega}{n}) \tag{6.1}$$

This non-dimensional number is investigated using the coupled URANS-FEM FSI solver. This coupled solver accounts for the interaction between fluid flow and structural velocities and acceleration, incorporating the fluid damping. The ratio of bending frequency to revolution rate, given in Equation 3.9, depends, among the propeller stiffness, fluid mass and diameter, on the structural mass of the propeller blade. For all these variables, a scaling relation has to be derived to obtain similarity. The parameter λ describes the scaling ratio, and the model length scale is defined as: $L_M = \frac{1}{\lambda} L_F$. For propeller model tests, the fluid density is considered comparable between freshwater and seawater. Hence, the scaling ratio between the model and full-scale fluid density equals 1. The structural density must follow this same scaling relation and must also be equal between the full-scale and model-scale propellers. The Young's modulus and angular velocity can be scaled using a combined Froude-Cauchy similarity, a Mach similarity or a combined Reynolds-Cauchy similarity approach to satisfy Equation 6.1. Table 6.1 summarises the scaling factors required to satisfy these similarity approaches, while Appendix B gives the derivation of these scaling relations.

Model tests that apply Mach similarity can use the same materials and employ similar composite layering strategies [48]. Elasticity, blade density, and Poisson's ratio should remain the same as in the full-scale case. The model tests should be conducted at full-size inflow velocity using Mach similarity [21]. This requirement imposes constraints on testing model-scaled propellers for fast vessels, as most facilities are unable to test at such high velocities or forces. The revolution rate is scaled with λ^{-1} to obtain an equal advance ratio. Mach-scaled model tests are performed at higher Froude numbers, underpredicting the gravitational force compared to the elastic and inertial forces.

The challenge of applying combined Froude-Cauchy similarity for model tests is finding an appropriate material [101]. A composite lay-up must be used, effectively reducing the Young's modulus by the scale factor while keeping the material density and Poisson ratio identical to those of the full-scale propeller material.

An advantage of Froude similarity is that the gravitational, elastic and inertial forces are equally scaled, only underpredicting the viscous force due to Reynolds number inequality.

Reynolds' similarity is impossible to obtain in towing tanks or cavitation tunnels [12], but can be obtained in numerical simulations. Viscous effects influence the rigid propeller performance characteristics, as concluded in Chapter 5. In the case of flexible propellers, boundary layer flow may affect the deformation of these propellers, which in turn impacts the overall performance indicators. Thus, Reynolds number considerations are important for model tests.

Variable	***Definition***	***Froude scale***	***Reynolds scale***	***Mach scale***
Froude number [-]	$Fn = V_a/\sqrt{gD}$	1	$\lambda^{3/2}$	$\lambda^{1/2}$
Reynolds number [-]	$Re = \rho V_a D/\mu$	$\lambda^{-3/2}$	1	λ^{-1}
Mach number [-]	$Ma = V_a/c_s$	$\lambda^{-1/2}$	λ^{1}	1
Advance velocity [m/s]	V_a	$\lambda^{-1/2}$	λ^{1}	1
Angular velocity [1/s]	n	$\lambda^{1/2}$	λ^{2}	λ^{1}
Density [kg/m^3]	ρ	1	1	1
Young's modulus [Pa]	E	λ^{-1}	λ^{2}	1
Elastic force [N]	$F_e \propto ED^2$	λ^{-3}	1	λ^{-2}
Gravitational force [N]	$F_g \propto \rho_s g D^3$	λ^{-3}	λ^{-3}	λ^{-3}
Hydrodynamic inertial force [N]	$F_H \propto \rho n^2 D^4$	λ^{-3}	1	λ^{-2}
Propeller inertial force [N]	$F_I \propto \rho_s n^2 D^4$	λ^{-3}	1	λ^{-2}
Viscous force [N]	$F_\mu \propto \mu V_a D$	$\lambda^{-3/2}$	1	λ^{-1}

Table 6.1: Scaling relations for Froude, Reynolds and Mach similarity

6.2. Simulation Input

Numerical simulations are conducted to determine the flexible propeller performance for a range of positive advance ratios in open-water conditions, as well as the deformation behaviour of the flexible propellers. These simulations are performed with the Wageningen C4-40 propeller, with a pitch ratio of 0.8. Figure 4.5 shows the outline of this propeller. Table 4.1 lists the main propeller properties.

This chapter compares a full-scale propeller with a diameter of 2 meters and a scaled propeller with a diameter of 0.25 meters. The numerical input is derived using the Reynolds–Cauchy similarity method, so the model-scale propeller has equal Reynolds and Cauchy numbers as the full-size propeller. The Cauchy number in these simulations is based on that of the model experiments conducted at MARIN. Table 6.1 lists the corresponding scaling relations used to determine the input setting. These settings are listed in Table 6.2. The simulations assume a submerged propeller operating in non-cavitating flow, where gravitational forces are small relative to inertial, elastic, and viscous forces [100]. As a result, the inequality in Froude number inherent to Reynolds–Cauchy scaling should not affect the results. Both Froude–Cauchy and Mach number scaling underestimate viscous forces due to inconsistent scaling of the Reynolds number. This chapter focuses solely on the scale results using the Cauchy number, whereas Chapter 7 examines the influence of the Reynolds number on the performance of flexible propellers.

	Full size propeller		***Scaled propeller***	
D [m]	2		0.25	
E [Pa]	$2 * 10^8$		$1.28 * 10^{10}$	
J	n [RPM]	V_a [m/s]	n [RPM]	V_a [m/s]
0.0	31.87	0.000	2039	0.000
0.1	31.83	0.106	2037	0.849
0.2	31.74	0.212	2031	1.693
0.3	31.57	0.316	2021	2.526
0.4	31.35	0.418	2007	3.344
0.5	31.07	0.518	1989	4.143
0.6	30.74	0.615	1968	4.919
0.7	30.37	0.709	1943	5.668
0.8	29.95	0.799	1917	6.389

Table 6.2: Input settings of the flexible full-size propeller and Reynolds-Cauchy model scaled propeller

6.3. Results

This section outlines the results for flexible propellers, comparing a model-scale propeller to a full-size configuration. The first part presents an open-water diagram displaying the open-water characteristics of both propellers. The following section presents the percentage differences in thrust and torque coefficients, as well as open-water efficiency. The third subsection shows plots of the steady-state propeller deformation. Finally, visualisations of the skin-friction coefficient and flow streamlines over the blades are given.

6.3.1. Open Water Diagram

Figure 6.1 presents the open water characteristics for positive advance ratios for the full-size and scaled flexible propellers. The open-water diagram displays the non-dimensional thrust coefficient, torque coefficient, and open-water propeller efficiency, as defined in Equations 2.7, 2.8, and 2.10, respectively.

Figure 6.1 shows that scale effects influence the open-water performance of the propeller. Both the thrust and torque coefficients are lower for the model-scale propeller compared to the propeller with D = 2 meters. The open-water efficiency is also reduced for the smaller propeller, since η_o depends on both coefficients.

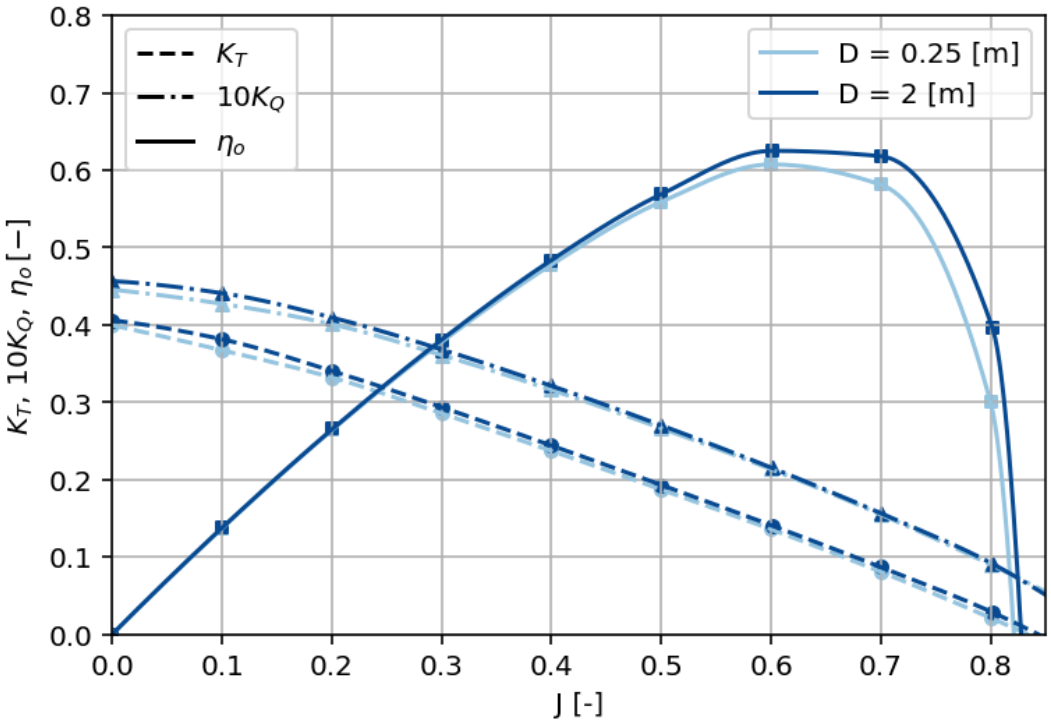

Figure 6.1: Open water diagram of the flexible Wageningen C4-40 propeller with a pitch ratio of 0.8 for two scales. Both the thrust and torque coefficients are lower for the model-scaled propeller compared to the full-size propeller, resulting in a decreased open-water efficiency for the propeller with D = 0.25 meter.

6.3.2. Percentage Differences Between Two Different-Sized Propellers

This section quantifies the order of magnitude of the difference between full-size and scaled propeller open water performance, which is visible in the open-water diagram in Figure 6.1.

Figure 6.2 shows the relative difference between the model-scale and full-scale propellers for the thrust coefficient, torque coefficient, and open-water efficiency over the tested range of advance ratios. The thrust coefficient of the model propeller differs by about -1.5% compared to the full-size case for the bollard pull condition. This difference is maximum for J equals 0.8 and equals -25.2%. The difference in K_Q lays between -0.8% and 3.1%. The maximum difference is found for an advance ratio of 0.1, while the smallest relative difference is found for J equals 0.6. The open-water efficiency is a combination of both K_T and K_Q, and the results can counteract each other when looking at the difference in η_o. The smallest percentage difference in open water efficiency is found for J equals 0.1, neglecting the bollard pull condition for which the open water efficiency, as defined in Equations 2.10, is always zero. This difference increases to -24.3% for J equals 0.8, mainly influenced by the large difference in thrust coefficient for this advance ratio when comparing the model-scale to the full-size propeller.

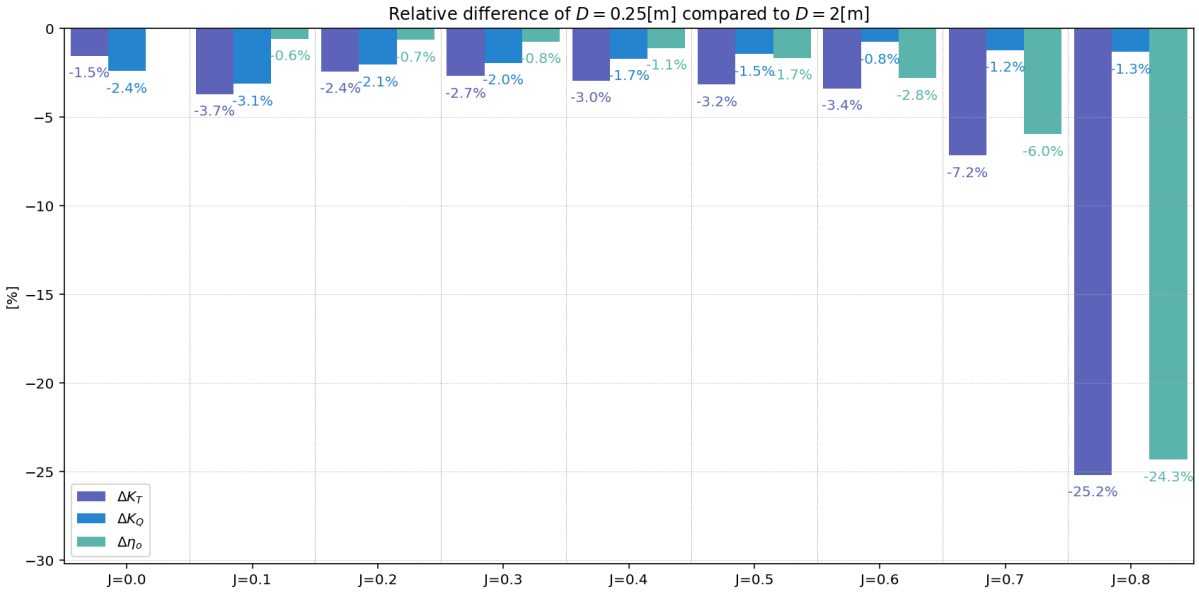

Figure 6.2: The percentage difference in K_T, K_Q, and η_o comparing the flexible model-scale propeller to the flexible full-size propeller over the tested range of advance ratios.

6.3.3. Flexible Propeller Deformation

The flexible propeller deformations influence the open-water performance. The bend-twist coupling of flexible blades results in a reduction in the pitch angle. This reduction in pitch at the tip leads to tip unloading, resulting in a decrease in thrust [101]. However, the deformation of flexible blades could also lead to camber deformation, as found by Lagendijk [62]. An increase in camber can counteract the effect of reduced pitch and enlarge the thrust. This section, therefore, examines the pitch and camber deformation to analyse their respective contributions to the performance of flexible propellers.

Figure 6.3 presents radial plots of the pitch and camber deformation of both full-size and model-scaled propellers for an advance ratio of 0.1. Figure 6.3a shows that the pitch ratio differs somewhat between the model-scale and full-scale propellers. The full-size propeller exhibits a more pronounced reduction in pitch ratio from mid-radius to the tip. The full-size propeller would therefore generate slightly less thrust compared to the scaled propeller. Figure 6.3b also reveals a minor difference in camber deformation for this heavily loaded case. The enhanced camber deformation observed for the model-scale propeller may contribute to a minor increase in thrust relative to the full-scale case. Nevertheless, the open-water diagram in Figure 6.1 indicates that the full-size propeller produces more thrust, opposite to the effect expected from the propeller deformations.

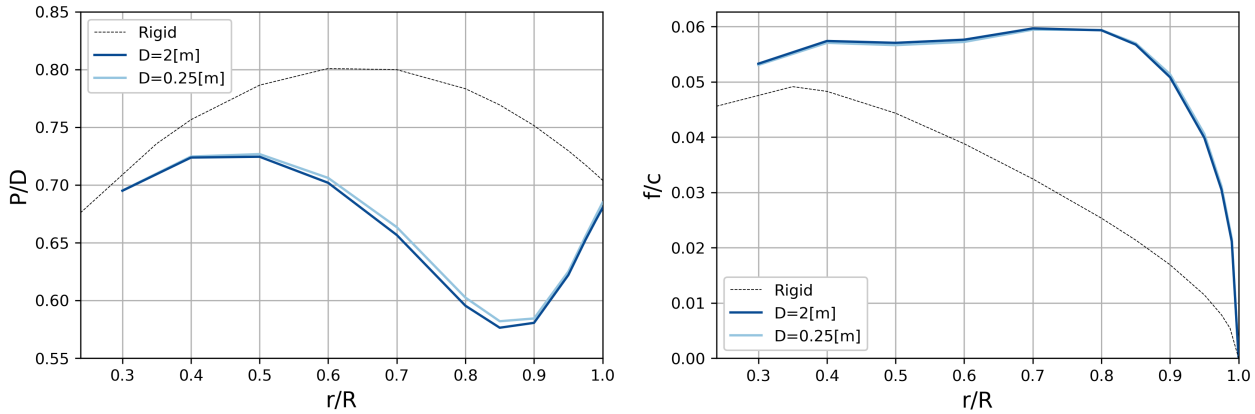

(a) Radial plot depicting the pitch deformation of both propellers, including the rigid C4-40 pitch ratio.

(b) Radial plot depicting the camber deformation of both propellers, including the rigid C4-40 pitch ratio.

Figure 6.3: Radial plots depicting the deformation of both the 2-meter diameter propeller and the 0.25-meter diameter propeller, including the rigid C4-40 pitch ratio for J equals 0.1.

Figures 6.4 present radial plots of the pitch and camber deformation of both full-size and model-scaled propellers for a J-value of 0.6. This advance ratio is around the optimal working condition of the flexible propeller. There is a minor difference in pitch deformation, as shown in Figure 6.4a. The full-size propeller depitches more at the tip, leading to tip unloading. Figure 6.4b indicates no differences in camber deformation between the two propellers. Thus, more thrust would be expected for the model scale propeller compared with the full-size propeller. However, the open-water diagram in Figure 6.1 shows the opposite, indicating that the scaled propeller generates less thrust than the full-size propeller.

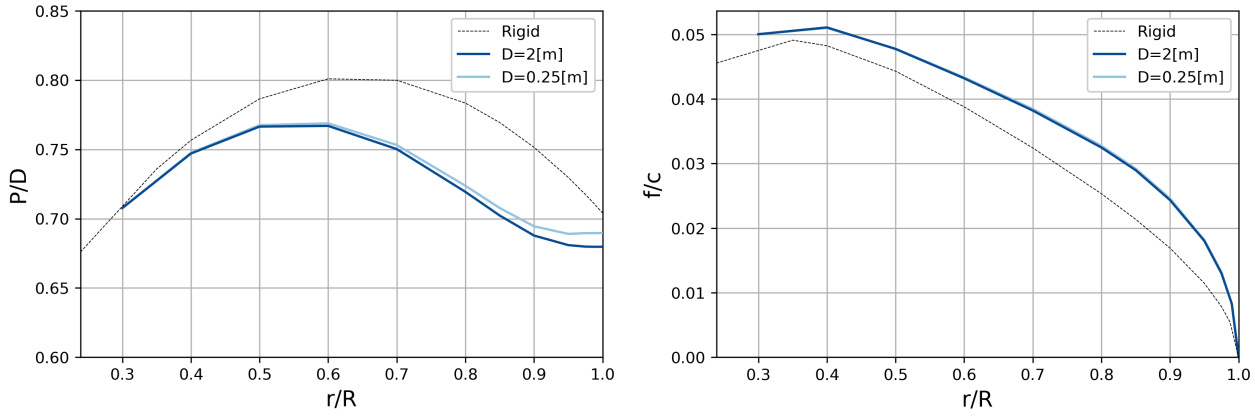

(a) Radial plot depicting the pitch deformation of both propellers, including the rigid C4-40 pitch ratio.

(b) Radial plot depicting the camber deformation of both propellers, including the rigid C4-40 pitch ratio.

Figure 6.4: Radial plots depicting the deformation of both the 2-meter diameter propeller and the 0.25-meter diameter propeller, including the rigid C4-40 pitch ratio for J equals 0.6.

Appendix C includes the camber and pitch deformations across the full range of tested advance ratios. There is a clear trend in which camber deformation decreases with increasing advance ratio, with no deformation detected for advance ratios near the most optimal working point. Heavily loaded cases exhibit the most camber deformation, predominantly located between r/R = 0.8 and 0.9. All advance ratios result in a reduction in pitch ratio. At higher J-values, this reduction is most significant at the tip, leading to tip unloading. For lower advance ratios, the location of maximum pitch reduction moves from the tip to radial positions around r/R = 0.85–0.9. This radial position aligns with the location of the most pronounced camber deformation. The plots indicate that under heavier loading, maximum deformation occurs between the tip and r/R = 0.7, with the pitch ratio rising again toward the tip. This behaviour is attributed to the helical geometry of the blade sections and the definitions of the classical design variables of marine propeller blades. Figure 6.5 shows the total blade deformation of both J equals 0.1 and 0.8 for the propeller with a diameter of 0.25 meters. The light blue coloured blade represents the deformed blade for a J value of 0.1, while the dark blue blade illustrates the blade deformation for an advance ratio of 0.8.

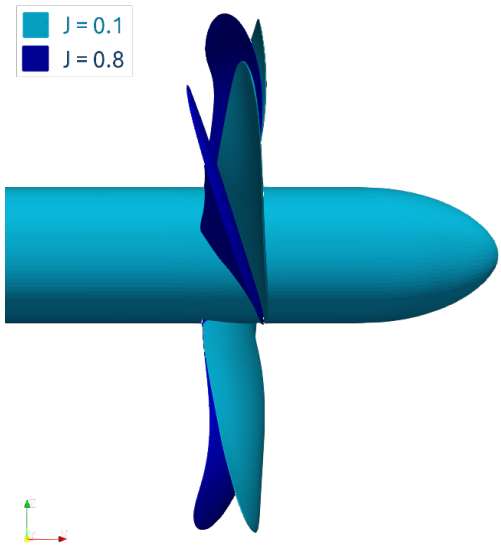

Figure 6.5: Blade deformation of the propeller with a diameter of 0.25 meters. The light blue coloured blade represents the deformed blade for a J value of 0.1, and the dark blue coloured blade for a J value of 0.8.

6.3.4. Skin Friction Coefficient and Streamlines

The flexible propeller deformations show opposite behaviour compared to what is found in the open-water results of the 2-meter diameter and the 0.25-meter diameter propellers. To explain the difference in open-water results between the two propellers, this section analyses the skin friction coefficient and streamlines over the blade surfaces for both propellers. Equation 5.2 expresses the skin friction in a non-dimensional form.

Figures 6.6 illustrate the skin friction coefficient and streamlines over the blades' suction and pressure sides for an advance ratio of 0.8 for both full-size and model-scale propellers. The most considerable relative

difference between the two propellers occurs at this advance ratio. The skin friction coefficient is higher on both the pressure and suction sides of the model-scaled propeller compared to the propeller with a diameter of 2 meters. The streamlines on the suction side of the propeller's blade with a diameter of 2 meters exhibit flow separation over almost the entire trailing edge, except for the tip region. In contrast, the model-scaled propeller has far less trailing edge separation. The direction of the streamlines is more circumferential, and flow separation only appears at the lower radii. The pressure side of the model-size blade exhibits a considerable leading edge vortex, while in Figure 6.6a this vortex is not so clear on the pressure side of the full-scale propeller. This vortex changes the load distribution over the blade [95], explaining the reduced thrust coefficient of the model scaled propeller in comparison with the full-size propeller for this operational condition.

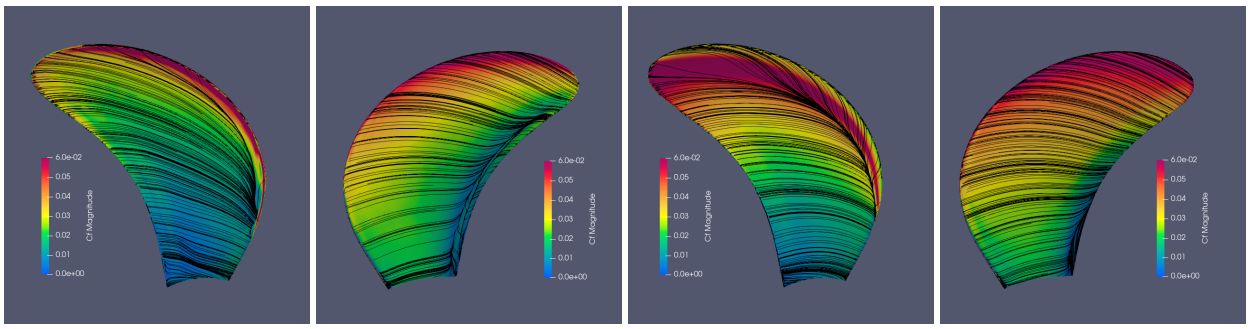

(a) Pressure side of the propeller with $D = 2[m]$ **(b)** Suction side of the propeller with $D = 2[m]$ **(c)** Pressure side of the propeller with $D = 0.25[m]$ **(d)** Suction side of the propeller with $D = 0.25[m]$

Figure 6.6: Streamlines and skin friction coefficient on the suction side of the flexible C4-40 propeller blade tested at a J of 0.8.

6.4. Discussion

The open-water diagram of a flexible propeller shows noticeable differences between the full-size and model-scale propellers, even with Reynolds-Cauchy similarity. Although minor variations in deformation are present, the open-water results do not align with what would be expected based on these deformation patterns. Additionally, the skin friction coefficient and streamlines reveal distinct flow patterns over the blades for both cases. For the higher advance ratios, the pressure side of the model-size blade exhibits a considerable leading-edge vortex, while this is not the case for the full-scale propeller. This vortex influences the load distribution over the blade [95], which in turn affects the performance results. This section examines additional aspects to investigate the causes of these differences.

Appendix C includes the rigid open water performance of both propellers. This open-water diagram also displays a difference in the results between the two different-sized propellers. The relative differences between the rigid cases, also provided in Appendix C, are generally of the same order of magnitude as those observed for the flexible propellers across most advance ratios. For all advance ratios, the differences between rigid and flexible results remain within 1.5%, except for J equals 0.8, where the thrust coefficient differs by –13.3% between the rigid propellers and -25.2% between the model and full-scale flexible propellers. Given that the rigid propellers are geometrically similar in non-dimensional terms, the observed performance discrepancies must arise from differences in the fluid flow. The Reynolds number is equal for both cases, and no cavitation models are used. It is thus reasonable to attribute these discrepancies to numerical artefacts in the flow solver rather than physical scale effects. These artefacts may also explain the minor differences observed in the deformation of the flexible propellers, despite the use of scaled material properties to obtain Cauchy similarity.

The ReFRESCO code executes in double-precision, so the impact of round-off errors is assumed negligible compared to the other errors [49]. The forces are converged for all instances, which Figures C.12-C.18 in Appendix C demonstrate. Hence, the results are arguably the result of discretisation errors.

Two additional simulations have been conducted to investigate this statement. First, the deformed geometry resulting from the flexible full-scale propeller simulation is scaled to a model-sized propeller with a diameter of 0.25 meters. This geometry is then tested in as a rigid configuration with an advance ratio of 0.7, using the same revolution rate, advance velocity, and similar mesh size as the initial model-scale propeller case for the same advance ratio. For J equals 0.7, the original full-scale propeller compared to the initial model scale propeller exhibited more flow separation near the trailing edge on the suction side, similar to Figure 6.6b. Figure 6.7 illustrates the skin friction coefficient and streamlines over the blades' suction and pressure sides for this new case. By comparison, Figure 6.7b shows less trailing edge flow separation on the suction side for the new case, with streamlines more aligned with those of the initial model-scale propeller. The figure

indicates that the observed differences in results are not due to the pitch ratio differences between the flexible propellers of Figure 6.4a. The relative difference in thrust coefficient of the initial propeller with D = 0.25 meter compared to the propeller with D = 2 meter is +7.7%. This difference is -4.8% for the new case (with D = 0.25 meter) compared to the initial model-scaled propeller. This decrease in K_T is in line with the minor difference in tip pitch ratio between the propellers, as argued in Section 6.3.3. When comparing the torque coefficient, the relative difference between the full-size and model propeller was +1.3%. This difference is equal to -3.6% for the new propeller case compared to the initial model-scaled propeller.

The second additional simulation is similar. Yet, now the deformed geometry resulting from the flexible model-scale case is upscaled to a propeller with a diameter of 2.0 meters. This geometry is tested again as a rigid configuration with an advance ratio of 0.7, using the same revolution rate, advance velocity, and similar mesh size as the initial full-size case for this advance ratio. Figure 6.7 illustrates the skin friction coefficient and streamlines over the blades' suction and pressure sides for this additional second case. Figure 6.7b shows less trailing edge flow separation on the suction side for this case, again with streamlines more aligned as those of the initial model-scale propeller. The grid refinement level of this second case and the initial case of the 2-meter diameter propeller is equal. Therefore, similar flow behaviour would be expected if the used grid was too coarse to capture certain flow behaviour. However, less trailing-edge flow separation is observed for this additional test compared to the initial full-size case. The relative difference in thrust coefficient of the initial propeller with D = 2.0 m compared to the propeller with D = 0.25 m is -7.2%. This difference is -9.6% for the new case (with D = 2 [m]) compared to the initial 2-meter diameter propeller. As there is more tip unloading for the initial full-size propeller, this extra decrease in K_T is opposite of what would be expected from the slight discrepancy in pitch ratio. When comparing the torque coefficient, the relative difference was -1.2% and is -3.5% for the new propeller case compared to the initial full-size case.

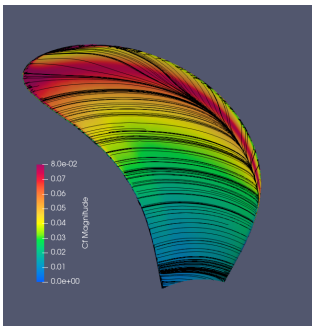

(a) Pressure side

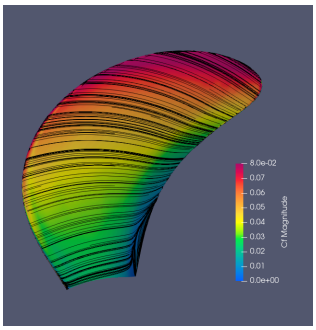

(b) Suction side

Figure 6.7: Deformed propeller geometry resulting from the flexible full-size propeller simulation tested as a rigid propeller with D = 0.25 meters for J equals 0.7.

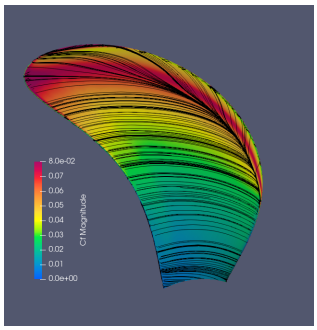

(a) Pressure side

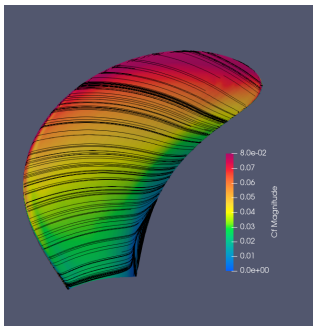

(b) Suction side

Figure 6.8: Deformed propeller geometry resulting from the flexible model-scale propeller simulation tested as a rigid propeller D = 2 meters for J equals 0.7.

The results suggest that the observed inequalities arise from numerical rather than physical scaling effects. The differences are arguably the result of discretisation errors, as the results are converged for all instances. Meanwhile, the additional tests showed that the same grid refinements still obtain different results. Therefore, the influence of the near-wall region is also researched. The average y^+-value of the initial simulation of the propeller with a diameter of 0.25 meters is 0.52, and that of the initial propeller with a diameter of 2 meters is 0.90. Both cases are below one, assumed sufficient to accurately represent the near-wall region and the shear-stresses [43]. However, the study of Eca et al. [23] concluded that with the use of the k-ω SST model of Menter [82], the numerical accuracy of a solution is more dependent on the magnitude of y^+ than on the grid refinement level. A third additional case is conducted. The flexible propeller with a diameter of 2 meters is simulated again for advance ratios of 0.6, 0.7 and 0.8, as these cases show the most significant percentage differences. The average y^+-value of these new simulations is 0.54. Figure 6.9 displays the open water diagram of the advance ratios for these additional tests for the flexible propeller with a diameter of 2 meters, as well as the initial results of the model scaled propeller for these three advance ratios. These new results show no discrepancies with the model-scaled propeller results.

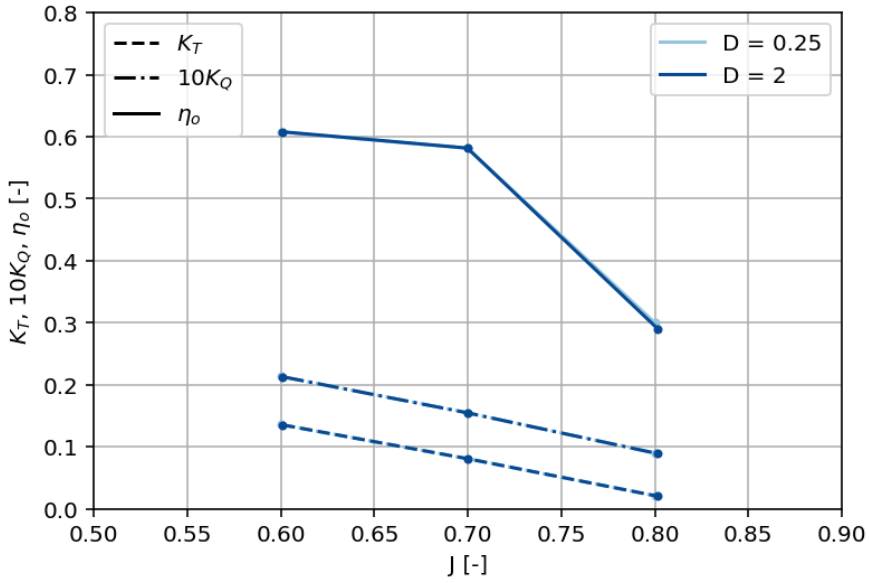

Figure 6.9: Part of the open water diagram of the flexible Wageningen C4-40 propeller with a pitch ratio of 0.8 for two scales. The results of the additional tests for the flexible propeller with a diameter of 2 meters are equal to those of the initial results of the model-scaled propeller.

For J equals 0.6, there is a percentage difference of -0.3% in thrust coefficient. The torque coefficient is -0.2% comparing the flexible model scale propeller with the flexible propeller with D=2 meters. For J equals 0.7, a percentage difference of +0.1% is found for the difference in thrust coefficient, and the torque coefficient is the same when comparing the flexible model scale propeller with the flexible propeller with D=2 meters. For J equals 0.8, these percentage differences are about -5% for the thrust coefficient, and -1% for the torque coefficient.

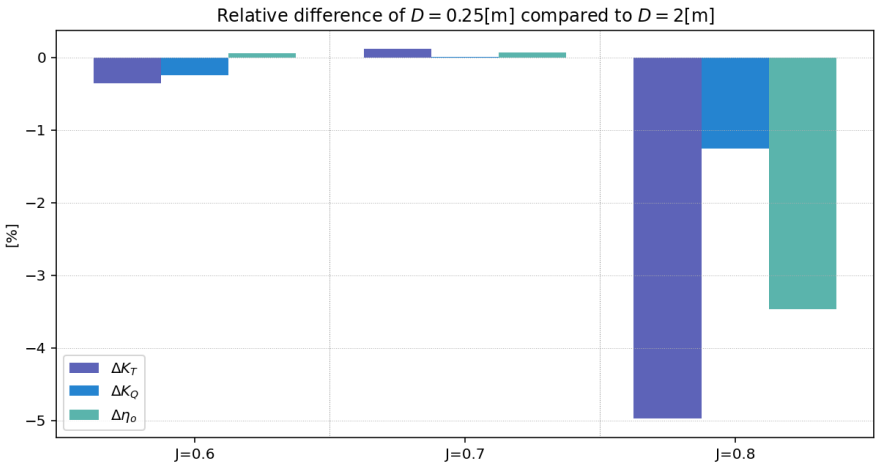

Figure 6.10: The percentage difference in K_T, K_Q, and η_o comparing the flexible model-scale propeller to the flexible full-size propeller for the three advance ratios of the additional tests.

Moreover, the deformation is identical between the two flexible propellers with different scales for both advance ratios. Figure 6.11 shows the radial plot depicting the pitch deformation of both propellers for J equals 0.8, including the rigid C4-40 pitch ratio.

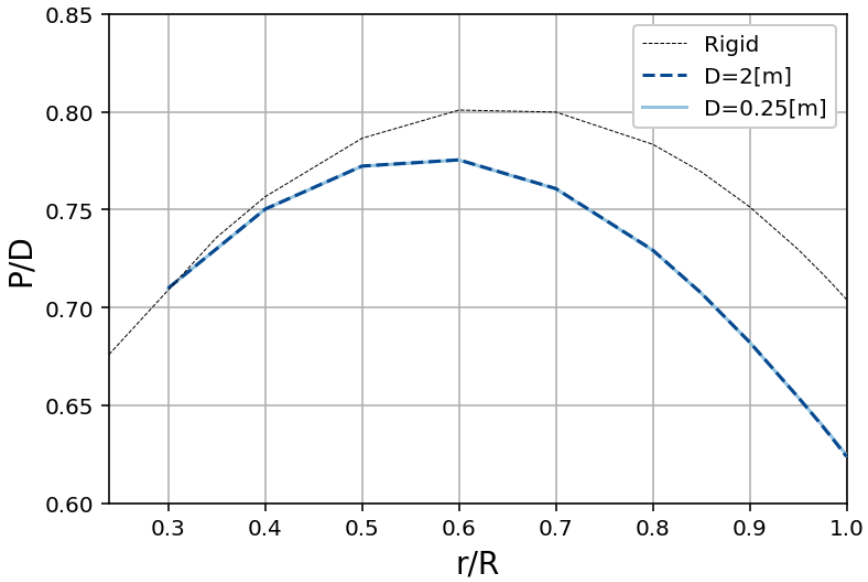

Figure 6.11: Radial plots depicting the pitch deformation of both the additional test of the 2-meter diameter propeller and the 0.25-meter diameter propeller, including the rigid C4-40 pitch ratio for J equals 0.8.

These results align with the conclusions of Eca et al. [23]. This study also found numerical errors larger than 5% for y^+-values $\simeq 1$. The simulations highlight the sensitivity of the near-wall region when using the $k-\omega$ SST model. Based on these observations, the disparities cannot be ascribed to physical scaling effects but rather to numerical artefacts. An equivalent Cauchy number, therefore, leads to an equal ratio between bending and inertial forces, resulting in correctly scaled relative blade deformation across propeller sizes. These findings indicate that Cauchy similarity can be applied in model testing to achieve comparable blade deformation and performance.

6.5. Conclusion

In this chapter, FSI simulations were carried out for flexible propellers in open-water conditions to answer the third sub-question of this thesis: *'What are the scale effects when satisfying the Cauchy number using a combined Reynolds-Cauchy similarity approach for flexible marine propellers?'* The results for two different-sized propellers are studied, including the open water diagram, the relative difference in results between the two propellers, plots of the flexible propeller deformation, and visualisations of the skin-friction coefficient and flow streamlines over the blades. All tests are performed with equal Reynolds number and Cauchy number.

The model-scaled propeller exhibits a relative difference in thrust and torque coefficient of less than 5% compared to the full-scale propeller. This difference in performance results is attributed to disparities in fluid flow, as equal deformation extents are found between both scales. Although initial simulations suggested larger-scale effects in the open-water results, as well as distinct pitch and camber deformation extents, additional tests revealed that numerical rather than physical scaling effects caused these disparities. In particular, the sensitivity to the y^+-value using the $k-\omega$ SST turbulence model of Menter [82] can lead to numerical errors larger than 5% for y^+-values $\simeq 1$. These numerical disparities alter the flow behaviour over the blades, as seen in the streamlines and skin-friction distribution, which may in turn influence the flexible deformation. Nevertheless, the simulations without these numerical artefacts confirm that Reynolds-Cauchy similarity for flexible marine propellers leads to correctly scaled blade deformation for propellers of different sizes. The elastic bending and inertial forces define the deformation extent, for which the Cauchy number, as defined in Equation 6.1, ensures a consistent ratio between these forces.

7

Reynolds Effects on Flexible Propellers

The forces involved in the deformation of flexible propellers include viscous forces, making Reynolds number considerations important. The Froude-Cauchy scaling and Mach scaling methods, presented in Chapter 6, both underpredict the viscous force compared to the other forces. The Reynolds number influences the rigid propeller open water performance, as concluded in Chapter 5. The inequality of Reynolds number during flexible propeller tests could affect the deformation of flexible propellers, further impacting the open-water characteristics. This chapter will answer the following sub-question:

'What are the Reynolds number effects on the performance of flexible marine propellers?'

This chapter presents the open-water characteristics of the flexible propeller for various Reynolds numbers, quantifying the effects of Reynolds numbers on flexible propellers in the numerical simulations. The first section gives an overview of the input settings. The second section presents the various results, including the open-water diagram, the relative difference in results between Reynolds numbers, plots of the flexible propeller deformation, and visualisations of the streamlines and skin friction over the blade surface. The final section provides a conclusion of this chapter.

7.1. Simulation Input

Numerical simulations are conducted to determine the flexible propeller performance for a range of positive advance ratios in open-water conditions. These simulations are performed with the Wageningen C4-40 propeller, with a pitch ratio of 0.8. Figure 4.5 shows the outline of this propeller. Table 4.1 lists the main propeller properties. All simulations in this chapter are performed with a propeller diameter of 2 meters.

Equation 5.1 presents the formulation of the Reynolds number following the ITTC definition. The operational conditions of the various Reynolds numbers are determined using this definition. The revolution rate and advance velocity are adjusted to ensure a constant Reynolds number over the range of advance ratios. Table 5.1 lists the revolution rate and advance velocities for all Reynolds numbers for the tested range of advance ratios.

All cases use an identical Cauchy number to have a fair comparison of deformation between varying Reynolds numbers. The Cauchy number, as formulated in Equation 6.1, must yield equal values to ensure equally scaled blade deformation for varying test conditions (using the same non-dimensional propeller geometry). The Cauchy number of these flexible simulations is based on the Cauchy number of the model experiments of MARIN. The Young's modulus is scaled accordingly to the revolution rate, while the structural density is kept constant for all cases. Table 7.1 specifies the Young's modulus for each Reynolds number case.

Re [-]	$1.0 * 10^5$	$1.0 * 10^6$	$1.0 * 10^7$	$5.0 * 10^7$
E [Pa]	$2.0 * 10^6$	$2.0 * 10^8$	$2.0 * 10^{10}$	$5.0 * 10^{11}$

Table 7.1: Young's modulus setting for the tested range of Reynolds numbers

7.2. Results

This section presents the test results for the flexible propellers across a range of Reynolds numbers. First, the open-water diagram for the different Reynolds numbers is presented, followed by a discussion of the percentage difference between thrust coefficient, torque coefficient, and open-water efficiency. Then, plots of the propeller deformation are shown. The final section includes visualisations of the skin friction coefficient and streamlines over the blades. The forces are converged for all instances, which Figures D.34-D.39 in Appendix D demonstrate.

7.2.1. Open Water Diagram

Figure 7.1 presents the open water characteristics for positive advance ratios for the range of Reynolds numbers tested. The open-water diagram displays the non-dimensional thrust coefficient, torque coefficient, and open-water propeller efficiency, as defined in Equations 2.7, 2.8, and 2.10, respectively.

Figure 7.1 shows that the Reynolds number has a visible effect on both K_T and K_Q. Larger Reynolds numbers result in a higher thrust coefficient for a specific advance ratio. The variation of the torque coefficient exhibits a trend opposite to that of the thrust coefficient. Higher Reynolds numbers result in a reduced torque coefficient for a given advance ratio. The open-water efficiency is a combination of both and increases for greater K_T values and smaller K_Q values. Therefore, a higher Reynolds number results in increased open-water efficiency for the same advance ratio. These effects are similar to those of the rigid propeller results in Figure 5.1.

The effect of the Reynolds number on the boundary layer is the same for the flexible cases as for the rigid ones, given in Chapter 5. Because no transition model is included in the simulations, a fully turbulent flow is solved for all Reynolds numbers. The turbulent boundary layer becomes thinner as the Reynolds number increases. Thinner boundary layers lead to reduced boundary layer separation, enabling the propeller blades to generate more lift while experiencing less drag.

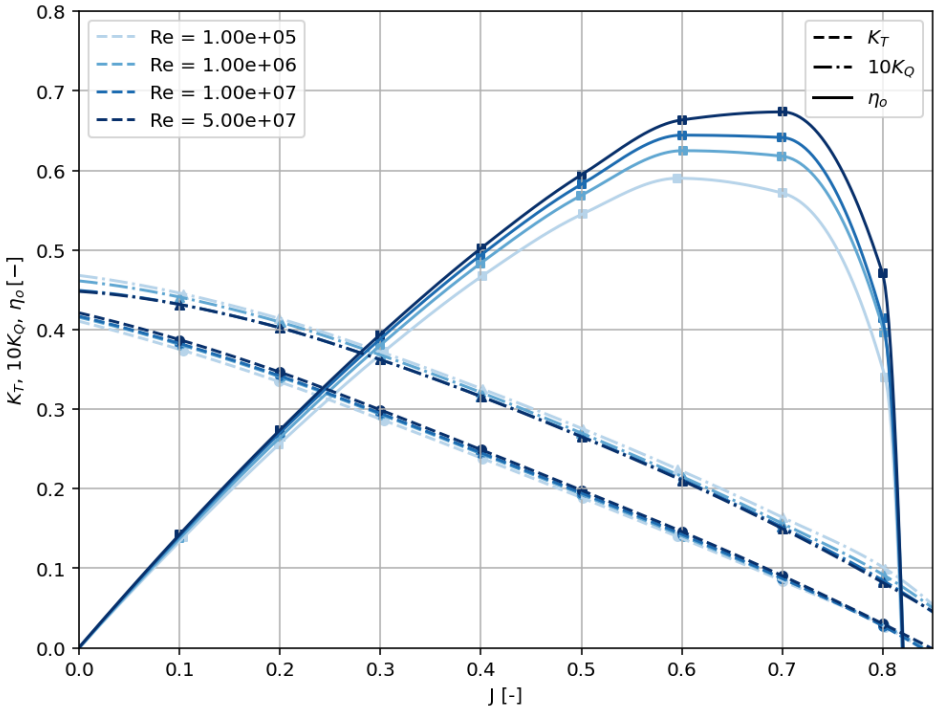

Figure 7.1: Open water diagram of the flexible Wageningen C4-40 propeller with a pitch ratio of 0.8 for a range of Reynolds numbers. The thrust coefficient and open-water efficiency increase for higher Reynolds numbers, while the torque coefficient decreases as the Reynolds number increases.

7.2.2. Percentage Difference Between Reynolds Numbers

An initial insight into the influence of Reynolds number on flexible propellers is obtained by comparing the observed Reynolds effects in flexible simulations with those of the rigid reference case. This section quantifies the magnitude of Reynolds effects by presenting the percentage differences across Reynolds numbers for the flexible propeller. These results are then compared to the corresponding differences found in the rigid propeller cases.

Figure 7.2 shows the percentage difference between the thrust coefficient, torque coefficient and open water efficiency for the different Reynolds numbers. All percentage differences are relative to the results of the Reynolds number equal to $5 * 10^7$. This Reynolds number corresponds to the expected Reynolds number for full-scale propeller operation. Figure 7.2 presents the results for an advance ratio of 0.8, where the most considerable difference between results is found. In line with the rigid results in Chapter 5 and the findings of Rijpkema et al. [88], the Reynolds number effects are more pronounced at higher advance ratios. For

lower advance ratios, a more extensive leading-edge vortex is observed, inducing flow reattachment and a turbulent boundary layer, which results in better agreement between Reynolds number cases. The same behaviour holds for the flexible propeller results, causing the larger differences between Reynolds numbers for higher advance. Appendix D presents the results of other advance ratios.

The relative difference of the torque coefficient between $Re = 1 * 10^5$ and $Re = 5 * 10^7$ equals 21.0% for the advance ratio of 0.8. For the rigid simulation, this difference equals 14.8%. The relative difference between the Reynolds numbers for the flexible propeller at an advance ratio of 0.1 is 3.1%, whereas for the rigid configuration, this difference is 1.1%. Across all advance ratios, the torque coefficient of the flexible propeller decreases as the Reynolds number increases.

Figure 7.2 shows a difference in thrust coefficient of -13.0% when comparing $Re = 1 * 10^5$ and $Re = 5 * 10^7$. This difference is -11.3% for the rigid simulations. The percentage difference of the flexible propeller tests for the other advance ratios varies between -3.4% and -7.4% between $Re = 1 * 10^5$ and $Re = 5 * 10^7$, which is of similar magnitude compared to the rigid test results.

The open-water efficiency is a combination of trust and torque coefficient and will decrease for lower K_T values and higher K_Q values. For all J-values η_o increases for higher Reynolds numbers. The difference in open water efficiency between $Re = 1 * 10^5$ and $Re = 5 * 10^7$ is -27.8% for the flexible propeller with J equals 0.8. For the rigid case, this difference is -22.5%. The increase in the percentage difference for the flexible propellers is predominantly influenced by the higher relative difference of the torque coefficient for this advance ratio. The smallest relative difference in open-water efficiency is found for J equals 0.1, excluding the bollard pull condition for which the open water efficiency given in Equation 2.10 is always zero. The difference in efficiency for J equals 0.1 between $Re = 1 * 10^5$ and $Re = 5 * 10^7$ equals -2.9% for the flexible configuration, and is -2.4% for the rigid case.

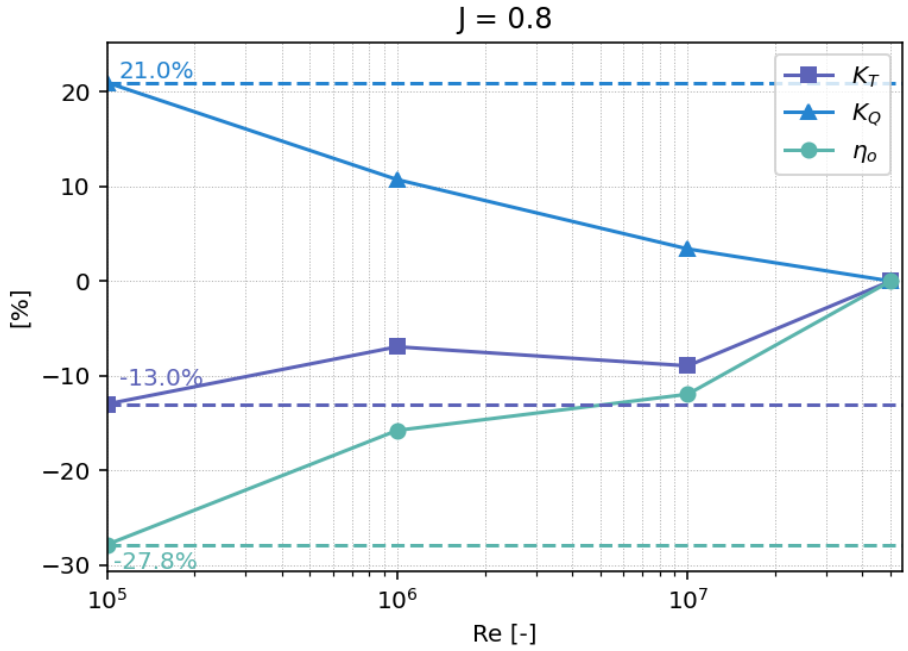

Figure 7.2: The percentage difference across Reynolds numbers, relative to $Re = 5 * 10^7$ for K_T, K_Q and η_o for the flexible C4-40 propeller tested at an advance ratio of 0.8.

7.2.3. Flexible Propeller Deformation

This section analyses the flexible propeller deformation across the tested range of Reynolds numbers. The bend-twist coupling of flexible blades can lead to a reduction of the pitch, resulting in a decrease in thrust [101]. However, camber deformation can counteract the effect of reduced pitch and enlarge the thrust as shown by Lagendijk [62]. Although the percentage differences in thrust coefficient between the Reynolds number cases of the flexible propeller are of the same order of magnitude as the rigid results, the deformed blade geometry could lead to similar thrust coefficients for both rigid and flexible configurations. It is therefore important to analyse the blade deformation to evaluate whether Reynolds effects influence the deformation behaviour of flexible propellers.

Figure 7.3 presents radial plots of the pitch and camber deformation of the tested Reynolds numbers for an advance ratio of 0.1. Figure 7.3b reveals a minor difference in camber deformation for the range of Reynolds numbers, as the camber deformation increases with the Reynolds number. This camber deformation should result in a slightly induced thrust force as the Reynolds number increases. Figure 7.3a shows that the pitch ratio differs as well for the various Reynolds numbers. The blades exhibit a more pronounced reduction in pitch ratio between the mid-radius and the tip as the Reynolds number increases. Since pitch reduction reduces blade loading, this effect can counteract the influence of camber deformation. The flexible propeller results indicate a smaller variation in K_T across Reynolds numbers than the rigid ones (which maintain a constant pitch ratio distribution). For the advance ratio of 0.1, the rigid cases show a thrust coefficient difference of -4.9% between $Re = 1 * 10^5$ and $Re = 5 * 10^7$, whereas the flexible cases show a variation of -3.5%. The results thus confirm that the pitch reduction counteracts the camber effect and the flexibility of the blades leads to a smaller variation in K_T across Reynolds numbers for this advance ratio.

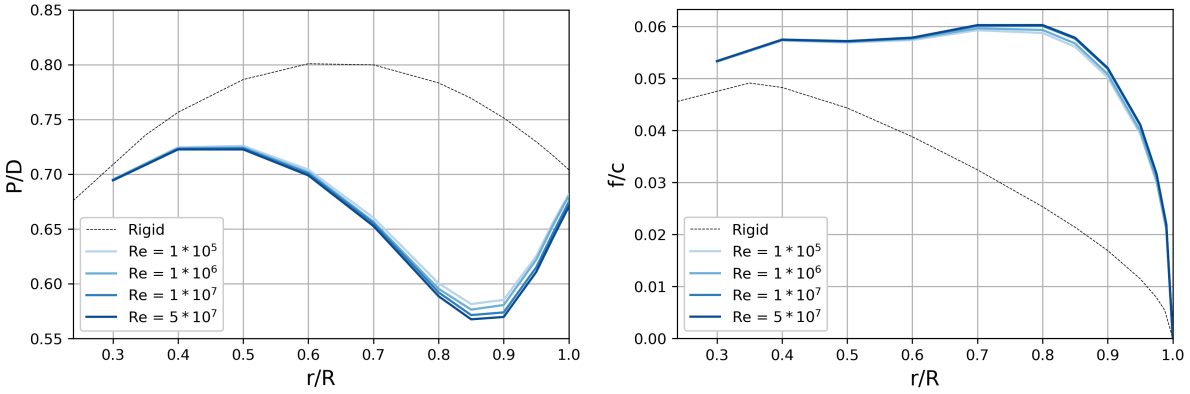

(a) Radial plot of the pitch deformation

(b) Radial plot of the camber deformation

Figure 7.3: Radial plots of the deformation of the flexible C4-40 propeller tested for a range of Reynolds numbers for J equals 0.1.

Figure 7.4 presents radial plots of the pitch and rake deformation of the blades for the range of Reynolds numbers for a J-value of 0.6. Figure 7.4a shows that the pitch ratio near the tip changes for the various Reynolds numbers. The lowest Reynolds number case has the most tip unloading, and the pitch ratio at the tip rises with increasing Reynolds number. The flexible test with the lowest Reynolds number would generate relatively less thrust compared to the case with the highest Reynolds number. Therefore, the difference between $Re = 1*10^5$ and $Re = 5*10^7$ would enlarge for the flexible configurations compared to the rigid cases where the blades are geometrically equal. This reasoning aligns with the results, although the difference is minor. The flexible cases indicate a difference of -11% between the lowest and highest Reynolds numbers, whereas this difference is -10.8% for the rigid simulations. Figure 7.4b visualises the rake deformation of the blades. In addition to the pitch deformation, the Reynolds number influences the rake deformation at the tip for J equals 0.6. This rake deformation slightly increases with the increasing Reynolds number. However, rake deformation is presumed not to affect the thrust results [62]. All Reynolds numbers reveal equal camber deformation for an advance ratio of 0.6.

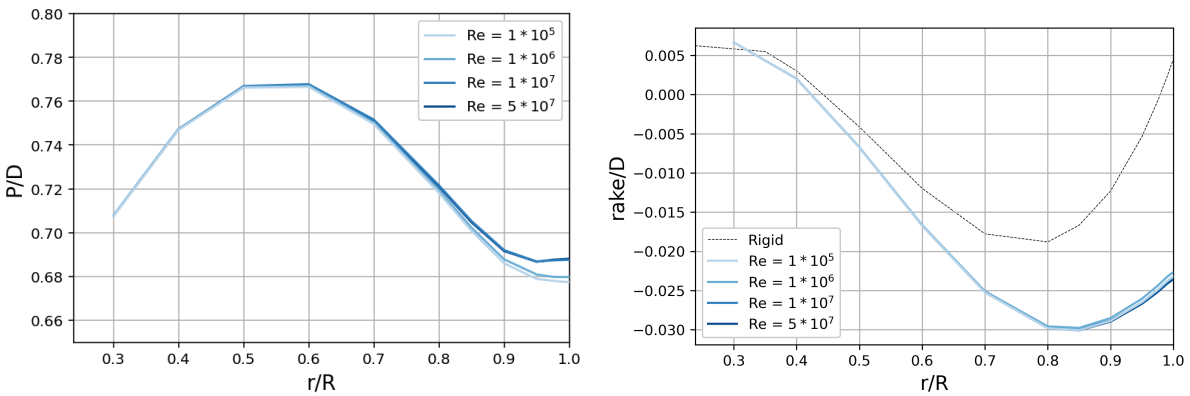

(a) Radial plot of the pitch deformation

(b) Radial plot of the rake deformation

Figure 7.4: Radial plots of the deformation of the flexible C4-40 propeller tested for a range of Reynolds numbers for J equals 0.6.

Appendix D includes the radial plots of the pitch and camber deformation for the entire range of advance ratios tested. For advance ratios below 0.4, the blades exhibit a more pronounced reduction in pitch ratio between the mid-radius and the tip as the Reynolds number increases. For advance ratios above 0.4, the pitch deformation shifts towards the tip. The lowest Reynolds number case has the most tip unloading for these advance ratios, and the pitch ratio rises with increasing Reynolds number. Camber deformation is affected by the Reynolds number only for advance ratios below 0.4, while no differences are found for higher values of J. These results show that the deformation extent of flexible propellers is sensitive to the Reynolds number, thereby indicating a sensitivity to viscous forces. The function f in the representation of the Cauchy number derived in Equation 3.10 should include the Reynolds number, as the results prove that this number is also essential for the correct scaling of the relative blade deformation.

7.2.4. Skin Friction Coefficient and Streamlines

To explain the difference in open-water results between Reynolds numbers as well as rigid and flexible propellers, this section analyses the skin friction coefficient and streamlines over the propeller blade surfaces. Equation 5.2 expresses the skin friction in a non-dimensional form.

Figures 5.3 and 5.4 illustrate the skin friction coefficient and streamlines over the flexible propeller blades' suction and pressure side for the tested Reynolds numbers for a J-value of 0.1. A decrease in the skin friction coefficient is visible with an increase in the Reynolds number on both the pressure and suction sides. Although this is similar to the rigid cases, the decrease in skin friction coefficient is more pronounced for the flexible propeller blades, which explains that the relative difference in torque coefficient between Reynolds numbers is higher for the flexible configuration. The streamlines become more circumferentially directed with increasing Reynolds numbers for both sides. For all Reynolds numbers, the streamlines show flow separation near the trailing edge on the blade's suction side. The separation region near the trailing edge decreases in size, similar to that for the rigid blades, as the radius decreases from higher to lower values on the suction side. Figure 7.5 reveals leading-edge vortices on the suction side of the flexible blades. The radii at which these vortices start to form are higher compared to the rigid cases, which can be attributed to the propeller deformation.

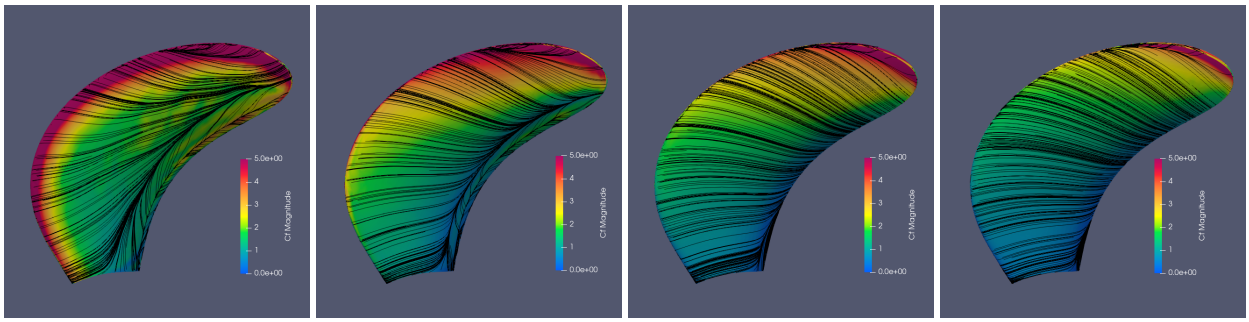

(a) $Re = 1 * 10^5$ **(b)** $Re = 1 * 10^6$ **(c)** $Re = 1 * 10^7$ **(d)** $Re = 5 * 10^7$

Figure 7.5: Streamlines and skin friction coefficient on the suction side of the flexible C4-40 propeller blade tested at a J of 0.1. For increasing Reynolds numbers, the skin friction coefficient decreases slightly. The streamlines are more circumferentially directed for higher Reynolds numbers.

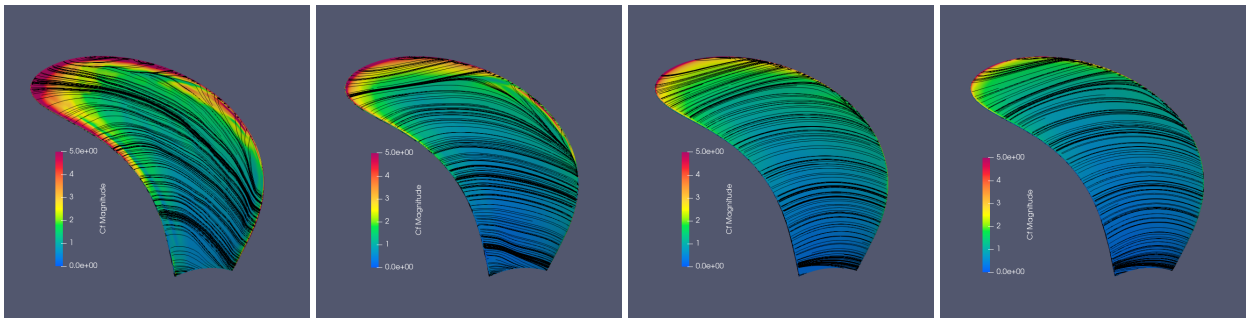

(a) $Re = 1 * 10^5$ **(b)** $Re = 1 * 10^6$ **(c)** $Re = 1 * 10^7$ **(d)** $Re = 5 * 10^7$

Figure 7.6: Streamlines and skin friction coefficient on the pressure side of the flexible C4-40 propeller blade tested at a J of 0.1. For increasing Reynolds numbers, the skin friction coefficient decreases slightly. The streamlines are more circumferentially directed for higher Reynolds numbers.

Figures 5.5 and 5.6 illustrate the skin friction coefficient and streamlines over the propeller blades' suction and pressure side for a J-value of 0.8. A decrease in C_F is visible, and the streamlines become more circumferentially directed with an increase in the Reynolds number on both the pressure and suction sides. For $Re = 1 * 10^5$ and $1 * 10^6$, there is some flow separation near the trailing edge on the suction side. Specially for $Re = 1 * 10^6$, this separation region is smaller than that for the rigid cases tested with the same Reynolds numbers, indicating that deformation lead to a better attached flow over the blade. The flexible propeller blades exhibit a clear leading-edge vortex for each Reynolds number case on the pressure side of the blades. The size of this vortex decreases as the radial positions at which it forms increase with the Reynolds number.

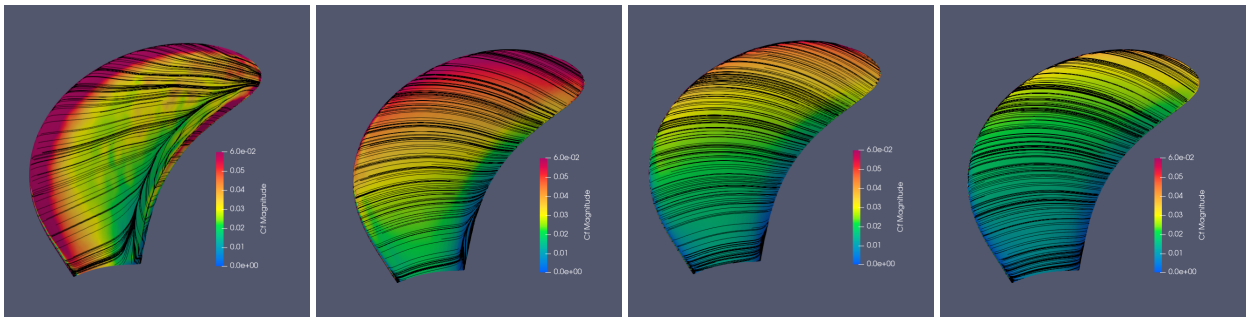

(a) $Re = 1 * 10^5$ **(b)** $Re = 1 * 10^6$ **(c)** $Re = 1 * 10^7$ **(d)** $Re = 5 * 10^7$

Figure 7.7: Streamlines and skin friction coefficient on the suction side of the flexible C4-40 propeller blade tested at a J of 0.8. For increasing Reynolds numbers, the skin friction coefficient decreases slightly. The streamlines are more circumferentially directed for higher Reynolds numbers.

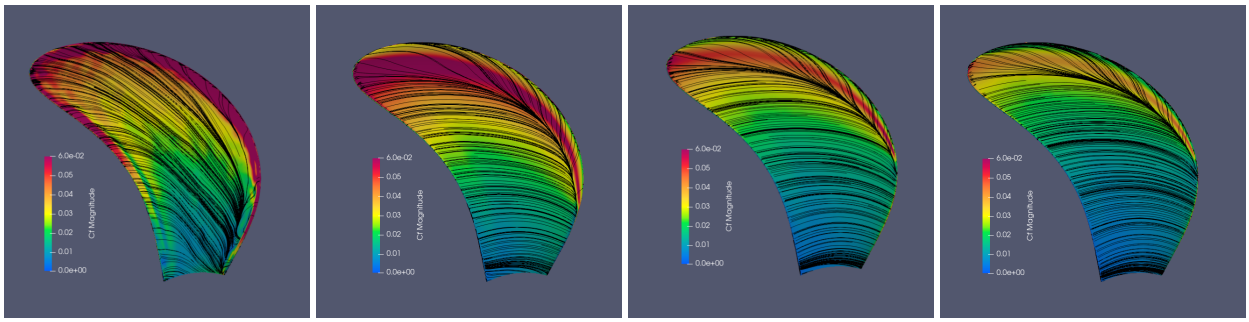

(a) $Re = 1 * 10^5$ **(b)** $Re = 1 * 10^6$ **(c)** $Re = 1 * 10^7$ **(d)** $Re = 5 * 10^7$

Figure 7.8: Streamlines and skin friction coefficient on the pressure side of the flexible C4-40 propeller blade tested at a J of 0.8. For increasing Reynolds numbers, the skin friction coefficient decreases slightly. The streamlines are more circumferentially directed for higher Reynolds numbers.

For higher Reynolds numbers, the boundary layer becomes thinner and has more energy [59], which explains that the boundary-layer shows a more circumferentially directed flow for higher Reynolds numbers. Although this is similar to the rigid blades, the streamlines over the flexible blades are somewhat different from those over the rigid ones. Also, the skin friction coefficient shows a more pronounced difference between Reynolds numbers for the flexible propeller blades. Both are associated with the deformation of the flexible blades. The streamlines on the flexible blades tested at higher advance ratios exhibit smaller flow separation regions than those of the rigid blades tested at the same Reynolds numbers, indicating that deformation can lead to a better attached flow over the blade. Appendix D shows the blade figures of all tested advance ratios.

7.3. Conclusion

In this chapter, FSI simulations were carried out for flexible propellers in open-water conditions to answer the fourth sub-question of this thesis: *'What are the Reynolds number effects on the performance of flexible marine propellers?'* The performance characteristics, deformation extent and boundary-layer flow are analysed for a range of Reynolds numbers, from minimal model scale Reynolds number ($Re = 1 * 10^5$) up to full-scale ($Re = 5 * 10^7$) Reynolds numbers. The flow solver is implemented with the $k-\omega$ SST turbulence model without the use of a transition model.

The results show that the deformation extent of flexible propellers is sensitive to viscous forces. Thus, the non-dimensional number controlling the deformation extent is also a function of the Reynolds number, as this number is observed to be essential for the correct scaling of the relative blade deformation. For high propeller loadings, i.e. low advance ratios, the flexible blades exhibit slightly enhanced camber deformation as well as more pronounced reduction in pitch ratio between the mid-radius and the tip as the Reynolds number increases. The pitch reduction counteracts the camber deformation, and the flexibility of the blades leads to a smaller variation in K_T across Reynolds numbers compared to the rigid results. For advance ratios above 0.4, the camber deformation is unaffected by the Reynolds number. In contrast, pitch deformation, as well as rake deformation, is observed at the propeller tip for these advance ratios. Lower Reynolds numbers lead to more tip unloading, and the flexibility of the blades leads to a minor increase in percentage difference in K_T across Reynolds numbers compared to the rigid cases.

The deformation of flexible propellers leads to a better attached flow over the blades and influences the skin friction and streamlines on the blade surface. For higher propeller loadings, the skin friction coefficient varies more strongly for the flexible propeller blades than for the rigid ones, explaining the larger relative difference found in the torque coefficient between Reynolds numbers for the flexible blades. Also, the leading-edge vortices on the suction side of the flexible blades start to form at higher radii compared to the rigid cases. Especially for the higher advance ratios, the flow separation region near the trailing edge on the suction side is smaller for the flexible blades due to the deformation, compared to the rigid cases.

Those effects have an impact on the open-water characteristics of the flexible C4-40 propeller. The variation of the Reynolds number shows an increase in the thrust coefficient and a decrease in the torque coefficient with increasing Reynolds number, similar to the rigid open water results. The effect on K_T between $Re = 1{*}10^5$ and $Re = 5{*}10^7$ lies between -3.4 and -13.0%, depending on the operating condition. This difference between $Re = 1 * 10^5$ and $Re = 5 * 10^7$ on K_Q is between 3.1 and 21.0%. The open-water efficiency is a combination of both and increases for higher Reynolds numbers. The relative difference between $Re = 1 * 10^5$ and $Re = 5 * 10^7$ on η_o lies for the flexible C4-40 propeller between -2.9 and -27.8% depending on the advance ratio.

8

Influence of Material Characteristics

The scaling methods pose challenges for model testing flexible marine propellers. Reynolds number similarity is impossible to achieve in towing tanks and cavitation tunnels. Mach scaling restricts the ability to perform fast vessel testing in most test facilities. Testing flexible model propellers using Froude-Cauchy similarity has the advantage of equally scaled inertial, gravitational and elastic forces, but gives challenges in finding an appropriate material [101]. A composite lay-up must be used, effectively reducing the Young's modulus by the scale factor while keeping the material density and Poisson ratio identical to those of the full-scale propeller material. Maljaars [70] concluded that the structural response of a composite Seiun-Maru propeller is quasi-static. In this regime, the blade's stiffness dominates the structural response, rather than its inertia due to mass. This could allow the use of a broader range of material properties to achieve the same deformation, making it easier to find a suitable material for model tests. Therefore, this chapter will answer the following question:

'What is the influence of structural density on the steady and dynamic response of a flexible marine propeller?'

The first section explains the various structural response regimes and discusses their influence on the deformation behaviour of the propeller blades. Next, the input settings for the performed simulations are provided. The third section presents the results of the simulations. The first part of this section analyses the steady-state response, including the open-water diagram, the relative difference between the open-water results, and the steady-state deformation of the flexible propeller blades. The second part presents the results regarding the dynamic behaviour of the blades. The final section provides the answer to the last sub-question and highlights the main conclusions of this chapter.

8.1. Structural Response Regime

The structural response of a propeller blade is the result of the ratio between excitation frequency, represented by ω, and natural frequency, symbolised by ω_n. The natural frequency is the frequency at which a system vibrates after an initial disturbance by an impulsive force [87] and is obtained by:

$$\omega_n = \sqrt{\frac{k}{m}} \tag{8.1}$$

In this equation, m is the mass and k the stiffness of the structure. The corresponding natural mode is the motion of the system at this natural frequency. There are n natural frequencies, each associated with its own mode shape, for a system having n degrees of freedom [87]. The natural frequency of a submerged structure is also affected by the presence of the water. The water causes an effect known as added mass, as the fluid works as an increase in effective mass of the system caused by the fluid motion around the object [59]. The added mass influences the wet natural frequency of the blades, symbolised by ω_0^{wet}. There is an additional hydrodynamic force, symbolised by $\mathbf{f_H}$, resulting from the fluid acting on the structure. The additional hydrodynamic force depends upon the displacements, velocities and accelerations of the propeller. From classical vibration theory, this hydrodynamic force vector is defined as:

$$\mathbf{f_H} = -M_a\ddot{x} - C_p\dot{x} - K_P x \tag{8.2}$$

In this equation, the matrices M_a and C_p are the added mass and damping matrices, respectively. The stiffness matrix, denoted by K_p, depends upon the immersion of the propeller. This matrix is zero and does not need to be considered further for a fully submerged propeller [12].

Depending on the ratio between excitation frequency and (wet) natural frequency, three regimes can describe the structural response of a linear mass-spring-damper system with oscillatory excitation [70]:

- A quasi-static regime, when $\omega << \omega_0^{wet}$. Stiffness dominates the structural response.
- A resonance regime, when $\omega = \omega_0^{wet}$. Damping dominates the structural response.
- A dynamic regime, when $\omega >> \omega_0^{wet}$. Mass dominates the structural response.

The ratio of the frequency of the dominant blade mode and the excitation frequency defines the structural response of a propeller blade. This ratio is known as the structural frequency ratio and is equal to:

$$\frac{\omega}{\omega_0^{wet}} \tag{8.3}$$

In general, the fundamental natural frequency of a propeller blade is the frequency of the first bending mode. The code Aster [26] structural solver generates the dry natural frequencies of the blades. The wet natural frequency also depends on the added mass. For metal propellers, the wet natural frequency is generally 62-64% of the dry value [12]. Fibre-reinforced plastics have a lower material density than metals. Hence, the fluid added mass has a more pronounced effect on the wet natural frequencies of composite propellers than on those of metal propellers. The rotational frequency is the lowest excitation frequency and is equal to $\omega = 2\pi n$ [70].

Maljaars [70] concluded that the structural response of a composite Seiun-Maru propeller is quasi-static. In this regime, the first bending mode and thus the blade's stiffness dominate the structural response. The Seiun-Maru propeller has relatively low blade frequencies due to the heavily skewed blades. Blade geometries with less skew probably have an even lower structural frequency ratio and are, ergo, also stiffness-dominated. Maljaars' study used different modelling choices for the development of a BEM-FEM coupled solver for non-uniform inflow. Although the study concluded that the structural response of flexible propellers is dominated by stiffness, a quasi-static FEM model of the structural response of flexible propellers is not recommended, as dynamic effects cannot be neglected. The fluid-added mass and hydrodynamic damping contributions are not negligible. Still, a reasonable hydro-elastic response is obtained, using closed-form expressions for the fluid-added mass and hydrodynamic damping terms in the study. Consequences of modelling errors in the fluid added mass are relatively small, confirming that the structural response of flexible propellers is stiffness-dominated.

8.2. Simulation Input

Numerical simulations are performed to obtain the open-water performance, steady-state deformation and dynamic behaviour for a range of positive advance ratios for various material densities. The influence of material properties is investigated using Reynolds similarity, ensuring that Reynolds number effects do not influence the results. The Young's modulus is equal to $1.28 * 10^{10}$ for each case. The impact of the structural mass is assessed by testing various material densities. Ideally, the structural density must follow the same scaling relation as the fluid density. The density of fluid is generally considered comparable between freshwater and seawater. Hence, density is assumed to be equal between the model and full-scale, resulting in a scaling factor of 1. Accordingly, the material density should also follow this factor and remain 1. A density ratio can express both densities as a single non-dimensional parameter and is used in place of the absolute density values. This ratio is defined as: ρ_s/ρ_f. Glass-epoxy composite material has a typical density of 1700 kg/m^3 [70], so for a composite marine propeller operating in water, the structure-to-fluid density ratio is about 1.7. Table 8.1 lists the density ratios of the simulations in this chapter, which change with a factor $\sqrt{2}$. It is assumed that a possible model-scale propeller material can be found within this tested range.

The simulations are performed with a uniform inflow, which, by definition, implies steady loading. The FSI simulations converge to a steady-state solution and a steady deformation of all the blades. The open-water performance of the flexible propellers and steady deformation are analysed using these converged solutions. The FSI simulations use a strongly coupled URANS-FEM approach. This strongly coupled approach leads to a converged solution for each time step between fluid flow and structural displacement [75]. The next time step uses the position and velocity of the structure as new initial conditions. Using this approach, the solution of each time step has a physical meaning, even though it is converging to the steady-state solution. The dynamic behaviour of the blades is analysed during the first time steps of the simulation, when the forces are still oscillating towards a steady-state solution.

The Code Aster [26] structural solver provides the modes and dry natural frequencies of the propeller blades. The dry natural frequency of a system scales with $\sqrt{1/m}$, following from Equation 8.1. The modal fluid added mass influences the wet natural frequency. Determining the added mass of complex geometries and accounting for non-linear effects, such as fluid flow separation, is challenging, as these effects significantly impact added mass [24, 85]. The coupled URANS-FEM FSI simulation accounts for the interaction between fluid flow and structural velocities and acceleration, including added mass effects.

This chapter analyses two propeller geometries. The steady-state simulations use the Wageningen C4-40 propeller, with a pitch ratio of 0.8. Figure 4.5 shows the outline of this propeller. Table 4.1 lists the main propeller properties for the C4-40 propeller. All the studied propellers in this chapter have a diameter of 0.25 meters. The C4-40 propeller has a considerable skew angle. Large skew is often used in flexible propellers [34, 62, 80], as it results in a larger de-pitching moment when loaded [71]. However, the bend-twist coupling and helical geometry of the blades complicate an analytical analysis of the dynamic behaviour. For blades with very high skew, rake or made of anisotropic material, the first mode may not be simple bending, but a combination of bending and twisting [100]. Therefore, the dynamic behaviour of a blade without skew and rake is analysed, along with the C4-40 propeller.

ρ_s/ρ_f $[-]$	1.2	1.7	2.4	3.4
ρ_f $[kg/m^3]$	998	998	998	998
ρ_s $[kg/m^3]$	1200	1700	2400	3400

Table 8.1: The density ratios of each case

8.3. Results

This section presents the results of flexible propeller simulations to examine the influence of the density ratio on the steady and dynamic behaviour of the blades. First, the steady-state results are presented, including the open-water diagram, the relative difference between the various cases, and plots of the deformation. Only the density ratio is adjusted, so the grid refinement and y^+-values are identical for all the cases. The second section presents the findings on the dynamic behaviour of the blades. In the time domain, the forces oscillate towards a converged solution. The dynamic behaviour is analysed in the frequency domain using a Fast Fourier transform.

8.3.1. Steady-State Results

The simulations assume a uniform fluid inflow to determine the open-water performance. The open-water performance of flexible propellers depends on the amplitude of the bending deformation, which is expressed in Equation 3.10. Each steady case is run over 1080 degrees. For all simulations, this was sufficient to achieve a steady-state solution, where forces and deformations remain constant between time steps. The convergence of the thrust force is demonstrated in Figures E.1-E.8 in Appendix E, which show the thrust coefficient over the time steps for all advance ratios.

Open Water Diagram

Figure 8.1 presents the open water characteristics for the positive advance ratios for the tested range of density ratios. The open-water diagram displays the non-dimensional thrust coefficient, torque coefficient, and open-water propeller efficiency, as defined in Equations 2.7, 2.8, and 2.10, respectively. Figure 8.1 reveals no difference in thrust coefficient, torque coefficient, and open-water propeller efficiency for all density ratios.

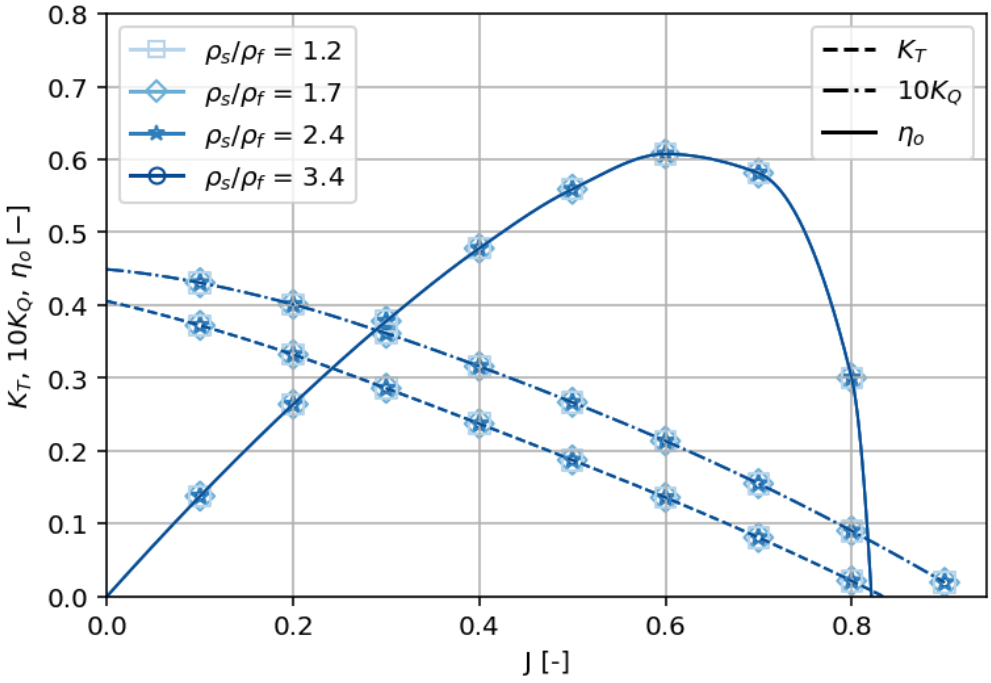

Figure 8.1: Open water diagram of the flexible Wageningen C4-40 propeller with a pitch ratio of 0.8 for a range of structural-to-fluid density ratios.

Percentage Difference Between Material Densities

This section quantifies the effect of material density on the steady-state results by presenting the percentage differences between the open-water results across density ratios for the flexible propeller tests. Figure 8.2 shows the percentage difference between the thrust coefficient, torque coefficient and open water propeller efficiency for an advance ratio of 0.5. All percentage differences are relative to the results of a density ratio of 1.7, as this is a typical density ratio for glass-epoxy composite materials operating in water. Figure 8.2 shows that the relative difference between the different cases is minimal. For all advanced ratios, the results are within ±0.1%. Additionally, the results show no systematic variation with changes in the structural-to-fluid density ratio.

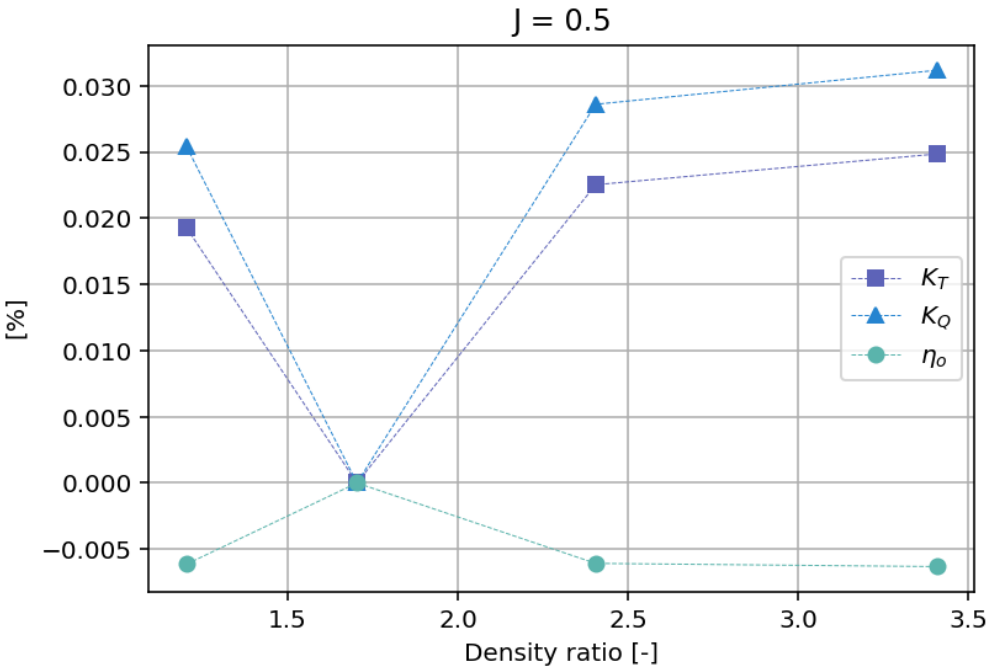

Figure 8.2: The percentage difference across structural-to-fluid density ratios, relative to a density ratio of 1.7 for K_T, K_Q and η_o for the flexible C4-40 propeller tested at an advance ratio of 0.5.

Flexible Propeller Deformation

This section analyses the flexible propeller deformation across the tested range of density ratios. Figure 8.3 presents radial plots of the pitch and camber deformation of the tested density ratios for an advance ratio of 0.5. Both Figure 8.3a and Figure 8.3b reveal no difference in camber and pitch deformation for the various density ratios. All lines are on top of each other. The blade deformation is equal for the tested range of material densities for all other advance ratios as well.

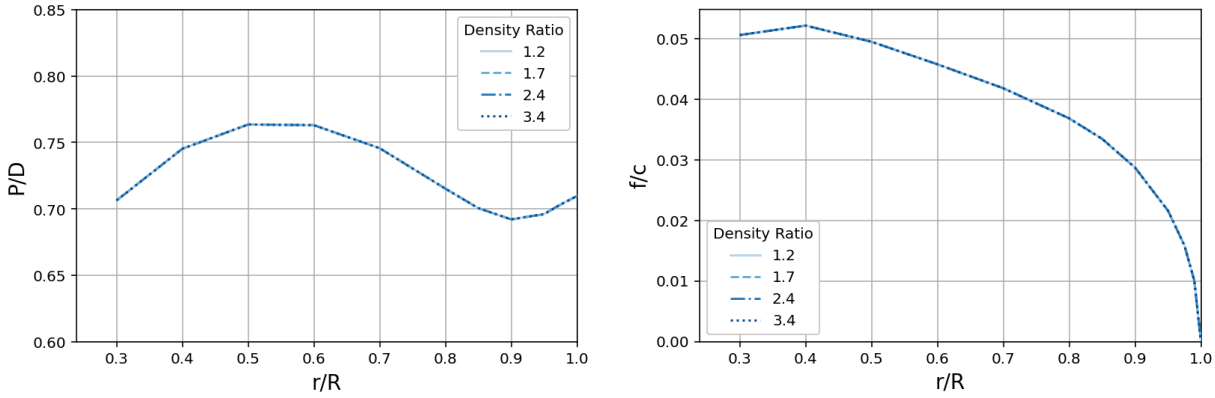

(a) Radial plot of the pitch deformation for a range of structural-to-fluid density ratios.

(b) Radial plot of the camber deformation for a range of structural-to-fluid density ratios.

Figure 8.3: Radial plots depicting the deformation of the flexible C4-40 propeller tested for a range of structural-to-fluid density ratios for J equals 0.5.

The results align with what is expected from the conclusions of Maljaars [70]. For the steady deformation of flexible marine propellers, a quasi-static structural response is observed. The material stiffness dominates the deformation and consequently the open-water performance. The ratio of bending frequency and revolution rate, as expressed in Equation 3.9, depends on the ratio of the bending force and hydrodynamic and propeller inertial forces. However, these results show that within the tested range of density ratios, the structural density does not affect the steady-state deformation. As a result, correctly scaling the propeller inertial force can be disregarded when determining the correct steady-state deformation. The contribution of fluid damping depends on the system's inertia and only affects the rate at which the system approaches equilibrium [77]. For this reason, it is excluded from the non-dimensional parameter used to control the extent of steady-state deformation. The steady deformation extent thus depends on the ratio of bending force to hydrodynamic inertial force and is a function of the viscous force (as already concluded in Chapter 7), which leads to the following representation of the Cauchy number:

$$Ca_{steady} = \frac{E}{\rho_f D^2 n^2} f(Re) \tag{8.4}$$

This form can be used to control the correct relative steady state deformation extent. If a suitable material for open-water model testing is unavailable, proper scaling of the stiffness is essential. In contrast, scaling the material density is shown to be less critical, as the influence of the material-to-fluid density ratio on the deformation and resulting open-water performance is negligible.

8.3.2. Dynamic Behaviour

For the open-water tests, with uniform inflow conditions, the simulations converge to a steady-state solution where the deformation of all blades is equal. For in-behind ship conditions, or generally cases with non-uniform inflow, the flexible propeller deforms to variations in fluid loading [62]. The deformation changes during revolution and depend on the rotational position of the blade. The non-uniform flow conditions complicate the hydro-elastic analyses [68]. In addition to the load variation of the wake field, the vibrational response of the propeller also affects the overall vibrational behaviour of the blade [12]. Both factors cause changes in the angle of attack, to which a flexible propeller will deform during a revolution. Relatively similar blade deformation during a revolution can be obtained if the bending frequency is scaled with the propeller's revolution rate, as derived in Equation 3.9. This form depends on the propeller inertial force and thus structural density. The structural dynamics influence the blade deformation and loading, thus affecting the propeller performance.

The effective mass of a linear mass-spring-damper system with oscillatory excitation influences the structural response in the dynamic regime [70]. The effective mass is a combination of both structural mass and

added mass for submerged structures. For a propeller vibrating in a fluid, the added mass and damping coefficients define the hydrodynamic forces and moments acting on the propeller. These are important for the evaluation of the vibration behaviours of submerged propellers [12]. Structural vibrations are an undesirable effect for marine propellers. Vibrations can cause unsteady thrust generation and produce strong hydrodynamic pressure fluctuations [94], which in turn lead to cavitation and underwater radiated noise. Inappropriate material scaling can affect the material behaviour [100], leading to incorrect conclusions about the structural vibrations of the propeller. The blade velocities and accelerations lead to nonzero hydrodynamic forces, as defined in Equation 8.2, which contribute to the system's equation of motion. The coupling between the structural blade vibration velocities and accelerations and fluid flow [68] affects the fluid-structure interaction.

Fast Fourier Transform

The relatively low stiffness of composites results in a hydroelastic response of composite propellers. The blade deformations influence the propeller loading and vice versa. Hence, the hydro-elastic response can be obtained by measuring the change in thrust and torque values [69]. The thrust forces exhibit oscillatory behaviour as the simulation converges towards a steady-state solution. The force signal is analysed in the frequency domain to analyse the blades' dynamic behaviour. This study uses a Fast Fourier transform, abbreviated as FFT. The Fast Fourier transform is a mathematical tool that converts a signal captured in the time domain to the frequency domain [44]. Figure 8.4 illustrates the perspectives of both domains. A signal in the time domain can be represented as a function of time h(t) and is decomposed into a series of harmonics. These harmonics appear in the frequency domain, which can be represented by a function of frequency H(ω). The two representations of the functions can transfer back and forth through the Fourier transform equations. The FFT uses the force of one blade in the x-direction over time and converts this signal to the frequency domain. The signal of an advance ratio of 0.1 is analysed, as the heavier-loaded conditions showed more oscillations in the force signal. Figures E.2-E.7 in Appendix E present the thrust coefficient over the time steps for the steady-state simulations, which demonstrate a larger force overshoot for the lower advance ratios. The obtained force harmonics provide insight into the wet natural frequency of a blade and the effect of the density ratio on the dynamic response.

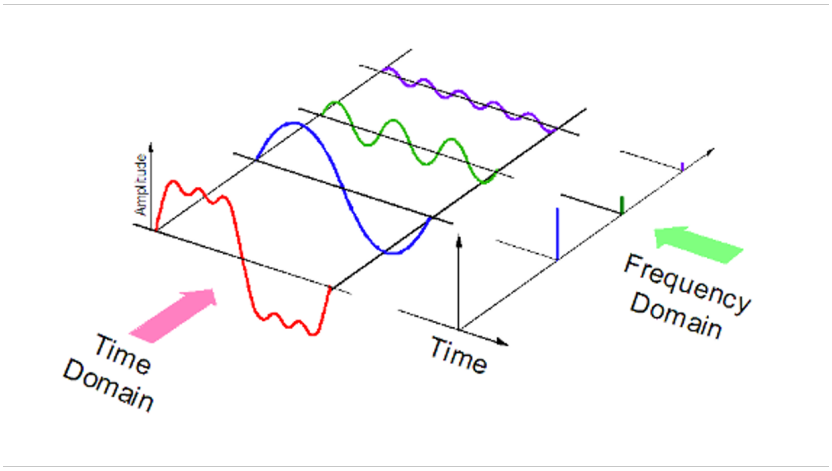

Figure 8.4: Perspectives of the time domain, which can be represented as a function of time h(t) and the frequency domain, represented by a function of frequency H(ω). The two representations of the functions can transfer back and forth through the Fourier transform equations. From Chen [16]

Analytical Solution for Free Vibration of Submerged Plates

An analytical representation of the free vibration of submerged plates is given by Newman [83] and Brennen [7]. The added mass formulas used in the analytical model are based on potential flow assumptions and strip theory. In general, added-mass effects depend on the nature of the vibrational mode, specifically whether it is bending, twisting or a combination of both. For pure bending, the analytical added mass term, m_a, per unit length is equal to:

$$m_a \approx \rho_f \frac{\pi}{4} b^2 \tag{8.5}$$

The total effective mass moment of inertia influences the vibrational mode for pure twisting. The analytical added mass moment of inertia, $I_{x,a}$, per unit length is represented by:

$$I_{x,a} = \rho_f \frac{\pi}{128} b^4 \tag{8.6}$$

The width b in both Equation 8.5 and 8.6 equals, for this study, the chord length of the propeller blade at r/R = 0.7.

From Equation 8.5 and 8.6, a simplified equation for the wet-to-dry frequency ratio follows. For pure bending, this is:

$$\frac{\omega_{wet}}{\omega_{dry}} = \sqrt{\frac{m_s}{m_s + m_a}} = \left(1 + \frac{\pi}{4}\frac{\rho_f}{\rho_s}\frac{b}{t}\right) \tag{8.7}$$

While for pure twisting, this is:

$$\frac{\omega_{wet}}{\omega_{dry}} = \sqrt{\frac{I_{x,s}}{I_{x,s} + I_{x,a}}} = \left(1 + \frac{3\pi}{32}\frac{\rho_f}{\rho_s}\frac{b}{t}\frac{b^2}{b^2 + t^2}\right) \tag{8.8}$$

In Equations 8.7 and 8.8, t represents the thickness; for this analysis, the propeller thickness at r/R = 0.7. Both the C4-40 propeller and the tested propeller without skew have the same chord ratio and thickness at this radial position. The analytical results are consequently the same for both propeller blades. Tables 8.2a and 8.2b summarise the analytical values of the wet-to-dry frequency ratio and the added-mass-to-structural-mass ratio for pure bending and pure torsion, respectively.

ρ_s/ρ_f $[-]$	1.2	1.7	2.4	3.4
$\omega_{wet}/\omega_{dry}$ $[-]$	0.25	0.29	0.34	0.40
m_a/m_s $[-]$	15	11	7.5	5.3

(a) Analytical results for pure bending

ρ_s/ρ_f $[-]$	1.2	1.7	2.4	3.4
$\omega_{wet}/\omega_{dry}$ $[-]$	0.39	0.45	0.51	0.58
$I_{x,a}/I_{x,s}$ $[-]$	5.6	3.9	2.8	2.0

(b) Analytical results for pure twisting

Table 8.2: The analytical values for the wet-to-dry frequency ratio and added-mass-to-structural-mass ratio for pure bending and twisting. The analytical representation is given by Brennen [7] and Newman [83]

Propeller Without Skew

Figure 8.5 shows the force signal in the frequency domain for the tested range of density ratios for the propeller with zero skew angle, from which the wet natural frequency of the blade follows. The peaks of the first frequency are very close to each other. Specifically for the three lowest density ratios, the first wet natural frequency of the blade is about equal to 126 Hz. The highest tested density ratio has a slightly higher force frequency, which is equal to 132 Hz. Table 8.3 lists the wet and dry frequencies, the wet-to-dry frequency ratio and the added-mass-to-structural mass ratio obtained for the blade without skew angle.

ρ_s/ρ_f $[-]$	1.2	1.7	2.4	3.4
ω_{dry} $[Hz]$	500.8	421.1	354.1	297.8
ω_{wet} $[Hz]$	126.4	126.4	125.5	132.5
$\omega_{wet}/\omega_{dry}$ $[-]$	0.25	0.30	0.35	0.44
m_a/m_s $[-]$	14.7	10.1	7.0	4.1

Table 8.3: The wet-to-dry frequency ratio and the added-mass-to-structural mass ratio for a range of density ratios for the skewless propeller following from the simulation results

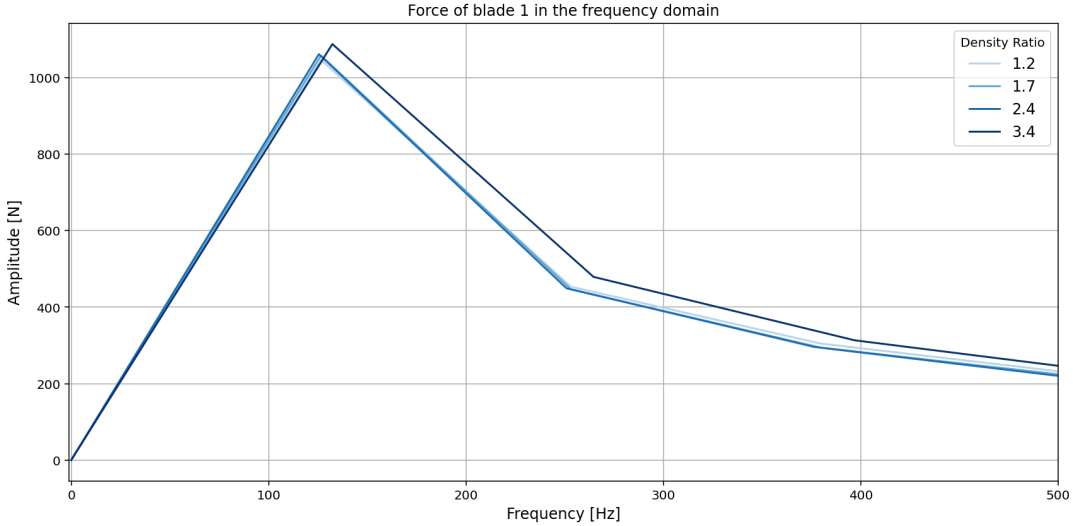

Figure 8.5: The propeller thrust force for a range of density ratios converted to the frequency domain. The signal is for the flexible propeller with zero skew angle and with a pitch ratio of 0.8.

The numerical results in Table 8.3 of the three lowest density ratios are about equal to the analytically obtained results for pure bending listed in Table 8.2a. There is a slight difference in results for a density ratio of 3.4. Figure 8.6 visualises these results. Figure 8.6a shows the analytical results obtained for the wet-to-dry frequency ratio of pure bending and pure torsion, as well as the results of the wet-to-dry frequency ratio for the propeller with zero skew angle. Figure 8.6b presents the analytical results obtained for the added-mass-to-structural mass ratio of pure bending and pure torsion, as well as the results of the added-mass-to-structural mass ratio for this zero skew propeller. The results of Table 8.3 demonstrate that scaling the density ratio with a factor $\sqrt{2}$, the dry natural frequency increases with a factor $\sqrt[4]{2}$. Ergo, when scaling the density ratio by a factor λ, it results in both the wet-to-dry frequency ratio and the added-mass-to-structural-mass ratio scaling by $\sqrt{\lambda}$.

For the skewless propeller, the first mode is pure bending, which is confirmed by the close match between the numerical results and the analytical formulas provided by Newman [83] and Brennen [7]. The wet natural frequency remains constant across a range of density ratios from 1.2 to 2.4, whereas the first wet natural frequency of a density ratio of 3.4 exhibits a minor difference. Glass-epoxy composite material has a typical density of 1700 kg/m^3 [70] and these results indicate that the structural density of materials used for model-sized propellers can differ at least 30% from the assumed full-size material density to obtain the same wet natural frequency in case the first mode is pure bending.

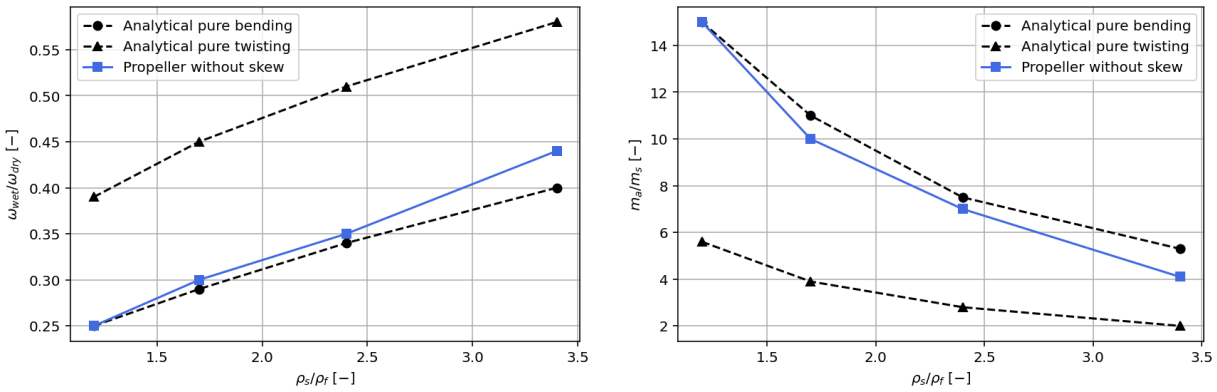

(a) The ratio $\omega_{wet}/\omega_{dry}$ for a range of density ratios.

(b) The ratio m_a/m_s for a range of density ratios.

Figure 8.6: The ratio $\omega_{wet}/\omega_{dry}$ and m_a/m_s for a range of density ratios for flexible propeller blades with zero skew angle. Analytical solutions for pure bending and twisting are compared with the numerical results of the flexible zero-skew propeller. The propeller results align well with the pure bending case, with only a minor discrepancy at the highest density ratio.

C4-40 Propeller

The C4-40 propeller blade has a considerable skew angle. For propeller blades with very high skew (or with high rake and anisotropic material properties), the first mode may not be simple bending, but a combination

of bending and twisting [100, 52]. Figure 8.7 shows the force signal in the frequency domain for the tested range of density ratios for the C4-40 propeller. The first force frequencies decrease with increasing density ratio. At a density ratio of 1.2, the first peak occurs at 188 Hz. For a ratio of 1.7, the frequency drops to 173 Hz, and further to 145 Hz for a ratio of 2.4. At the highest tested ratio of 3.4, the first peak is at 102 Hz. Table 8.4 lists the dry and wet natural frequencies for the tested range of density ratios, as well as the wet-to-dry frequency ratio and the added-mass-to-structural mass ratio.

ρ_s/ρ_f $[-]$	1.2	1.7	2.4	3.4
ω_{dry} $[Hz]$	444.5	373.5	314.3	264.1
ω_{wet} $[Hz]$	188.2	173.2	144.8	101.5
$\omega_{wet}/\omega_{dry}$ $[-]$	0.42	0.46	0.46	0.38
m_a/m_s $[-]$	4.6	3.7	3.4	5.8

Table 8.4: The wet-to-dry frequency ratio and the added-mass-to-structural mass ratio for a range of density ratios for the C4-40 propeller following from the simulation results

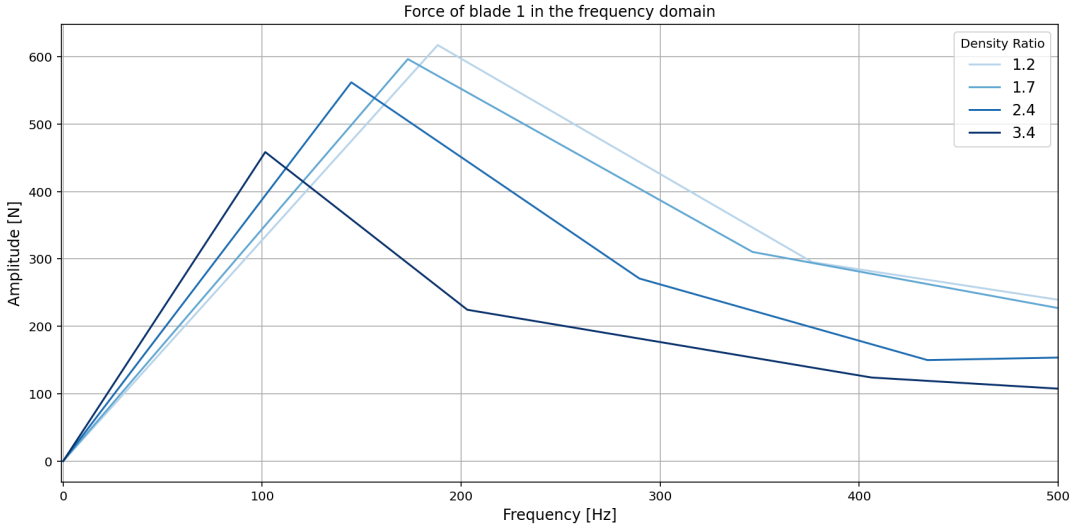

Figure 8.7: The propeller thrust force for a range of density ratios converted to the frequency domain. The signal is for the flexible Wageningen C4-40 propeller with a pitch ratio of 0.8.

The results in Table 8.4 are unequal to the results for pure bending or pure twisting in Table 8.2a and 8.2b, respectively. Hence, the first mode does not correspond to a pure bending or pure torsion mode, but instead is a combination of bending and twisting. This result is in line with what would be expected for this propeller with considerable skew as mentioned by Young [100]. Figure 8.8 visualises the ratio $\omega_{wet}/\omega_{dry}$ and m_a/m_s for a range of density ratios for the flexible Wageningen C4-40 propeller with a pitch ratio of 0.8. Figure 8.8a shows the analytical results obtained for the wet-to-dry frequency ratio of pure bending and pure torsion, as well as the results of the wet-to-dry frequency ratio for the flexible C4-40 propeller. Both the analytical results for pure bending and pure twisting show an increase in the wet-to-dry frequency ratio with increasing density ratio. The results of the flexible C4-40 propeller do not show this increase but display a non-monotonic trend with the density ratio. The same applies to Figure 8.6b, which presents the analytical results obtained for the added-mass-to-structural mass ratio of pure bending and pure torsion, as well as the results of the added-mass-to-structural mass ratio for this flexible C4-40 propeller. Again, a non-monotonic trend with structural density is evident in the results of the flexible C4-40 propeller. In contrast, both results for analytical pure bending and pure twisting show a decrease in the added mass-to-structural mass ratio as the density ratio increases.

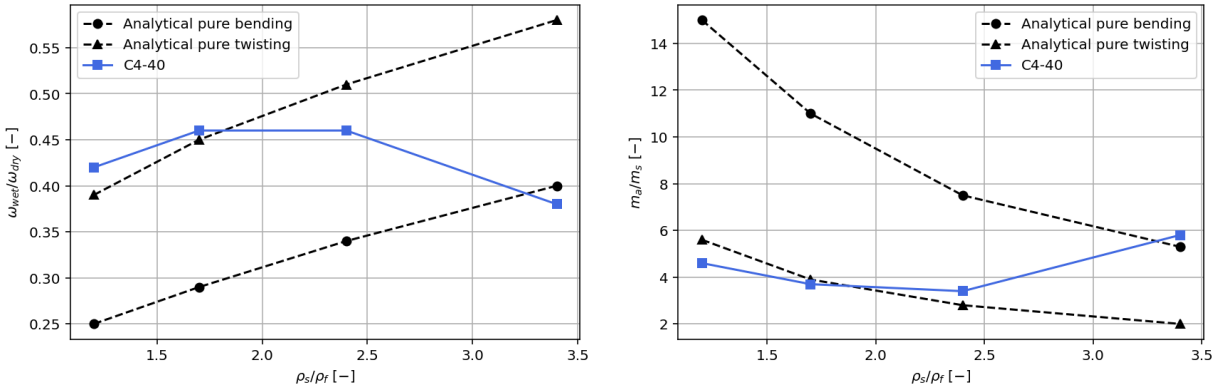

(a) The ratio $\omega_{wet}/\omega_{dry}$ for a range of density ratios.

(b) The ratio m_a/m_s for a range of density ratios.

Figure 8.8: The ratio $\omega_{wet}/\omega_{dry}$ and m_a/m_s for a range of density ratios for flexible C4-40 propeller blades. Analytical solutions for pure bending and twisting are compared with the numerical results of the flexible C4-40 propeller.

The variations in density alter the balance between structural mass and hydrodynamic added mass, as well as the wet natural frequency and dry natural frequency. The added-mass-to-structural mass ratio is lower for the C4-40 propeller compared to the zero-skew propeller and thus pure bending results (except for the highest tested density ratio). This result is expected from the analytical results, as the added mass has a greater effect on bending-dominated modes compared to torsional-dominated modes. Additionally, the wet-to-dry frequency ratio is higher for the C4-40 propeller compared to the zero-skew propeller, and thus, pure bending results (except for the highest tested density ratio). These results indicate that the first mode of the C4-40 propeller is a combination of both bending and twisting.

The non-monotonic trend in the wet-to-dry frequency ratio and the added-mass-to-structural-mass ratio arises because the wet natural frequency varies in an unsystematic manner. These variations indicate that structural density influences the added mass. Since the submerged modal frequency and mode shape determine the added mass, they are affected by the structural-to-fluid density ratio. The effect of structural density on the results is related to the coupled bend-twist mode shape. Consequently, the wet-to-dry frequency ratio and the added-mass-to-structural-mass ratio of coupled modes vary with the structural density. The structural density affects the dynamic response.

Therefore, the structural density must be scaled correctly for flexible propeller model experiments to achieve similar dynamic blade behaviour, which controls the overall performance of flexible propellers in non-uniform inflow conditions. For these conditions, the deformation extent is a ratio of the elastic force and hydrodynamic force, and a function of the fluid damping, viscous force and propeller inertia force, for which the definition of the Cauchy number is:

$$Ca_{unsteady} = \frac{E}{\rho_f D^2 n^2} f(Re, \zeta, \frac{\omega}{n}) \tag{8.9}$$

8.4. Discussion

The Fast Fourier transform separates the force signal over time into multiple harmonics, which one would expect to convert into discrete frequencies in the frequency domain. However, the signal in the frequency domain is also dependent on the damping factor of a system. The more rapidly a signal decays in time, the broader the peak in the corresponding frequency domain [47]. Figure 8.9 illustrates this concept, which is a physical effect of the decaying force signal on the frequency.

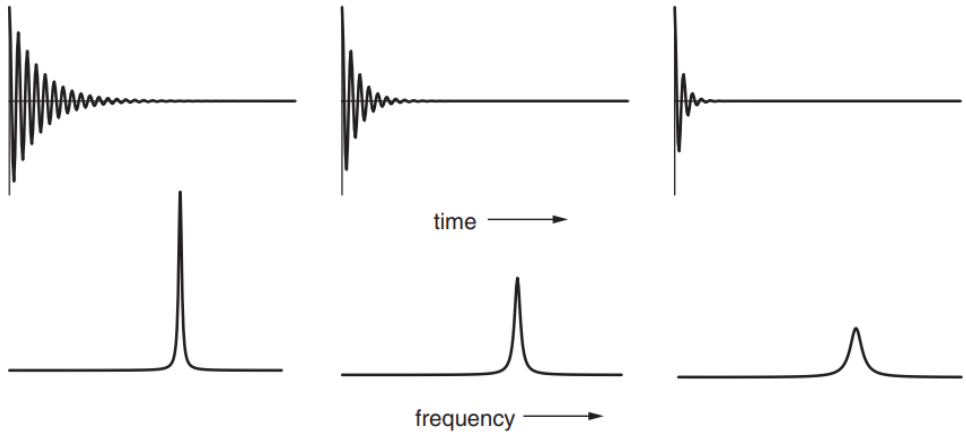

Figure 8.9: A more rapid decay of a signal in time leads to a broader peak in the corresponding frequency spectrum. From Keeler [47]

The Fast Fourier transform is applied over the force signal in time. The simulations are performed in a non-cavitating flow with uniform flow conditions. Consequently, the hydro-elastic response of the blades directly influences the propeller loading and vice versa. For this reason, the variations in thrust are used to derive the hydro-elastic response. However, the blade displacement field is usually more suitable for dynamic analyses than thrust values. The displacement field is not an integrated value in contrast to the thrust [69]. Furthermore, the numerical settings can significantly impact the obtained thrust values. Due to numerical limitations, precise data on deformation over time was not available. It is therefore recommended to perform additional research and validate the obtained results with the blade displacements.

The results are compared with other studies. For metal propeller blades, the modal fluid added mass is approximately 2.5 times the structural mass [12]. The fluid added mass has a larger effect on the wet natural frequencies of composite blades due to the lower material density of composites [70]. Accordingly, the effect of added mass on the natural frequencies would decrease as the ratio of solid-to-fluid density increases. In Table 8.4, the added mass effect indeed reduces for increasing material density, except for the case with the highest density ratio, hence the largest tested structural density. An increase in the added mass-to-structural mass ratio is observed for this case.

A study by Tian et al. [94] has experimentally and numerically determined the wet and dry natural frequencies of a plastic model propeller. The plastic propeller has similar material properties to those investigated in this study, and the solid-to-fluid density ratio equals 1.2. According to the study by Tian et al., the first wet natural frequency was approximately 40% of the dry natural frequency. This value is in the same order of magnitude as the frequency ratio in Table 8.4 found in this study.

8.5. Conclusion

In this chapter, FSI simulations were carried out for flexible propellers in open-water conditions to answer the fourth sub-question of this thesis: *'What is the influence of structural density on the steady and dynamic response of a flexible marine propeller?'* The open-water performance characteristics and steady-state deformation extent of the flexible C4-40 propeller for a range of structural-to-fluid density ratios are analysed. Additionally, the dynamic behaviour of the flexible C4-40 propeller and a propeller with a zero skew angle is studied. The hydro-elastic response is obtained by measuring the change in thrust and torque values as these exhibit oscillatory behaviour as the simulation converges towards a steady-state solution. The force signal is analysed in the frequency domain to study the blades' dynamic behaviour using a Fast Fourier transform.

The open-water performance and steady-state deformation extent are independent of the structural density. The structural response is quasi-static, meaning that material stiffness dominates the deformation extent and consequently the open-water performance. Incorrect scaled structural density, hence, errors in the magnitude of the propeller inertial force have no considerable influence on the steady-state deformation extent. The steady deformation extent thus depends on the ratio of bending force to hydrodynamic inertial force, and is a function of the viscous force, which leads to the following representation of the Cauchy number:

$$Ca_{steady} = \frac{E}{\rho_f D^2 n^2} f(Re) \tag{8.10}$$

This form can be used to control the steady state deformation extent. The modal frequencies describe the dynamic behaviour of propeller blades, which influences the deformation of flexible propellers in unsteady conditions. The first mode of the propeller without skew is observed to be a pure bending mode. For this zero-skew propeller, the wet natural frequency remains constant across a range of density ratios from 1.2 to 2.4. For pure bending modes, the results indicate that the structural density of materials used for model-sized propellers can differ by up to 30% from the full-size material density to achieve the same wet natural frequency.

The first mode of the C4-40 propeller is a combination of bending and twisting modes. The added mass has a smaller effect on coupled modes compared to bending-dominated modes. The numerical results of the C4-40 indicate that the structural density impacts coupled bend-twist mode shapes. This result leads to the conclusion that the structural density determines the dynamic behaviour of coupled modes and thus the deformation extent in unsteady flow conditions, such as a propeller operating in non-uniform flow.

The overall performance of flexible propellers depends on the deformation of the blades during revolution in non-uniform inflow conditions. For these conditions, the deformation extent can be controlled by the ratio of the elastic force to hydrodynamic force, and is a function of the fluid damping, viscous force and ratio of natural frequency (altered by the structural density) to revolution rate. The non-dimensional form to control the deformation extent in unsteady conditions is:

$$Ca_{unsteady} = \frac{E}{\rho_f D^2 n^2} f(Re, \zeta, \frac{\omega}{n}) \tag{8.11}$$

9 Discussion

The outcomes of this study have provided insights into the scaling of flexible marine propellers for model tests. This thesis project has adopted the workflow developed by Lagendijk [62] to perform FSI simulations and analyse the deformation behaviour of flexible propellers. This workflow is used to analyse the rigid propeller performance of the C4-40 propeller as well. The first section of this discussion provides validation of the rigid test results, as well as the sources of errors introduced by using numerical methods. The second section of this discussion addresses the limitations of this study, which stem from its scope. Recommendations for further research are presented, following from these limitations.

9.1. Validation of the Rigid Results

The results of the rigid propeller simulations in Chapter 5 are compared with the CFD reference data obtained by MARIN [73]. The CFD results of MARIN are for the same propeller geometry, the C4-40 propeller with a pitch ratio of 0.8. The data consists of two model-scaled Reynolds numbers tests and one full-scale Reynolds number test. The Reynolds number is defined at r/R = 0.7, following the same definition as given in Equation 5.1. The MARIN calculations are performed using a frozen rotor approach, with a uniform velocity at the inflow, constant level of turbulence quantities and constant pressure at the far-field boundary and outflow. No-slip wall conditions are set for the propeller and hub surfaces. Cavitation effects are neglected. MARIN has also utilised the standard k-ω SST model developed by Menter [82].

Figure 9.1 shows the open water diagram of both the results obtained in this study and those of MARIN. The Reynolds numbers of the results of MARIN are equal to $1.7*10^5$, $4.5*10^5$ and $4.0*10^7$, and are compared with the results of $1.0*10^5$, $5.0*10^5$ and $5.0*10^7$ of this study. The results do not align with each other, which raises the question of what causes this discrepancy.

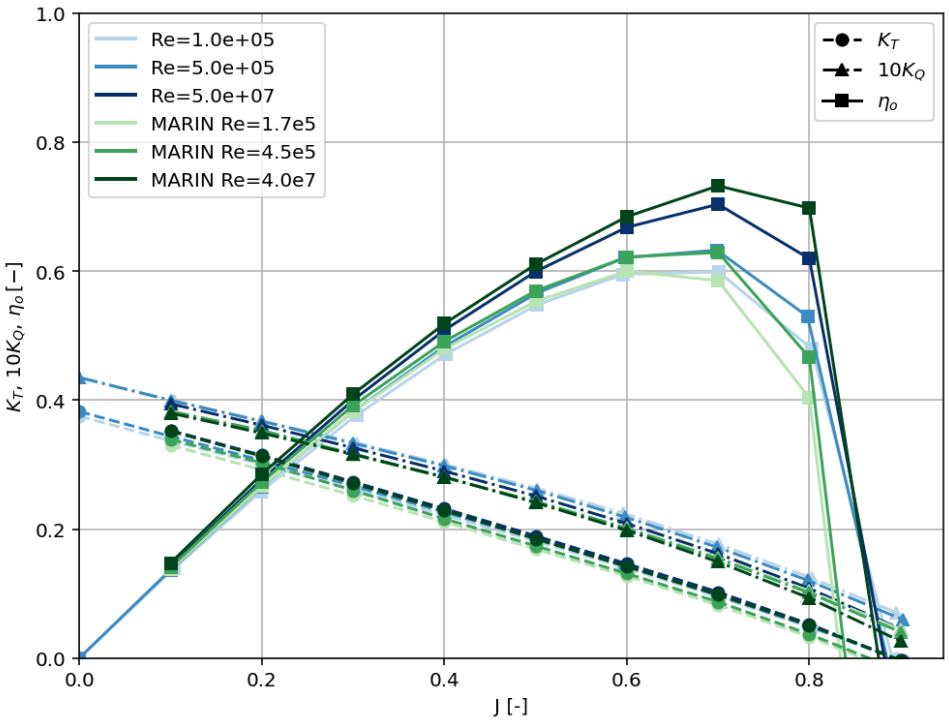

Figure 9.1: Open water diagram of the rigid Wageningen C4-40 propeller with a pitch ratio of 0.8 for different Reynolds numbers. The diagram presents the results of this study and the CFD results of MARIN [73].

9.1.1. Numerical Errors

Generally, numerical errors of a CFD solution include three components [22]:

- The round-off error, due to the finite precision of computers
- The iterative error, which is due to the non-linear character of the momentum equation and transport equations of the turbulence model, as well as the uncoupling of these equations in the solution process
- The discretisation error, being a consequence of the transformation of the continuum equations into a system of algebraic equations

The finite precision of the computer will introduce round-off errors. These errors may affect the result significantly if the round-off errors accumulate [64]. The ReFRESCO code executes in double-precision, thereby assuming that the impact of round-off errors on numerical uncertainty is negligible compared to the other errors [49].

The motion equations are solved iteratively. The difference between the two iterations becomes smaller as the solution converges. The solution is supposed to have been reached once a given convergence criterion is met. Consequently, this will introduce iterative errors [64]. This iterative error is primarily monitored by the residuals and can be expressed using different norms, for instance, the L_2 norm [22]. This norm is defined by:

$$L_2(\Delta\phi) = \sqrt{\frac{\sum(|\Delta\phi_i|)^2}{N_p}} \tag{9.1}$$

In this equation, $\Delta\phi$ stands for the local change of the flow quantity ϕ and N_p is the total number of nodes on a given grid. The L_2 value for the normalised residual of all transport equations below a value of $1 * 10^{-6}$ ensures that the primary source of numerical uncertainty is the contribution from the discretisation error [49]. The discretisation by FEM and FVM approximates the continuous functions as discrete models, which introduce discretisation errors. The impact of discretisation errors decreases with a finer grid. By gradually refining the grid, a grid-independent result can be obtained [64].

The solutions of all simulations are checked. Appendices A, C, and D include plots of the thrust coefficient over the time steps. The plots show that the force solution is converged for all instances. The L_2 residuals of the velocity, pressure and turbulence quantities are not for all the cases below $1 * 10^{-6}$, indicating that iterative errors are not negligible. However, in complex turbulence flows, it is not guaranteed that this L_2 convergence criterion can be achieved [22]. The cases with stagnated iterative convergence still had L_2-values below $1 * 10^{-4}$. Improved convergence in the calculations can be achieved by adjusting explicit relaxation factors or modifying specific limiters and correction terms. Additionally, mesh quality and the transitions between cell layers can influence the magnitude of the iterative error. Although the L_2 norm is above $1 * 10^{-6}$, the solutions have converged for all the cases in this report. Therefore, it can be assumed that discretisation errors mainly influence differences in results, yet the size of the iterative error is not negligible. The rigid results in this study are only used to compare the Reynolds number effect between rigid and flexible cases. For the purpose of this study, these numerical errors and discrepancies between rigid results are considered reasonable to obtain valid conclusions about the scaling approaches for model-scaled open-water tests of flexible propellers.

9.2. Model Limitations and Assumptions

This section discusses the limitations of this study, which follow from its scope. The fluid solver applies the k–ω SST turbulence model of Menter [82], without a transition model, which means that a fully turbulent boundary layer is solved. The first part of this section discusses the impact of this assumption and the motivation for excluding a transition model. The second part examines the isotropic material assumption, considers how anisotropy may change the deformation response, and gives recommendations for further work on material scaling. Next, the section addresses the assumption of a linear constitutive relation for the structural response. It then evaluates the restriction of uniform inflow and explains why further research is needed with unsteady inflow conditions. Finally, the assumption that centrifugal and Coriolis forces are neglected is addressed.

9.2.1. Resolving Fully Turbulent Flow Behaviour

The coupled URANS–FEM FSI simulation enables the assessment of the interaction between the deformable propeller and fluid. The fluid solver uses a finite-volume method and is implemented with the k–ω SST turbulence model of Menter [82], without any transition models. Model-scale Reynolds numbers, typically around $1 * 10^6$ or lower, often experience laminar flow over significant portions of the blades. As no transition models

are implemented, a fully turbulent flow is solved across the tested range of Reynolds numbers. The numerical simulations may underestimate the actual Reynolds-number effects, as model-scale experiments often include flow transition. This transition could further amplify differences in deformation, thus affecting the propeller performance.

Although the use of a transition model could investigate the effect of partly laminar flow, the study of Kerkvliet et al. [49] illustrates the limitations of the use of transition models. Their study analysed the predictive capabilities of the $\gamma - Re_\theta$ turbulent-transition model and found that there is a strong dependence of the inlet turbulence quantities on the predicted performance. This high sensitivity poses a limitation to the model's applicability. The inlet turbulence quantities may not be realistic from a physics point of view, but depend on the Reynolds number and the propeller loading condition. Achieving equal flow behaviour over the blades between experiments and simulations can only be achieved if the onset of transition and possible flow separation is known a priori. The implementation of a transition model, supported by experimental data on the flow behaviour of flexible blades across Reynolds numbers, would be valuable for future research. Both experimental and numerical research enable a more detailed investigation of Reynolds-number effects on flexible propellers, providing further insight into how laminar flow affects both deformation and performance.

9.2.2. Limitation of Isotropic Material Characteristics

The structural characteristics of a composite material depend on its components, geometry, and the distribution of the fibres and matrix. The ply stacking sequence and the fibres' orientation through the material's thickness can result in an anisotropic material response. This study, however, is limited to isotropic material characteristics. The anisotropic material response enables the use of a bend-twist coupling in the design of flexible marine propellers. When the propeller is loaded with positive ship speed and positive propeller speed, the thrust generates a bending force in the forward direction on the blades, causing rake deformation. The coupling twists the blade, resulting in a reduction in the pitch angle. This study obtained similar deformation behaviour for the C4-40 propeller using isotropic material properties. The first mode shape of the C4-40 propeller is observed to be a combined bend-twist mode. It is generally accepted that for propellers with high skew and or rake, the first mode is a combined bend-twist mode.

While anisotropic materials may induce increased or reduced deformation along specific directions, the deformation characteristics are anticipated to remain comparable to those established in this study using isotropic material properties. An effective composite lay-up should be used for model experiments of anisotropic full-size configurations. Using a combined Froude-Cauchy similarity approach, this lay-up should reduce Young's modulus by the scale factor whilst keeping material density and Poisson ratio identical to the full-scale propeller material. This study is limited to the response deformations of propellers. Recommendations for further research include scaling failure stresses and, thus, failure modes.

9.2.3. The Use of a Linear Elastic Constitutive Model

The time-domain simulations in this study use a flow solver with a linear two-way coupling to the structural solver, implying the use of a linear elastic constitutive model for the propeller material. The linearity of this elastic stress-strain relation indicates that the stress and strains are linearly proportional to one another. This assumption is valid for small material strains. Zarruk et al. [32] experimentally investigated the hydroelastic response of six flexible hydrofoils, including two composite hydrofoils of carbon-fibre reinforced plastic. This study demonstrated that deformation in hydrofoils scales linearly with the applied load in the prestall region, confirming a linear elastic response. Maljaars [69] similarly found relatively small blade deflections and validated a coupled BEM–FEM approach under steady inflow, assuming geometrically linear elasticity. His validation involved three small-scale flexible propellers, one made from isotropic epoxy and two with distinct laminate lay-ups.

9.2.4. Limitation of Uniform Inflow Conditions

In this study, the simulations are conducted with uniform inflow, using an absolute-formulation steady approach. The URANS equations are solved in the moving reference frame but written in terms of absolute reference frame quantities. The combination of variations of hydrodynamic loading due to the non-uniform wake field and the vibrational behaviour of a propeller influences the global vibrational characteristics of a propeller, as described by Carlton [12]. The vibrations introduce a variation in the angle of attack, leading to variations in the hydrodynamic reaction load. For metal propellers, variations in angle of attack are small, and the resulting vibratory loading is assumed to vary linearly. This linearity enables the use of superposition, allowing for the separate determination of excitation and reaction loads. In contrast, this linear assumption may not be valid for composite propellers, where the interaction between excitation and reaction can lead to non-linear behaviour.

Carlton's remarks highlight the need for further research into the behaviour of composite propellers in non-uniform flow conditions, which would necessitate geometrically non-linear finite element formulations and unsteady CFD simulations. The absolute-formulation approach, as implemented in this study, results in steady conditions by definition and thus can not be used to perform unsteady simulations. Unsteady simulations are possible with a combination of boundary conditions or using a moving-grid formulation (MVG), in which the URANS equations are then written and solved in the earth-fixed reference frame [75].

9.2.5. Neglecting Centrifugal and Coriolis Forces

A rotating propeller operating at constant angular speed experiences non-zero centrifugal and Coriolis forces. The Coriolis force introduces a velocity-dependent term that acts as additional damping. Nevertheless, its contribution is generally negligible compared to the hydrodynamic damping. Therefore, this force component can be omitted in the analyses of flexible propellers [70]. The centrifugal force acts radially, pulling the blades away from the hub. This effect depends on the structural density. The centrifugal force introduces radial stresses within both the blades and the hub. The centrifugal forces also result in an additional stiffening effect, referred to as centrifugal stiffening. This effect, however, is generally negligible for conventional propeller designs and may only be necessary for very high rotational speed applications [12].

The centrifugal forces are not included in fluid-structure interaction analysis in this study. This assumption is made because the centrifugal forces act primarily in-plane with the propeller rotation, while the hydrodynamic loads that govern blade deformation act out of plane. Consequently, the influence of centrifugal forces on the blade deflection is expected to be much smaller than that of the hydrodynamic bending loads.

10 Conclusion

This study assesses the scaling of flexible marine propellers for model testing using time-domain fluid–structure interaction simulations. These simulations are conducted with a coupled URANS–FEM solver, testing the Wageningen C4-40 propeller geometry with a pitch ratio of 0.8. The flow solver is implemented with the $k-\omega$ SST turbulence model without the use of a transition model. This analysis is performed with uniform inflow conditions and is limited to isotropic materials. The performance characteristics of flexible marine propellers depend on their deformation extent. Accordingly, this thesis aims to answer the following research question:

Which non-dimensional parameter controls the deformation extent of flexible marine propellers?

A set of non-dimensional relations of the physical quantities involved in the testing of flexible marine propellers is derived using the Buckingham Π-theorem [10]. The non-dimensional relations should be equal on two scales to obtain full geometrical, kinematic and dynamic similarity. Generally, it is accepted that achieving complete dynamic similarity is impossible for rigid model propeller testing. The deformation ability of flexible marine propellers introduces additional scaling laws. This thesis derives that the amplitude of blade deformation can be expressed as a form of the Cauchy number. This non-dimensional parameter represents the ratio of elastic forces to hydrodynamic inertial forces. Additionally, this parameter is a function of fluid damping and the ratio of the modal frequency to the propeller's revolution rate.

The derived non-dimensional parameter is tested using a combined Reynolds-Cauchy similarity approach for two geometrically similar propellers with different diameters. The relative deformation extent of both scales is identical. The model-scaled propeller exhibits a relative difference in thrust and torque coefficient of less than 5% compared to the full-size propeller. The open-water efficiency depends on both coefficients and is within the same percentage difference. Additional tests demonstrate that numerical rather than physical scaling effects alter the flow behaviour over the blades. In particular, the sensitivity to the y^+-value using the $k-\omega$ SST turbulence model of Menter [82] can lead to numerical errors larger than 5% for y^+-values $\simeq 1$. In conclusion, the difference in performance results can be attributed to disparities in fluid flow, and the simulations have confirmed that the ratio of elastic bending to hydrodynamic inertial forces controls the deformation extent of flexible marine propellers.

The Reynolds number represents the ratio of inertial to viscous forces. Achieving full-size Reynolds numbers of the order 10^7 in propeller test facilities is impossible, yet boundary layer behaviour depends highly on this parameter. Numerical simulations resolving a fully turbulent flow are executed to determine the Reynolds number effect of both rigid and flexible propellers. The thrust coefficients increase and the torque coefficients decrease as Reynolds numbers increase for both rigid and flexible propellers. For the flexible propeller, the thrust coefficient between $Re = 1 * 10^5$ and $Re = 5 * 10^7$ increases between 3.4 and 13.0%, depending on the advance ratio. The torque coefficient reduction is between 3.1 and 21.0% for the flexible propellers between $Re = 1 * 10^5$ and $Re = 5 * 10^7$ for the tested range of advance ratios. The open-water efficiency is a combination of K_T and K_Q; consequently, larger Reynolds numbers lead to higher open-water efficiencies. The deformation of flexible propellers improves flow attachment over the blades. Yet, small deformation differences are observed in pitch ratio, camber-to-chord ratio, and rake-to-diameter ratio across the tested range of Reynolds numbers. This study indicates that the deformation extent of flexible propellers is sensitive to viscous forces. Thus, the non-dimensional parameter controlling the deformation extent should also be a function of the Reynolds number.

The combined Froude-Cauchy similarity approach is most suitable for performing flexible propeller model tests, as it scales the gravitational, elastic, and inertial forces equally. This approach also enables testing at advance velocities lower than those at full scale, which are feasible to obtain in cavitation tunnels and towing tanks. However, this approach poses challenges in finding an appropriate material for model-size propellers.

This thesis investigates the incorrect scaling of structural density and observes that the structural-to-fluid density ratio does not influence the extent of the steady-state deformation. The open water characteristics differ by less than 0.1% across variations in the structural-to-fluid density ratio. These results are in line with expectations, as a quasi-static blade response is governed by stiffness rather than by propeller inertia. Ergo, if a suitable material for open-water model testing is unavailable, proper scaling of the stiffness is essential. In contrast, this study indicates that scaling the material density is less important for the steady deformation response.

Contrary to the steady-state response, the structural-to-fluid density ratio does become important in unsteady conditions for flexible marine propellers. A non-uniform wakefield, as occurs in the behind operation, poses such a condition. The modal frequencies describe the dynamic behaviour of the propeller blades, and should scale with the propeller's revolution rate to obtain similar blade deformation in unsteady flows. This study analyses the modal frequencies in the frequency domain using a Fast Fourier transform. This analysis indicates that the first mode of vibration is a pure bending mode for propellers with zero skew angle. Generally, for propellers with high skew, rake, or made from anisotropic materials, the first mode is a combined bend-twist mode. It is observed that the added mass has a smaller effect on coupled modes compared to more bending-dominated modes, in line with analytical results. While it is observed that the structural density of materials used for model tests can vary by up to 30% from the full-size material density to achieve the same wet natural frequency for pure bending modes, the structural-to-fluid density impacts the wet natural frequency of combined bend-twist modes. In conclusion, the deformation extent in unsteady conditions is a function of the ratio of the modal frequency to the propeller revolution rate, which makes it sensitive to the structural density.

These conclusions lead to the answer of the main research question: *'Which non-dimensional parameter controls the deformation extent of flexible marine propellers?'*. This non-dimensional parameter is derived from non-dimensional analyses and is a form of the Cauchy number. For the steady-state conditions, the deformation extent can be controlled by the ratio of elastic force to hydrodynamic inertial force, and depends on the Reynolds number:

$$Ca_{steady} = \frac{E}{\rho_f D^2 n^2} f(Re) \tag{10.1}$$

In unsteady conditions, the modal frequency should scale with the propeller's revolution rate for relatively similar blade deformation. The propeller's inertial force, hence, structural density influences the modal frequency. Thus, the deformation extent of flexible propellers in unsteady conditions can be controlled with the ratio of elastic force to hydrodynamic inertial force, and depends on the Reynolds number, as well as the fluid damping and ratio of the modal frequency to revolution rate:

$$Ca_{unsteady} = \frac{E}{\rho_f D^2 n^2} f(Re, \zeta, \frac{\omega}{n}) \tag{10.2}$$

This thesis is limited to the response deformations of flexible propellers with isotropic material properties. The anisotropic material response enables the use of a bend-twist coupling in the design of flexible marine propellers. This study achieves combined coupling with the use of the geometric shape of the blades rather than of material properties, which resulted in a comparable deformation response. Nevertheless, the scaling of failure stresses and, thus, failure modes requires further investigation. In conclusion, this study enhances the understanding of flexible propeller scaling. It offers insights that are essential for improving flexible propeller model test accuracy and enhancing the accuracy of full-scale flexible propeller performance predictions, with the end goal of designing more efficient marine propulsion systems.

10.1. Recommended Model Testing Approach for Flexible Marine Propellers

While the scaling laws for model testing of rigid marine propellers are well established, the deformation ability of flexible marine propellers introduces additional scaling laws, for which the non-dimensional numbers presented above offer a basis for accurate scaling of flexible propellers in both experimental and computational studies. This section will provide a recommended practical approach for scaling flexible marine propellers in experimental studies.

Geometric similarity should and can always be obtained regarding thickness-to-chord ratio, chord-to-diameter ratio, camber-to-chord ratio, skew angle and pitch ratio. Propeller blades have a non-uniform cross-section

to avoid cavitation and to maximise efficiency and control. Specifically for flexible propellers, considerable skew angles are used as these result in a larger de-pitching moment when loaded. It is thus crucial to satisfy geometric similarity in all three dimensions so that the model-scale propeller accurately replicates the full-size propeller hydrodynamics.

Kinematic similarity is obtained by performing model-scale tests with the same advance ratio as the full-size propeller. The advance ratio establishes a fixed relationship between advance velocity and revolution rate and should always be obtained. The advance ratio, i.e. the angle of attack, determines the propeller loading, hence the resulting force of the propeller blade. By adjusting either or both the advance velocity and revolution rate, kinematic similarity can always be ensured.

Dynamic similarity between model- and full-scale propellers cannot be achieved in experimental facilities. A combined Froude–Cauchy similarity approach is recommended for testing flexible propeller models. While this method leads to reduced Reynolds numbers, which may affect the deformation, Reynolds number similarity cannot be achieved in towing tanks or cavitation tunnels. Model-scale propellers often experience partly laminar flow over their blades, rather than fully turbulent flow, as full-size propellers do. Because of this, the differences in deformation and performance in experiments are expected to increase at Reynolds numbers typical for model tests, although this requires further study. The use of turbulators in flexible propeller model tests is advised to improve consistency of testing. Additional improvements may be achieved by developing CFD-based extrapolation methods, which could bridge the gap between model-scale experiment results and full-scale propeller performance.

In practice, it is challenging to find a material that can satisfy all structural scaling requirements using a combined Froude-Cauchy scaling approach. For the open-water model testing of flexible propellers, proper scaling of stiffness is essential. This study indicates that the structural density does not need to be scaled as strictly for the steady deformation response of flexible propellers. In contrast, the structural density does affect the dynamic behaviour of flexible model propellers and should be scaled correctly to obtain equal blade deformation in unsteady conditions. Thus, performing model tests with incorrectly scaled structural density is not suitable for predicting the full-scale propeller response under these conditions. It is recommended to use model tests with incorrectly scaled structural densities solely for validating numerical solvers, rather than for predicting full-scale dynamic performance.

References

[1] R. McNeel et al. *Rhinoceros 3d, version 7*. 2025. URL: https://www.rhino3d.com/.

[2] M.M. Bernitsas, D. Ray, and P. Kinley. *Kt, Kq and Efficiency curves for the Wageningen B-Series Propellers*. 237. Michigan: The University of Michigan, 1981.

[3] R. Biswas and R.C. Strawn. "Tetrahedral and hexahedral mesh adaptation for CFD problems". In: *Applied Numerical Mathematics* 26.1 (1998), pp. 135–151. ISSN: 0168-9274.

[4] J Blasques, C. Berggreen, and P. Andersen. "Hydro-Elastic Analysis and Optimization of a Composite Marine Propeller". In: *Marine Structures* 23.1 (2010), pp. 22–38.

[5] J. Bosschers. "Propeller Tip-Vortex Cavitation and its Broadband Noise". PhD thesis. Renkum: Universiteit Twente, 2018.

[6] C. Brennen. "Cavitation and Bubble Dynamics". In: *Cavitation and Bubble Dynamics* 44 (1995).

[7] C.E. Brennen. *A review of added mass and fluid inertial forces*. Port Hueneme, California: Naval Civil Engineering Laboratory, 1982.

[8] C.E. Brennen. "Law of the Wall". In: *An Internet Book on Fluid Dynamics*. Caltech, Oct. 2006.

[9] A.J.L.L. Buchner. "The Governing Equations of Fluid Mechanics". Lecture. ME45042: Advanced Fluid Dynamics. Delft, Oct. 16, 2023.

[10] E. Buckingham. "On physically similaar systems: Illustrations of the use of dimensional equations". In: *A journal of experimental and theoretical physics*. 2nd ser. 4 (1914), pp. 345–376.

[11] L.C. Burrill. "Sir Charles Parsons and Cavitation". In: *The Institute of Marine Engineers* 63.8 (1951).

[12] J.S. Carlton. "Propeller geometry". In: *Marine Propellers and Propulsion*. Second. Elsevier, 2007. ISBN: 978-07506-8150-6.

[13] J.S. Carlton. "Propeller Performance Characteristics". In: *Marine Propellers and Propulsion*. Third. Elsevier, 2012. ISBN: 978-0-08-097123-0.

[14] CFD Online. *Skin friction coefficient*. CFD Online. Jan. 2016. URL: https://www.cfd-online.com/Wiki/Skin_friction_coefficient.

[15] B. Chen et al. "Design, Fabrication and Testing of Pitch-Adapting (Flexible) Composite Propellers". In: (2006).

[16] K. Chen. *Denoising Data with Fast Fourier Transform*. Medium. 2020.

[17] O. Colomés et al. "Elements and shape functions". In: *Finite Elements in Civil Engineering and Geosciences*. Delft: Delft University of Technology, 2023.

[18] R.A. Cumming, W.B. Morgan, and R.J. Boswell. "Highly Skewed Propellers". In: The Annual Meeting of Society of Naval Architects and Marine Engineers. 3. 1972.

[19] I.M. Daniel and O. Ishai. *Engineering Mechanics of Composite Materials*. Second Edition. Oxford University Press, 2006. ISBN: 978-0-19-515097-1.

[20] Directorate-General for Environment. "Zero pollution and Biodiversity: First ever EU-wide limits for underwater noise". In: *European Commission* (2022).

[21] A. Ducoin and Y.L. Young. "Scaling of the Hydroelastic Response of Flexible Lifting Bodies in Transitional and Turbulent Flows". In: vol. 5. 2013. DOI: 10.1115/OMAE2013-11121.

[22] L. Eca and M. Hoekstra. "On the Influence of the Iterative Error in the Numerical Uncertainty of Ship Viscous Flow Calculations". In: *26th Symposium on Naval Hydrodynamics* (Sept. 17, 2006).

[23] L. Eca, F.S. Pereira, and G. Vaz. "Viscous flow simulations at high Reynolds numbers without wall functions: Is y+ 1 enough for the near-wall cells?" In: *Computers & Fluids* 170.15 (July 2018), pp. 157–175.

[24] J.N. Fernando, G.D. Weymouth, and D.E. Rival. "On the limits of added-mass theory in separated flows and with varying initial conditions". In: *Fluids and Structures* 93 (2019).

[25] J.P. Franc. "Partial Cavity Instabilities and Re-Entrant Jet". In: Fourth International Symposium on Cavitation. 2001.

[26] Electricité de France. *Finite element code aster, analysis of structures and thermomechanics for studies and research*. URL: https://code-aster.org.

[27] R.E. Froude. “On the Part Played in Propulsion by Difference in Pressure”. In: *Transaction of the Institute of Naval Architects* 30 (1889), pp. 390–405.

[28] T. Götz et al. *Overview Of The Impacts Of Anthropogenic Underwater Sound In The Marine Environment*. OSPAR Commission, 2009.

[29] J. Grevink. “Fixed pitch propellers”. Lecture. Lecture. MT44006: Future Marine Propulsion Systems. Delft, 2024.

[30] C. Groth, S. Porziani, and M. Biancolini. “Radial Basis Functions Vector Fields Interpolation for Complex Fluid Structure Interaction Problems”. In: *Fluids* 6 (Sept. 2021), p. 314.

[31] S. Gudmundsson. “The Anatomy of the Airfoil”. In: *General Aviation Aircraft Design*. Second. Elsevier, 2022. ISBN: 978-0-12-818465-3.

[32] Z.A. Gustavo et al. “Experimental study of the steady fluid–structure interaction of flexible hydrofoils”. In: *Journal of Fluids and Structures* 51 (2014), pp. 326–343. ISSN: 0889-9746.

[33] J. Haider et al. “Explicit solid dynamics in OpenFOAM”. In: Sixth ESI OpenFOAM user conference. Hamburg, Germany, 2018.

[34] X.D. He, Y. Hong, and R.G. Wang. “Hydroelastic optimisation of a composite marine propeller in a non-uniform wake”. In: *Ocean Engineering* 39 (2012), pp. 14–23. ISSN: 0029-8018.

[35] J.A. Hildebrand. “Anthropogenic and natural sources of ambient noise in the ocean”. In: *Marine Ecology Progress Series* 395 (2009), pp. 5–20.

[36] R.Y. Hudson et al. *Coastal hydraulic models*. 5. Fort Belvoir: Coastal engineering research center, 1979.

[37] S.A. Hughes. *Physical models and laboratory techniques in coastal engineering*. Vol. 7. World Scientific, 1993.

[38] IdealSimulations. *Courant number in CFD simulations*. IdealSimulations. URL: https://www.idealsimulations.com/resources/courant-number-cfd/.

[39] International Maritime Organization. *2023 IMO Strategy on Reduction of GHG Emissions from Ships*. Resolution MEPC.377(80). International Maritime Organization, 2023.

[40] International Maritime Organization. “Action plan agreed to reduce underwater noise from ships”. In: *International Maritime Organization* (2024).

[41] ITTC. *Performance Prediction Method*. Recommended Procedures and Guidelines. International Towing Tank Conference (ITTC), 2011.

[42] ITTC. *Procedure Open Water Test*. Recommended Procedures and Guidelines. International Towing Tank Conference (ITTC), 2021.

[43] G. Jacobi. “Ship Hydrodynamics with OpenFOAM –Session 2”. Lecture. Lecture. Delft, 2024.

[44] Morgan Jones. “Chapter 4 - Test Equipment Principles”. In: *Building Valve Amplifiers*. Second Edition. Oxford: Newnes, 2014, pp. 235–380. ISBN: 978-0-08-096638-0.

[45] S.H. Jongsma, E.T.A. van der Weide, and J. Windt. “Implementation & Verification Of A Partitioned Strong Coupling Fluid-Structure Interaction Approach”. In: 12th International Conference on Hydrodynamics (ICHD). Egmond aan Zee, The Netherlands, Sept. 18, 2016.

[46] N.D. Katopodes. “Viscous Fluid Flow”. In: *Free-Surface Flow*. Butterworth-Heinemann, 2019, pp. 324–426. ISBN: 978-0-12-815489-2.

[47] J. Keeler. “Fourier Transformation and Data Processing”. In: *Lectures by James Keeler*. Cambrigde: The Department of Chemistry at the University of Cambridge, 2011.

[48] S. Kellas and J. Morton. *Strength Scaling in Fiber Composites*. NASA Contractor Report 4335. NASA, 1990.

[49] M Kerkvliet et al. “A Numerical Study on Model Propeller Performance Prediction Including Transitional and Passively Controlled Boundary Layer Considerations”. In: *Eighth International Symposium on Marine Propulsors*. smp’24. Berlin, Germany, Mar. 2024.

[50] M. Kerkvliet. *Open Water Characteristics C4-40*. E-mail. June 23, 2025.

[51] H. de Koning Gans. *Froude schaling en dimensie-analyse*.

[52] M.R. Kramer, Z. Liu, and Y.L. Young. “Free vibration of cantilevered composite plates in air and in water”. In: *Composite Structures* 95 (2013), pp. 254–263. ISSN: 0263-8223.

[53] U.R. Kristiansen, W. Soedel, and J.F. Hamilton. “An investigation of scaling laws for vibrating beams and plates with special attention to the effects of shear and rotatory inertia”. In: *Journal of Sound and Vibration* 20.1 (1972), pp. 113–122.

[54] G. Kuiper. *Physics of cavitation: Cavitation Inception*. 2012.

[55] G. Kuiper. *Resistance and Propulsion 1*. 2002.

[56] G. Kuiper. *Types of cavitation: Bubble Cavitation*. 2012.

[57] G. Kuiper. *Types of cavitation: Sheet Cavitation*. 2012.

[58] G. Kuiper. *Vortex Cavitation*. 2012.

[59] P.K. Kundu, I.M. Cohen, and D.R. Dowling. *Fluid Mechanics*. Sixth. Elsevier, 2016. ISBN: 978-0-12-405935-1.

[60] L.P. Lagendijk. “Optimisation of flexible composite ship propellers”. Lecture. Lecture. MT44061: Advanced Course in Resistance and Propulsion. Delft, Mar. 15, 2023.

[61] L.P. Lagendijk. “The road to improved propeller designs”. Lecture. Lecture. MT44061: Advanced Course in Resistance and Propulsion. Delft, Mar. 13, 2024.

[62] L.P. Lagendijk et al. “Simulation workflow for flexible marine propellers”. In: 26th Numerical Towing Tank Symposium. Duisburg, Germany, 2024.

[63] M. Lancaster et al. *Shipping and Underwater Noise*. World Wide Fund for Nature, 2021. URL: https://www.wwf.nl/globalassets/pdf/nieuws/wwf-shipping-and-underwater-noise-report-2021.pdf.

[64] L. Larsson and H.C. Raven. *Ship Resistance and Flow*. First. New Jersey: The Society of Naval Architects and Marine Engineers, 2010.

[65] Y.J. Lee and C.C. Lin. “Optimized design of composite propellers”. In: *Mechanics of Advanced Materials and Structures* 11.1 (2010), pp. 17–30.

[66] *Lift Pressure Distribution*. 2021. URL: https://aviation.stackexchange.com/questions/83293/lift-pressure-distribution.

[67] C.C. Lin, Y.J. Lee, and C.S. Hung. “Optimization and Experiment of Composite Marine Propellers”. In: *Composite Structures* 89.2 (2009), pp. 206–215.

[68] P. J. Maljaars et al. “BEM–FEM coupling for the analysis of flexible propellers in non-uniform flows and validation with full-scale measurements.” In: *Journal of Fluids and Structures* 95 (2020).

[69] P. J. Maljaars et al. “Validation of a steady BEM-FEM coupled simulation with experiments on flexible small scale propellers”. In: *Fifth International Symposium on Marine Propulsion* (2017).

[70] P.J. Maljaars. “Hydo-Elastic Analysis of Flexible Marine Propellers”. PhD thesis. Delft: Delft University of Technology, 2019.

[71] P.J. Maljaars and M.L. Kaminski. “Hydo-Elastic Analysis of Flexible Marine Propellers: An Overview”. In: (2015).

[72] B.C. Mandal and H.P. Mazumdar. “The Importance of the Law of the Wall”. In: *International Journal of Applied Mechanics and Engineering* 20.4 (2015), pp. 857–869.

[73] MARIN. *Open-Water Data Case 1 Tripping JIP*.

[74] Marin. “CRS Propagate workshop Part III: Propeller Geometry”. Wageningen.

[75] Marin. *ReFRESCO Theory Manual*. Wageningen: Marin, 2017.

[76] G. Marsh. “A new start for marine propellers?” In: *Reinforced Plastics* 48.11 (2004), pp. 34–38.

[77] J. Moore and et al. “Viscous Damped Free Vibrations”. In: *Mechanics Map*. LibreTexts, 2025.

[78] M.R. Motley and Y.L. Young. “Scaling of the Transient Hydroelastic Response and Failure Mechanisms of Self-Adaptive Composite Marine Propellers”. In: *International Journal of Rotating Machinery* 2012.1 (2012).

[79] A.P. Mouritz et al. “Review of advanced composite structures for naval ships and submarines”. In: *Composite Structures* 53.1 (2001), pp. 21–42. ISSN: 0263-8223.

[80] N.L. Mulcahy, B.G. Prusty, and C.P. Gardiner. “Hydroelastic tailoring of flexible composite propellers”. In: *Ships and Offshore Structures* 5.4 (2010), pp. 359–370.

[81] J. Murad. *What is y+?* SimScale. 2020.

[82] NASA. *The Menter Shear Stress Transport Turbulence Model*. Langley Research Center: Turbulence Modeling Resource. 2024.

[83] J.N. Newman. *Marine Hydrodynamics*. The MIT Press, 1977.

[84] B.W. Pearce. “Ventilated Supercavitating Hydrofoils for Ride Control of High-Speed Craft”. PhD Thesis. Launceston, Australia: University of Tasmania, May 2011.

[85] R. Pinguet et al. “CFD analysis of added mass, damping and induced flow of isolated and cylinder-mounted heave plates at various submergence depths using an overset mesh method”. In: *Journal of Fluids and Structures* 109 (2022). ISSN: 0889-9746.

[86] Propulsion Committee of 23rd ITTC. *Testing and Extrapolation Methods Propulsion; Cavitation Description of Cavitation Appearances*. Recommended Procedures and Guidelines. International Towing Tank Conference (ITTC), 2002.

[87] S.S. Rao. *Mechanical Vibrations*. Fifth Edition. Pearson Education, 2011.

[88] D. Rijpkema, J. Baltazar, and J. Falcao de Campos. “Viscous flow simulations of propellers in different Reynolds number regimes”. In: *smp’15*. Fourth International Symposium on Marine Propulsors. Austin, Texas, USA, 2015.

[89] Samya. *Streamlines showing air moving around an airfoil*. URL: `https://stock.adobe.com/es/images/streamlines-showing-air-moving-around-an-airfoil-flow-past-a-wing-higher-and-lower-flow-velocity-vector-illustration-isolated-on-white-background/596926217?asset_id=596926217`.

[90] R.S. Solomon and R.P. Ravinder. “Bend-Twist Coupling and its Effect on Cavitation Inception of Composite Marine Propeller”. In: *International Journal of Mechanical Engineering and Technology* 5 (2014), pp. 306–314.

[91] R. Stigter. “Introduction to Cavitation Inception”. Lecture. MT44060: Advanced Course in Resistance and Propulsion. Delft, Netherlands, Mar. 20, 2024.

[92] H. Streckwall, L. Greitsch, and M. Scharf. “An advanced Scaling Procedure for Marine Propellers”. In: Third International Symposium on Marine Propulsors. Launceston, Australia, 2013.

[93] A.E. Tekkaya and C. Soyarslan. *Finite Element Method*. Springer Berlin Heidelberg, 2014.

[94] J. Tian et al. “Flow-induced vibration analysis of elastic propellers in a cyclic inflow: An experimental and numerical study”. In: *Applied Ocean Research* 65 (2017), pp. 47–59. ISSN: 0141-1187.

[95] Y. Tian and S. Kinnas. “Modeling of Leading Edge Vortex and its Effects on Propeller Performance”. In: *smp’11*. Second International Symposium on Marine Propulsors. 2011, 2011.

[96] J. Weersma. “A study on a new scaling approach for flexible marine propellers”. Definition study. Delft: Delft University of Technology, Mar. 2025.

[97] H.C.J. van Wijngaarden. *Performing Model Scale Testing on Composite Propellers*.

[98] H. K. Woud and D. Stapersma. *Design of Propulsion and Electric Power Generation Systems*. IMarEST, 2012. ISBN: 1-902536-47-9.

[99] D.F. Young et al. *A Brief Introduction to Fluid Mechanics*. Fifth Edition. John Wiley & Sons, Inc., 2011. ISBN: 978-0470-59679-1.

[100] Y.L. Young. “Dynamic hydroelastic scaling of self-adaptive composite marine rotors”. In: *Composite Structures* 92.1 (2010), pp. 97–106. ISSN: 0263-8223.

[101] Y.L. Young et al. “Adaptive Composite Marine Propulsors and Turbines: Progress and Challenges”. In: *Applied Mechanics Reviews* 68 (2016).

[102] O.C. Zienkiewicz, R.L. Taylor, and J.Z. Zhu. *The Finite Element Method: Its Basis and Fundamentals*. Sixth Edition. Elsevier, 2005.

A

Rigid Propeller Results for a Range of Reynolds Number

A.1. Percentage Difference Across Reynolds Numbers

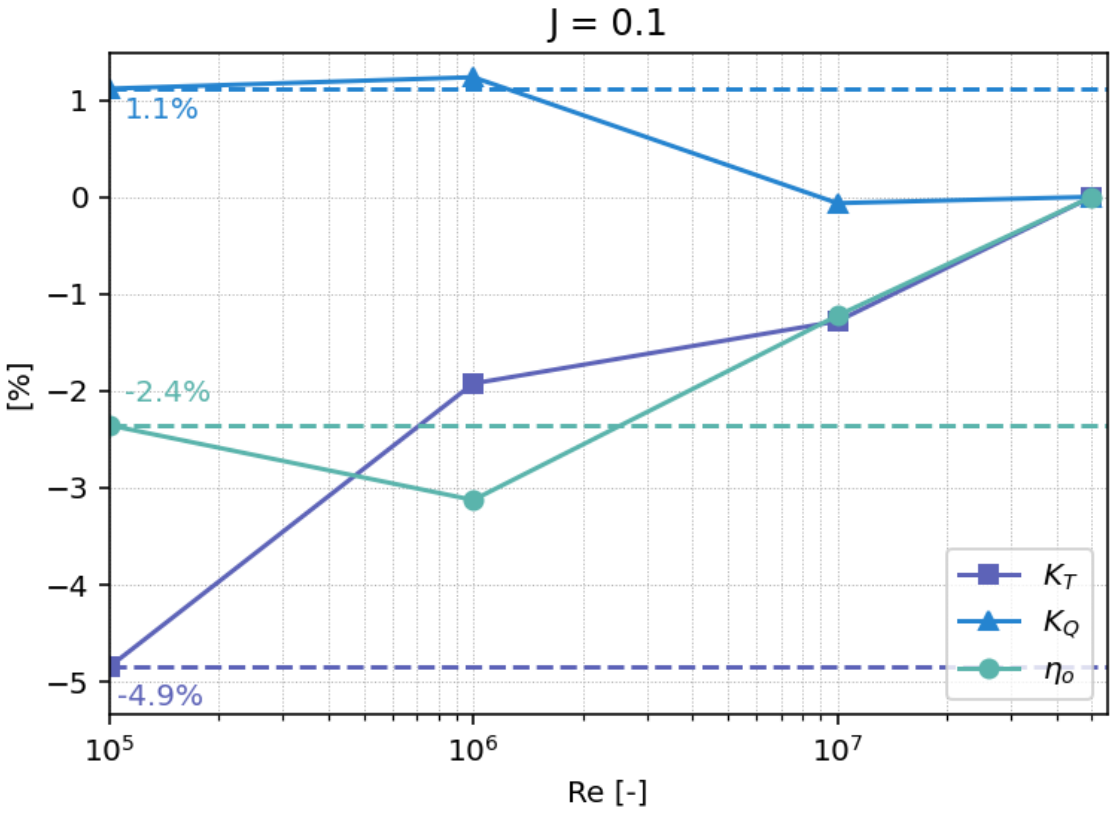

Figure A.1: The percentage difference across Reynolds numbers for K_T, K_Q and η_o for the rigid C4-40 propeller tested at an advance ratio of 0.1.

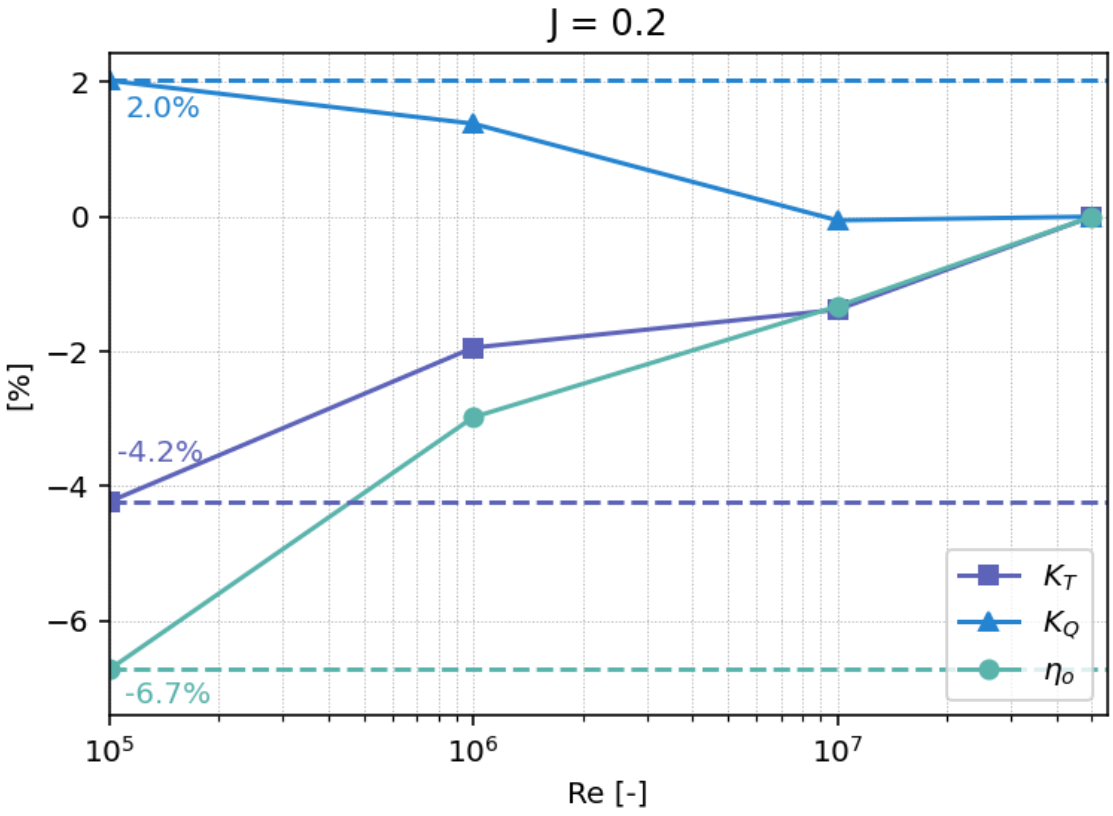

Figure A.2: The percentage difference across Reynolds numbers for K_T, K_Q and η_o for the rigid C4-40 propeller tested at an advance ratio of 0.2.

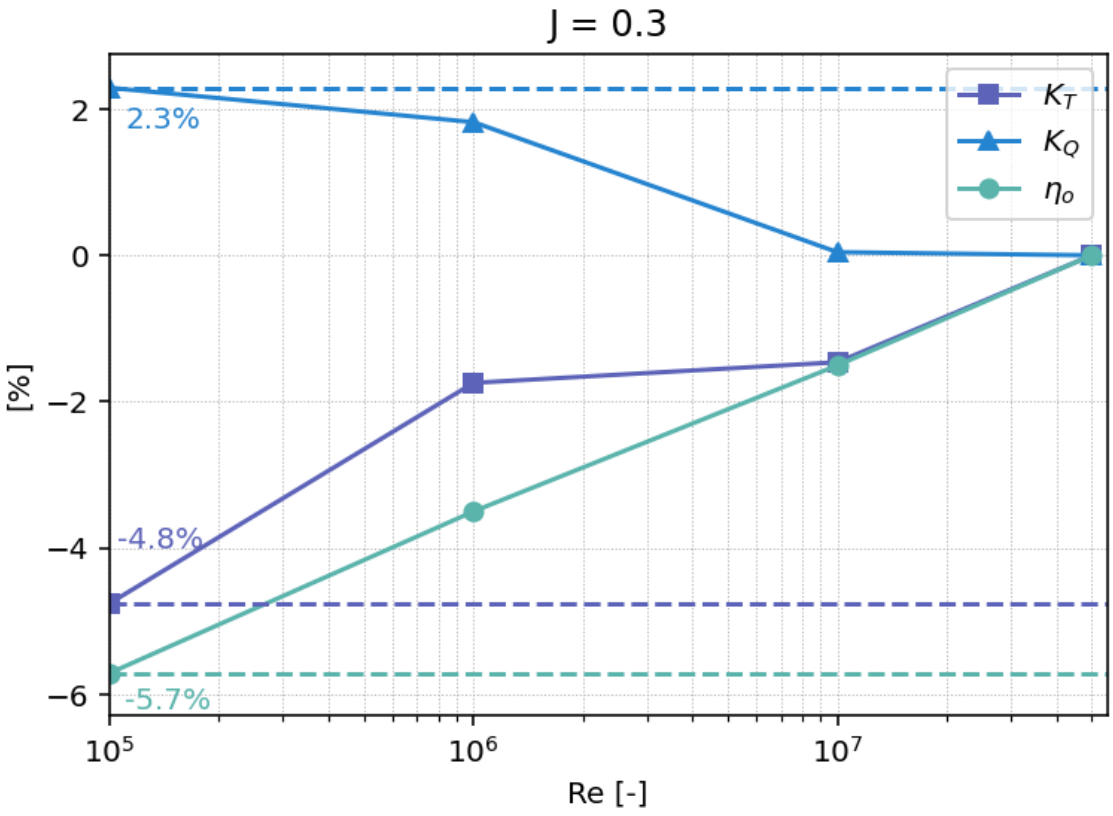

Figure A.3: The percentage difference across Reynolds numbers for K_T, K_Q and η_o for the rigid C4-40 propeller tested at an advance ratio of 0.3.

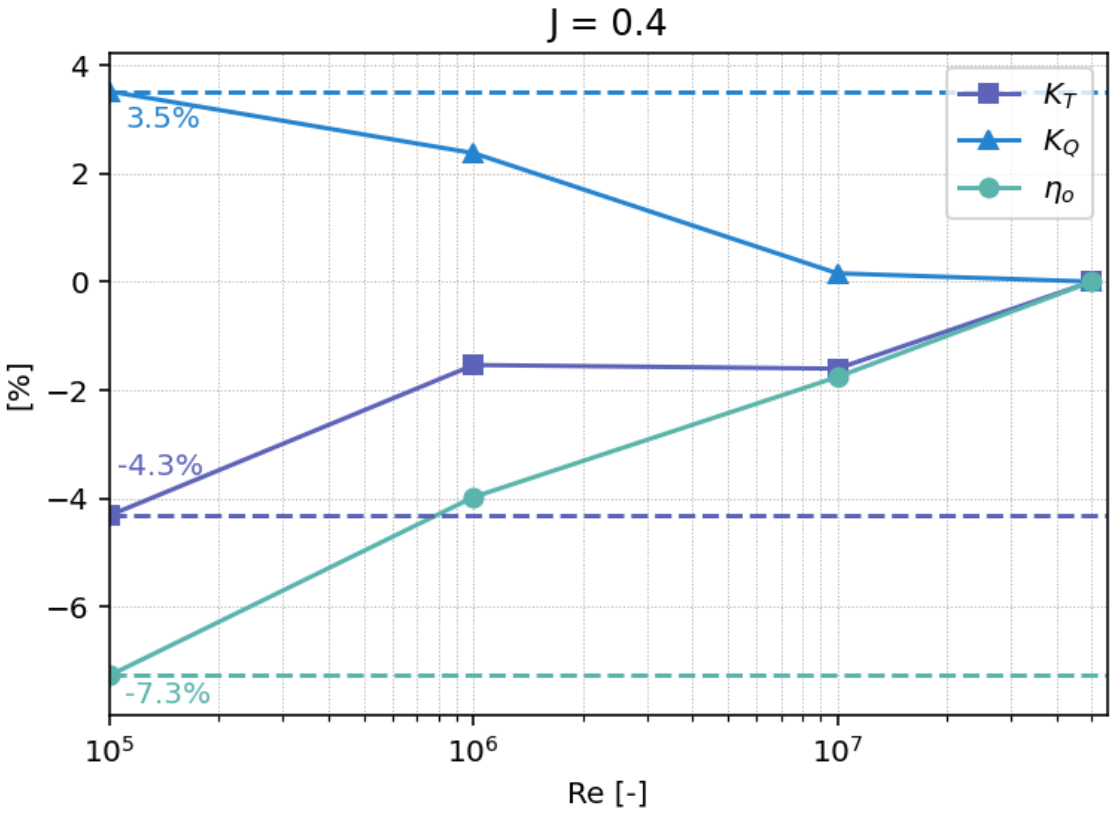

Figure A.4: The percentage difference across Reynolds numbers for K_T, K_Q and η_o for the rigid C4-40 propeller tested at an advance ratio of 0.4.

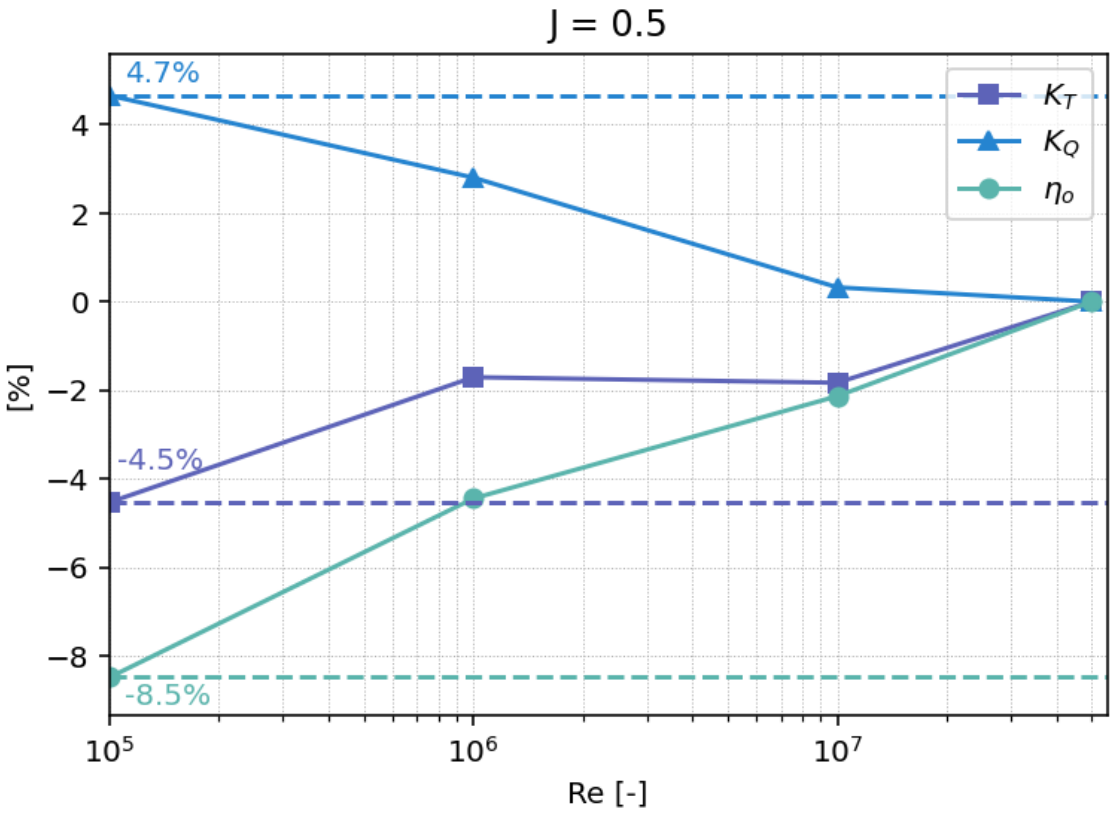

Figure A.5: The percentage difference across Reynolds numbers for K_T, K_Q and η_o for the rigid C4-40 propeller tested at an advance ratio of 0.5.

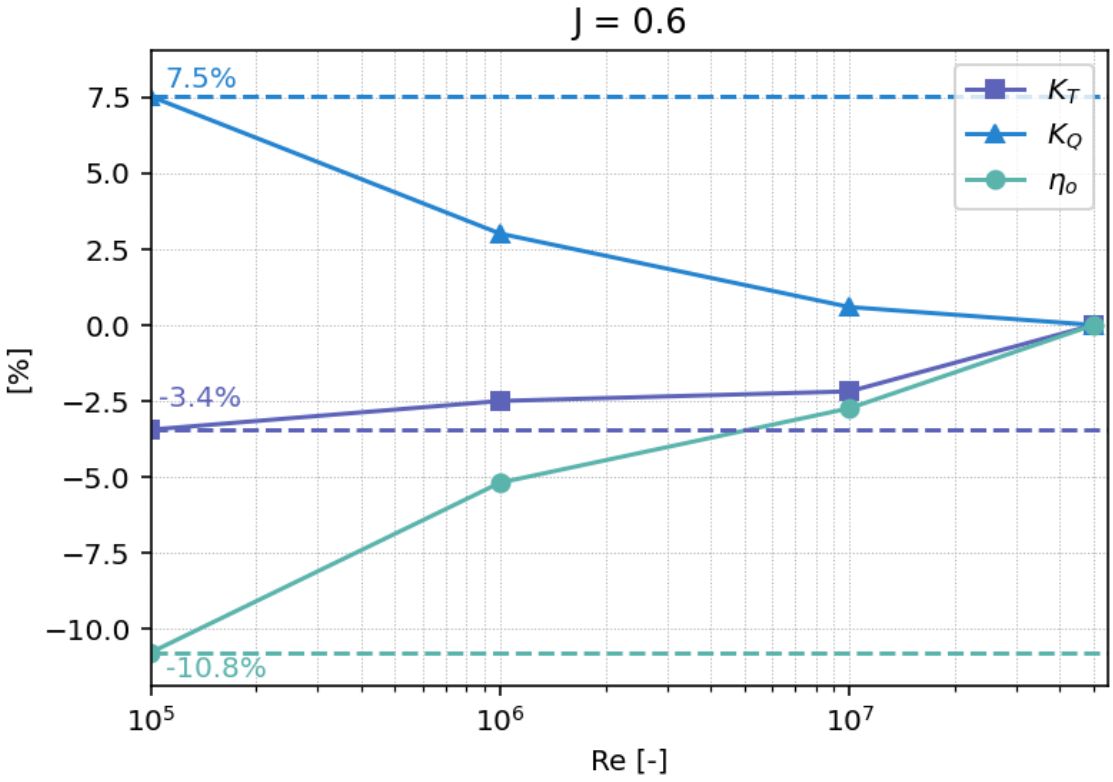

Figure A.6: The percentage difference across Reynolds numbers for K_T, K_Q and η_o for the rigid C4-40 propeller tested at an advance ratio of 0.6.

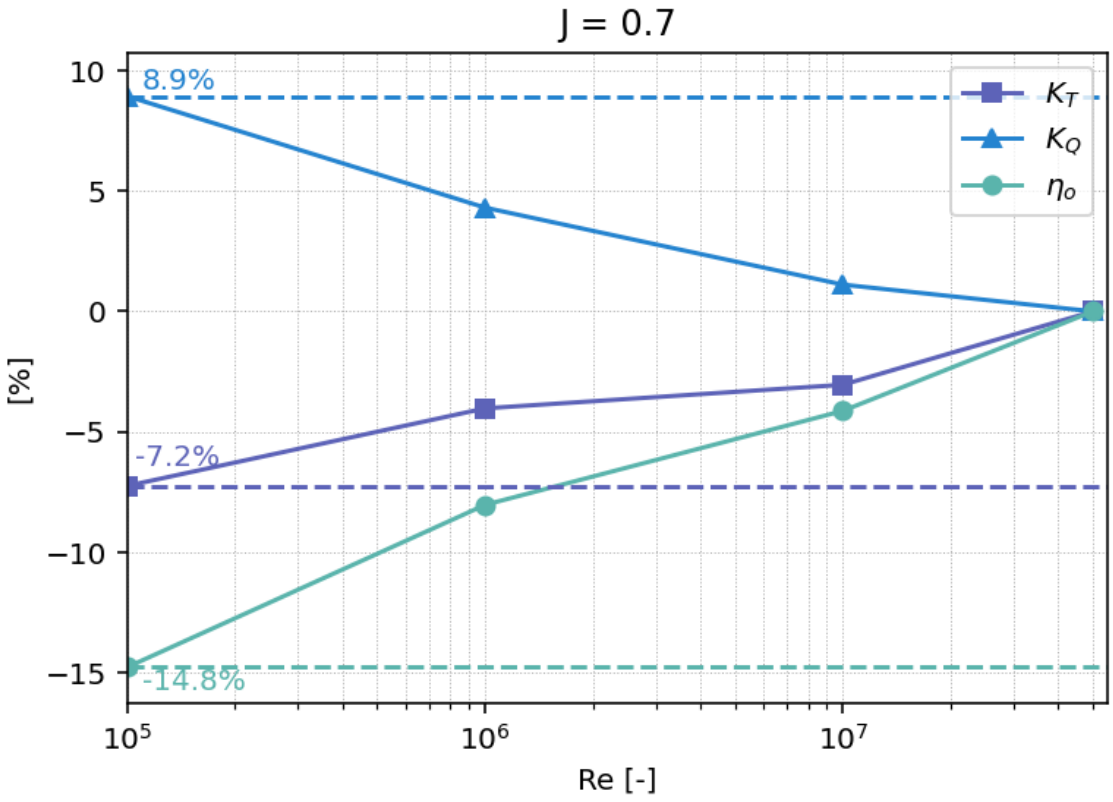

Figure A.7: The percentage difference across Reynolds numbers for K_T, K_Q and η_o for the rigid C4-40 propeller tested at an advance ratio of 0.7.

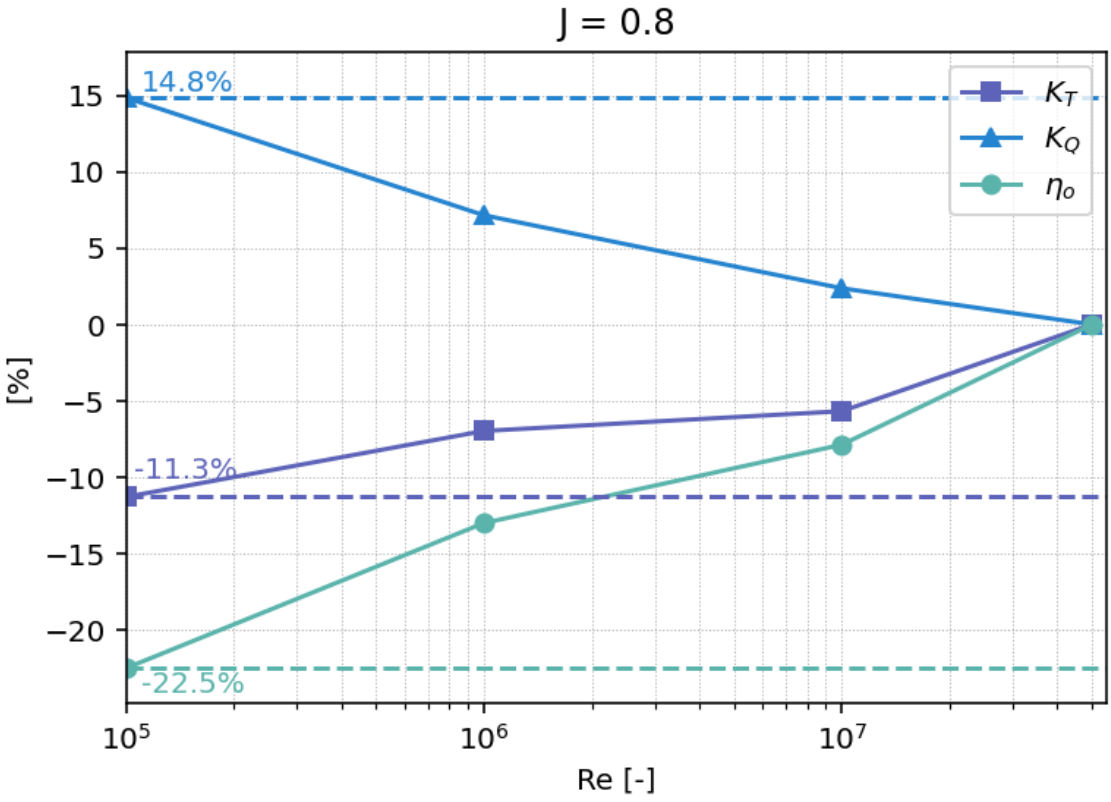

Figure A.8: The percentage difference across Reynolds numbers for K_T, K_Q and η_o for the rigid C4-40 propeller tested at an advance ratio of 0.8.

A.2. Streamlines and Skin Friction Coefficient

J-Value of 0.1

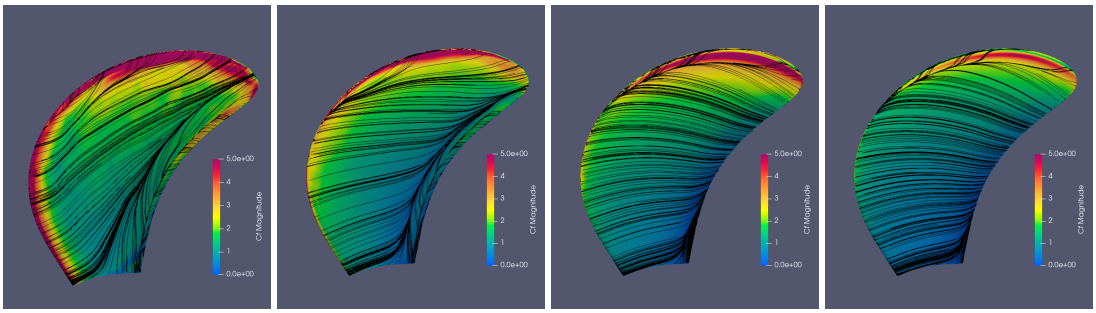

(a) $Re = 1 * 10^5$ **(b)** $Re = 1 * 10^6$ **(c)** $Re = 1 * 10^7$ **(d)** $Re = 5 * 10^7$

Figure A.9: Streamlines and Skin Friction coefficient on the suction side of the rigid C4-40 propeller blade tested at a J of 0.1.

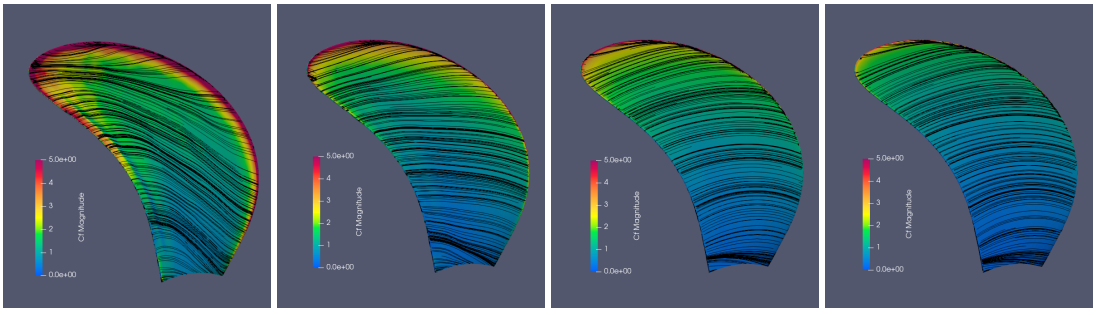

(a) $Re = 1 * 10^5$ **(b)** $Re = 1 * 10^6$ **(c)** $Re = 1 * 10^7$ **(d)** $Re = 5 * 10^7$

Figure A.10: Streamlines and skin friction coefficient on the pressure side of the rigid C4-40 propeller blade tested at a J of 0.1.

J-Value of 0.2

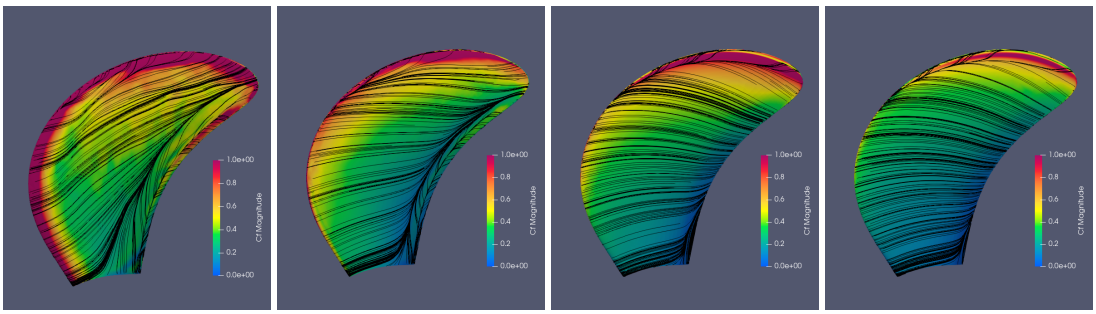

(a) $Re = 1 * 10^5$ **(b)** $Re = 1 * 10^6$ **(c)** $Re = 1 * 10^7$ **(d)** $Re = 5 * 10^7$

Figure A.11: Streamlines and Skin Friction coefficient on the suction side of the rigid C4-40 propeller blade tested at a J of 0.2.

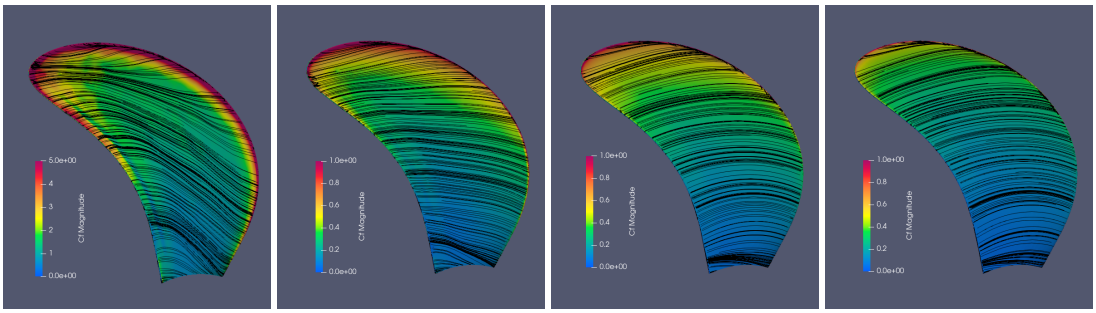

(a) $Re = 1 * 10^5$ **(b)** $Re = 1 * 10^6$ **(c)** $Re = 1 * 10^7$ **(d)** $Re = 5 * 10^7$

Figure A.12: Streamlines and skin friction coefficient on the pressure side of the rigid C4-40 propeller blade tested at a J of 0.2.

J-Value of 0.3

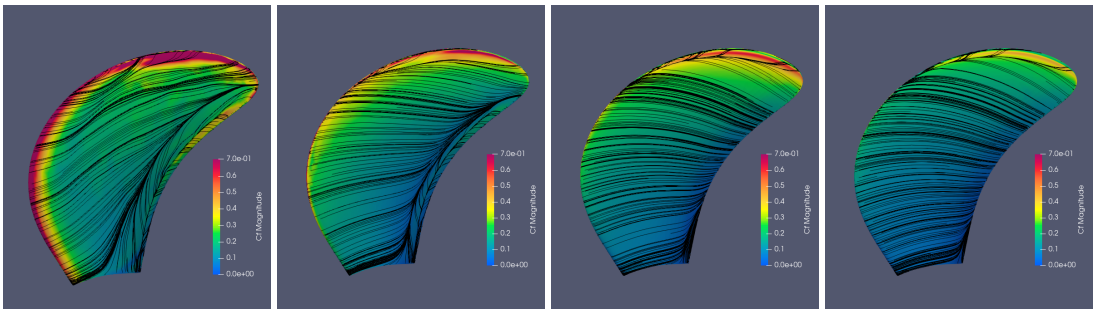

(a) $Re = 1 * 10^5$ **(b)** $Re = 1 * 10^6$ **(c)** $Re = 1 * 10^7$ **(d)** $Re = 5 * 10^7$

Figure A.13: Streamlines and Skin Friction coefficient on the suction side of the rigid C4-40 propeller blade tested at a J of 0.3.

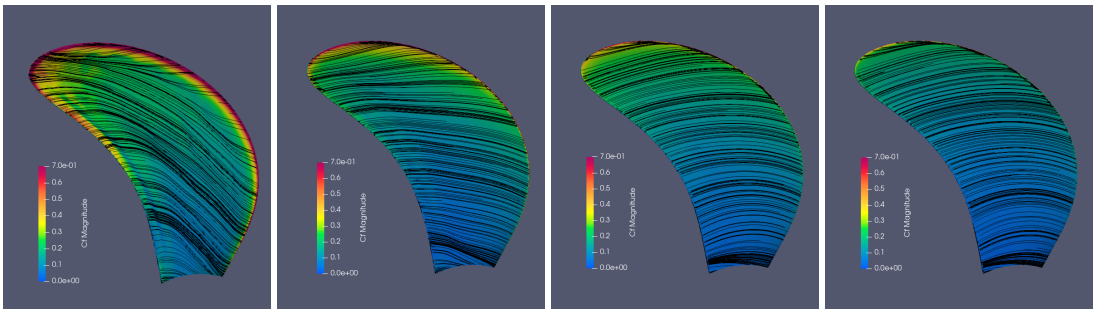

(a) $Re = 1 * 10^5$ **(b)** $Re = 1 * 10^6$ **(c)** $Re = 1 * 10^7$ **(d)** $Re = 5 * 10^7$

Figure A.14: Streamlines and skin friction coefficient on the pressure side of the rigid C4-40 propeller blade tested at a J of 0.3.

J-Value of 0.4

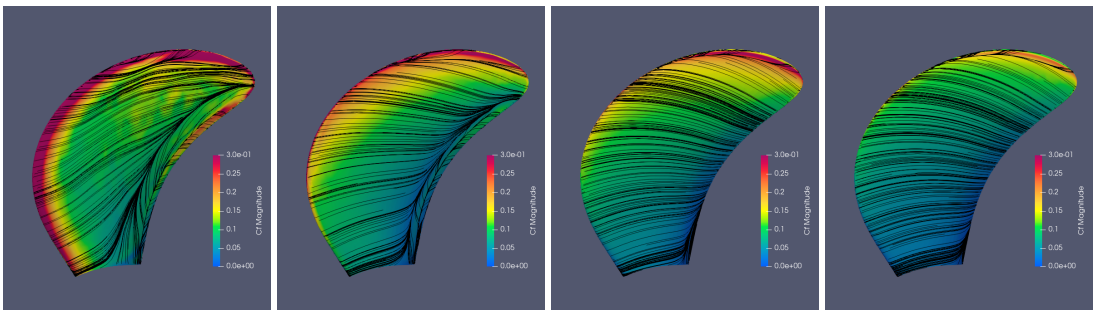

(a) $Re = 1 * 10^5$ **(b)** $Re = 1 * 10^6$ **(c)** $Re = 1 * 10^7$ **(d)** $Re = 5 * 10^7$

Figure A.15: Streamlines and Skin Friction coefficient on the suction side of the rigid C4-40 propeller blade tested at a J of 0.4.

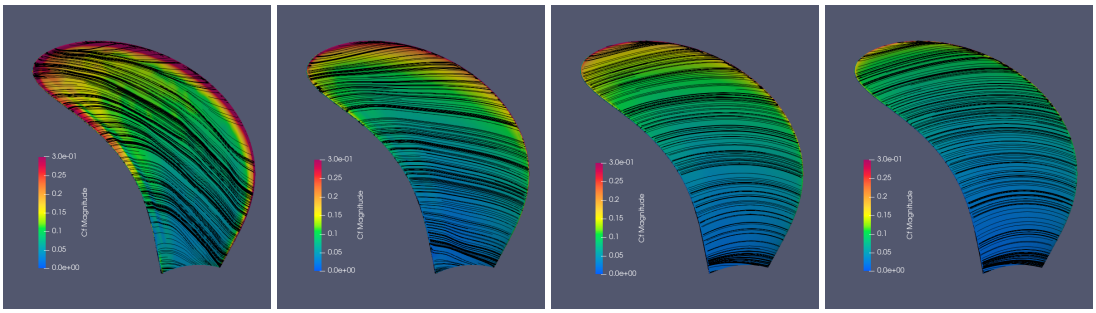

(a) $Re = 1 * 10^5$ **(b)** $Re = 1 * 10^6$ **(c)** $Re = 1 * 10^7$ **(d)** $Re = 5 * 10^7$

Figure A.16: Streamlines and skin friction coefficient on the pressure side of the rigid C4-40 propeller blade tested at a J of 0.4.

J-Value of 0.5

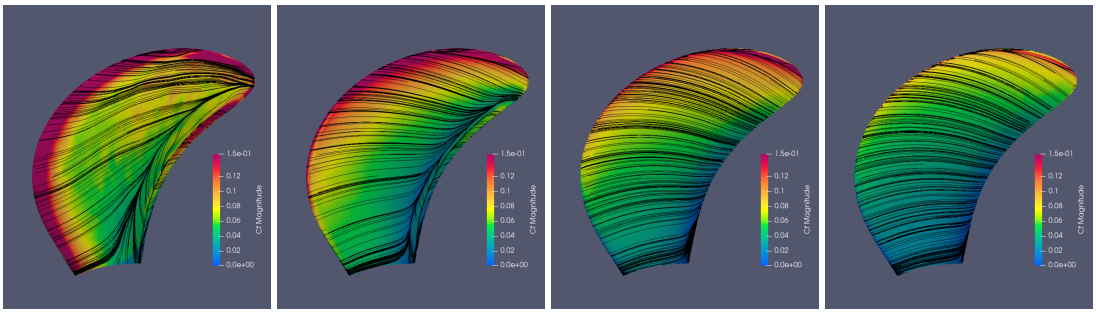

(a) $Re = 1 * 10^5$ **(b)** $Re = 1 * 10^6$ **(c)** $Re = 1 * 10^7$ **(d)** $Re = 5 * 10^7$

Figure A.17: Streamlines and Skin Friction coefficient on the suction side of the rigid C4-40 propeller blade tested at a J of 0.5.

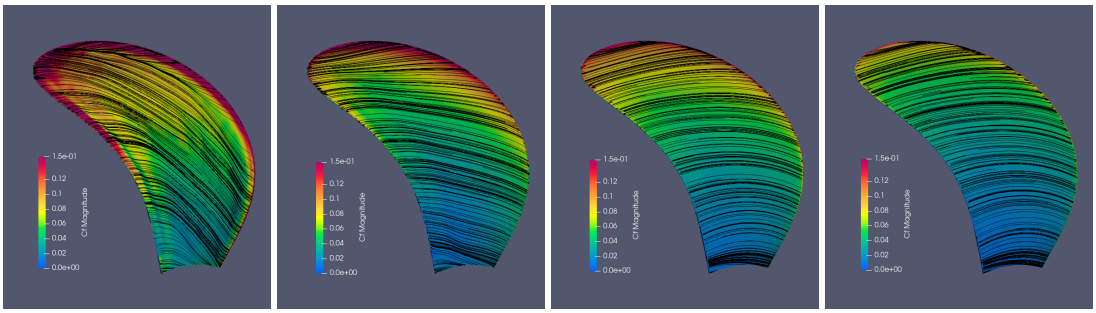

(a) $Re = 1 * 10^5$ **(b)** $Re = 1 * 10^6$ **(c)** $Re = 1 * 10^7$ **(d)** $Re = 5 * 10^7$

Figure A.18: Streamlines and skin friction coefficient on the pressure side of the rigid C4-40 propeller blade tested at a J of 0.5.

J-Value of 0.6

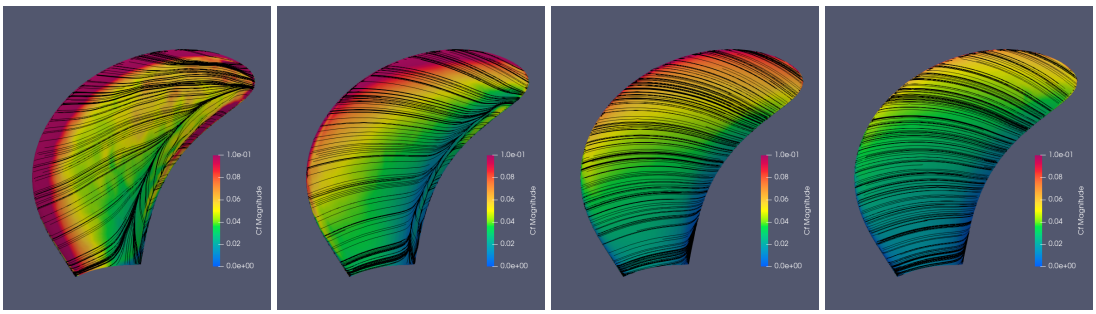

(a) $Re = 1 * 10^5$ **(b)** $Re = 1 * 10^6$ **(c)** $Re = 1 * 10^7$ **(d)** $Re = 5 * 10^7$

Figure A.19: Streamlines and Skin Friction coefficient on the suction side of the rigid C4-40 propeller blade tested at a J of 0.6.

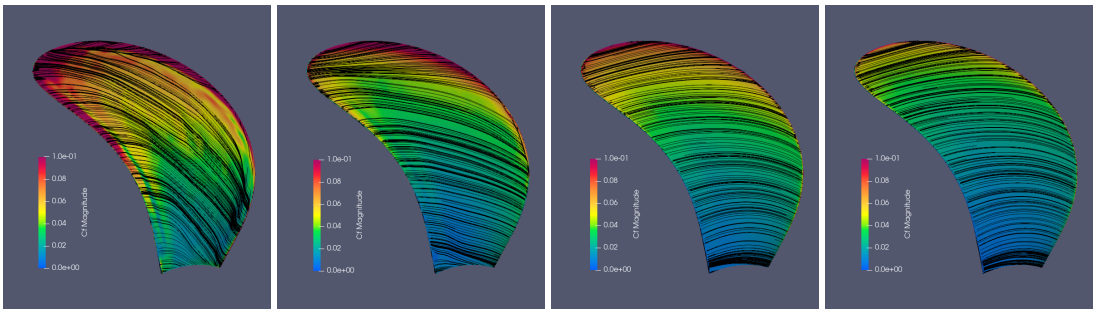

(a) $Re = 1 * 10^5$ **(b)** $Re = 1 * 10^6$ **(c)** $Re = 1 * 10^7$ **(d)** $Re = 5 * 10^7$

Figure A.20: Streamlines and skin friction coefficient on the pressure side of the rigid C4-40 propeller blade tested at a J of 0.6.

J-Value of 0.7

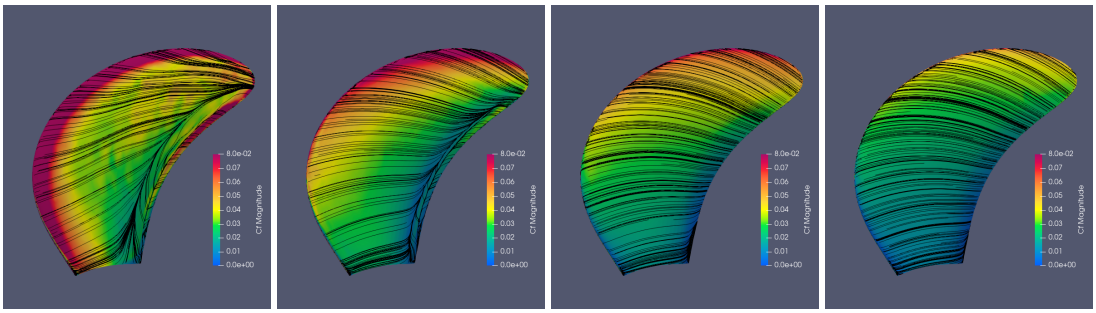

(a) $Re = 1 * 10^5$ **(b)** $Re = 1 * 10^6$ **(c)** $Re = 1 * 10^7$ **(d)** $Re = 5 * 10^7$

Figure A.21: Streamlines and Skin Friction coefficient on the suction side of the rigid C4-40 propeller blade tested at a J of 0.7.

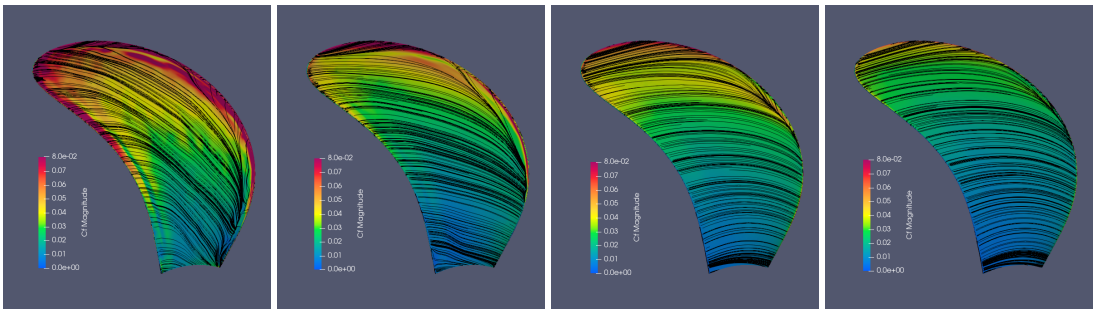

(a) $Re = 1 * 10^5$ **(b)** $Re = 1 * 10^6$ **(c)** $Re = 1 * 10^7$ **(d)** $Re = 5 * 10^7$

Figure A.22: Streamlines and skin friction coefficient on the pressure side of the rigid C4-40 propeller blade tested at a J of 0.7.

J-Value of 0.8

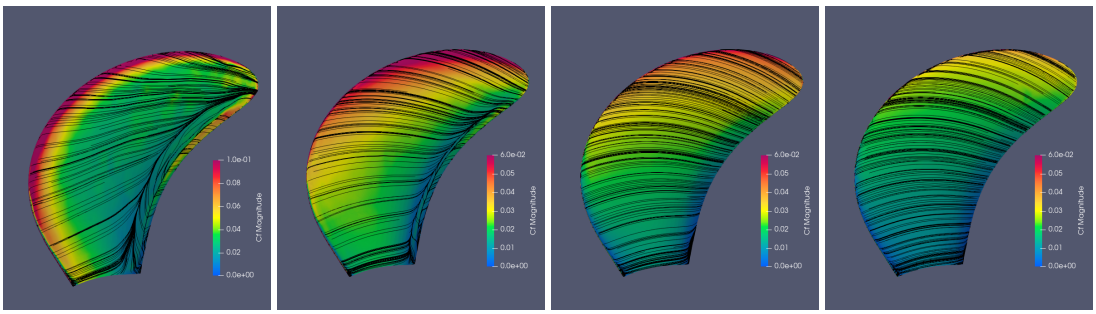

(a) $Re = 1 * 10^5$ **(b)** $Re = 1 * 10^6$ **(c)** $Re = 1 * 10^7$ **(d)** $Re = 5 * 10^7$

Figure A.23: Streamlines and Skin Friction coefficient on the suction side of the rigid C4-40 propeller blade tested at a J of 0.8.

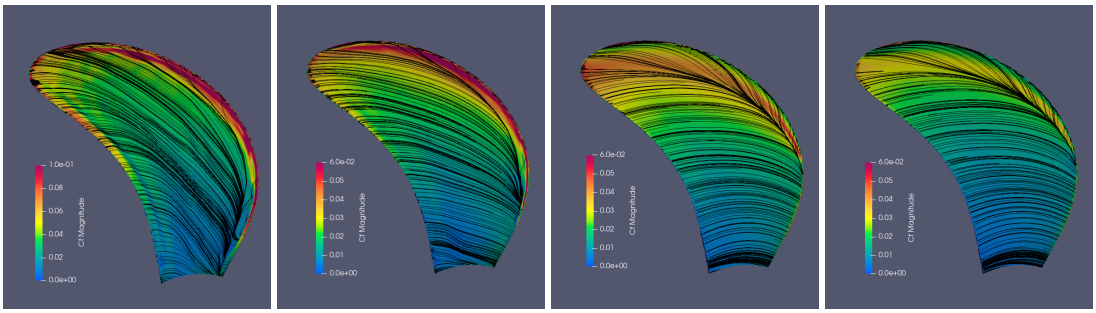

(a) $Re = 1 * 10^5$ **(b)** $Re = 1 * 10^6$ **(c)** $Re = 1 * 10^7$ **(d)** $Re = 5 * 10^7$

Figure A.24: Streamlines and skin friction coefficient on the pressure side of the rigid C4-40 propeller blade tested at a J of 0.8.

A.3. Thrust Coefficient Convergence

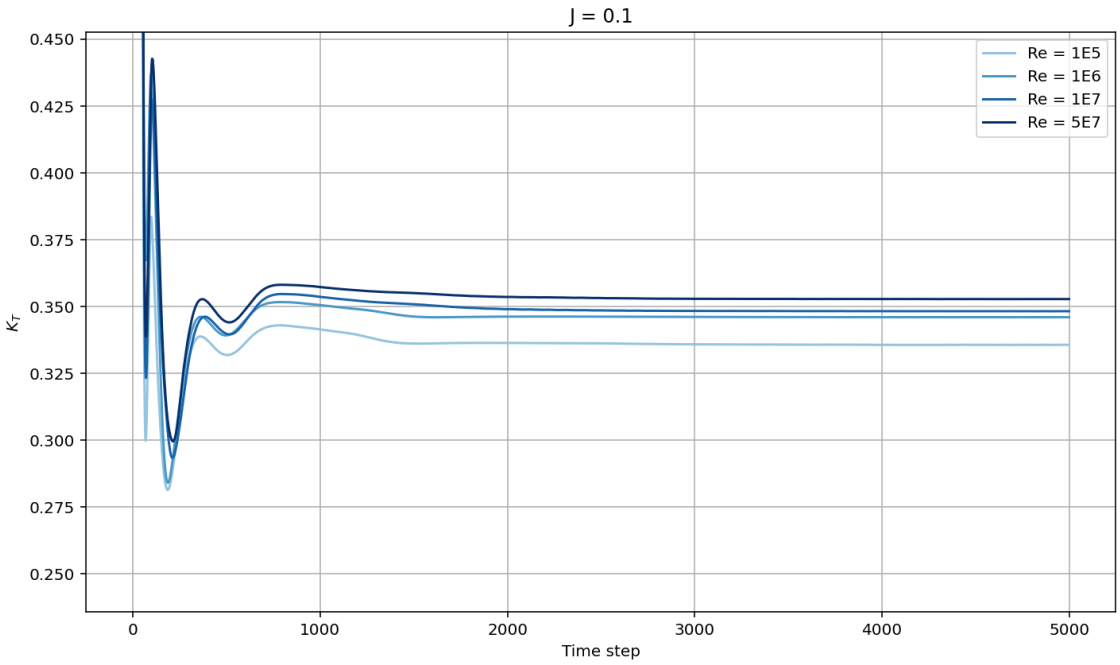

Figure A.25: The thrust coefficient over time for J equals 0.1, plotted for the rigid Wagningen C4-40 propeller with a pitch ratio of 0.8 for the range of Reynolds numbers. The plot demonstrates a convergence solution in each case.

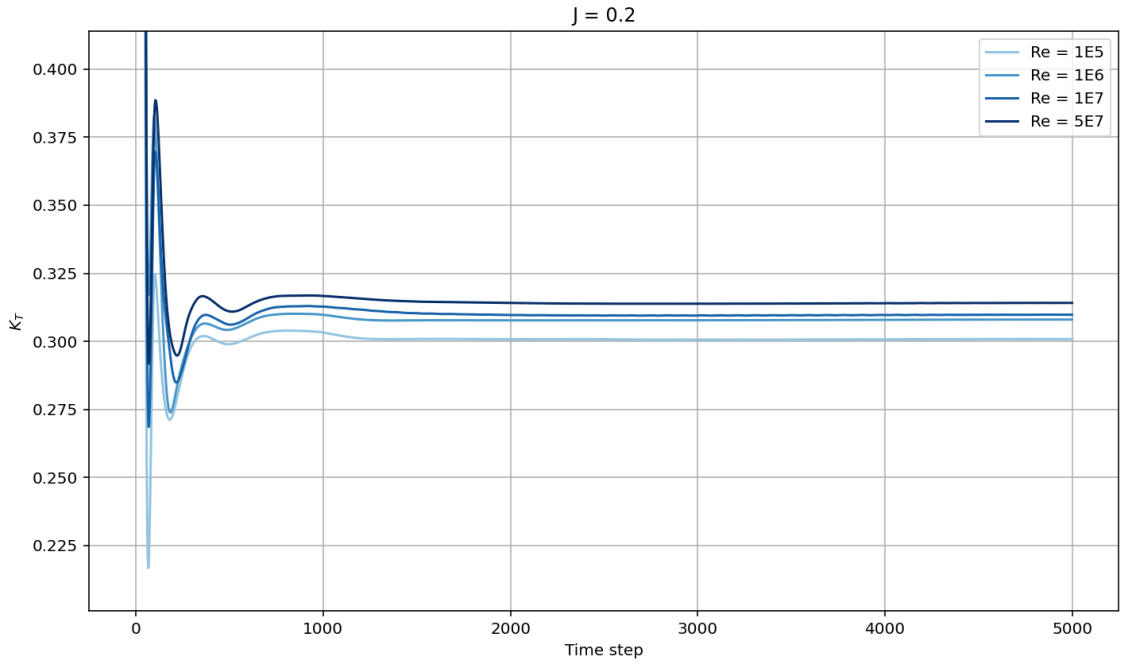

Figure A.26: The thrust coefficient over time for J equals 0.2, plotted for the rigid Wagningen C4-40 propeller with a pitch ratio of 0.8 for the range of Reynolds numbers. The plot demonstrates a convergence solution in each case.

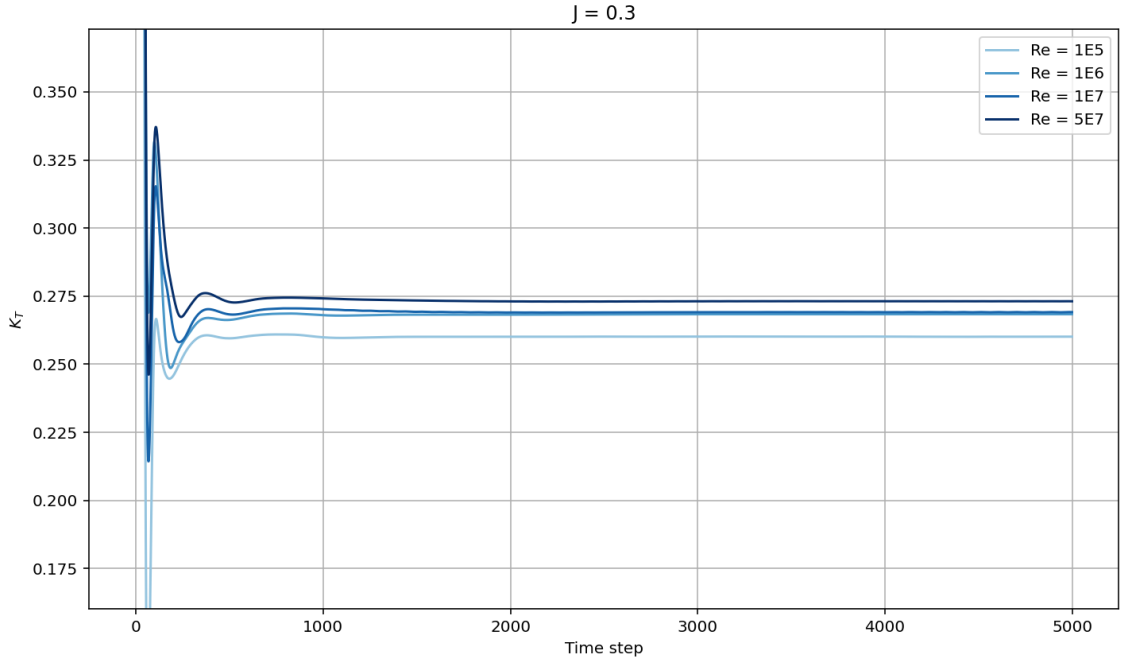

Figure A.27: The thrust coefficient over time for J equals 0.3, plotted for the rigid Wagningen C4-40 propeller with a pitch ratio of 0.8 for the range of Reynolds numbers. The plot demonstrates a convergence solution in each case.

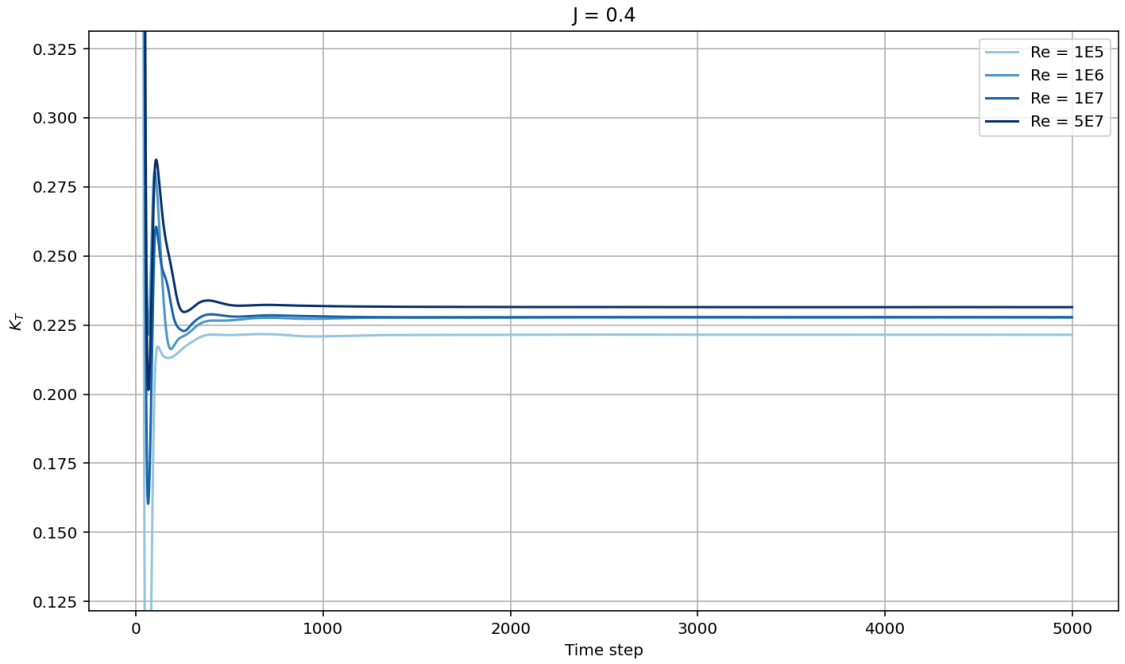

Figure A.28: The thrust coefficient over time for J equals 0.4, plotted for the rigid Wagningen C4-40 propeller with a pitch ratio of 0.8 for the range of Reynolds numbers. The plot demonstrates a convergence solution in each case.

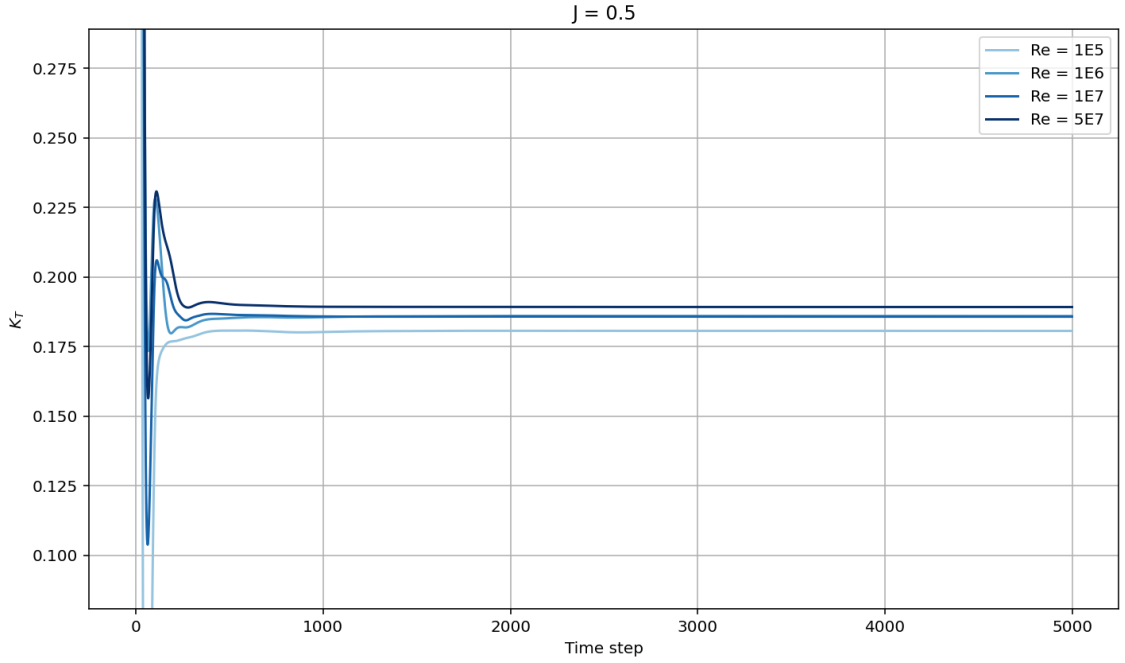

Figure A.29: The thrust coefficient over time for J equals 0.5, plotted for the rigid Wagningen C4-40 propeller with a pitch ratio of 0.8 for the range of Reynolds numbers. The plot demonstrates a convergence solution in each case.

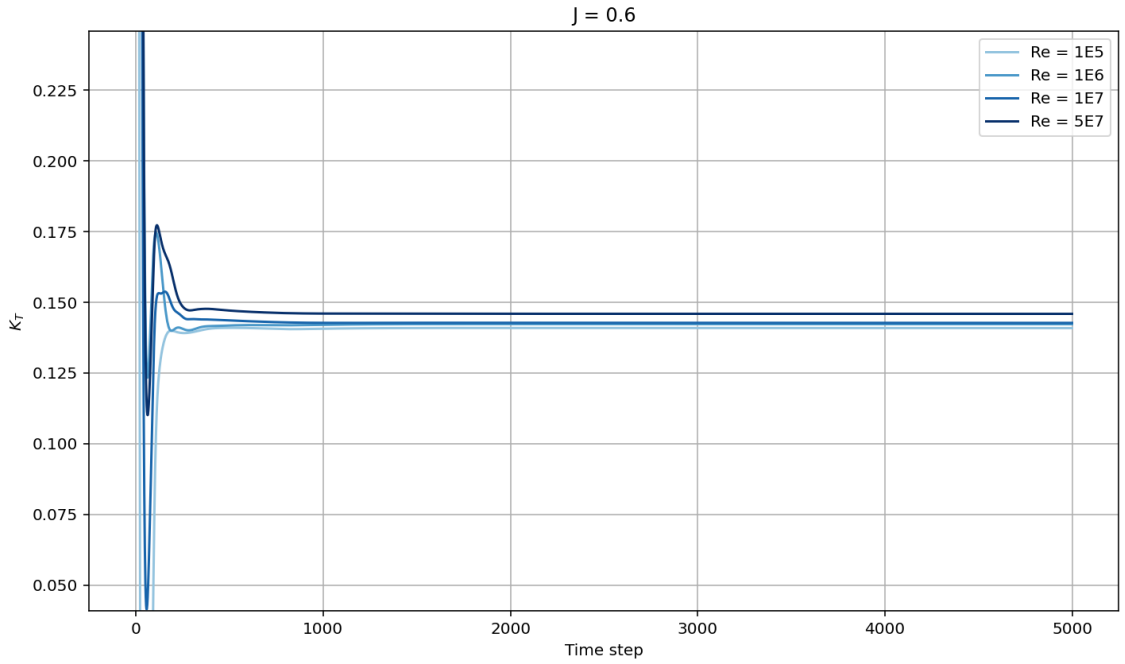

Figure A.30: The thrust coefficient over time for J equals 0.6, plotted for the rigid Wagningen C4-40 propeller with a pitch ratio of 0.8 for the range of Reynolds numbers. The plot demonstrates a convergence solution in each case.

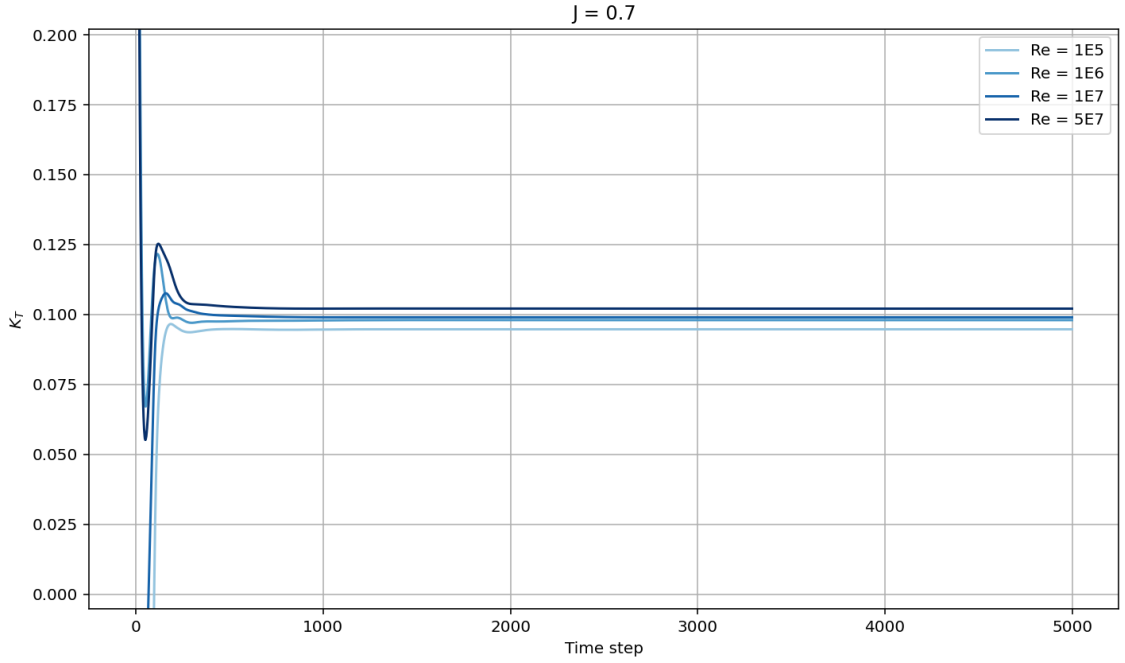

Figure A.31: The thrust coefficient over time for J equals 0.7, plotted for the rigid Wagningen C4-40 propeller with a pitch ratio of 0.8 for the range of Reynolds numbers. The plot demonstrates a convergence solution in each case.

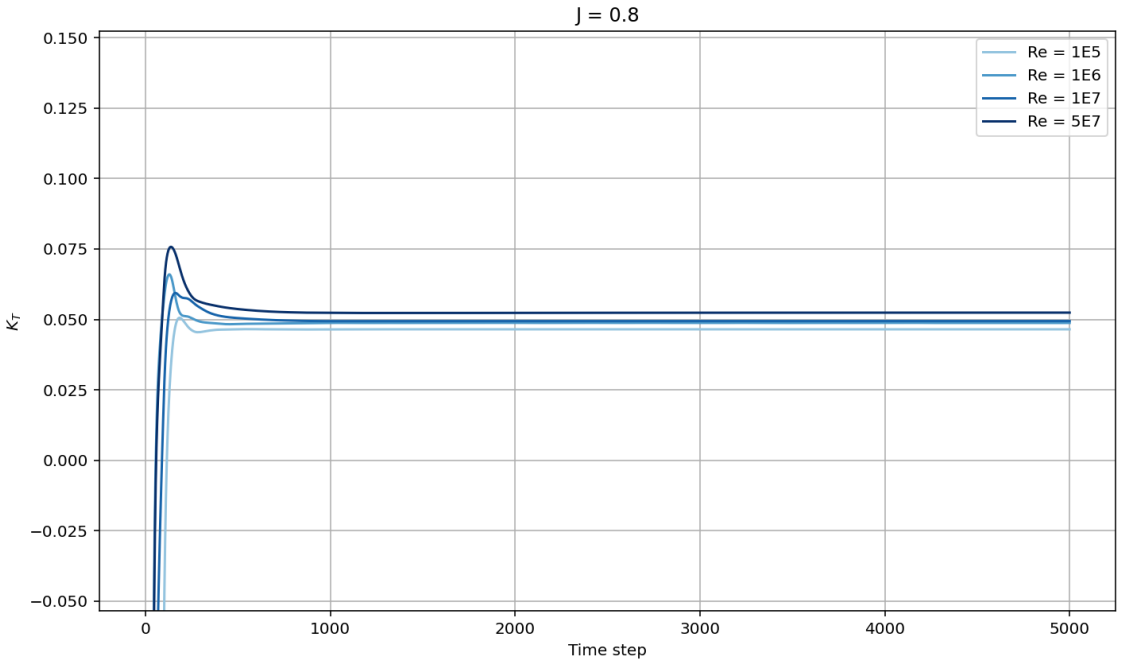

Figure A.32: The thrust coefficient over time for J equals 0.8, plotted for the rigid Wagningen C4-40 propeller with a pitch ratio of 0.8 for the range of Reynolds numbers. The plot demonstrates a convergence solution in each case.

B

Derivation of the Scaling Relations for Froude Similarity, Reynolds Similarity, and Mach Similarity

Model and scale effects can be avoided by satisfying all similarity laws. The similarity laws are defined using non-dimensional parameters. Most model tests use Froude similarity, Reynolds similarity or Mach similarity. The scaling factors for all relevant quantities are then derived from these non-dimensional numbers [51]. Complete geometric similarity is assumed in all cases, with the model length scale defined as:

$$L_M = \frac{1}{\lambda} L_F \tag{B.1}$$

The fluid properties—such as density, viscosity, speed of sound, and saturated vapour pressure—are considered comparable between freshwater and seawater. Hence, these properties are assumed equal between the model and full scale when deriving the scaling factors. Furthermore, the gravitational constant is equal for both the model and the full scale. The derivation of the scaling factors for the variables given in Table 6.1 are demonstrated in this Chapter.

Velocity scaling

To achieve Froude similarity, the velocity is calculated based on the definition of the Froude number, $Fr = V_a/\sqrt{gD}$:

$$Fn_M = Fn_F \tag{B.2}$$

$$\frac{V_{a_F}}{\sqrt{gD_F}} = \frac{V_{a_M}}{\sqrt{gD_M}} \Leftrightarrow \frac{V_{a_m}}{V_{a_f}} = \frac{\sqrt{gD_M}}{\sqrt{gD_F}} = \frac{\sqrt{\frac{1}{\lambda}D_F}}{\sqrt{D_F}} \tag{B.3}$$

For Froude similarity, the velocities are scaled as:

$$V_{a_M} = \sqrt{\frac{1}{\lambda}} V_{a_F} \tag{B.4}$$

The velocity scale for Reynolds similarity is obtained using the definition of the Reynolds number, $Re = \rho V_a D/\mu$:

$$Re_M = Re_F \tag{B.5}$$

$$\frac{\rho_M V_{a_M} L_M}{\mu_M} = \frac{\rho_F V_{a_F} L_F}{\mu_F} \Leftrightarrow \frac{V_{a_M}}{V_{a_F}} = \frac{L_F}{L_M} = \frac{L_F}{\frac{1}{\lambda} L_F} \tag{B.6}$$

The velocities for Reynolds similarity scale as:

$$V_{a_M} = \lambda V_{a_F} \tag{B.7}$$

In the case of Mach similarity, the velocity scale is determined from the definition of the Mach number, $Ma = V_a/c_s$:

$$Ma_M = Ma_F \tag{B.8}$$

$$\frac{V_{a_M}}{c_s} = \frac{V_{a_F}}{c_s} \Leftrightarrow \frac{V_{a_M}}{V_{a_F}} = \frac{c_s}{c_s} \tag{B.9}$$

So, the velocities for Mach similarity scale as:

$$V_{a_M} = V_{a_F} \tag{B.10}$$

Time scaling
Time scaling can be derived from the scaling of length and velocity.

$$L = UT \Leftrightarrow T = L/U$$

Thus, for Froude similarity, time will scale as:

$$T_M = \sqrt{\frac{1}{\lambda}} T_F \tag{B.11}$$

In the case of Reynolds similarity, time will scale as:

$$T_M = \frac{1}{\lambda^2} T_F \tag{B.12}$$

And for the Mach similarity, time will scale as:

$$T_M = \frac{1}{\lambda} T_F \tag{B.13}$$

Frequency scaling
The unit of frequency is $\left[\frac{1}{T}\right]$. Therefore, for Froude similarity, frequency will scale as:

$$\omega_M = \sqrt{\lambda}\omega_F \tag{B.14}$$

For Reynolds similarity, frequency will scale as:

$$\omega_M = \lambda^2 \omega_F \tag{B.15}$$

And in the case of Mach similarity, frequency will scale as:

$$\omega_M = \lambda \omega_F \tag{B.16}$$

Elastic modulus scaling
The Cauchy number represents the relationship between Young's modulus and inertial force. The Young's modulus can be scaled using its definition: $Ca = E/\rho U^2$.

This leads to:

$$Ca_M = Ca_F \tag{B.17}$$

$$\frac{E_F}{\rho U_F^2} = \frac{E_M}{\rho U_M^2} \Leftrightarrow \frac{E_M}{E_F} = \frac{U_M^2}{U_F^2} \tag{B.18}$$

So, the elastic modulus for Froude similarity scale as:

$$E_M = \frac{1}{\lambda} E_F \tag{B.19}$$

For Reynolds similarity, the elastic modulus will scale as:

$$E_M = \lambda^2 E_F \tag{B.20}$$

And in the case of Mach similarity, the elastic modulus scale as:

$$E_M = E_F \tag{B.21}$$

Force scaling

Two systems are dynamically similar if there is similarity of masses and forces. The forces on a systems element in fluid mechanics problems consist of (hydrodynamic) inertia, gravity, viscous, surface tension, elastic compression and pressure forces. The hydrodynamic inertial force is proportional to $\rho_f n^2 D^4$. The propeller centripetal forces are proportional to mass and centripetal acceleration, hence, $\rho_s n^2 D^4$. The propeller elastic deflection scales as $w_{load} l^3/EI$. The load w_{load} is proportional to $\rho_f n^2 D^4$, l to D and I to D^4. So, the elastic bending force is proportional to ED^2. When considering the torsional deflection force, the shear modulus replaces the Young's modulus. Because the shear modulus and Young's modulus have to scale equal, an additional requirement is that the Poisson's ratio for the model and full scale are equal. Scaling all forces is impossible when comparing model-scale and full-scale models. However, one or more forces may not contribute to the flow phenomenon under consideration. Others may have only a slight effect or be related to the most significant force. Therefore, scale model tests simulate a particular state of fluid motion by considering that either gravity or viscous forces predominate. Since inertial reaction is always present in the flow phenomenon, it follows that inertial forces must be considered in any particular flow situation [36]. The following forces scale as:

$$\begin{aligned}
F_H &\propto \rho_f n^2 D^4 && \text{(Hydrodynamic inertial force)} \\
F_i &\propto \rho_s n^2 D^4 && \text{(Structural inertial force)} \\
F_g &\propto g\rho_s D^3 && \text{(Gravitational force)} \\
F_e &\propto ED^2 && \text{(Elastic force)} \\
F_\mu &\propto \mu U D && \text{(Viscous force)} \\
F_{st} &\propto \sigma D && \text{(Surface tension force)} \\
F_{pr} &\propto PD^2 && \text{(Pressure force)}
\end{aligned} \tag{B.22}$$

Table 6.1 presents a summary of the scaling relations for Froude number, Reynolds number, and Mach number similarity.

C

Flexible Marine Propellers Results using Cauchy Number-

C.1. Flexible Propeller Deformation

J-Value of 0.1

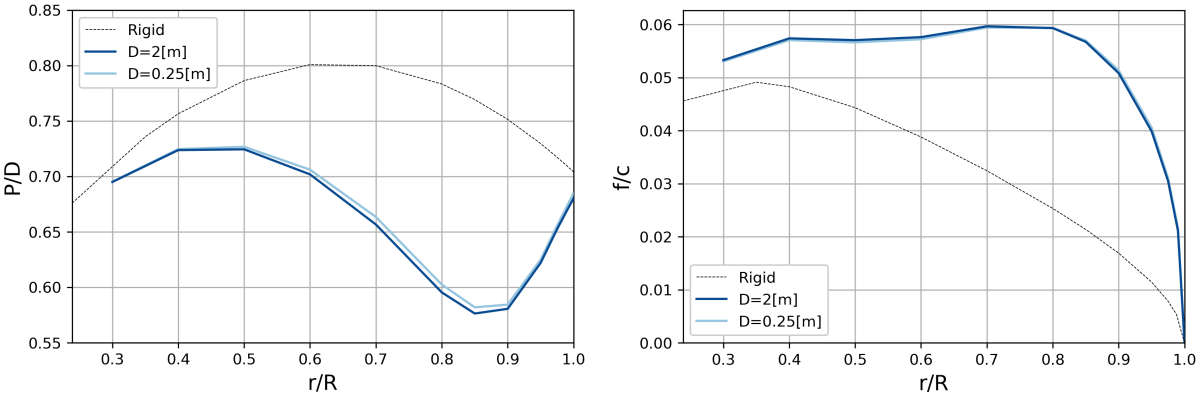

(a) Radial plot depicting the pitch deformation of both propellers, including the rigid C4-40 pitch ratio.

(b) Radial plot depicting the camber deformation of both propellers, including the rigid C4-40 pitch ratio.

Figure C.1: Radial plots depicting the deformation of both the 2-meter diameter propeller and the 0.25-meter diameter propeller, including the rigid C4-40 pitch ratio for J equals 0.1.

J-Value of 0.2

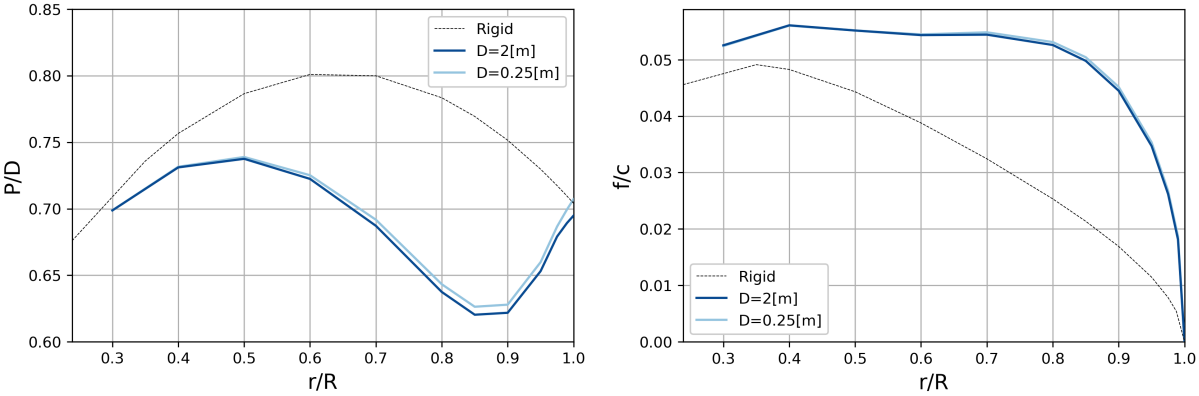

(a) Radial plot depicting the pitch deformation of both propellers, including the rigid C4-40 pitch ratio.

(b) Radial plot depicting the camber deformation of both propellers, including the rigid C4-40 pitch ratio.

Figure C.2: Radial plots depicting the deformation of both the 2-meter diameter propeller and the 0.25-meter diameter propeller, including the rigid C4-40 pitch ratio for J equals 0.2.

J-Value of 0.3

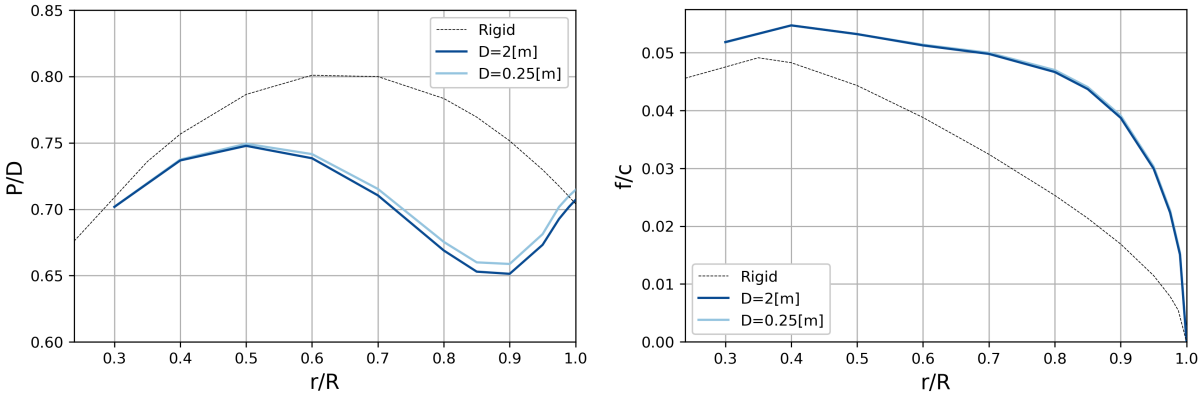

(a) Radial plot depicting the pitch deformation of both propellers, including the rigid C4-40 pitch ratio.

(b) Radial plot depicting the camber deformation of both propellers, including the rigid C4-40 pitch ratio.

Figure C.3: Radial plots depicting the deformation of both the 2-meter diameter propeller and the 0.25-meter diameter propeller, including the rigid C4-40 pitch ratio for J equals 0.3.

J-Value of 0.4

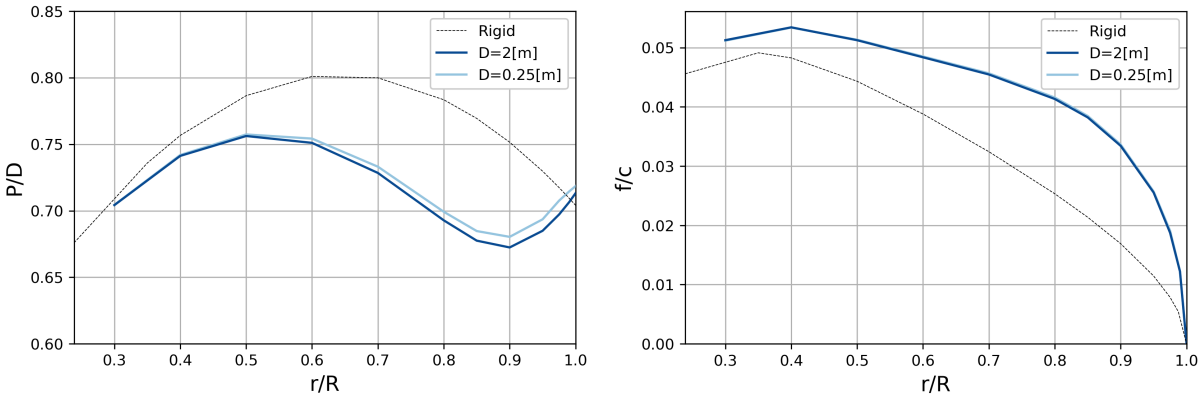

(a) Radial plot depicting the pitch deformation of both propellers, including the rigid C4-40 pitch ratio.

(b) Radial plot depicting the camber deformation of both propellers, including the rigid C4-40 pitch ratio.

Figure C.4: Radial plots depicting the deformation of both the 2-meter diameter propeller and the 0.25-meter diameter propeller, including the rigid C4-40 pitch ratio for J equals 0.4.

J-Value of 0.5

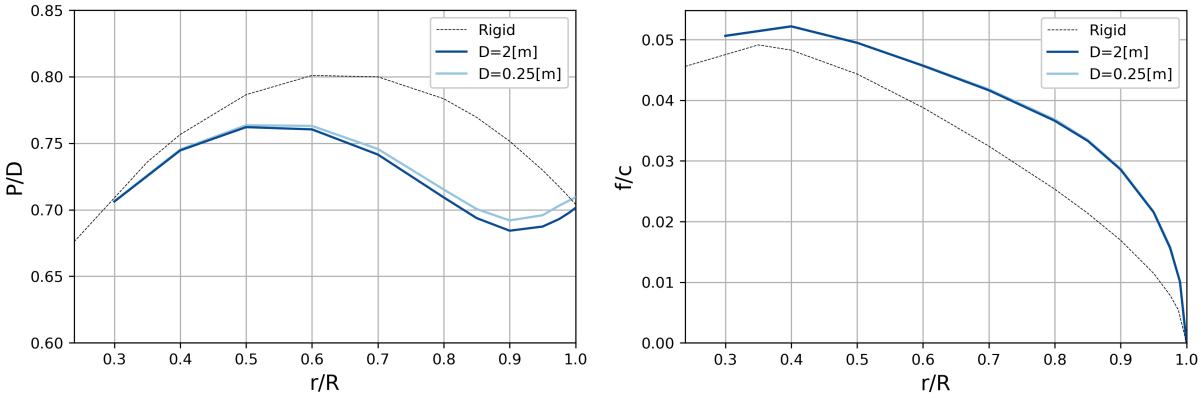

(a) Radial plot depicting the pitch deformation of both propellers, including the rigid C4-40 pitch ratio.

(b) Radial plot depicting the camber deformation of both propellers, including the rigid C4-40 pitch ratio.

Figure C.5: Radial plots depicting the deformation of both the 2-meter diameter propeller and the 0.25-meter diameter propeller, including the rigid C4-40 pitch ratio for J equals 0.5.

J-Value of 0.6

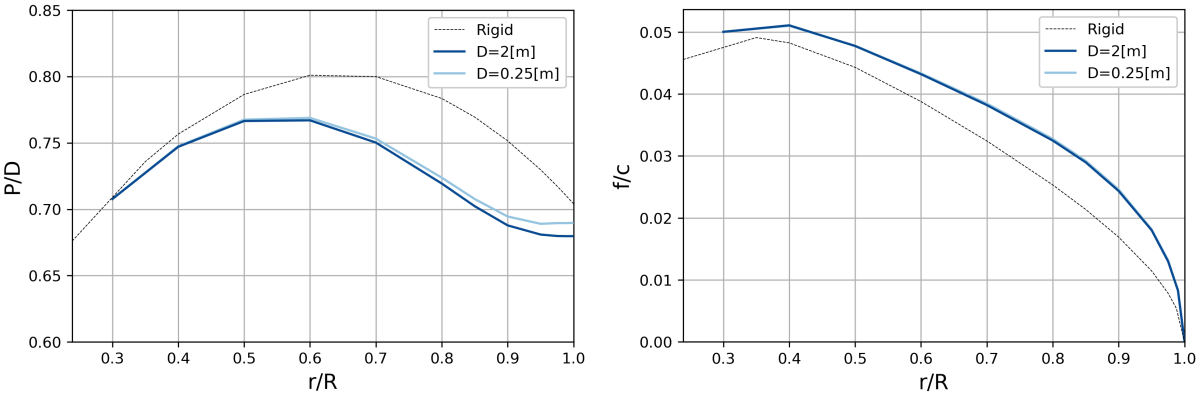

(a) Radial plot depicting the pitch deformation of both propellers, including the rigid C4-40 pitch ratio.

(b) Radial plot depicting the camber deformation of both propellers, including the rigid C4-40 pitch ratio.

Figure C.6: Radial plots depicting the deformation of both the 2-meter diameter propeller and the 0.25-meter diameter propeller, including the rigid C4-40 pitch ratio for J equals 0.6.

J-Value of 0.7

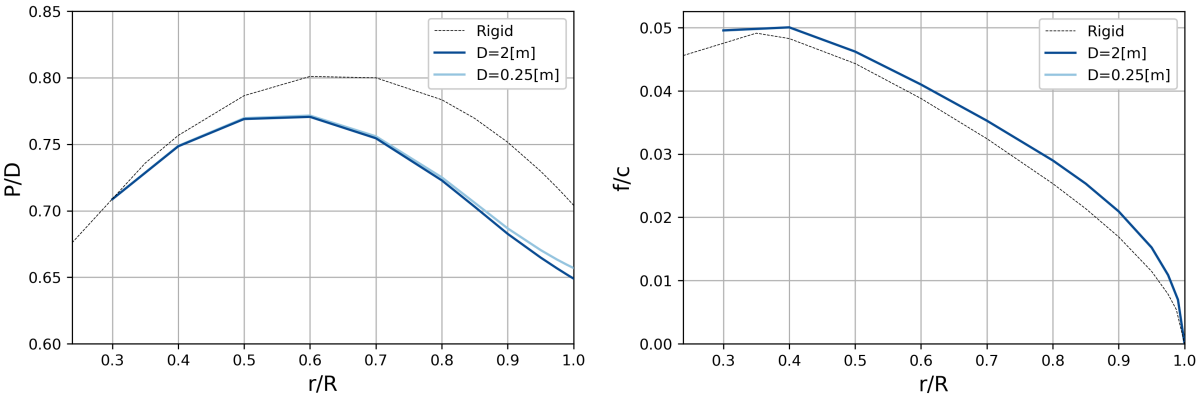

(a) Radial plot depicting the pitch deformation of both propellers, including the rigid C4-40 pitch ratio.

(b) Radial plot depicting the camber deformation of both propellers, including the rigid C4-40 pitch ratio.

Figure C.7: Radial plots depicting the deformation of both the 2-meter diameter propeller and the 0.25-meter diameter propeller, including the rigid C4-40 pitch ratio for J equals 0.7.

J-Value of 0.8

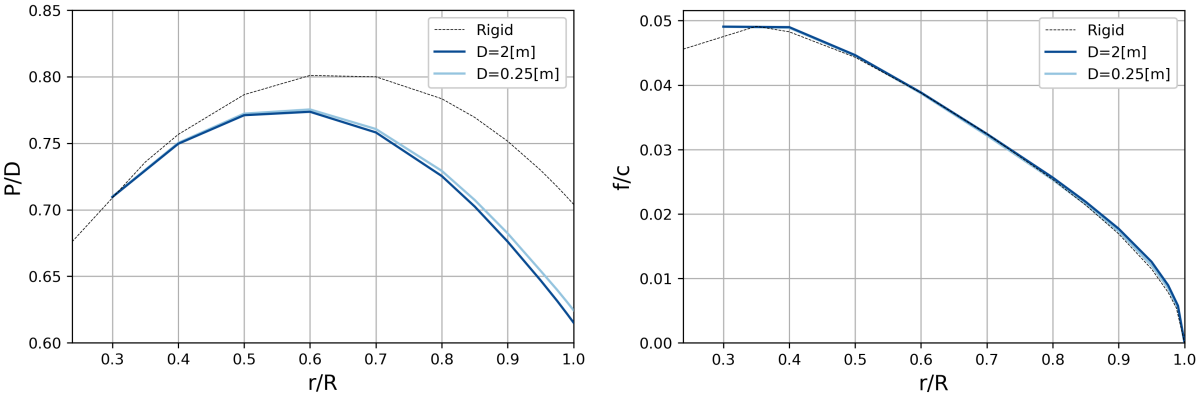

(a) Radial plot depicting the pitch deformation of both propellers, including the rigid C4-40 pitch ratio.

(b) Radial plot depicting the camber deformation of both propellers, including the rigid C4-40 pitch ratio.

Figure C.8: Radial plots depicting the deformation of both the 2-meter diameter propeller and the 0.25-meter diameter propeller, including the rigid C4-40 pitch ratio for J equals 0.8.

C.2. Rigid Open Water Diagram

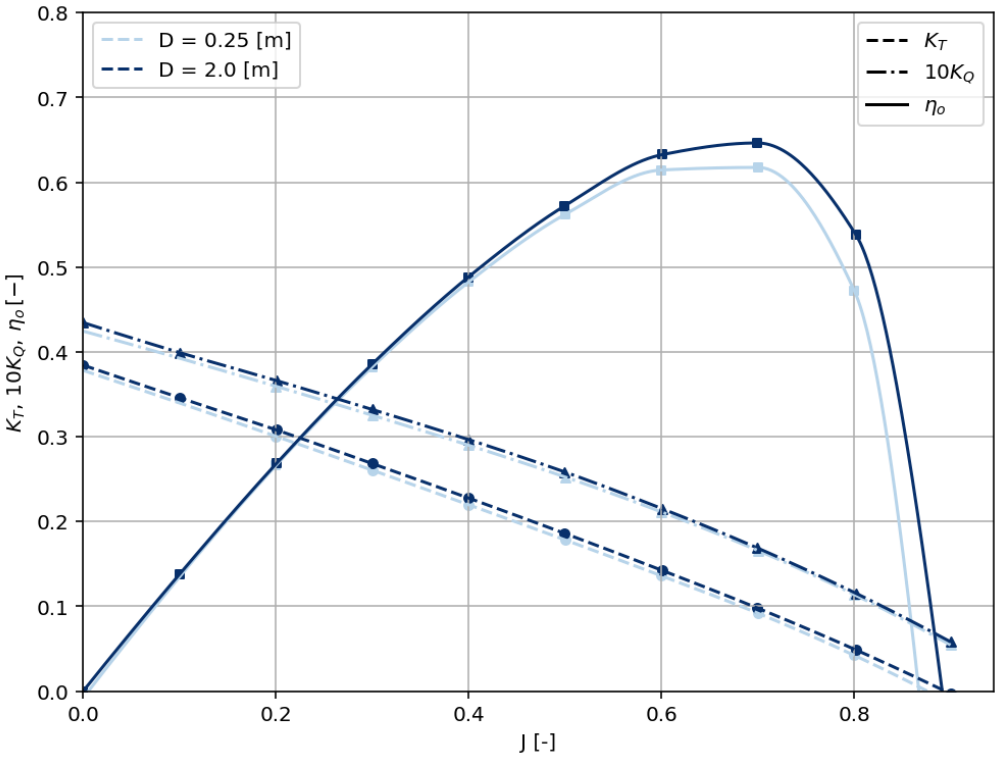

Figure C.9: Open water diagram of the rigid Wagningen C4-40 propeller with a pitch ratio of 0.8 for a propeller with a diameter of 2 meters and a model-scaled propeller with a diameter of 0.25 meters, $Re = 1 * 10^6$.

C.3. Percentage Difference of the Rigid Open Water Results

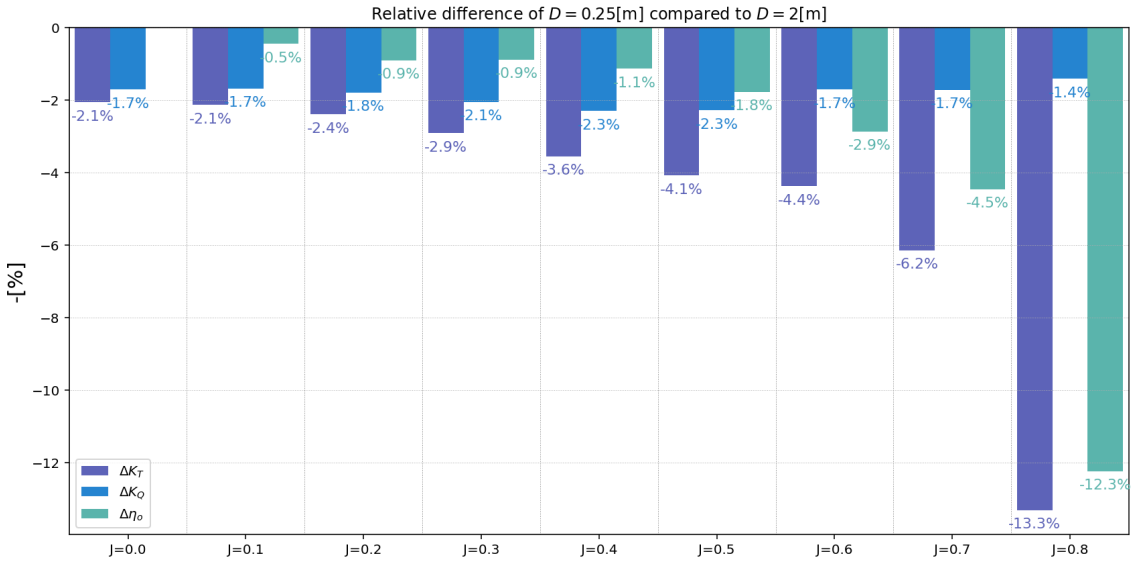

Figure C.10: The percentage difference for the thrust and torque coefficient and open water efficiency comparing the model scaled propeller to the full size propeller over the range of advance ratios.

C.4. Thrust Coefficient Convergence

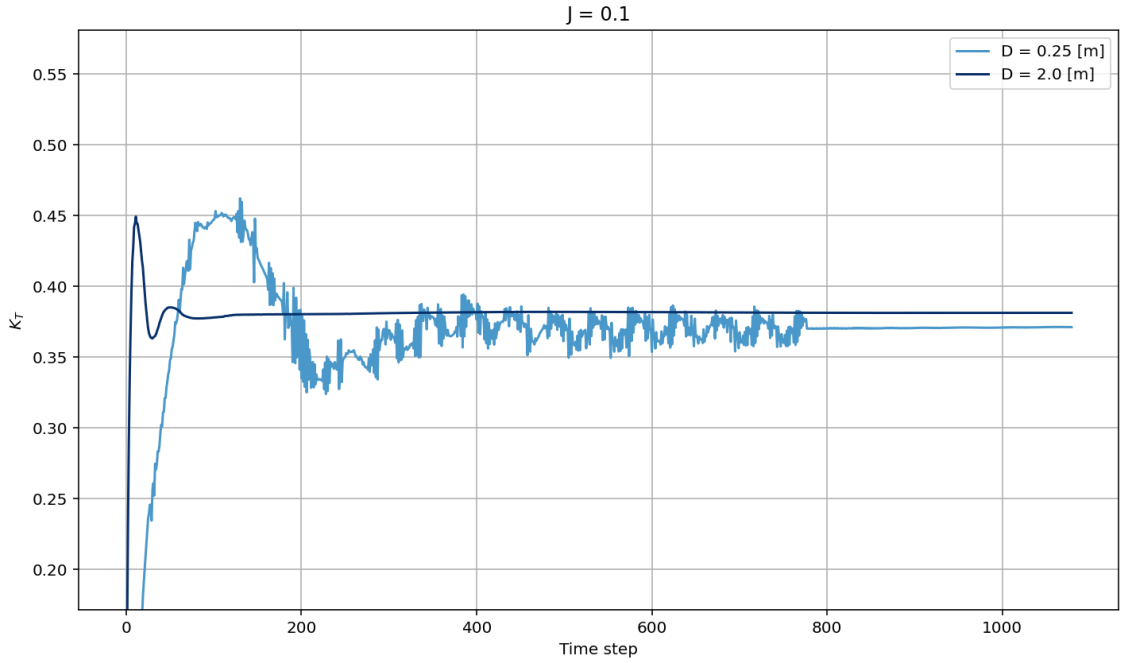

Figure C.11: The thrust coefficient over time for J equals 0.1, plotted for the range of Reynolds numbers. The plot demonstrates a convergence solution in each case.

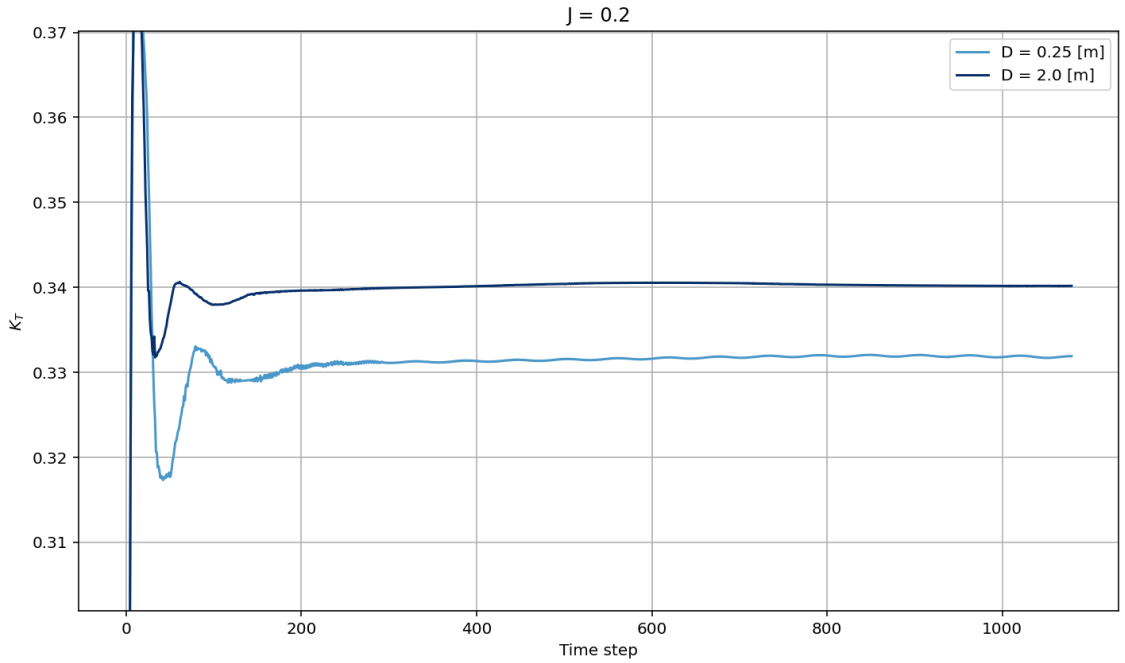

Figure C.12: The thrust coefficient over time for J equals 0.2, plotted for the flexible Wagningen C4-40 propeller with a pitch ratio of 0.8 for a propeller with a diameter of 2 meters and a model-scaled propeller with a diameter of 0.25 meters. The plot demonstrates a convergence solution in each case.

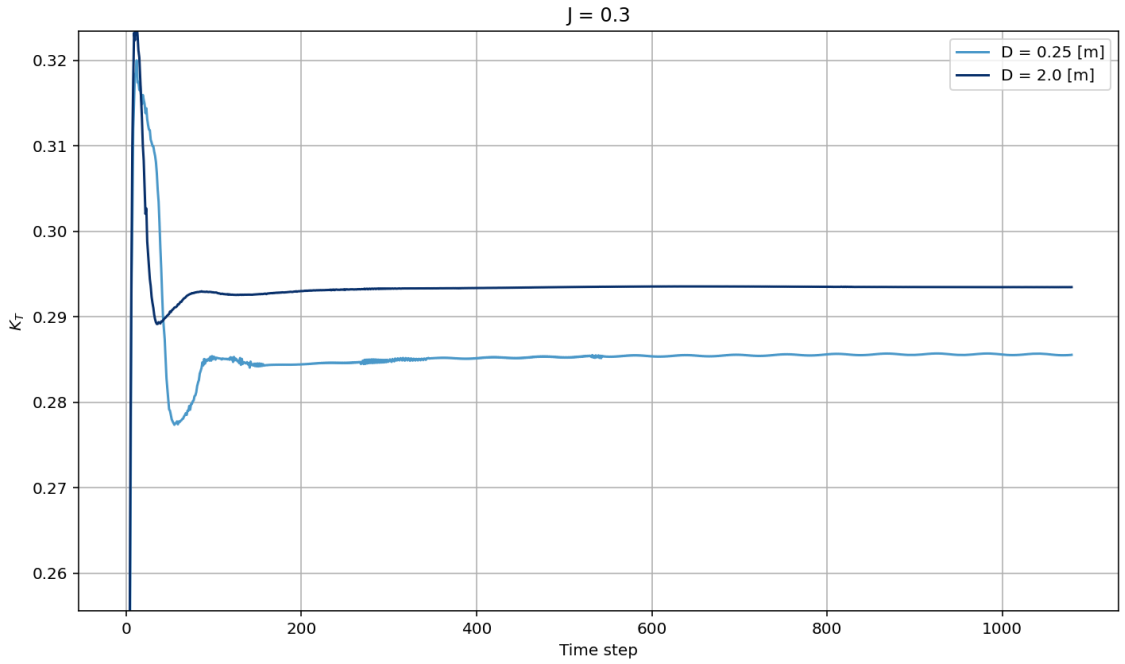

Figure C.13: The thrust coefficient over time for J equals 0.3, plotted for the flexible Wagningen C4-40 propeller with a pitch ratio of 0.8 for a propeller with a diameter of 2 meters and a model-scaled propeller with a diameter of 0.25 meters. The plot demonstrates a convergence solution in each case.

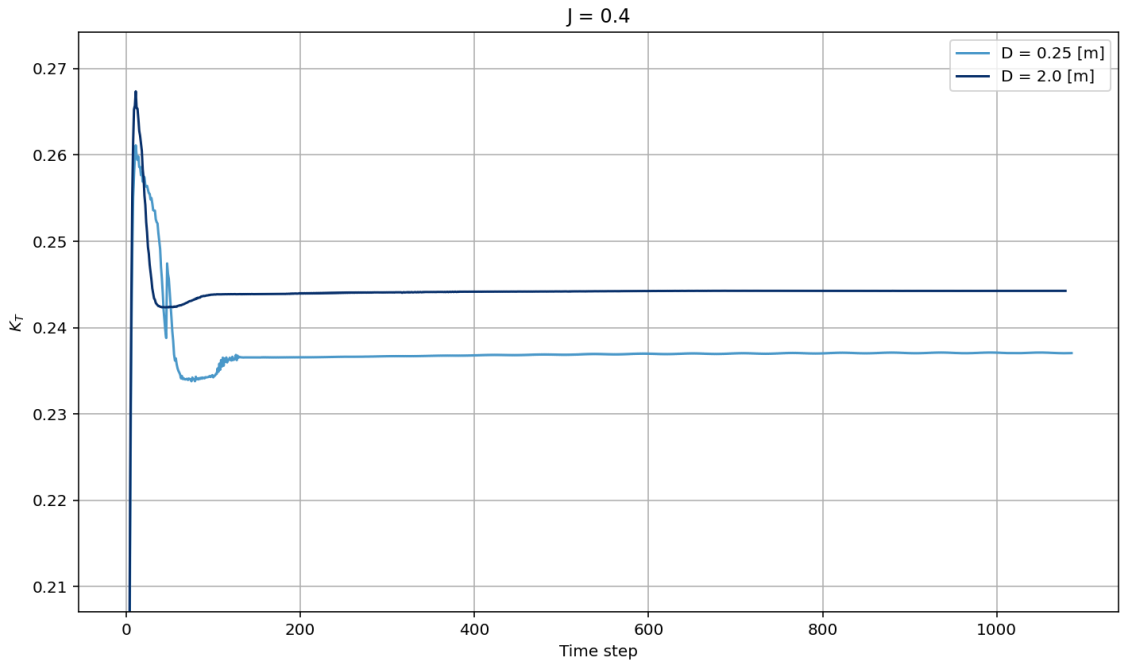

Figure C.14: The thrust coefficient over time for J equals 0.4, plotted for the flexible Wagningen C4-40 propeller with a pitch ratio of 0.8 for a propeller with a diameter of 2 meters and a model-scaled propeller with a diameter of 0.25 meters. The plot demonstrates a convergence solution in each case.

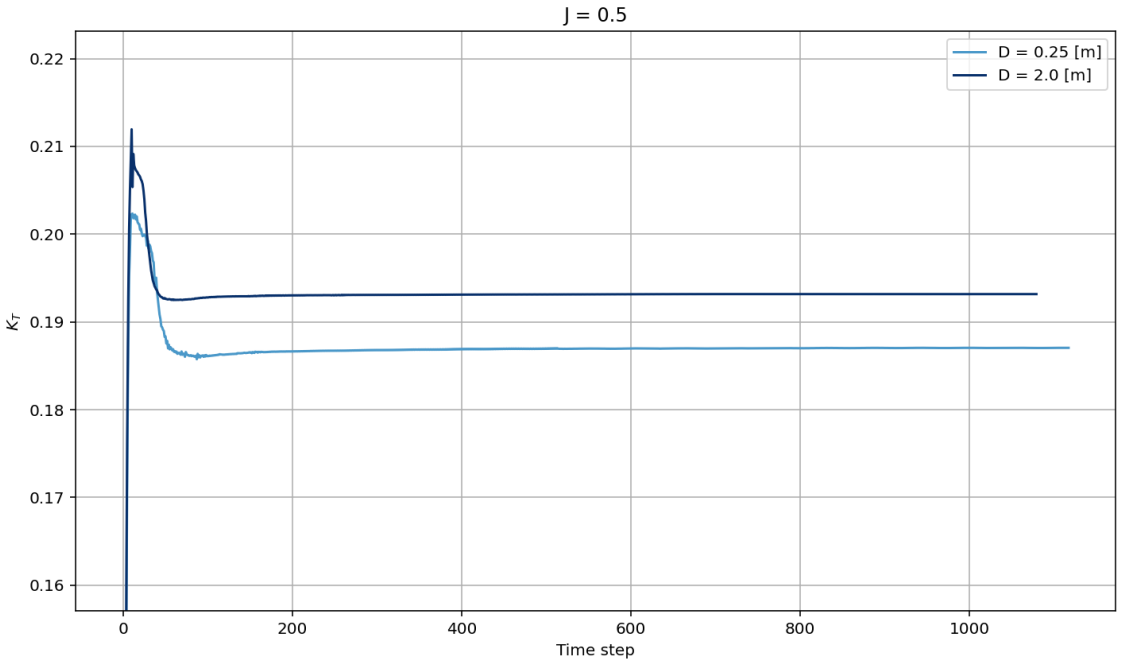

Figure C.15: The thrust coefficient over time for J equals 0.5, plotted for the flexible Wagningen C4-40 propeller with a pitch ratio of 0.8 for a propeller with a diameter of 2 meters and a model-scaled propeller with a diameter of 0.25 meters. The plot demonstrates a convergence solution in each case.

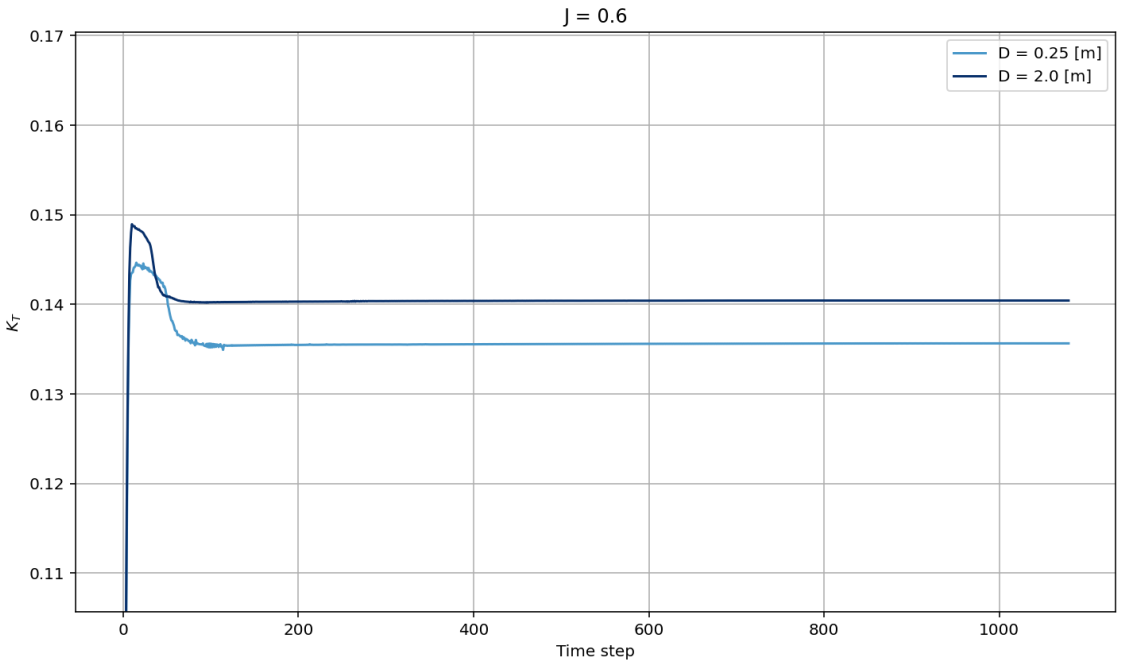

Figure C.16: The thrust coefficient over time for J equals 0.6, plotted for the flexible Wagningen C4-40 propeller with a pitch ratio of 0.8 for a propeller with a diameter of 2 meters and a model-scaled propeller with a diameter of 0.25 meters. The plot demonstrates a convergence solution in each case.

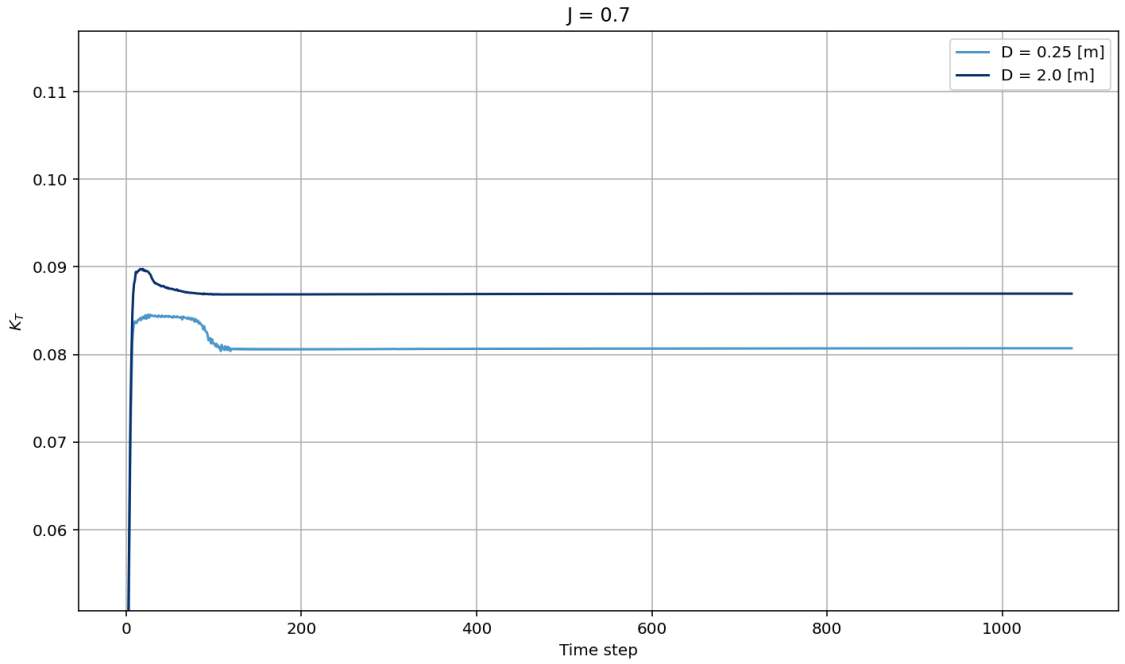

Figure C.17: The thrust coefficient over time for J equals 0.7, plotted for the flexible Wagningen C4-40 propeller with a pitch ratio of 0.8 for a propeller with a diameter of 2 meters and a model-scaled propeller with a diameter of 0.25 meters. The plot demonstrates a convergence solution in each case.

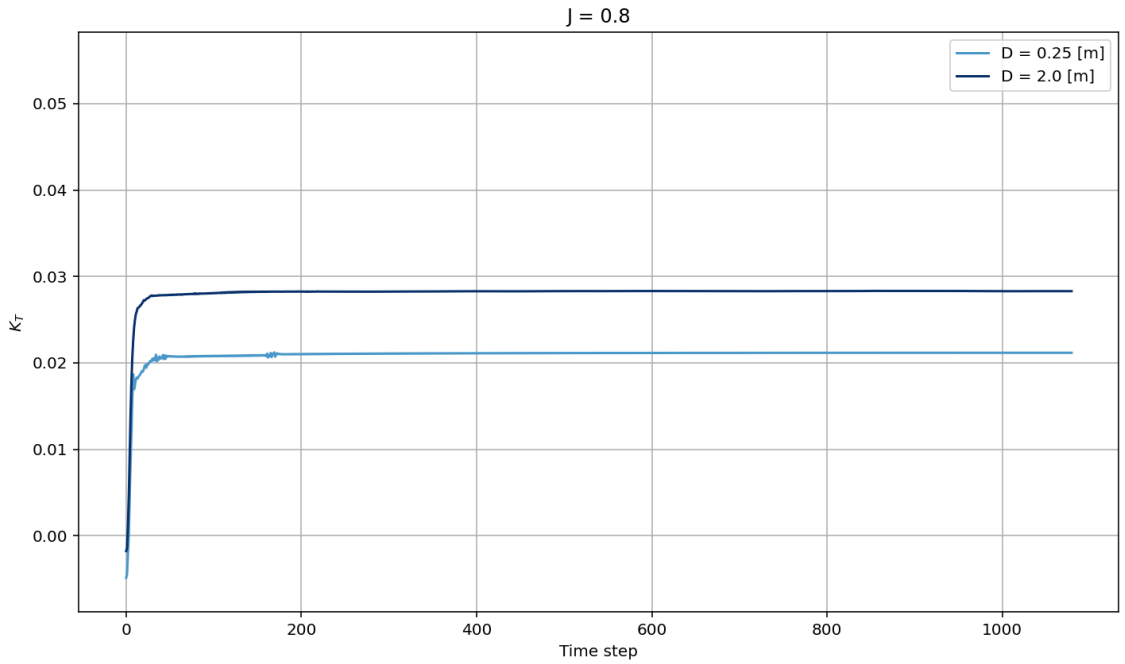

Figure C.18: The thrust coefficient over time for J equals 0.8, plotted for the flexible Wagningen C4-40 propeller with a pitch ratio of 0.8 for a propeller with a diameter of 2 meters and a model-scaled propeller with a diameter of 0.25 meters. The plot demonstrates a convergence solution in each case.

D

Flexible Propeller Results for a Range of Reynolds Number

D.1. Percentage Difference Across Reynolds Numbers

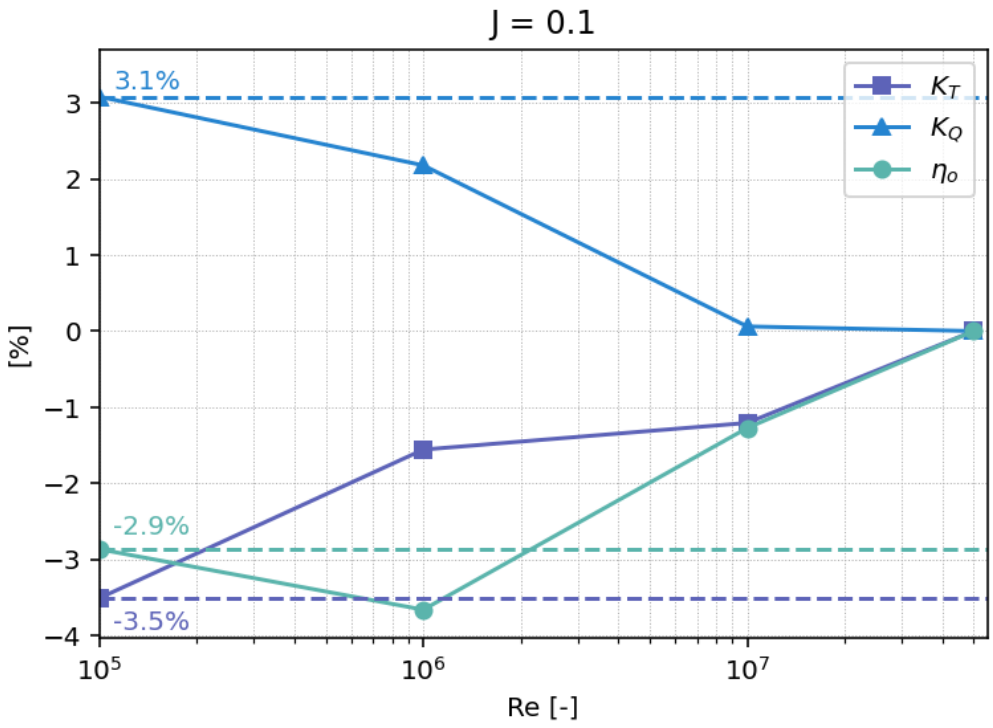

Figure D.1: The percentage difference across Reynolds numbers for K_T, K_Q and η_o for the flexible C4-40 propeller tested at an advance ratio of 0.1.

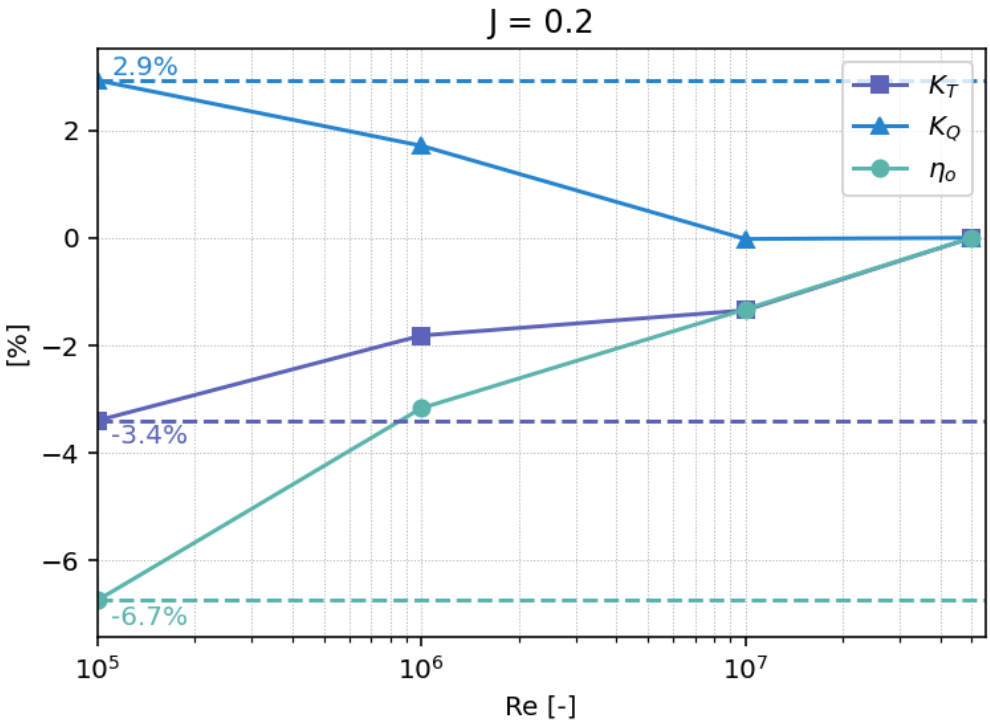

Figure D.2: The percentage difference across Reynolds numbers for K_T, K_Q and η_o for the flexible C4-40 propeller tested at an advance ratio of 0.2.

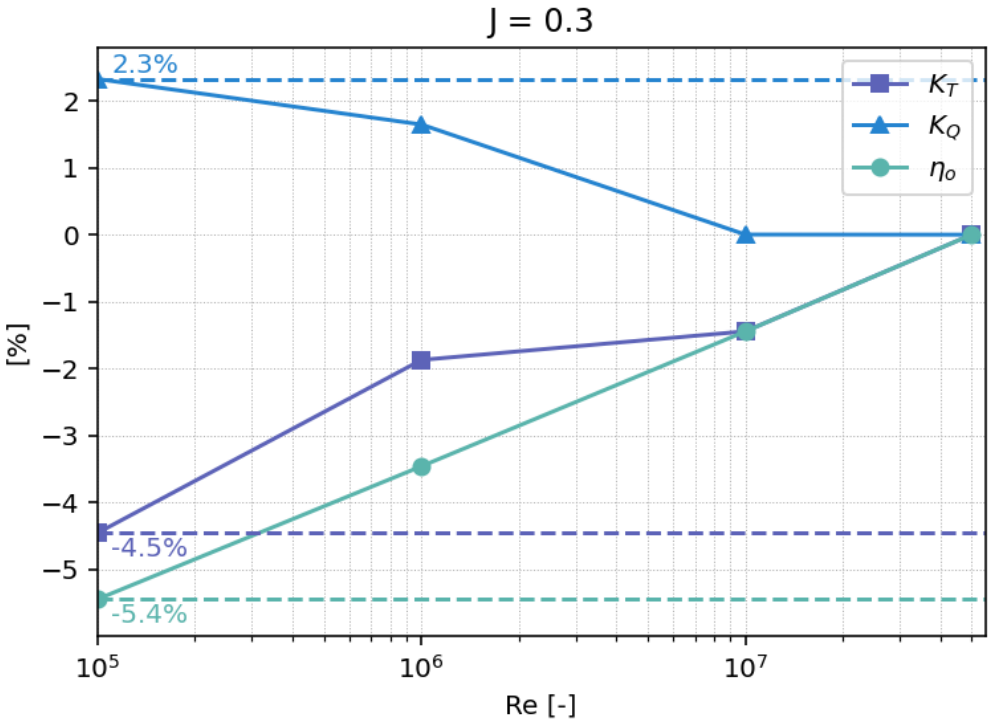

Figure D.3: The percentage difference across Reynolds numbers for K_T, K_Q and η_o for the flexible C4-40 propeller tested at an advance ratio of 0.3.

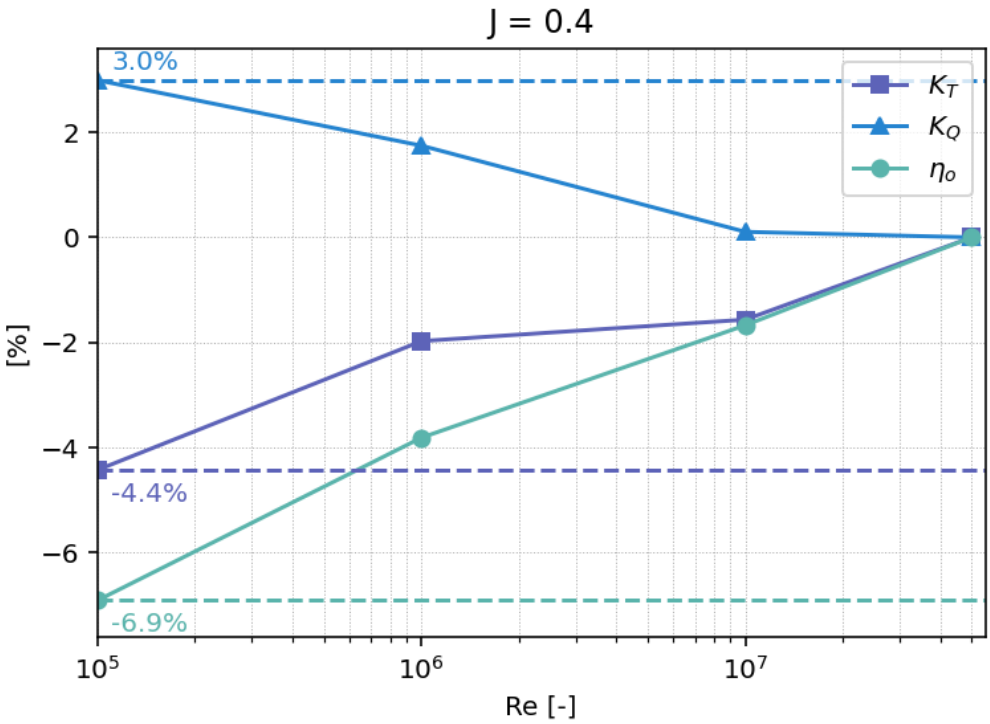

Figure D.4: The percentage difference across Reynolds numbers for K_T, K_Q and η_o for the flexible C4-40 propeller tested at an advance ratio of 0.4.

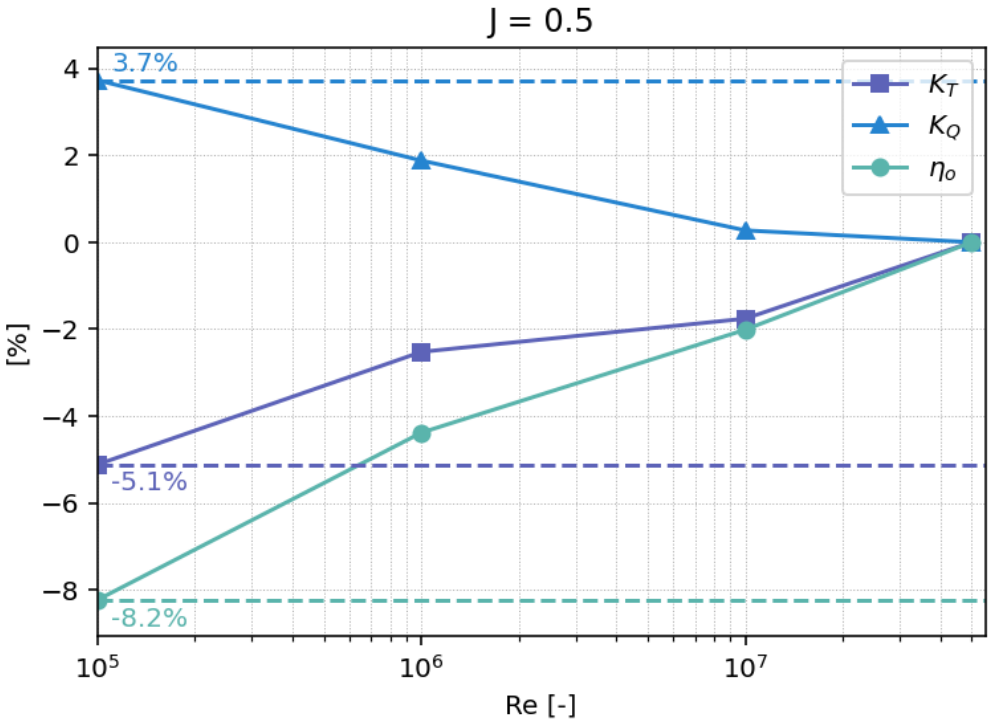

Figure D.5: The percentage difference across Reynolds numbers for K_T, K_Q and η_o for the flexible C4-40 propeller tested at an advance ratio of 0.5.

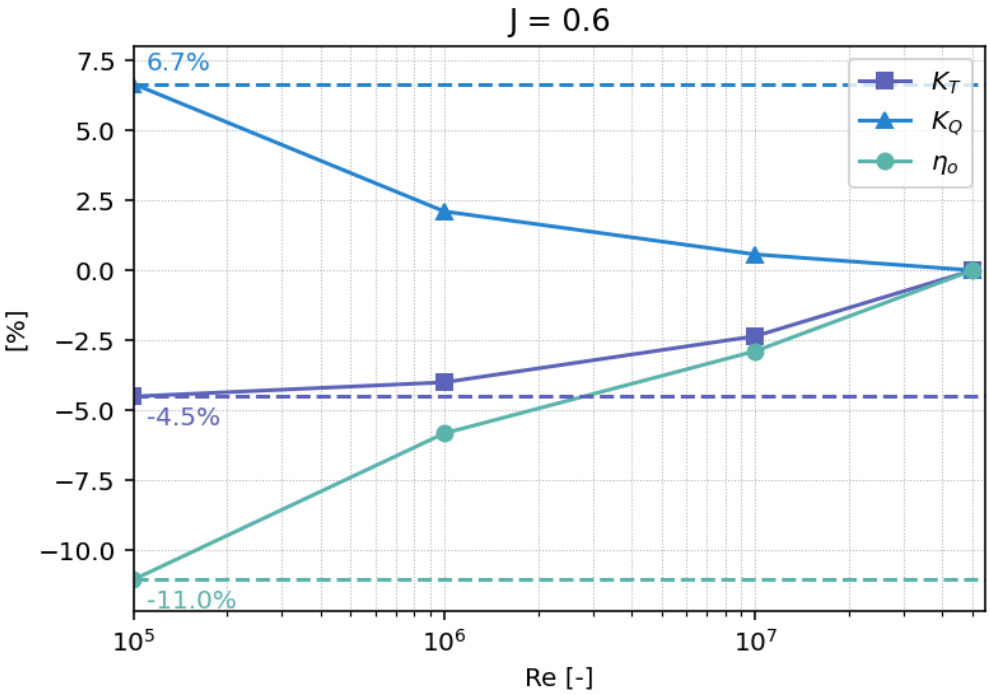

Figure D.6: The percentage difference across Reynolds numbers for K_T, K_Q and η_o for the flexible C4-40 propeller tested at an advance ratio of 0.6.

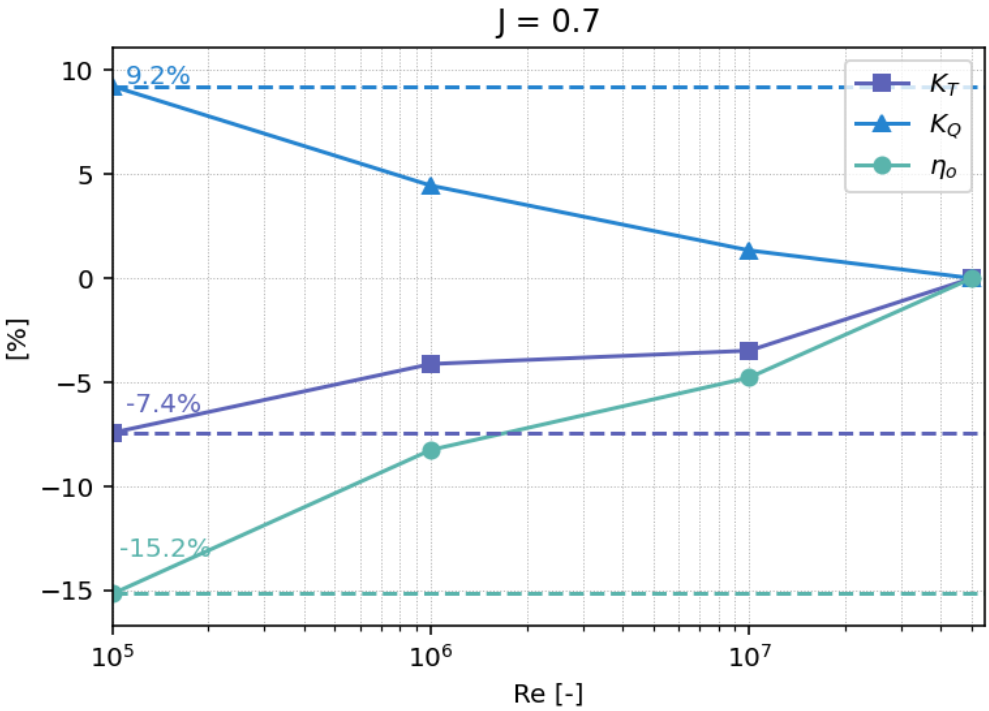

Figure D.7: The percentage difference across Reynolds numbers for K_T, K_Q and η_o for the flexible C4-40 propeller tested at an advance ratio of 0.7.

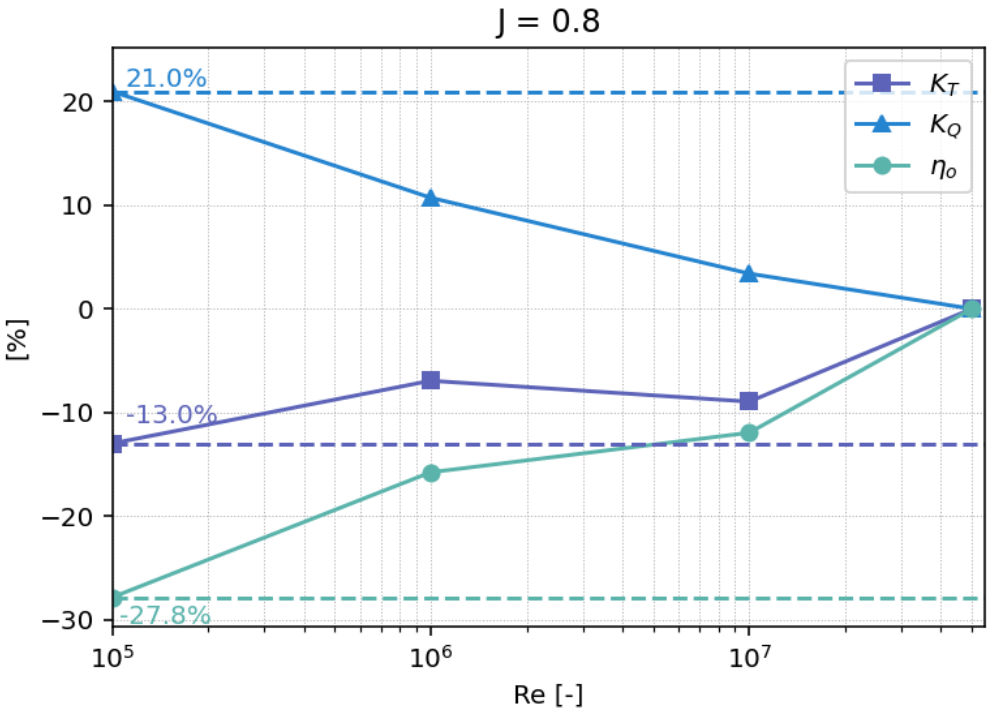

Figure D.8: The percentage difference across Reynolds numbers for K_T, K_Q and η_o for the flexible C4-40 propeller tested at an advance ratio of 0.8.

D.2. Flexible Propeller Deformation

J-Value of 0.1

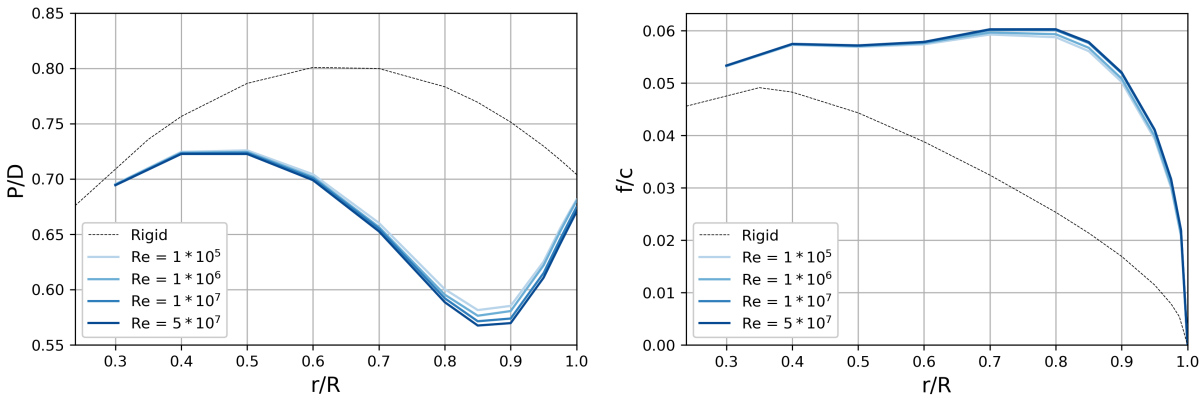

(a) Radial plot depicting the pitch deformation over the range of Reynolds numbers, including the rigid C4-40 pitch ratio.

(b) Radial plot depicting the camber deformation over the range of Reynolds numbers, including the rigid C4-40 camber ratio.

Figure D.9: Radial plots depicting the deformation of the flexible propellers for a range of Reynolds numbers, including the rigid C4-40 pitch ratio for J equals 0.1.

J-Value of 0.2

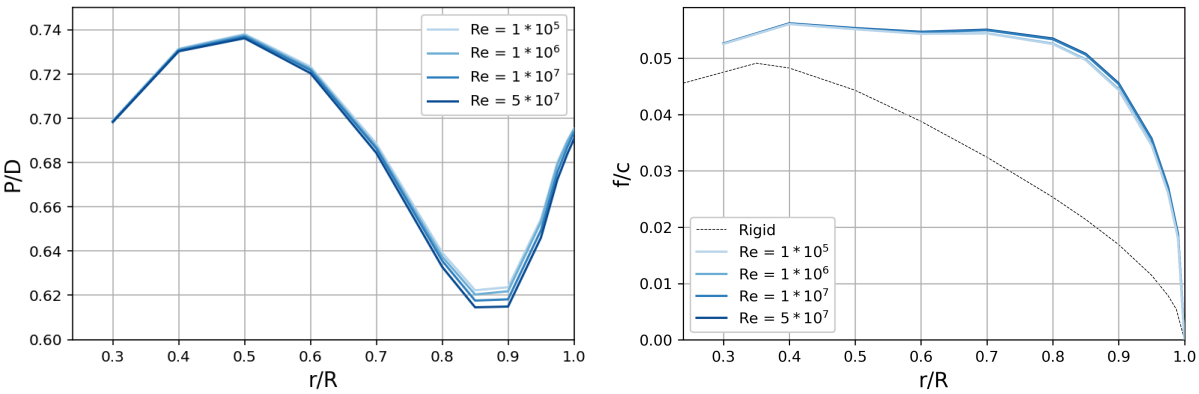

(a) Radial plot depicting the pitch deformation over the range of Reynolds numbers, including the rigid C4-40 pitch ratio.

(b) Radial plot depicting the camber deformation over the range of Reynolds numbers, including the rigid C4-40 camber ratio.

Figure D.10: Radial plots depicting the deformation of the flexible propellers for a range of Reynolds numbers, including the rigid C4-40 pitch ratio for J equals 0.2.

J-Value of 0.3

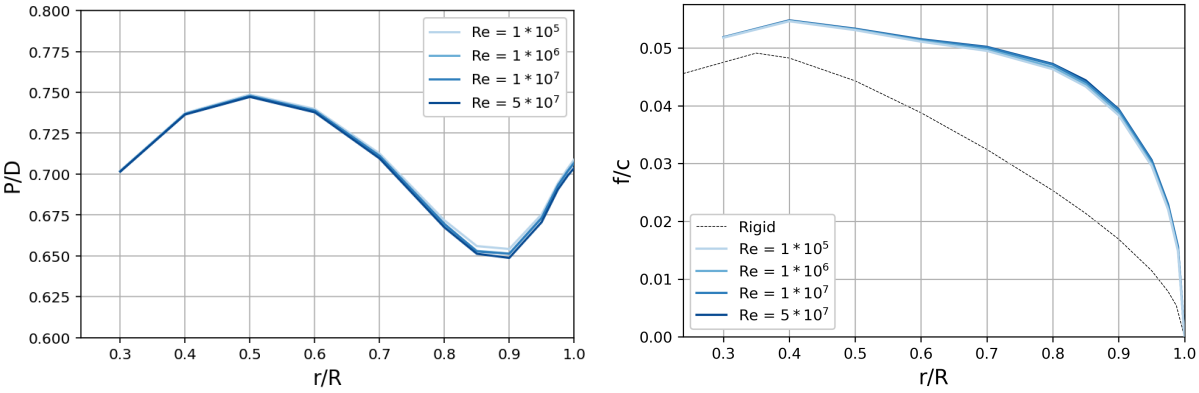

(a) Radial plot depicting the pitch deformation over the range of Reynolds numbers, including the rigid C4-40 pitch ratio.

(b) Radial plot depicting the camber deformation over the range of Reynolds numbers, including the rigid C4-40 camber ratio.

Figure D.11: Radial plots depicting the deformation of the flexible propellers for a range of Reynolds numbers, including the rigid C4-40 pitch ratio for J equals 0.3.

J-Value of 0.4

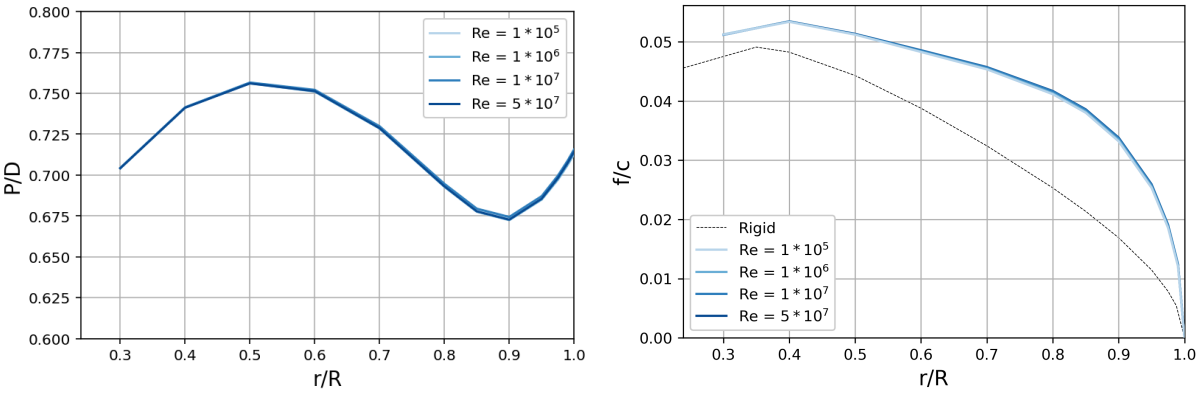

(a) Radial plot depicting the pitch deformation over the range of Reynolds numbers, including the rigid C4-40 pitch ratio.

(b) Radial plot depicting the camber deformation over the range of Reynolds numbers, including the rigid C4-40 camber ratio.

Figure D.12: Radial plots depicting the deformation of the flexible propellers for a range of Reynolds numbers, including the rigid C4-40 pitch ratio for J equals 0.4.

J-Value of 0.5

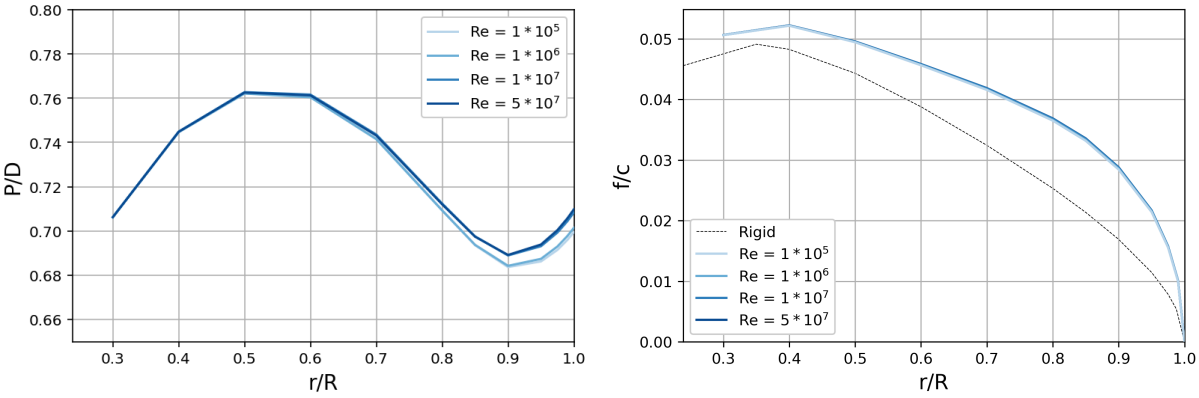

(a) Radial plot depicting the pitch deformation over the range of Reynolds numbers, including the rigid C4-40 pitch ratio.

(b) Radial plot depicting the camber deformation over the range of Reynolds numbers, including the rigid C4-40 camber ratio.

Figure D.13: Radial plots depicting the deformation of the flexible propellers for a range of Reynolds numbers, including the rigid C4-40 pitch ratio for J equals 0.5.

J-Value of 0.6

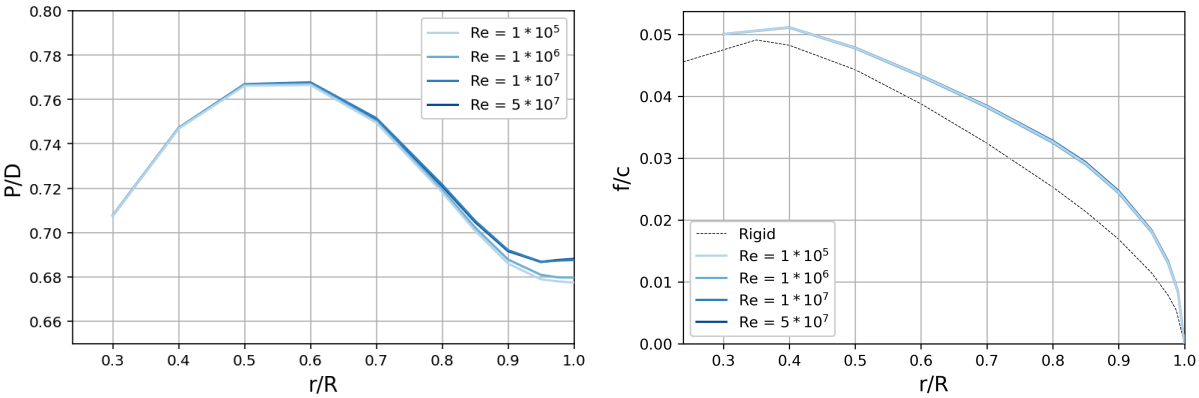

(a) Radial plot depicting the pitch deformation over the range of Reynolds numbers, including the rigid C4-40 pitch ratio.

(b) Radial plot depicting the camber deformation over the range of Reynolds numbers, including the rigid C4-40 camber ratio.

Figure D.14: Radial plots depicting the deformation of the flexible propellers for a range of Reynolds numbers, including the rigid C4-40 pitch ratio for J equals 0.6.

J-Value of 0.7

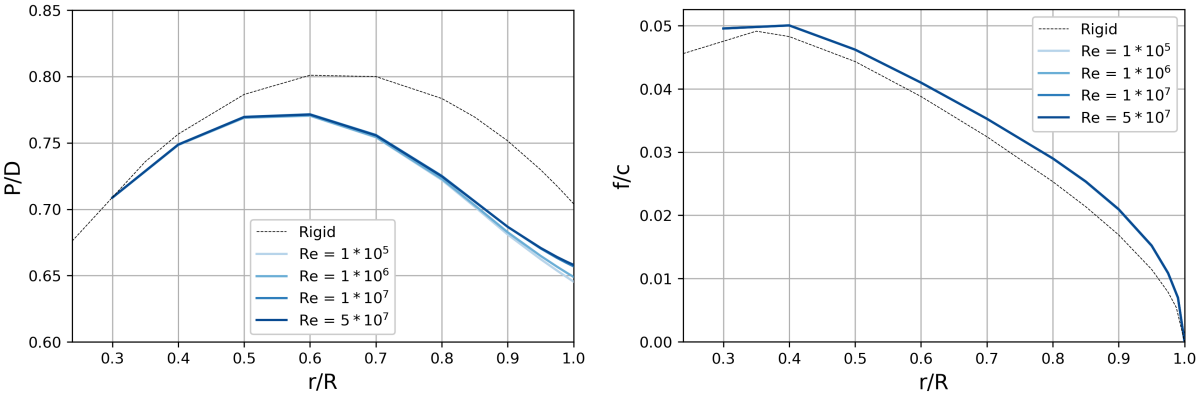

(a) Radial plot depicting the pitch deformation over the range of Reynolds numbers, including the rigid C4-40 pitch ratio.

(b) Radial plot depicting the camber deformation over the range of Reynolds numbers, including the rigid C4-40 camber ratio.

Figure D.15: Radial plots depicting the deformation of the flexible propellers for a range of Reynolds numbers, including the rigid C4-40 pitch ratio for J equals 0.7.

J-Value of 0.8

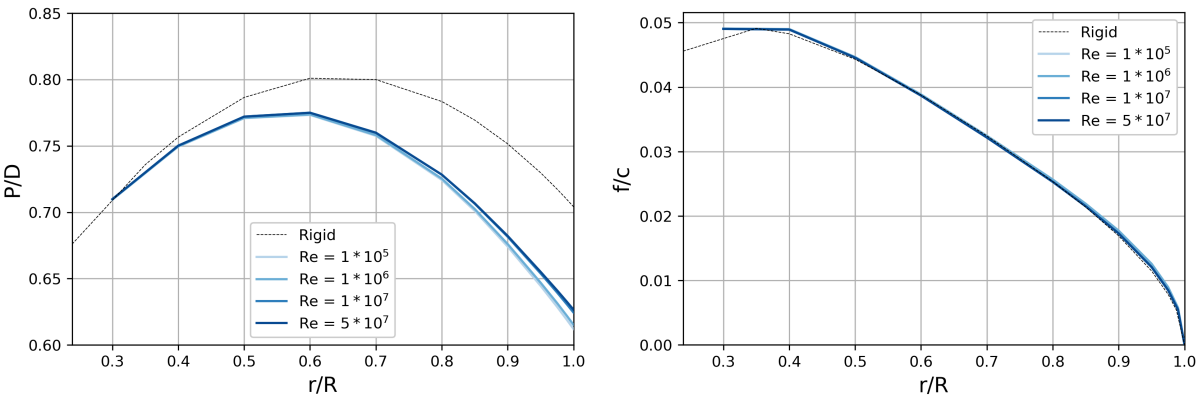

(a) Radial plot depicting the pitch deformation over the range of Reynolds numbers, including the rigid C4-40 pitch ratio.

(b) Radial plot depicting the camber deformation over the range of Reynolds numbers, including the rigid C4-40 camber ratio.

Figure D.16: Radial plots depicting the deformation of the flexible propellers for a range of Reynolds numbers, including the rigid C4-40 pitch ratio for J equals 0.8.

D.3. Streamlines and Skin Friction Coefficient

J-Value of 0.1

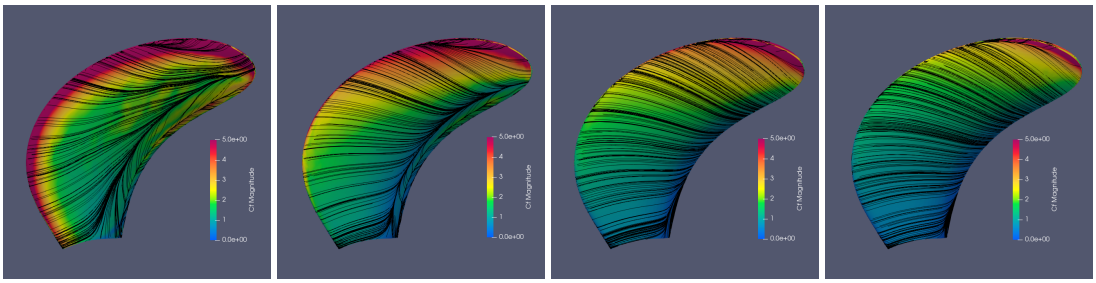

(a) $Re = 1 * 10^5$ **(b)** $Re = 1 * 10^6$ **(c)** $Re = 1 * 10^7$ **(d)** $Re = 5 * 10^7$

Figure D.17: Streamlines and Skin Friction coefficient on the suction side of the flexible C4-40 propeller blade tested at a J of 0.1.

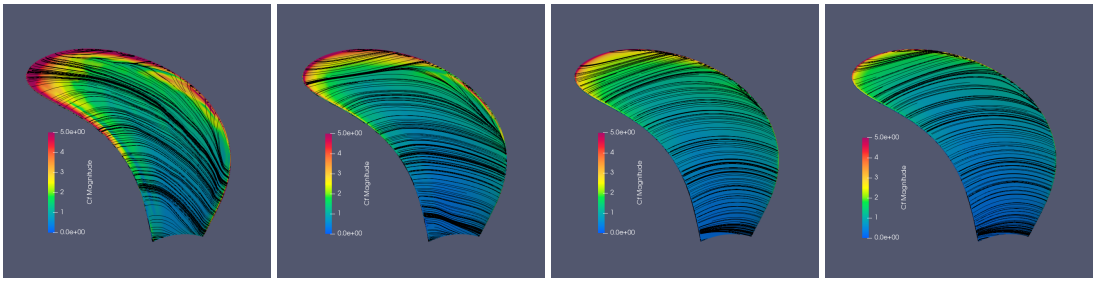

(a) $Re = 1 * 10^5$ **(b)** $Re = 1 * 10^6$ **(c)** $Re = 1 * 10^7$ **(d)** $Re = 5 * 10^7$

Figure D.18: Streamlines and skin friction coefficient on the pressure side of the flexible C4-40 propeller blade tested at a J of 0.1.

J-Value of 0.2

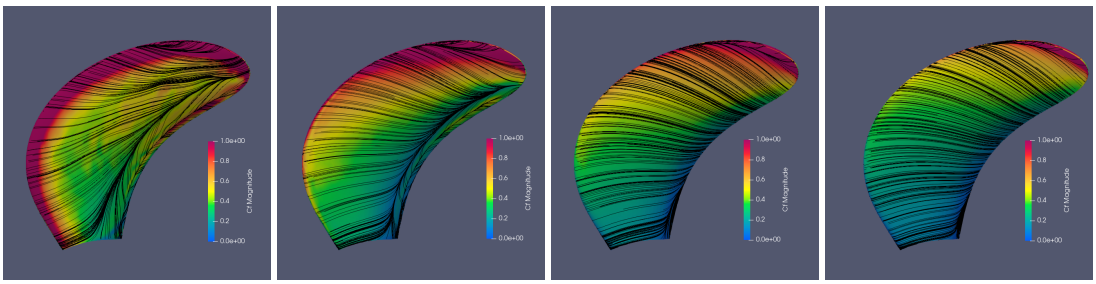

(a) $Re = 1 * 10^5$ **(b)** $Re = 1 * 10^6$ **(c)** $Re = 1 * 10^7$ **(d)** $Re = 5 * 10^7$

Figure D.19: Streamlines and Skin Friction coefficient on the suction side of the flexible C4-40 propeller blade tested at a J of 0.2.

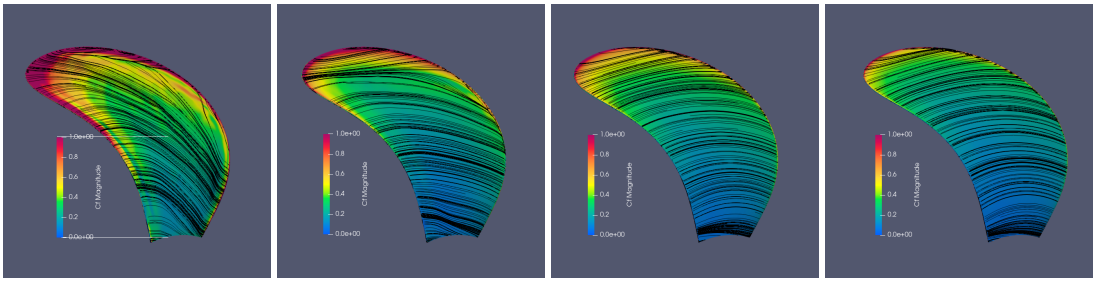

(a) $Re = 1 * 10^5$ **(b)** $Re = 1 * 10^6$ **(c)** $Re = 1 * 10^7$ **(d)** $Re = 5 * 10^7$

Figure D.20: Streamlines and skin friction coefficient on the pressure side of the flexible C4-40 propeller blade tested at a J of 0.2.

J-Value of 0.3

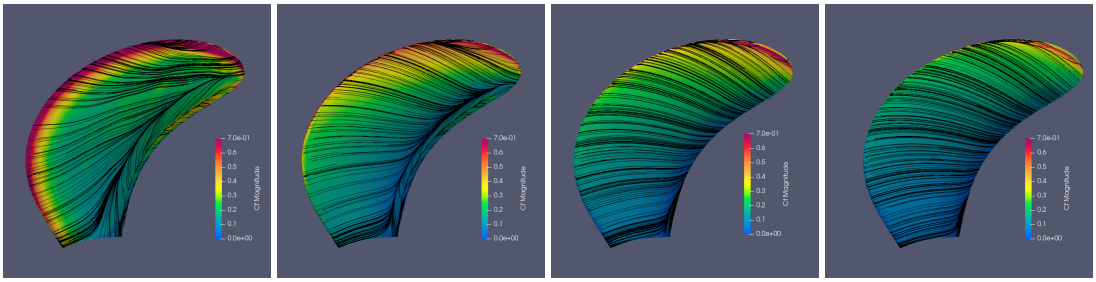

(a) $Re = 1 * 10^5$ **(b)** $Re = 1 * 10^6$ **(c)** $Re = 1 * 10^7$ **(d)** $Re = 5 * 10^7$

Figure D.21: Streamlines and Skin Friction coefficient on the suction side of the flexible C4-40 propeller blade tested at a J of 0.3.

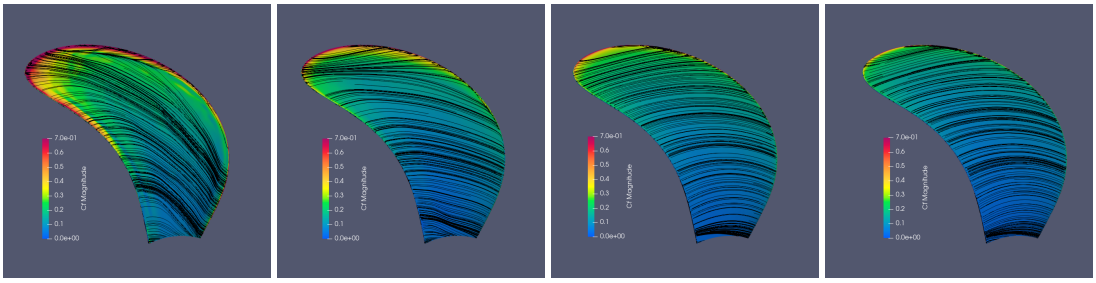

(a) $Re = 1 * 10^5$ **(b)** $Re = 1 * 10^6$ **(c)** $Re = 1 * 10^7$ **(d)** $Re = 5 * 10^7$

Figure D.22: Streamlines and skin friction coefficient on the pressure side of the flexible C4-40 propeller blade tested at a J of 0.3.

J-Value of 0.4

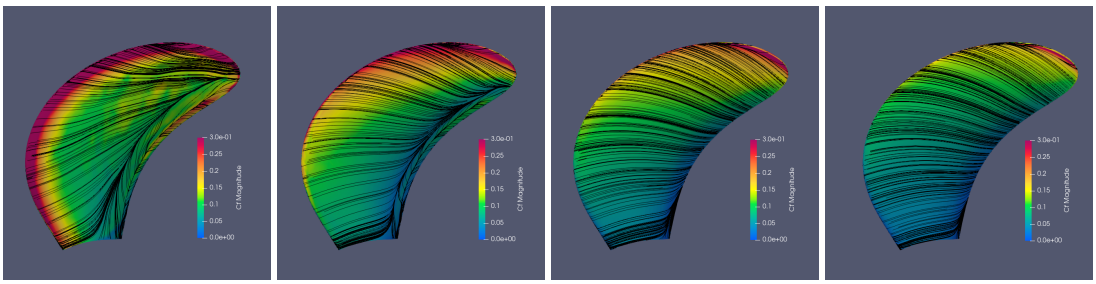

(a) $Re = 1 * 10^5$ **(b)** $Re = 1 * 10^6$ **(c)** $Re = 1 * 10^7$ **(d)** $Re = 5 * 10^7$

Figure D.23: Streamlines and Skin Friction coefficient on the suction side of the flexible C4-40 propeller blade tested at a J of 0.4.

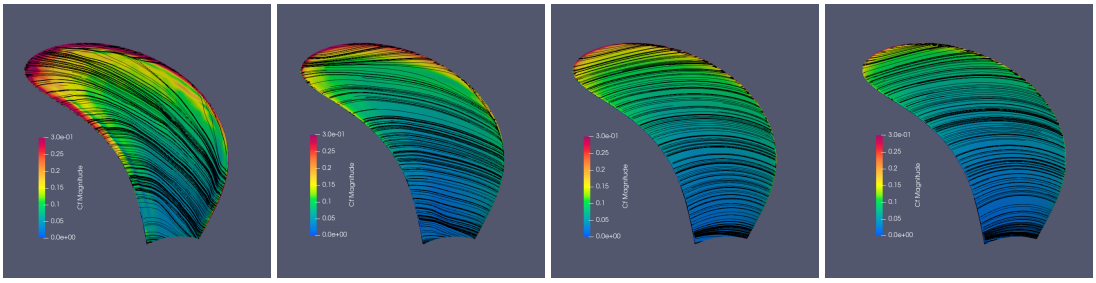

(a) $Re = 1 * 10^5$ **(b)** $Re = 1 * 10^6$ **(c)** $Re = 1 * 10^7$ **(d)** $Re = 5 * 10^7$

Figure D.24: Streamlines and skin friction coefficient on the pressure side of the flexible C4-40 propeller blade tested at a J of 0.4.

J-Value of 0.5

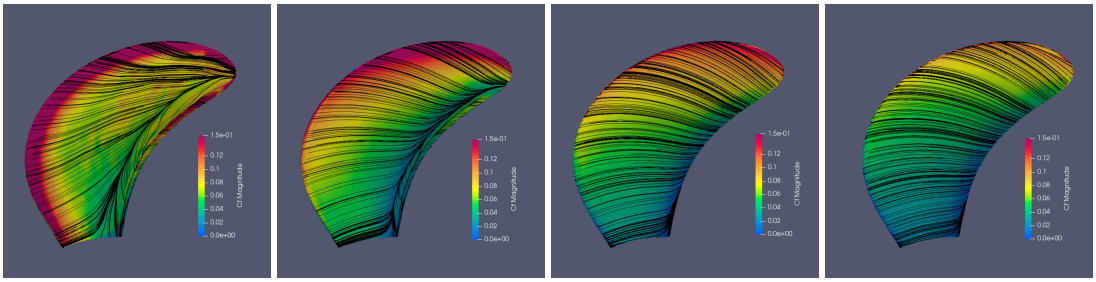

(a) $Re = 1 * 10^5$ **(b)** $Re = 1 * 10^6$ **(c)** $Re = 1 * 10^7$ **(d)** $Re = 5 * 10^7$

Figure D.25: Streamlines and Skin Friction coefficient on the suction side of the flexible C4-40 propeller blade tested at a J of 0.5.

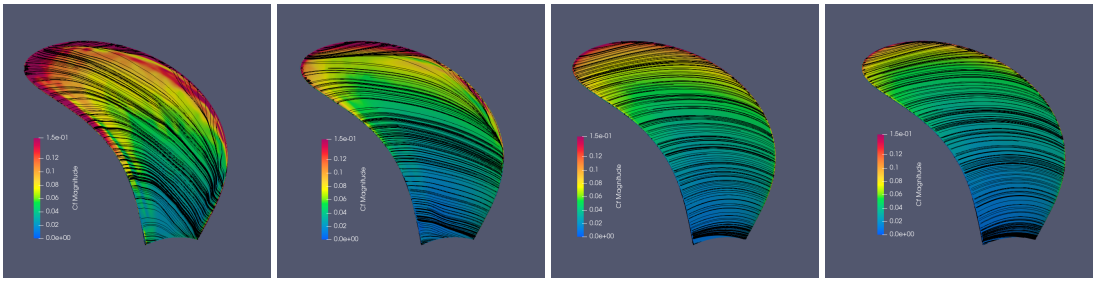

(a) $Re = 1 * 10^5$ **(b)** $Re = 1 * 10^6$ **(c)** $Re = 1 * 10^7$ **(d)** $Re = 5 * 10^7$

Figure D.26: Streamlines and skin friction coefficient on the pressure side of the flexible C4-40 propeller blade tested at a J of 0.5.

J-Value of 0.6

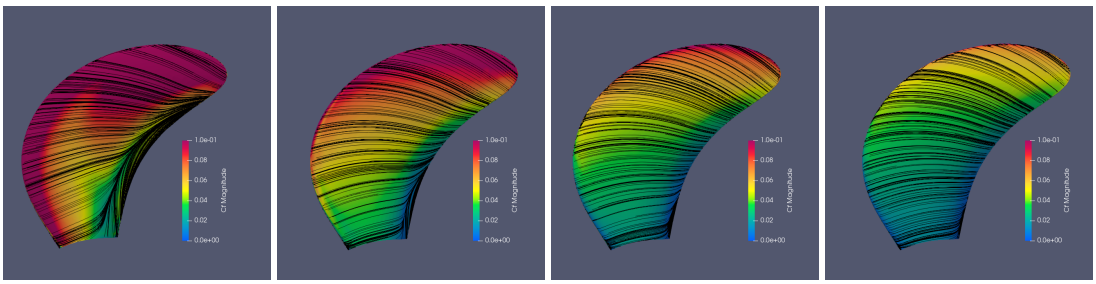

(a) $Re = 1 * 10^5$ **(b)** $Re = 1 * 10^6$ **(c)** $Re = 1 * 10^7$ **(d)** $Re = 5 * 10^7$

Figure D.27: Streamlines and Skin Friction coefficient on the suction side of the flexible C4-40 propeller blade tested at a J of 0.6.

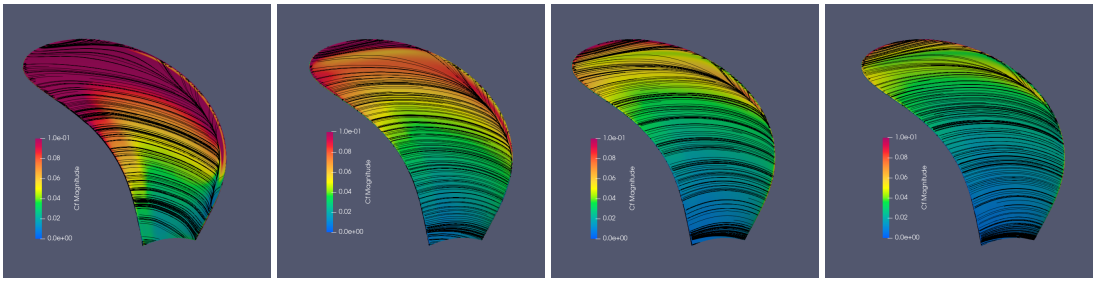

(a) $Re = 1 * 10^5$ **(b)** $Re = 1 * 10^6$ **(c)** $Re = 1 * 10^7$ **(d)** $Re = 5 * 10^7$

Figure D.28: Streamlines and skin friction coefficient on the pressure side of the flexible C4-40 propeller blade tested at a J of 0.6.

J-Value of 0.7

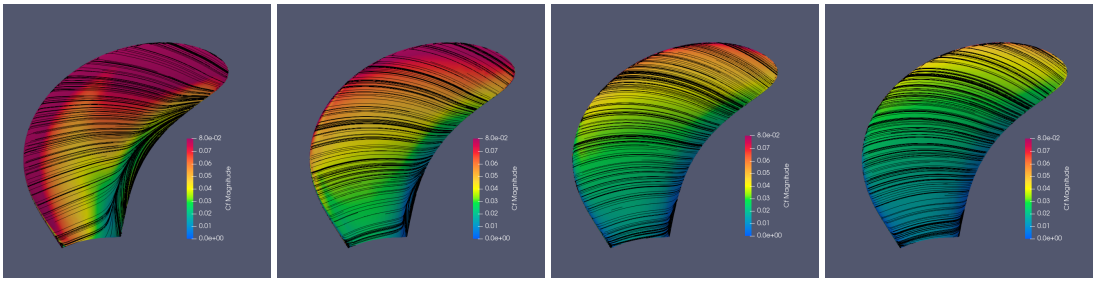

(a) $Re = 1 * 10^5$ **(b)** $Re = 1 * 10^6$ **(c)** $Re = 1 * 10^7$ **(d)** $Re = 5 * 10^7$

Figure D.29: Streamlines and Skin Friction coefficient on the suction side of the flexible C4-40 propeller blade tested at a J of 0.7.

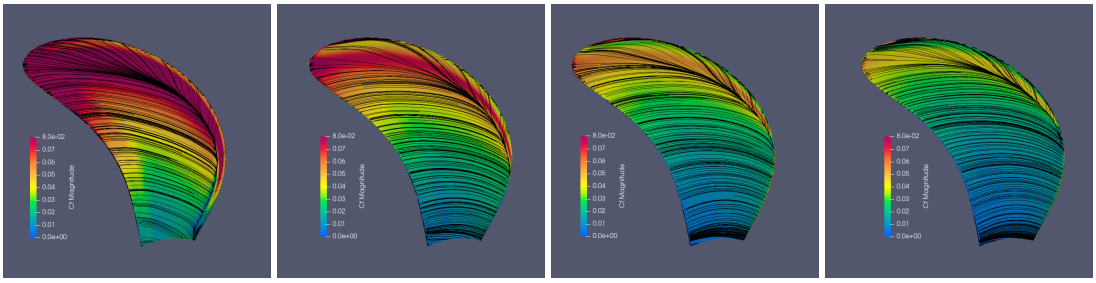

(a) $Re = 1 * 10^5$ **(b)** $Re = 1 * 10^6$ **(c)** $Re = 1 * 10^7$ **(d)** $Re = 5 * 10^7$

Figure D.30: Streamlines and skin friction coefficient on the pressure side of the flexible C4-40 propeller blade tested at a J of 0.7.

J-Value of 0.8

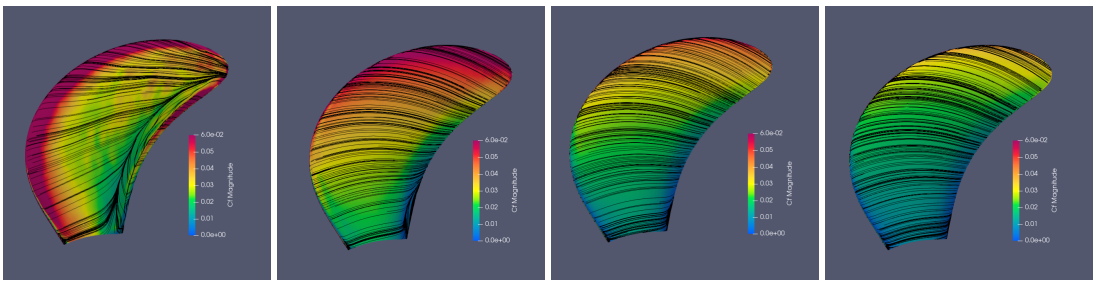

(a) $Re = 1 * 10^5$ **(b)** $Re = 1 * 10^6$ **(c)** $Re = 1 * 10^7$ **(d)** $Re = 5 * 10^7$

Figure D.31: Streamlines and Skin Friction coefficient on the suction side of the flexible C4-40 propeller blade tested at a J of 0.8.

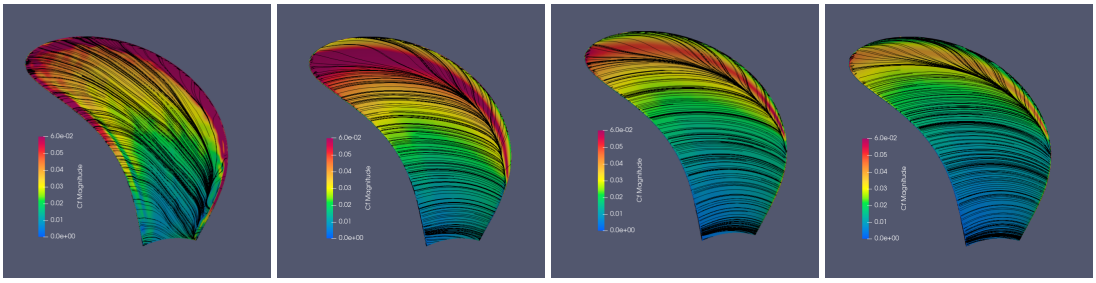

(a) $Re = 1 * 10^5$ **(b)** $Re = 1 * 10^6$ **(c)** $Re = 1 * 10^7$ **(d)** $Re = 5 * 10^7$

Figure D.32: Streamlines and skin friction coefficient on the pressure side of the flexible C4-40 propeller blade tested at a J of 0.8.

D.4. Thrust coefficient convergence

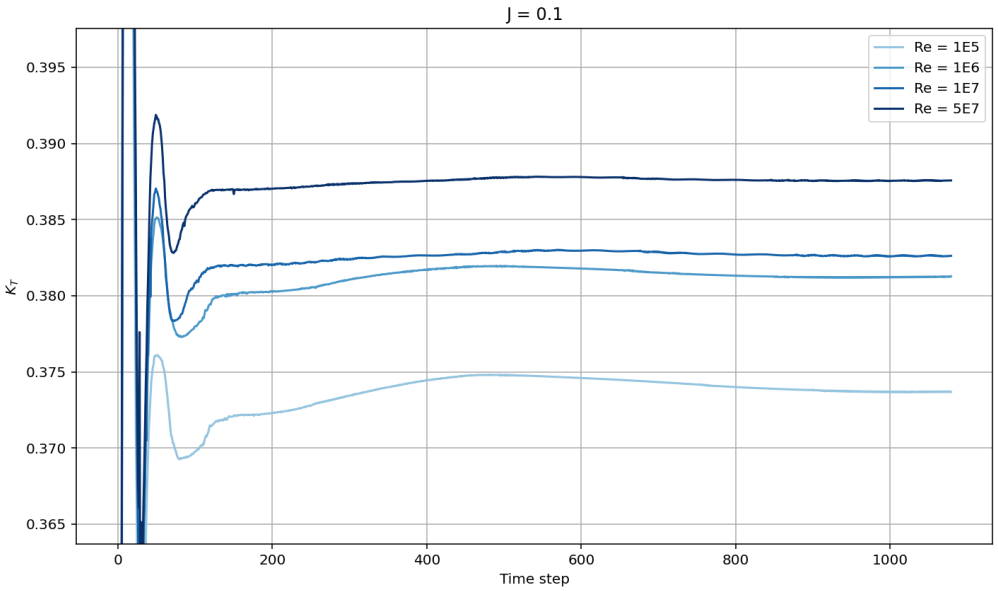

Figure D.33: The thrust coefficient over time for J equals 0.1, plotted for the flexible Wagningen C4-40 propeller with a pitch ratio of 0.8 for the range of Reynolds numbers. The plot demonstrates a convergence solution in each case.

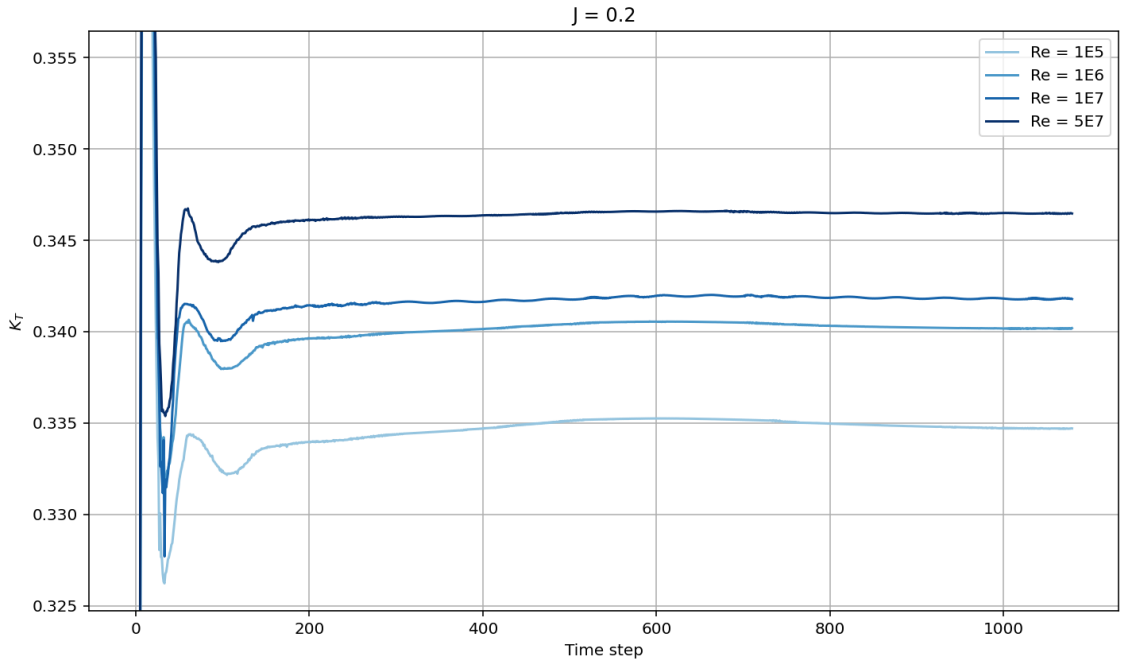

Figure D.34: The thrust coefficient over time for J equals 0.2, plotted for the flexible Wagningen C4-40 propeller with a pitch ratio of 0.8 for the range of Reynolds numbers. The plot demonstrates a convergence solution in each case.

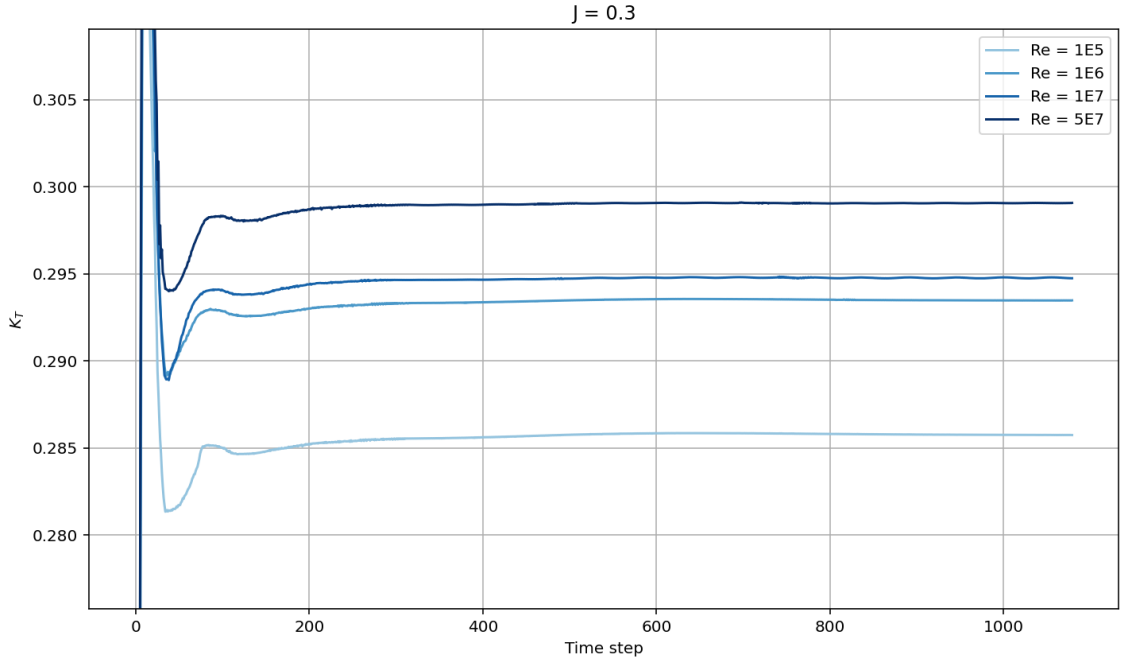

Figure D.35: The thrust coefficient over time for J equals 0.3, plotted for the flexible Wagningen C4-40 propeller with a pitch ratio of 0.8 for the range of Reynolds numbers. The plot demonstrates a convergence solution in each case.

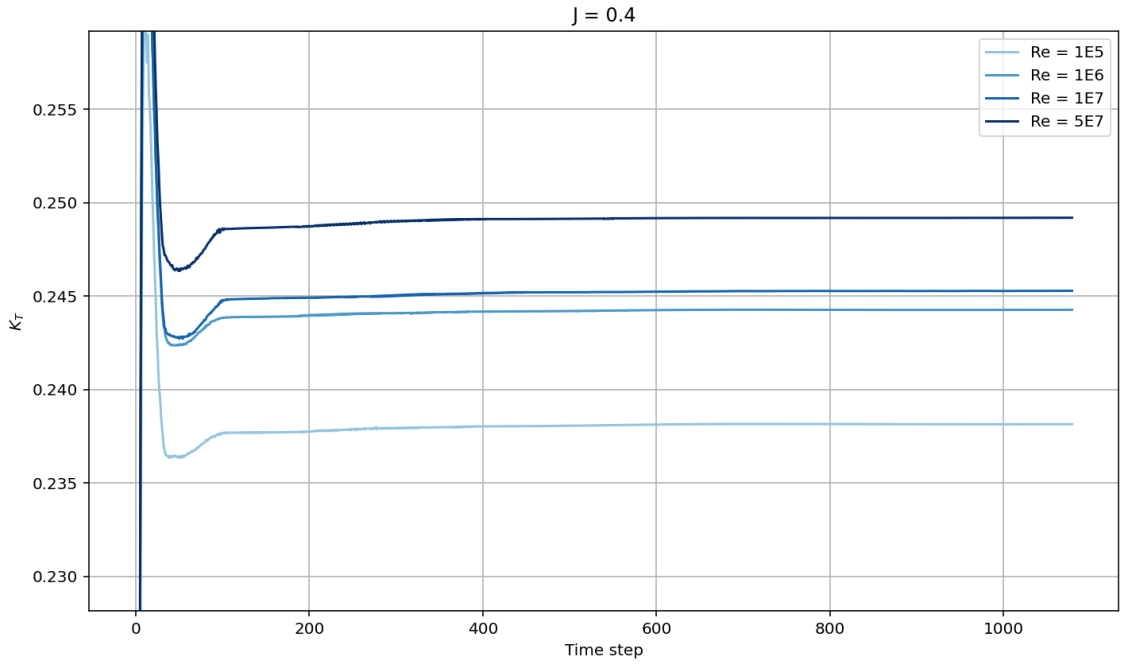

Figure D.36: The thrust coefficient over time for J equals 0.4, plotted for the flexible Wagningen C4-40 propeller with a pitch ratio of 0.8 for the range of Reynolds numbers. The plot demonstrates a convergence solution in each case.

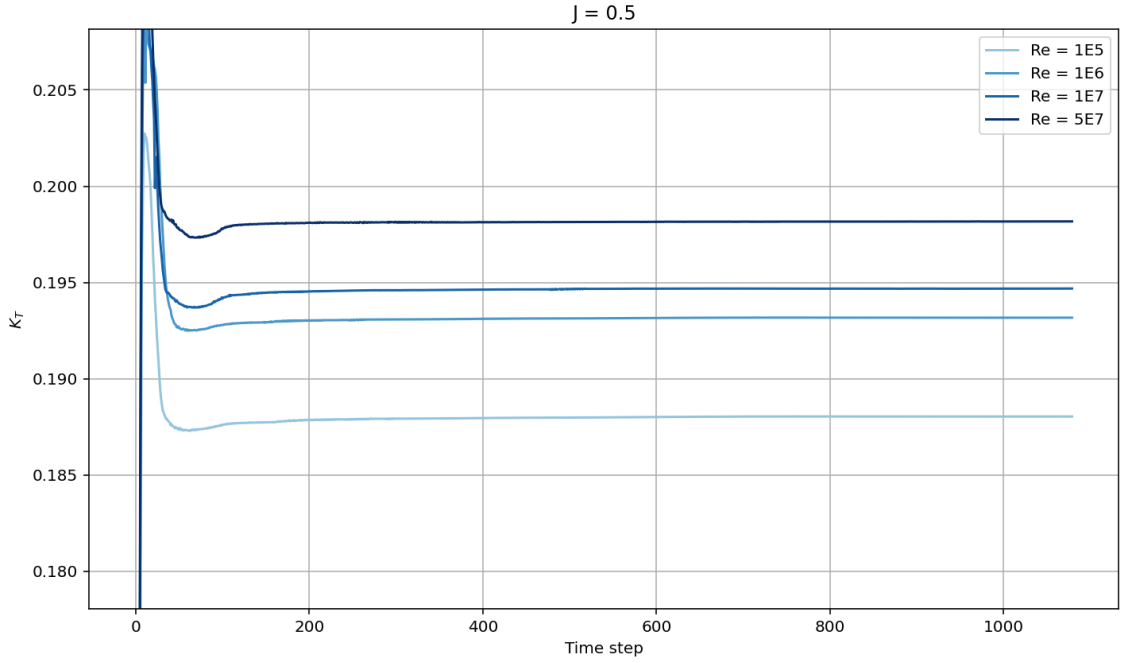

Figure D.37: The thrust coefficient over time for J equals 0.5, plotted for the flexible Wagningen C4-40 propeller with a pitch ratio of 0.8 for the range of Reynolds numbers. The plot demonstrates a convergence solution in each case.

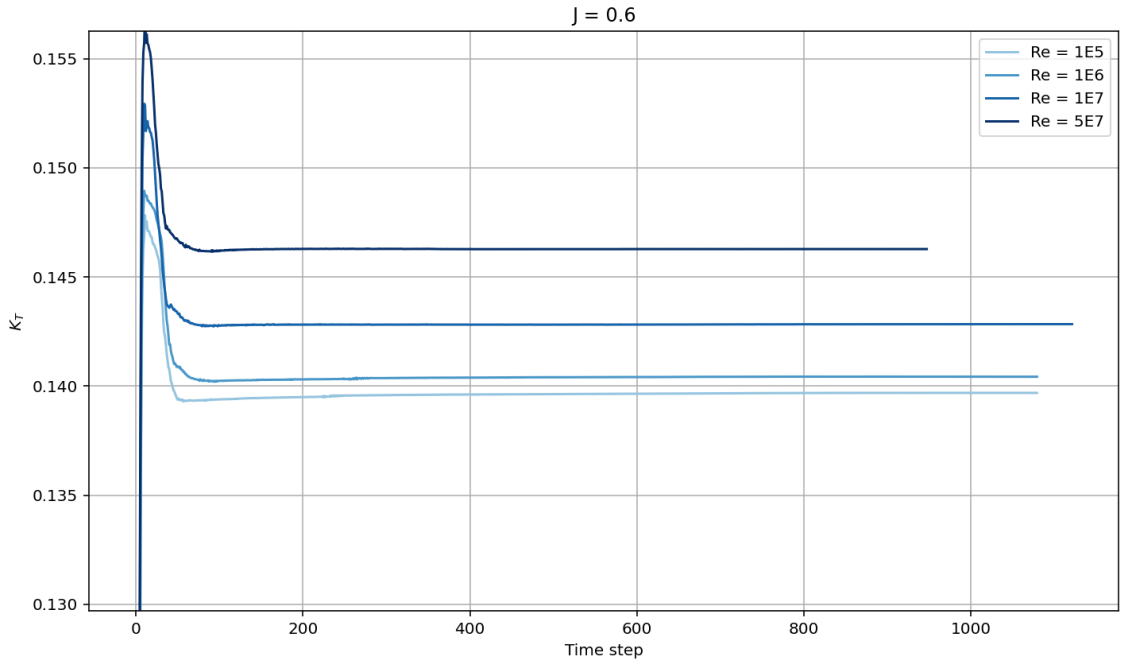

Figure D.38: The thrust coefficient over time for J equals 0.6, plotted for the flexible Wagningen C4-40 propeller with a pitch ratio of 0.8 for the range of Reynolds numbers. The plot demonstrates a convergence solution in each case.

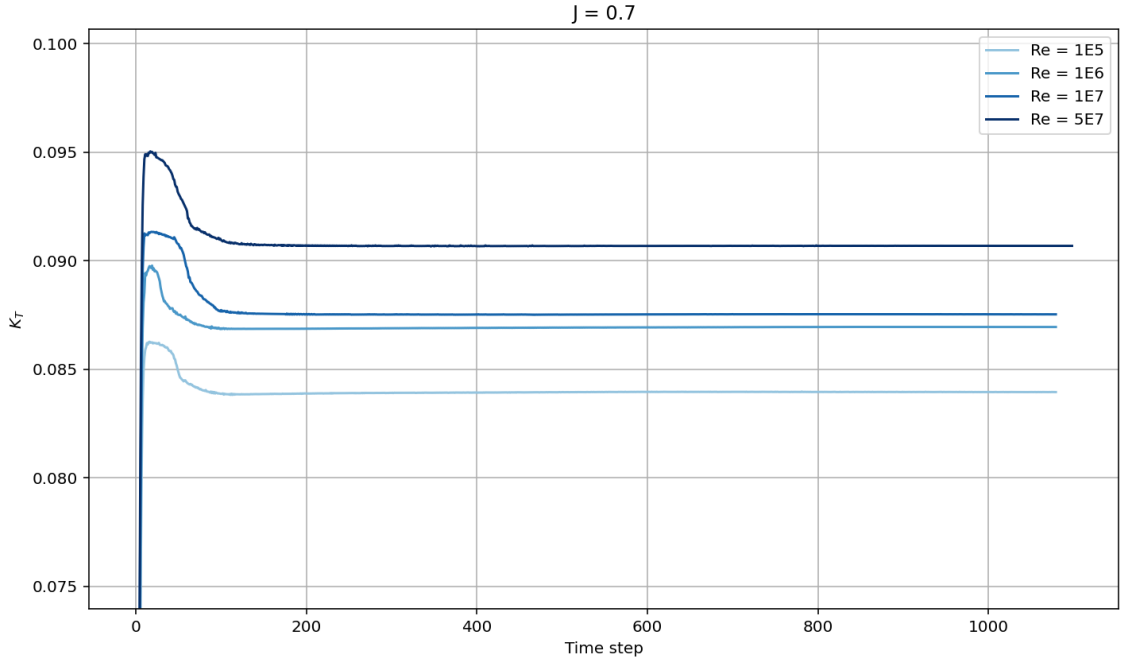

Figure D.39: The thrust coefficient over time for J equals 0.7, plotted for the flexible Wagningen C4-40 propeller with a pitch ratio of 0.8 for the range of Reynolds numbers. The plot demonstrates a convergence solution in each case.

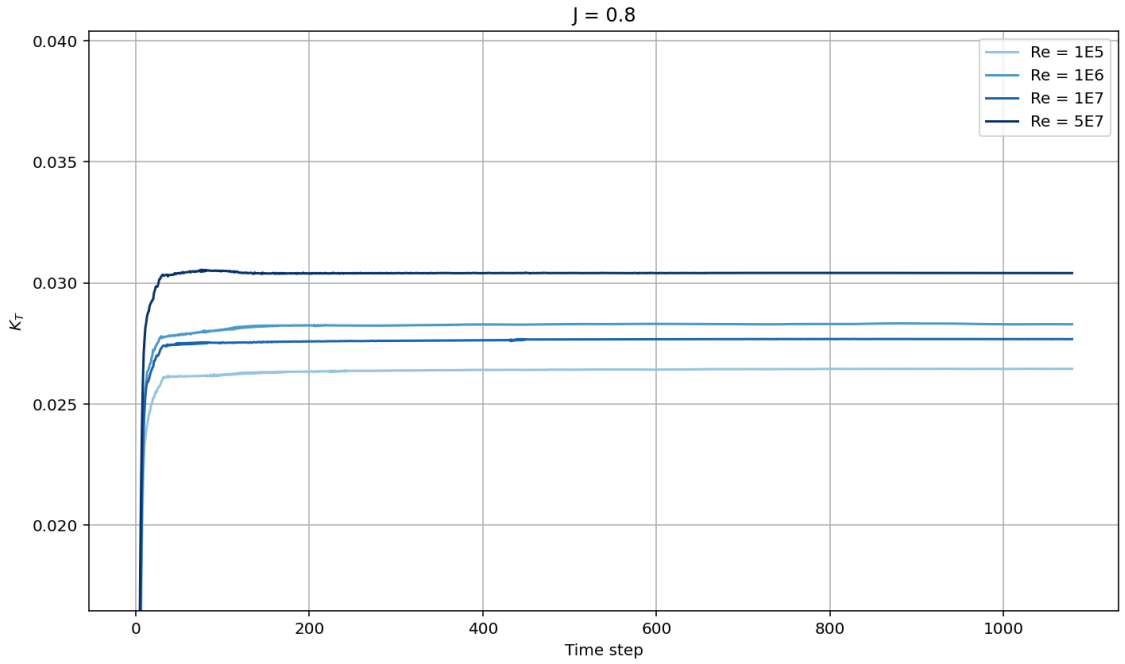

Figure D.40: The thrust coefficient over time for J equals 0.8, plotted for the flexible Wagningen C4-40 propeller with a pitch ratio of 0.8 for the range of Reynolds numbers. The plot demonstrates a convergence solution in each case.

E

Test Results Across a Range of Fluid-To-Structure Density Ratios

E.1. Thrust Coefficient Convergence

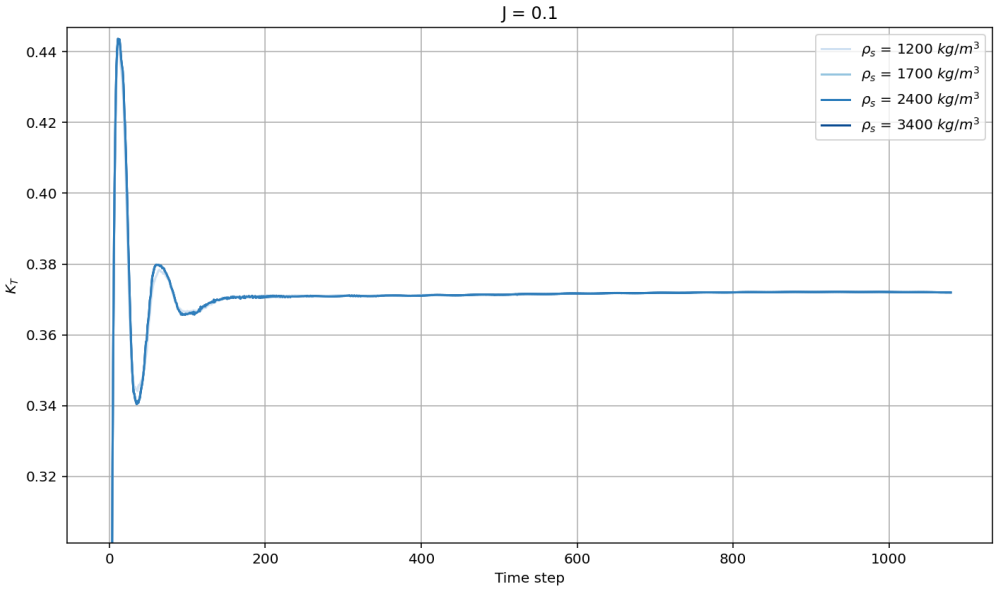

Figure E.1: The thrust coefficient over time for J equals 0.1, plotted for the flexible Wagningen C4-40 propeller with a pitch ratio of 0.8 for the range of Reynolds numbers. The plot demonstrates a convergence solution in each case.

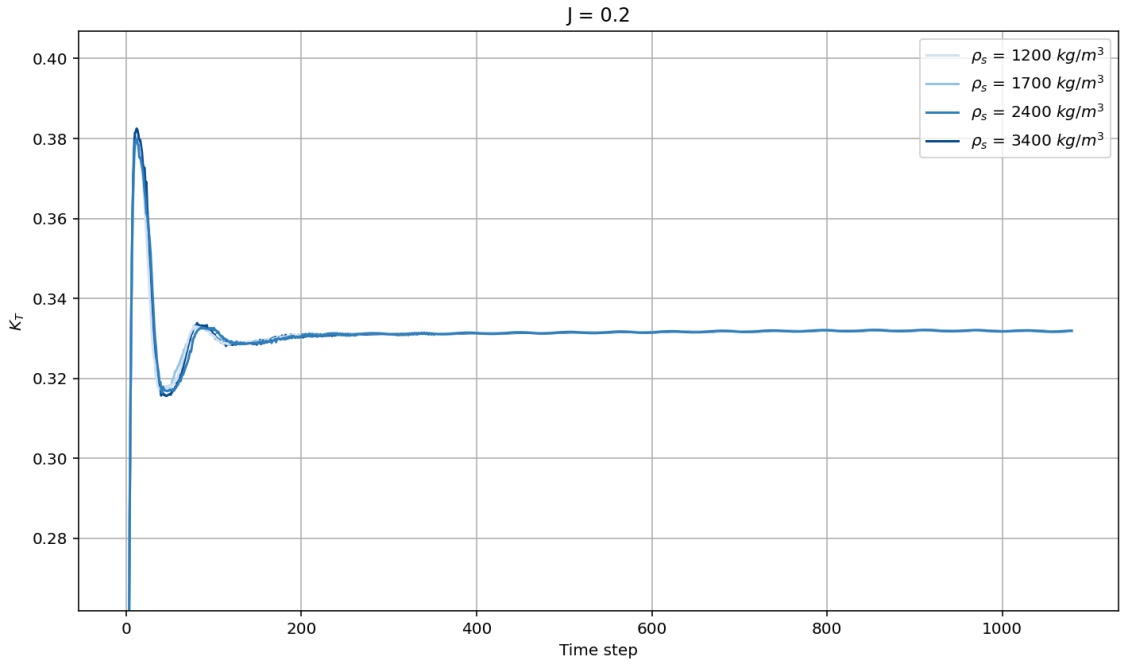

Figure E.2: The thrust coefficient over time for J equals 0.2, plotted for the flexible Wagningen C4-40 propeller with a pitch ratio of 0.8 for a range of density ratios. The plot demonstrates a convergence solution in each case.

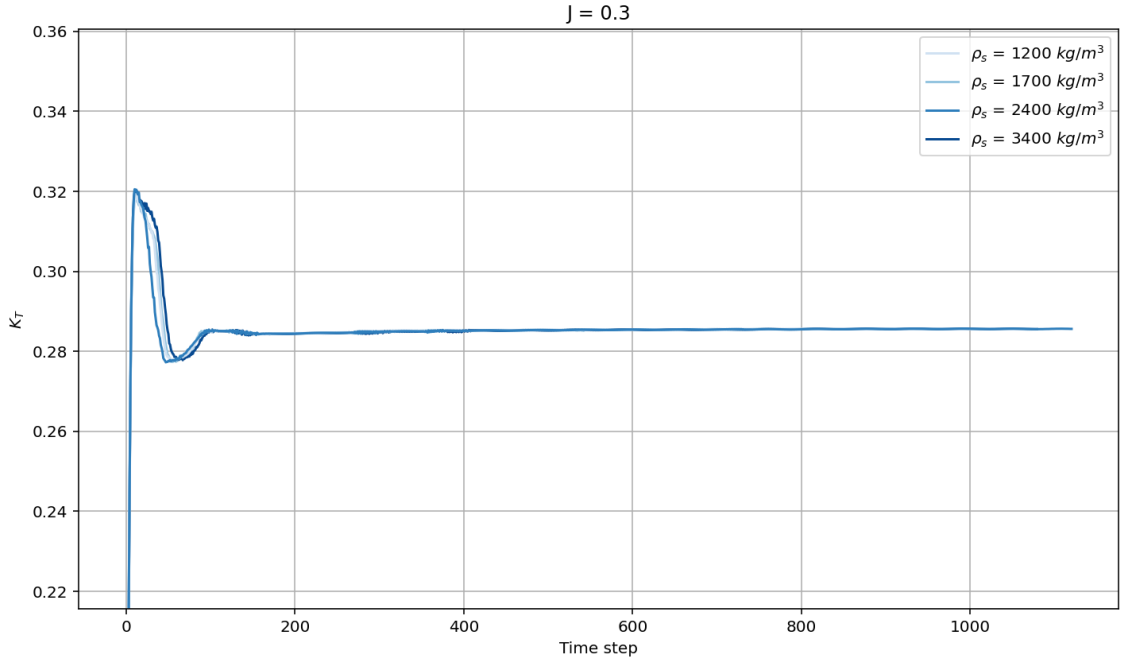

Figure E.3: The thrust coefficient over time for J equals 0.3, plotted for the flexible Wagningen C4-40 propeller with a pitch ratio of 0.8 for a range of density ratios. The plot demonstrates a convergence solution in each case.

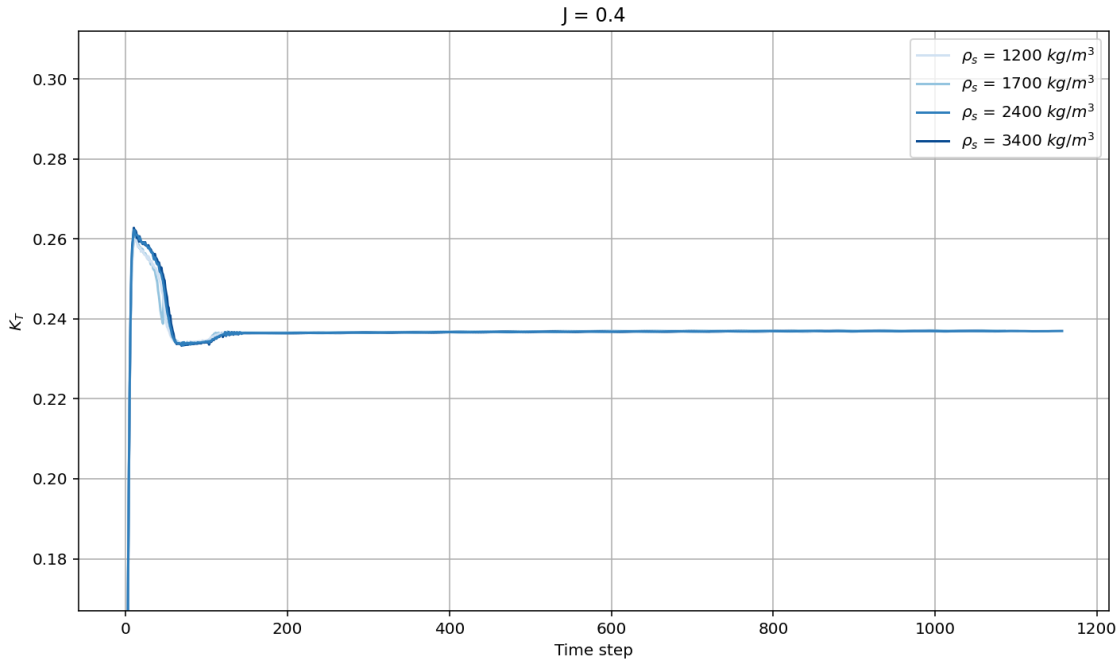

Figure E.4: The thrust coefficient over time for J equals 0.4, plotted for the flexible Wagningen C4-40 propeller with a pitch ratio of 0.8 for a range of density ratios. The plot demonstrates a convergence solution in each case.

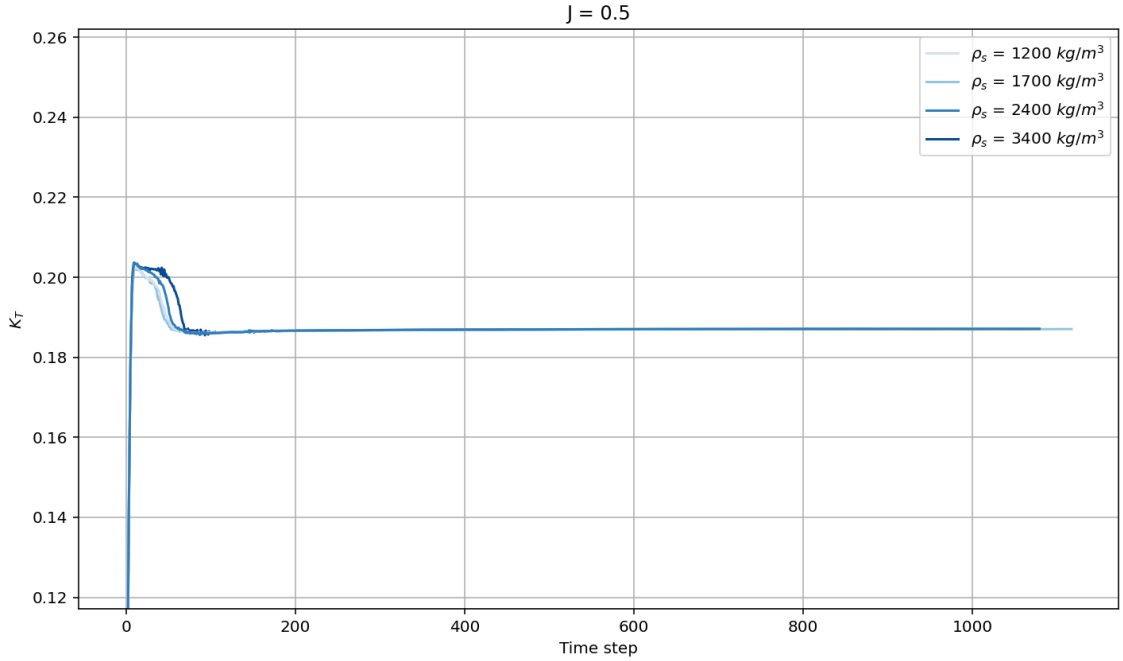

Figure E.5: The thrust coefficient over time for J equals 0.5, plotted for the flexible Wagningen C4-40 propeller with a pitch ratio of 0.8 for a range of density ratios. The plot demonstrates a convergence solution in each case.

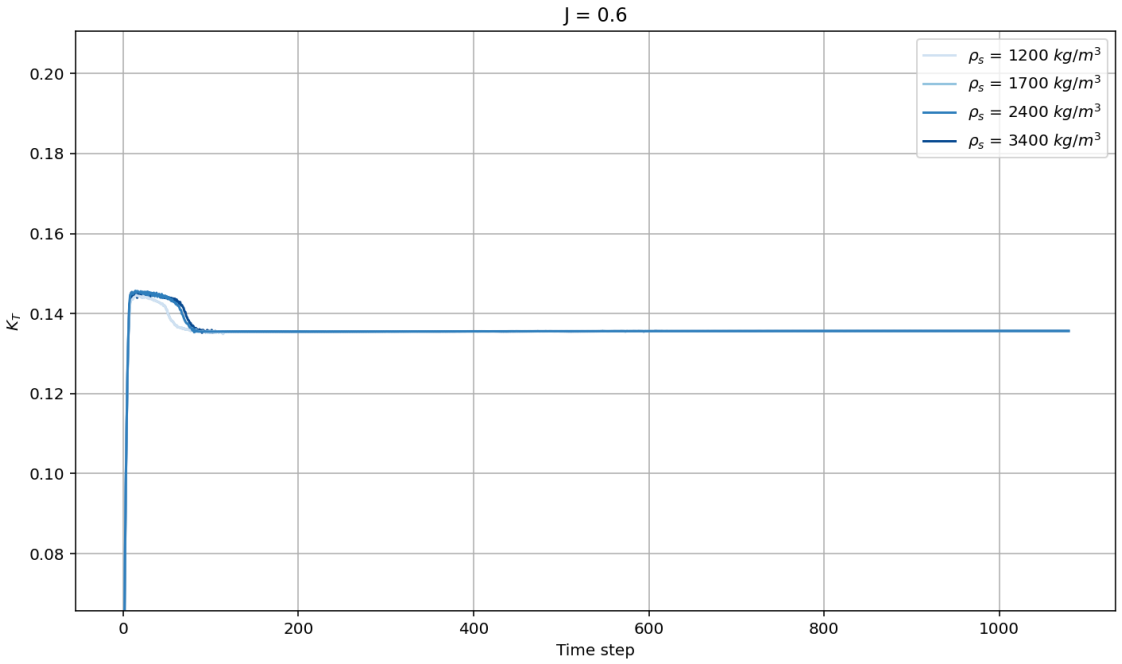

Figure E.6: The thrust coefficient over time for J equals 0.6, plotted for the flexible Wagningen C4-40 propeller with a pitch ratio of 0.8 for a range of density ratios. The plot demonstrates a convergence solution in each case.

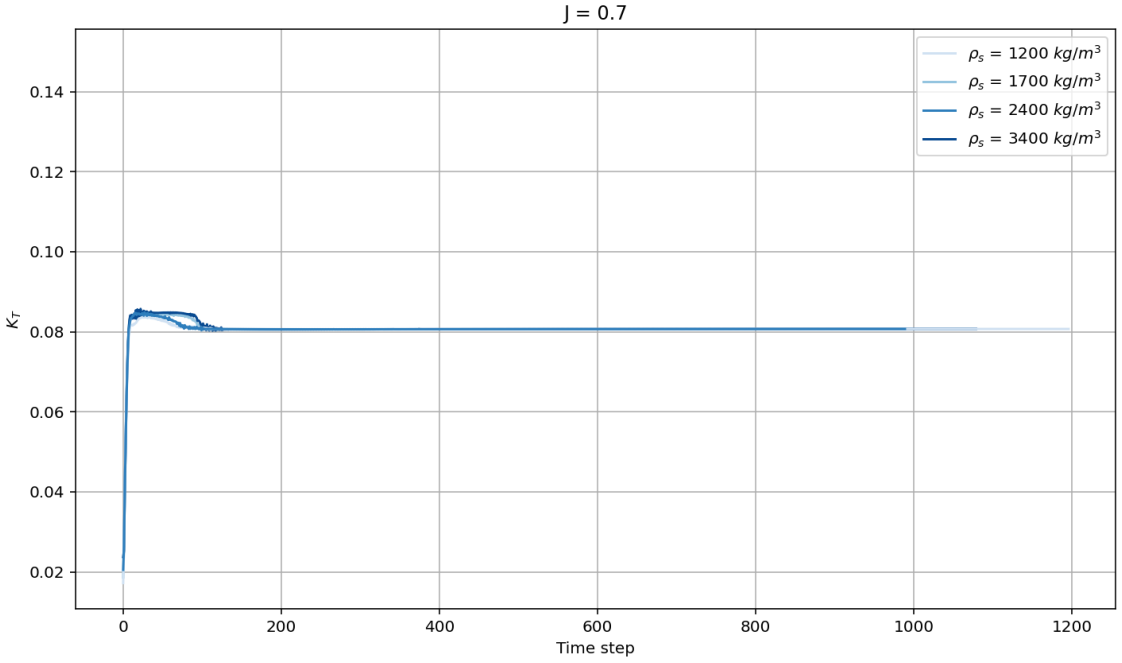

Figure E.7: The thrust coefficient over time for J equals 0.7, plotted for the flexible Wagningen C4-40 propeller with a pitch ratio of 0.8 for a range of density ratios. The plot demonstrates a convergence solution in each case.

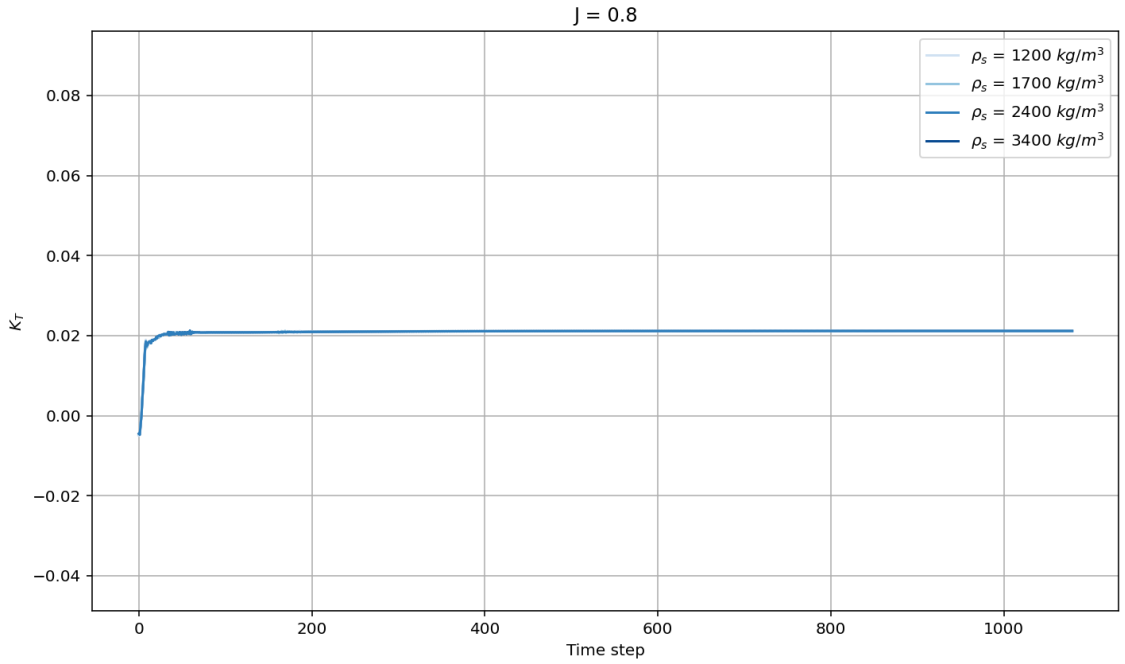

Figure E.8: The thrust coefficient over time for J equals 0.8, plotted for the flexible Wagningen C4-40 propeller with a pitch ratio of 0.8 for a range of density ratios. The plot demonstrates a convergence solution in each case.